Lava flow thickness estimation on the Moon and Mercury based on modeling the topographic degradation of partially buried impact craters

Jun Du

UNIVERSITÉ CÔTE D'AZUR

ÉCOLE DOCTORALE
SCIENCES FONDAMENTALES ET APPLIQUÉES

北京大學
PEKING UNIVERSITY

THÈSE DE DOCTORAT

Estimation de l'épaisseur des coulées de lave sur la Lune et le Mercure basée sur la modélisation de la dégradation topographique de cratères d'impact

Jun DU

Laboratoire Lagrange

Présentée en vue de l'obtention du grade de docteur en Terre, Univers, Espace
d'Université Côte d'Azur
et d'Université de Pékin
Dirigée par : Mark A. Wieczorek
Co-encadrée par : Wenzhe Fa
Soutenue le : 03/12/2019

Devant le jury, composé de :
Patrick Michel, Recherche, UCA
Marco Delbo, Recherche, UCA
Qiming Zeng, Professeur, PKU
Nan Zhang, Professor, PKU
Yang Liu, Professeur, CAS
Zongyu Yue, Professeur, CAS

国家留学基金管理委员会 · CHINA SCHOLARSHIP COUNCIL

Declaration

I declare that this dissertation has not been previously accepted in substance for any degree and is not being concurrently submitted in candidature for any degree. 1 state that this dissertation is the result of my own independent investigation/work, except where otherwise stated. I hereby give consent for my dissertation, if accepted, to be available for photocopying and understand that any reference to or quotation from my thesis will receive an acknowledgement.

DU Jun

Beijng, China

December 1, 2019

Résumé

Dans cette étude, les cratères partiellement enterrés dans la maria lunaire et dans les plaines lisses septentrionales de Mercure ont été identifiés à l'aide de données récemment acquises concernant l'optique, l'élévation et la composition, et les épaisseurs de coulées de lave proches des cratères partiellement enterrés ont été estimées par modélisation numérique de leur dégradation topographique.

Au chapitre 1, je présente d'abord le contexte géologique des plaines volcaniques de la Lune et de Mercure. Ensuite, je vais résumer toutes les méthodes qui ont été utilisées pour estimer l'épaisseur des coulées de lave sur la Lune et Mercure, ainsi que les progrès de la recherche sur la dégradation topographique du cratère.

Au chapitre 2, je présente les ensembles de données de télédétection utilisés dans cette étude. Ensuite, les critères utilisés pour identifier les cratères partiellement enterrés sont discutés. Une méthode d'estimation de l'épaisseur des coulées de lave est proposée ultérieurement, basée sur la dégradation topographique de cratères partiellement enterrés. L'épaisseur de coulée de lave la mieux adaptée a ensuite été déterminée en minimisant la différence entre le profil final modélisé et le profil observé.

Au chapitre 3, afin de résoudre l'équation de diffusion topographique, le profil d'altitude d'un nouveau cratère d'impact est construit comme condition initiale. Pour les cratères d'impact frais lunaires, nous avons construit un ensemble de profils topographiques qui prennent en compte à la fois la taille des cratères et les types de cibles. Pour les nouveaux cratères d'impact sur Mercure, nous avons construit des profils topographiques qui incluent uniquement des cratères de transition et complexes.

Comme décrit au chapitre 4, les épaisseurs de basalte ont été inversées en utilisant 41 cratères de maria dont les bords sont complètement exposés. Le résultat montre que les épaisseurs estimées en basalte mare varient de 33 à 455 m, avec

une valeur médiane de 105 m. Nous avons ensuite calculé le volume total et le taux d'éruption des basaltes des maria lunaires et avons constaté que le taux estimé d'éruption des basaltes des maria atteignait un sommet de 3,4 Ga, puis diminuait avec le temps, indiquant un refroidissement progressif de l'intérieur de la lune. Nous avons également constaté que la diffusivité topographique des cratères lunaires augmente avec le diamètre et est presque invariante dans le temps.

Au chapitre 5, je présente un résultat similaire pour Mercure. Les épaisseurs de coulées de lave ont été inversées pour 21 cratères dont les bords ont été exposés. Le résultat montre que les épaisseurs de coulées de lave varient de 23 à 536 m, avec une valeur médiane de 228 m. Nous avons également calculé le volume total des coulées de lave. Le paramètre de diffusivité topographique sur la Lune est plus faible que sur Mercure, ce qui indique que le flux météoritique d'impact sur la Lune est moins important.

Comme indiqué au chapitre 6, il reste quelques problèmes à résoudre à l'avenir. Tout d'abord, j'ai utilisé une géométrie axisymétrique simple lors de la résolution analytique de l'équation de diffusion topographique et n'ai pas envisagé un processus de dégradation topographique entièrement tridimensionnel. Deuxièmement, les diffusivités topographiques inversées présentent un large intervalle d'incertitude et ne sont pas bien contraintes. Troisièmement, les cratères complexes ont généralement un mécanisme de formation compliqué et un fond géologique et une morphologie de cratère variables, ce qui entraîne une variabilité et une incertitude considérables des relations morphométriques du cratère.

MOTS CLÉS: cratère partiellement enterré, dégradation topographique, épaisseur des coulées de lave, morphométrie du cratère

Abstract

In this study, partially buried craters on the lunar maria and the northern smooth plains of Mercury were identified using recently acquired optical, elevation, and composition data, and lava flow thicknesses near partially buried craters were estimated by numerically modeling their topographic degradation.

In Chapter 1, I first introduce the geologic background of the volcanic plains on the Moon and Mercury. Next, I will summarize all the methods that have been used to estimate the lava flow thicknesses on the Moon and Mercury, as well as the research progress on the crater topographic degradation.

In Chapter 2, I present the remote sensing datasets used in this study. Then, the criteria used to identify partially buried craters are discussed. A lava flow thickness estimation method is later proposed based on the topographic degradation of partially buried craters. The best fitting lava flow thickness was then determined by minimizing the difference between the modeled final profile and the observed profile.

In Chapter 3, in order to solve the topographic diffusion equation, the elevation profile of a fresh impact crater is constructed as the initial condition. For lunar fresh impact craters, we constructed a set of topographic profiles that consider both crater sizes and target types. For fresh impact craters on Mercury, we constructed topographic profiles that only include transitional and complex craters.

As described in Chapter 4, the basalt thicknesses were inverted using 41 mare craters whose rims are completely exposed. The result shows that the estimated mare basalt thicknesses vary from 33 to 455 m, with a median value of 105 m. We then calculated the total volume and eruption rate of lunar mare basalts, and found that the estimated eruption rate of mare basalts peaked at 3.4 Ga and then decreased with time, indicating a progressive cooling of the lunar interior. We also found that the topographic diffusivity of lunar craters increases with diameter and

is almost invariant with time.

In Chapter 5, I present a similar result for Mercury. The lava flow thicknesses were inverted for 21 craters whose rims were exposed. The result shows that the lava flow thicknesses vary from 23 to 536 m, with a median value of 228 m. We also calculated the total volume of the lava flows. The topographic diffusivity on the Moon is smaller than that on Mercury, indicating the impact flux on the Moon is lower.

As shown in Chapter 6, there are some remaining issues that need to be solved in the future. First, I employed a simple axisymmetric geometry when analytically solving the topographic diffusion equation and did not consider a fully three-dimensional topographic degradation process. Second, the inverted topographic diffusivities have a large range of uncertainty and are not well constrained. Third, complex craters usually have complicated formation mechanism and a variable geologic background and crater morphology, resulting in considerable variability and uncertainty in the crater morphometric relations.

KEY WORDS: partially buried crater, topographic degradation, lava flow thickness, crater morphometry

Contents

Contents ..... **vii**

Chapter 1 Introduction **1**

1.1 Background 1

1.2 Scientific Significances 6

1.2.1 Volcanism 7

1.2.2 Impact Cratering 8

1.3 Overview of Previous Methods 9

1.3.1 Mare Basalt Thickness 9

1.3.2 Smooth Plains Thickness 18

1.3.3 Crater Degradation on the Moon 21

1.3.4 Crater Degradation on Mercury 23

1.4 Objectives and Outlines 25

Chapter 2 Data and Methods **27**

2.1 Overview 27

2.2 Data 29

2.2.1 The Moon 29

2.2.2 Mercury 34

2.3 Identification of Partially Buried Craters 41

2.4 Lava Flow Thickness Estimation Method 46

2.4.1 Model Descriptions 46

2.4.2 Model Setup 50

2.4.3 Uncertainty Analyses 52

Chapter 3 Initial Shape Modeling of Fresh Craters **55**
3.1 Method Overview 55
3.2 Database, Preprocessing, and Classification 57
3.2.1 Database 57
3.2.2 Preprocessing 58
3.2.3 Classification 62
3.3 Methods 65
3.3.1 Definitions of Morphometric Parameters 65
3.3.2 Simple Craters 66
3.3.3 Transitional and Complex Craters 67
3.4 Results and Comparisons 70
3.4.1 The Moon 70
3.4.2 Mercury 86
3.5 Effect of Crater Degradation on Rim Height 98
3.5.1 The Moon 99
3.5.2 Mercury 101

Chapter 4 Mare Basalt Thickness on the Moon **103**
4.1 Database and Classification of Buried Craters 103
4.1.1 Case Studies of Buried Craters 106
4.1.2 Spatial Distribution and Statistics of Buried Craters 109
4.2 Mare Basalt Thickness Estimation Results 112
4.3 Discussions 115
4.3.1 Comparison with Other Techniques 115
4.3.2 Cumulative Volume and Eruption Rates of Mare Basalts 121
4.3.3 Scale and Temporal Dependence of Crater Degradation 124

Chapter 5 Lava Flow Thickness on Mercury **129**
5.1 Database and Classification of Buried Craters 129
5.1.1 Case Studies of Buried Craters 131
5.1.2 Spatial Distribution and Statistics of Buried Craters 134
5.2 Lava Flow Thickness Estimation Results 138

5.3 Discussion 142
5.3.1 Comparison with Other Techniques 142
5.3.2 Total Volume of the Lava Flows 143
5.3.3 Scale Dependence of Crater Degradation 145

Chapter 6 Conclusions 149
6.1 Summary of This Study 149
6.2 Outlook for Lava Flow Thickness Estimation on Mars 150

Bibliography 153

Appendix A The Moon 175
A.1 Buried Crater Database 175
A.2 Mare Basalt Thickness Estimation Results 189

Appendix B Mercury 201
B.1 Buried Crater Database 201
B.2 Lava Flow Thickness Estimation Results 232

Chapter 1 Introduction

1.1 Background

Impact cratering and volcanism are the two major processes shaping the surface of the Moon and Mercury. Impact cratering created large topographic relief on the surface, whereas volcanic products filled in the topographic lows and produced new surfaces. Impact cratering and volcanism also act on each other as well. On the one hand, impact cratering produced stress conditions in the crust that favour the ascent of the magma (Michaut and Pinel, 2018). On the other hand, lavas might either partially or completely bury a previously formed impact crater depending on the thickness of the flow and the height of the crater rim. As a result, the observed planetary surface morphology and the size-frequency distribution of surface craters have been evolving due to the combined effect of crater formation and lava flow emplacement.

The lunar maria are composed of iron-rich basalts that were originally generated by partially melting the mantle, then driven by excess pressure at or below the crust-mantle boundary to propagate upward through dikes, and finally extruded out to form larger-scale, effusive plains over the lunar surface (Figure 1.1) (Head, 1976; Head and Wilson, 2017; Wilson and Head, 1981, 2017). Radiometric measurements of lunar samples and crater-counting of basaltic units suggest that most of the mare basalts erupted from 4 to 1.2 Ga (Head, 1976; Hiesinger et al., 2011) with a few exceptions of extremely old and young basaltic units being recorded. For example, rare basaltic clasts in lunar meteorites have ages as old as 4.36 Gyr (Snape et al., 2018), some pre-basin basalts were covered by ejecta from basins such as Imbrium and Orientale (known as cryptomaria) (Bell and Hawke, 1984), and some isolated irregular mare patches were dated to as young as 50 Myr in age (Braden et al., 2014). As a first-order approximation, the volume of mare basalts can be simply estimated as the product of their surface area and thickness. In early studies, the

total surface area of mare basalts was estimated to be about 6.2×10^6 km^2, covering ~17% of the lunar surface (Head, 1975). The mare basalt thickness, however, varies from place to place, from several meters to several kilometers.

In addition to volcanic eruptions, another process shaping the Moon's surface is impact cratering events resulted from the meteoroid bombardments. These craters could be so large that they created large cracks in the crust that favour the propagation of magmas. Or, these craters were later partially or completely buried by subsequent lava flows. Finally, the youngest craters formed on today's lunar surface. The stratigraphic relation in the lunar maria therefore can be summarized as follows. (1) During the very early stage, some craters may form on the highland materials, of which the crater rims must have a highland composition. If the crater rim height is larger than the total basalt thickness, this crater would still be observed nowadays on the lunar surface with an exposed crater rim. Otherwise, this crater would be buried by subsequent lava flows and can not be traced later. (2) Then, multiple phases of lava flows with different thicknesses and FeO/TiO_2 contents may erupt and emplace on the lunar surface, accompanying with the formation of another certain number of craters. These craters formed on the mare basalts, of which the crater rims should have a mare composition. If the crater rim height is larger than the summed thickness of lava flows emplaced after the crater formation, this crater would be observable with an exposed crater rim. Otherwise, this crater would be buried by subsequent lava flows and can not be identified any more. (3) As a result, the observed size-frequency distribution of lunar craters has been evolving all the time due to the combined effect of crater formation and basalt emplacement. We therefore conclude that impact craters (e.g., morphology, rim/ejecta composition, and size-frequency distribution) could provide important clues on the stratigraphy studies (e.g., thickness and age) of lunar maria.

Similar to lunar maria, the northern smooth plains on Mercury are also made of magmas that were generated by partially melting the mantle and then reached to the surface to form large-scale, effusive lava plains (Figure 1.2) (Denevi et al., 2013; Head et al., 2011). In composition, these magmatic materials are similar to terrestrial basalts and komatiites based on their diagnostic characteristics in the X-ray fluorescence data (Denevi et al., 2013; Head et al., 2011). Unlike lunar maria that consist of individual units with different ages, the surface age within the northern

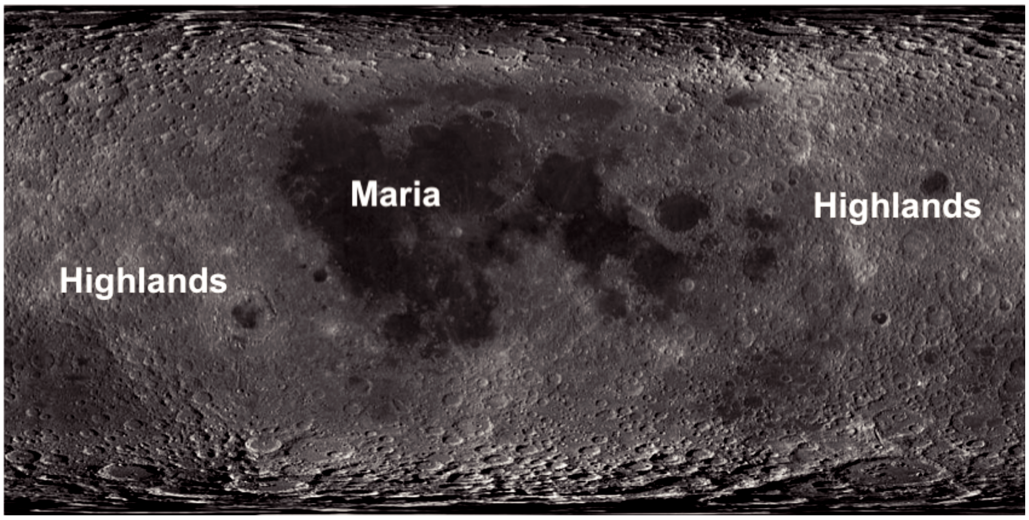

Figure 1.1: The LROC/WAC global albedo image of the Moon. The dark areas are mare basalts. The bright areas are highlands.

smooth plains does not vary significantly from place to place and has almost the same age of 3.7 Gyr (Ostrach et al., 2015). This age corresponds approximately to the age of the youngest impact basin on the Moon (Orientale). The surface area of the northern smooth plains was estimated to be 4.7×10^6 km^2, or about 6% of the total surface area of the planet. The thickness of the lava flow in this region, however, is much poorly constrained than that in lunar maria, mainly due to the reason that there are only two planetary missions that have visited Mercury with a few scientific payloads. Nevertheless, based on the rim heights of completely buried craters, the lava flow thicknesses were estimated to be at least 0.7–2 km (Head et al., 2011; Ostrach et al., 2015). Inferred from the width of the graben, the lava flows were calculated to be at least 2 km thick (Watters et al., 2012). Obviously, both methods can only give a lower bound of the lava flow thickness, and we still lack a precise, quantitative estimate.

In this study, we focus on using the morphology of impact craters that are partially buried by lava flows, in order to estimate the thickness of lavas that were emplaced after the crater formed. Using lunar craters as examples, the continuous ejecta blanket of a normal, unflooded crater usually extends about one crater radius from the crater rim (Moore et al., 1974). A partially buried crater forms when a lava flow covers the distal low-elevation ejecta, leaving the high-elevation rim crest visible (Baldwin, 1970; Eggleton, 1961; Marshall, 1963) (Figures 1.3a and b). Note that craters could also be infilled or buried by ejecta from nearby craters (Xie and

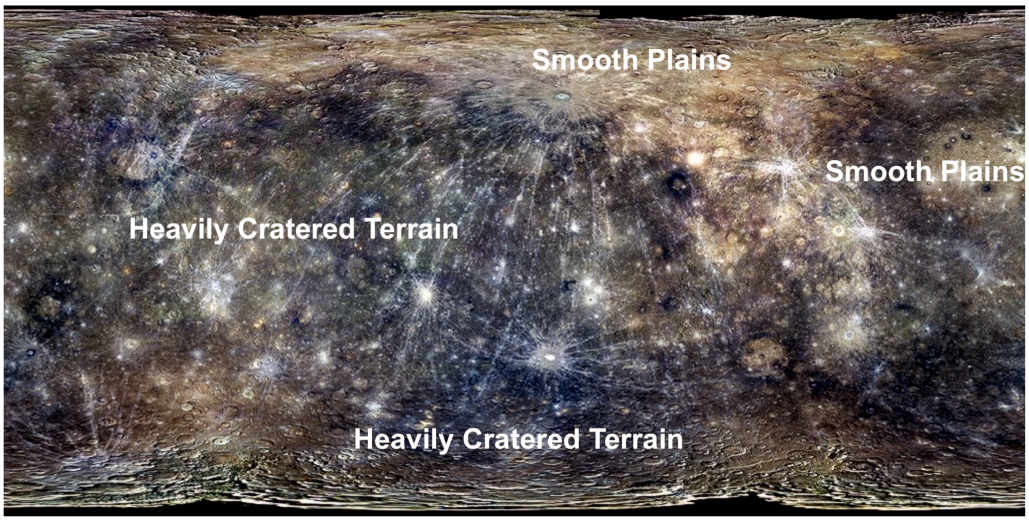

Figure 1.2: The MESSENGER/MDIS global albedo image of Mercury. The bright areas are smooth plains. The dark areas are heavily cratered terrain.

Zhu, 2016), but craters partially buried by ejecta deposits will not be considered in this study.

The lava flow thickness surrounding a partially buried crater can be calculated if two quantities are known: the total rim height as defined by the elevation difference between the rim crest and pre-flooding background surface, and the exposed rim height with respect to the present-day surroundings (De Hon, 1974). The lava flow thickness here refers to the elevation difference between the surface of the lava flow and the pre-flooding background that is beyond the crater ejecta region. In practice, the exposed rim height was easily measurable, whereas the total rim height was estimated based on the observed morphology of fresh craters. Previous studies used scaling relations between crater rim height and diameter of fresh craters (Baldwin, 1949, 1963; Pike, 1972, 1967, 1977) to estimate the total rim height and hence the lava flow thickness. Note that the fresh craters defined here are usually Copernican and Eratosthenian in age as defined by Pike (1977), although there are other definitions of fresh craters (e.g, those who have optical rays as defined by Werner and Medvedev (2010)). This technique can be seen in Figures 1.3a and c where a fresh-looking partially buried crater Brayley is shown. In this case, the basalt thickness (T_{b}) is equal to the total rim height of a fresh crater (h_{f}, predicted by present-day crater diameter) minus the measured exposed rim height (h_{e}). Using early topography data (e.g., Lunar Topographic Orthophotomap/LTO and Lunar Astronautical Chart/LAC) on the Moon, mare basalts near partially buried craters

in the western (45°S–45°N; 90°W–10°E) and eastern (30°S–30°N; 0–100°E) maria were estimated to be 400 and 200 to 400 m thick on average, respectively (De Hon and Waskom, 1976; De Hon, 1979b).

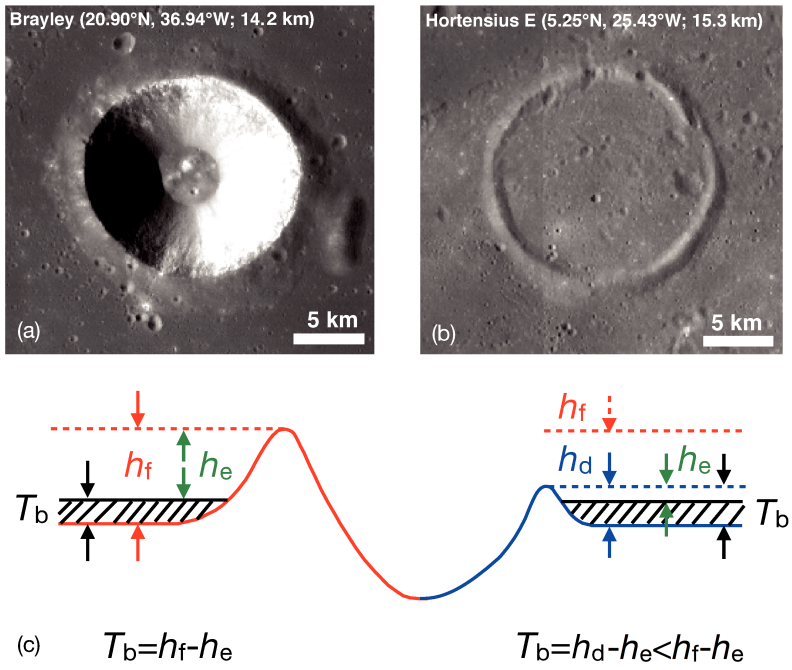

Figure 1.3: An example of a fresh partially buried crater Brayley (D=14.2 km) (a). An example of a degraded partially buried crater Hortensius E (D=15.3 km) (b). A diagram showing how to estimate the thickness of mare basalts around a partially buried crater (c). In (c), T_b is the basalt thickness, h_f is the total rim height of a fresh crater, h_e is the exposed rim height, and h_d is the total rim height of a degraded crater.

However, craters on the Moon and Mercury suffer from continual meteoroid bombardment and other mass-wasting processes. As a result, with increasing time, the crater diameter should increase and the rim height should decrease due to the downslope movement of rim materials. If the initial rim height were used to determine the lava flow thickness, then the lava flow thickness would be overestimated if the crater erosion were significant. An example can be seen in Figures 1.3b and c where a degraded partially buried crater Hortensius E is shown. In this case, the basalt thickness (T_b) is equal to the total rim height of the degraded crater (h_d) minus the measured exposed rim height (h_e), and the total rim height of the degraded crater (h_d) is definitely larger than that of the fresh crater (h_f).

To account for crater degradation, Hörz (1978) randomly selected 82 lunar highland craters with different degradation states and measured their rim heights.

As the obtained median rim height is only 58% of that for fresh lunar craters (Pike, 1977), Hörz (1978) then simply reduced all the basalt thickness estimates in De Hon and Waskom (1976) and De Hon (1979b) by a factor of two. The resulting, revised median mare basalt thickness on the lunar nearside was estimated to be smaller than 300 m. Nevertheless, the classification of ages and degradation states for the lunar highland craters in Hörz (1978) was largely qualitative, and therefore, a quantitative topographic degradation model is here invoked to better quantify the rim height reduction as a function of time.

High-resolution and high-quality remote sensing datasets have been acquired from the latest planetary exploration missions. Examples are the Lunar Reconnaissance Orbiter (LRO) mission to the Moon that launched in 2009, and the MErcury Surface, Space ENvironment, GEochemistry, and Ranging (MESSENGER) mission that inserted into Mercury's orbit in 2011. In addition, the understanding of topographic degradation mechanisms of impact craters has also been greatly improved. Both factors make it possible to reconstruct the databases of partially buried craters on the Moon and Mercury and better constrain the lava flow thicknesses around them. In this study, partially buried craters on lunar maria and the northern smooth plains of Mercury were identified using recently acquired optical, elevation, and composition data, and lava flow thicknesses near partially buried craters were estimated by numerically modeling their topographic degradation.

1.2 Scientific Significances

The core idea of this study is to estimate the thickness of the volcanic lava flow through morphologic studies of impact craters. Estimating the thickness of the volcanic materials is therefore the fundamental scientific goal of this study, and by doing so we hope to deepen our understanding of planetary volcanism. Studying the topographical degradation of impact craters is a necessary tool to achieve this scientific goal. Moreover, the inversion results obtained by a crater topographic degradation model (such as topographic diffusivity) can in turn aid our understanding of the crater degradation mechanisms. Therefore, the results obtained in this study can help to better understand the internal thermal evolution and surface processes of terrestrial planets from two aspects: volcanism and impact cratering.

1.2.1 Volcanism

The lava flow thickness and the resulting volume of the volcanic materials that erupted and emplaced on the planet's surface are of great scientific significance, because they can constrain the thermal evolution of the planet, reveal the sources and styles of volcanism, and contribute to the subsequent tectonic activity and lithospheric deformation (Head, 1982; Solomon and Head, 1979, 1980). We next explain in detail how the lava flow thickness estimation improves our understanding on these aspects.

For the thermal evolution of the planet, once the thickness is obtained, the volume and eruption rate of the lava flows can be calculated if the surface area and age are known. The volume of the lava flows on the surface can reveal the degree to which the planet is partially melted and the volume of the produced melt, which in turn helps to understand the mineral composition and temperature distribution within the planet. The eruption rate of the lava flow can reveal the thermal evolution history of the planet and thus help to understand the temporal variation of the thermal state of the planet. In particular, the estimated volume and eruption rate of the lava flow can be used to further constrain the theoretical thermal-chemical evolution model of the Moon and Mercury (Laneuville et al., 2013; Padovan et al., 2017).

For the type and source of volcanic eruptions, it might be deduced from the thickness and volume of the lava flows. The volcanic eruptions mainly have three types: (1) a calm, fluid-type event forming effusive plains, (2) a violent, explosive event with high gaseous content, and (3) an intermediate type between the two. If there are multiple lava flow thickness estimates in the region, we can then produce an interpolated isopach map, which may help us to locate the source vent where the lava flows came from.

After the volcanic lava flows were emplaced in a large basin, a tensile stress field may form at the edge to develop concentric circular graben, and a compressive stress field may form at the center to produce wrinkle ridges (Hiesinger and Head, 2006). No matter a graben or a wrinkle ridge formed, it is closely related to the thickness, cooling, and strength of the lava flow (Freed et al., 2012). In addition, the volcanic fillings may also result in downward deformation of the underlying crust, which is also directly related to the thickness of the lava flows. The study of how much

the crustal layer has deformed can provide us some hints on the strength, viscosity, temperature and heat flow of the crust and thus deepen our understanding of the thermal and dynamic evolution of the planet.

Using recently acquired high-quality and high-resolution remote sensing data, the lava flow thickness obtained by other methods have been updated and further improved. However, for impact craters partially buried by lava flows, the global database has not been updated for nearly 50 years, and the effect of crater rim erosion on the overestimation of lava flow thickness has never been quantitatively considered. Therefore, it is necessary to reinvestigate the lava flow thicknesses around partially buried craters on the Moon and Mercury, and we hope to obtain a more comprehensive understanding of the planetary volcanism.

1.2.2 Impact Cratering

As a by-product, the topographic diffusivity obtained from this study also provides an opportunity to look into the mechanisms of the crater topographic degradation. This quantity, however, can only be estimated when the age of the surface unit embaying the partially buried crater is known independently. To be more specific, it can allow us to investigate whether or not the crater topographic degradation is diameter- or time-dependent. Once the topographic diffusivity can be well constrained, it would provide another tool to date the crater based on the crater morphology.

On the other hand, solving the topographic diffusion equation requires the initial elevation profiles of fresh craters, which we will construct in this study. We will develop a more complete version for lunar craters that considers both crater size and target type, and will build the first initial elevation profiles ever for craters on Mercury. By doing so, we also need to update the morphometric parameters for fresh craters on the two planetary bodies, and our updated results supersede previous ones as we used the most recent elevation data, the same database of fresh craters, and the same method to extract the elevation profiles for all the studied morphometric parameters.

1.3 Overview of Previous Methods

1.3.1 Mare Basalt Thickness

Mare basalt thicknesses have been investigated by many studies, which can be divided into four general classes: direct measurements using elevation differences of lava flow fronts and layering features in crater walls (Robinson et al., 2012; Schaber, 1973; Stickle et al., 2016), subsurface sounding radar using a spaceborne or ground penetrating radar (Oshigami et al., 2014; Phillips et al., 1973; Xiao et al., 2015), geophysical techniques based on seismology and gravity (Cooper et al., 1974; Gong et al., 2016; Talwani et al., 1973), and investigations of impact craters, including partially buried craters, composition of crater ejecta, and modification of the crater size-frequency distribution (De Hon, 1974; Hiesinger et al., 2002; Thomson et al., 2009). Each of these methods measures a different "thickness" (total thickness, thickness of the last flow, or thickness since a crater formed), and has different spatial and temporal resolutions. As a result, the total volume of mare basalts on the Moon is still poorly constrained.

The most straightforward technique for estimating basalt thicknesses is the direct measurement of the height of a lava flow front and layering structures in lava tube skylights and crater inner walls. This method usually gives the thicknesses of younger lava flows close to the lunar surface. The best documented lava flow fronts are those that formed during the Eratosthenian period in Mare Imbrium (Figure 1.4a). Using the shadow length measurement technique performed on the Apollo 14–17 metric photographs and the Lunar Orbiter III images, the extensive lava flows there were measured to be 1–96 m in thickness (Gifford and El-Baz, 1981; Schaber, 1973; Schaber et al., 1976, 1975). More recently, much lower lava flow fronts that are 8–11 m in thickness have also been identified in Mare Imbrium using the Lunar Orbiter Laser Altimeter (LOLA) digital elevation model (DEM) data (Wu et al., 2018), and it becomes a consensus now that all these measured lava flow front heights are indicative of an eruption mode with an extremely high effusion rate (Schaber et al., 1976; Wu et al., 2018). Three lava tube skylights have been spotted in Marius Hills, Mare Tranquillitatis, and Mare Ingenii using the Lunar Reconnaissance Orbiter Camera/Narrow Angle Camera (LROC/NAC) images. Their steep inner walls consist of five to eight layers that were found to be 3–14 m in thick-

ness based on shadow length measurements, with an uncertainty of 1 m (Robinson et al., 2012) (Figure 1.4b). Layering structures were also found in the crater walls of 13 fresh lunar craters. The flow thicknesses at these impact sites were estimated to be 48–400 m with uncertainties of 16–80 m based on the LROC/Wide Angle Camera (WAC) digital terrain model (DTM), LROC/NAC images, and Selenological and Engineering Explorer/Multi-band Imager (SELENE/MI) images (Oshigami et al., 2012; Stickle et al., 2016) (Figure 1.4c). However, it should be noted that few optical images are favorable for the recognition of such layering structures and shadow length measurements, and these features always present large surface slopes and hence can be easily masked out by mass-wasting events or covered by newly formed regolith, both making it difficult to apply this method to estimate the basalt thickness over a large region (Hiesinger et al., 2011).

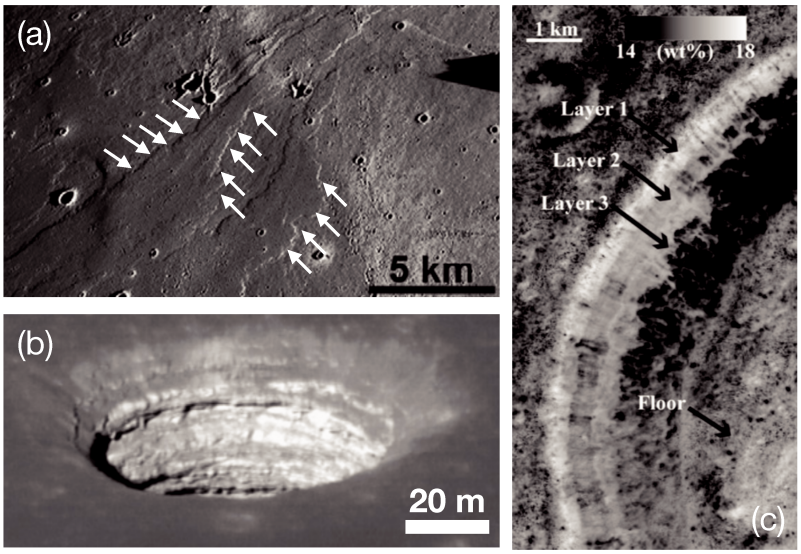

Figure 1.4: The lava flow fronts in Mare Imbrium (Head, 1976) (a), layering structures in the inner walls of a skylight in Mare Tranquillitatis (Robinson et al., 2010) (b) and the Bessel crater in Mare Serenitatis (Oshigami et al., 2012) (c).

As a result of the penetration capability of radar waves, subsurface reflectors can be directly observed by spaceborne radar sounders and ground penetrating radars. The basalt thickness can be determined by converting the apparent depth of subsurface reflections to the actual depth using an assumed dielectric permittivity. The observed thickness of mare basalts could be the total thickness or only the thickness of superficial layers depending on the penetration depth of the radar wave. Based on the 5-MHz Apollo 17 Lunar Sounder Experiment (ALSE) data and assuming a

dielectric permittivity of 8.7, subsurface reflectors were identified at mean depths of 0.9 and 1.6 km in southern Mare Serenitatis (Peeples et al., 1978; Sharpton and Head, 1982), at a mean depth of 1.4 km in Mare Crisium (Peeples et al., 1978), and at depths of 0.6–1.0 m in Oceanus Procellarum (Cooper et al., 1994) (Figure 1.5a). In the 5-MHz SELENE/Lunar Radar Sounder (LRS) data, one to five basaltic layers were detected with thicknesses of 73–460 m in nearside maria, with uncertainties of 125–400 m (Ishiyama et al., 2013; Kobayashi et al., 2012; Ono et al., 2009; Oshigami et al., 2009, 2012, 2014) (Figure 1.5b). The Chang'E-3 Lunar Penetrating Radar (LPR) also performed subsurface sounding experiments along its survey track on the surface of the Moon (near 44.12°N, 19.51°W), and the 60-MHz observations revealed multiple layering structures in the mare basalts (Figure 1.5c). Zhang et al. (2015) found three basalt layers with thicknesses of 25, 130 and 195 m, and Xiao et al. (2015) identified four basalt layers with thicknesses of 42, 80, 100, and 120 m. We note that the estimated mare basalt thickness from radar observations depends on the poorly constrained dielectric permittivity (Ishiyama et al., 2013), and that signal artifacts produced by the radar itself could make it difficult to detect deep seated reflectors (Li et al., 2018).

Geophysical techniques based on gravity and seismology data have also been used to investigate basalt thicknesses. These methods depend on the density contrast between mare and highland materials, and therefore can provide the total basalt thickness. Using the seismic refraction data collected at the Apollo 17 landing site, the total basalt thickness near the Taurus-Littrow valley was estimated to be 1.4 km (Cooper et al., 1974) (Figure 1.6a). During the Apollo 17 mission, a Bouguer anomaly was also recorded by the traverse gravimeter experiment (TGE) at the Taurus-Littrow landing site, which can be explained by the presence of a 1 km-thick laccolith of mare basalts (Talwani et al., 1973). Derived from the Doppler tracking data of the Lunar Prospector, two Bouguer anomalies were found in the Marius Hills volcanic complex, which may imply two local lenses of basaltic materials with thicknesses of 3.0–3.3 and 6.2–12.9 km, respectively (Kiefer, 2013). With newly acquired gravity data from the Gravity Recovery and Interior Laboratory (GRAIL) mission, the total basalt thickness on the western nearside hemisphere (19°S–45°N, 68°W–8°W) was estimated to be 740 m on average, with one-sigma upper and lower bounds of 1.62 km and 100 m (Gong et al., 2016) (Figure 1.6b). Though the seismic

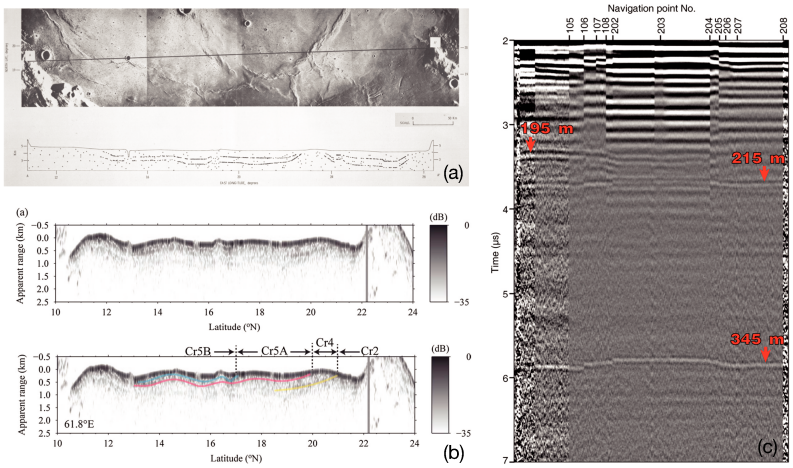

Figure 1.5: Subsurface reflectors detected in southern Mare Serenitatis: the upper panel presents the optical image and the radar footprint, and the lower panel shows the positions of the identified subsurface reflectors (Peeples et al., 1978) (a). Subsurface reflectors detected in eastern Mare Crisium: the upper panel presents the raw radar image, and the lower panel shows the positions of the identified subsurface layers (Oshigami et al., 2014) (b). The subsurface radar image and the identified subsurface interfaces from ground penetrating radar data on the surface of the Moon near the Chang'E-3 landing site (Zhang et al., 2015) (c).

estimate is applicable for a small region near the Apollo 17 landing site, the gravity inversions provide average thicknesses over circular regions with radii between 240 and 600 km (Gong et al., 2016). It should be noted that results based on geophysical techniques sometimes depend on poorly constrained properties such as the density and porosity of the subsurface materials.

The morphology of partially buried craters is another way to estimate the mare basalt thickness. On the Moon, the continuous ejecta blanket of a normal, unflooded crater usually extends about one crater radius from the crater rim (Moore et al., 1974). If the distal, low-elevation ejecta were later covered by the basaltic lava flow whereas the proximal, high-elevation rim crest still protrudes above the mare plain, a partially buried crater would form (e.g., Eggleton (1961), Marshall (1963), and Baldwin (1970)). As a result, the extent of exposed crater ejecta would be smaller than one crater radius with an abrupt transition between the unburied crater ejecta and the surrounding lava flow. By this definition, the mare basalt thickness around a partially buried crater can therefore be calculated as the difference in the current total and exposed rim heights (Figure 1.3). In previous studies, the scaling relations

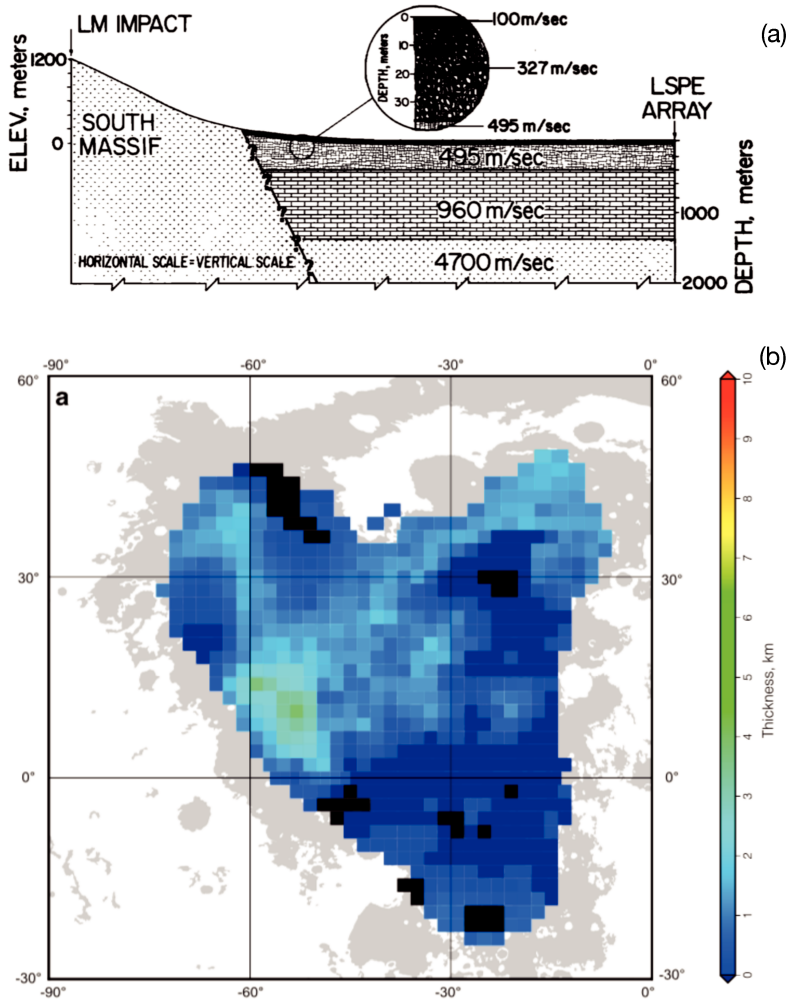

Figure 1.6: The subsurface structures near the Apollo 17 landing site as interpreted from the seismic experiment (Cooper et al., 1974) (a). The inverted basalt thicknesses on the nearside lunar maria based on the GRAIL data (Gong et al., 2016) (b).

between crater diameter and rim height for a fresh lunar crater (e.g., Baldwin (1949, 1963) and Pike (1972, 1967, 1977)) have always been used to substitute the current total rim height. However, craters on the Moon suffer from continual meteoroid bombardment, and as a result, the crater diameter increases and rim height decreases due to the downslope movement of ejecta materials. In such a case, if the current crater diameter and the resulting, predicted initial rim height were still used to determine the basalt thickness, the basalt thickness would be overestimated.

So far the most complete and systematic investigations on mare basalt thickness by this technique are those from De Hon (1974), De Hon (1975), De Hon and Waskom (1976), De Hon (1977), De Hon (1978), De Hon (1979a), and De Hon (1979b). Using the topography data derived from the Apollo stereo-images (LTO),

Earth-based telescopic photography (LAC), shadow length measurements (Lunar Orbiter images), and Earth-based radar observations, mare basalts in western and eastern maria were estimated to be 400 and 200–400 m on average, respectively, with local lenses exceeding 1.5 km in the basin centers. Later on, to take into account the crater degradation effect, Hörz (1978) firstly selected a group of highland craters with different degradation states to study the time-dependence of crater rim height, and then applied the obtained time-dependent rim height to reinvestigate the mare basalt thicknesses using the LTO elevation datasets. The resulting, corrected mare basalt thickness on the lunar nearside was found to be < 300 m in median, which is almost a factor-of-two reduction as compared with previous estimates without considering the crater degradation process. However, the classification of degradation states for lunar craters in Hörz (1978) was subjective and qualitative. How old the selected craters are crucial as the precise rim height reduction depends on the age of the crater, which must be considered when estimating the basalt thickness using this technique. Therefore a theoretical modeling on the crater degradation history is invoked to characterize the rim erosion process as a function of time, crater size, and target properties.

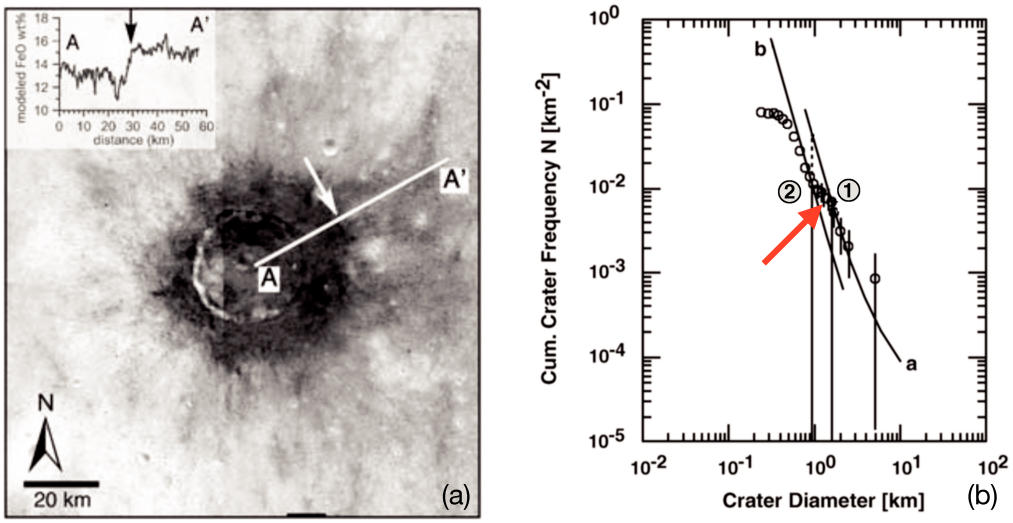

Figure 1.7: An example of a crater that excavated highland materials low in FeO content (Thomson et al., 2009) (a). An example illustrating how the crater size-frequency distribution was affected by lava flooding (Hiesinger et al., 2002) (b). In (a), the FeO content along AA′ is given in the inset. The dark region has a low FeO content and the bright region is typical mare. In (b), the deflection point is seen between Point 1 and Point 2 (red arrow).

Impact craters excavate materials from depths of about one-tenth of their diameter and thus provide a window on the composition of materials below the surface (Croft, 1980; Melosh, 1989). For craters in the maria, the presence (or not) of anorthositic highland materials in the ejecta blanket constrains the total thickness of mare basalts at the impact site. An example is seen in the Clementine-derived FeO content map shown in Figure 1.7a, where the crater Timocharis excavated low-FeO content materials (dark) under the mare region (bright). Using the spectral images collected by Lunar Orbiter, Galileo Earth/Moon Encounter, Clementine Ultraviolet/Visible (UV/VIS), Chang'E-1 Interference Imaging Spectrometer (IIM), SELENE/MI, and Chandrayaan-1/Moon Mineralogy Mapper (M^3), lava flows in four nearside maria (Oceanus Procellarum, Serenitatis, Humorum and Imbrium) were estimated to be 17–2000 m thick (Budney and Lucey, 1998; Chen et al., 2018; Thomson et al., 2009; Weider et al., 2010; Wu et al., 2018), and the total thicknesses in six farside basins (Apollo, Ingenii, Poincare, Freundlich-Sharonov, Mendel-Rydberg, and South Pole-Aitken) were inferred to be 31–3640 m (Pasckert et al., 2018; Taguchi et al., 2017; Yingst and Head, 1997), with uncertainties of 0.6–360 m.

Mare basaltic flooding can also affect the size-frequency distribution of craters found on a geologic unit. During the emplacement of lava flows, some portion of the smallest craters are completely buried. The existence of such a discontinuity in the crater size-frequency distribution can be used to estimate the flow thickness (Hiesinger et al., 2002; Neukum and Horn, 1976) (Figure 1.7b). This method returns the thickness of the uppermost, youngest lava flows. For seven nearside mare regions (Oceanus Procellarum, Imbrium, Tranquillitatis, Humorum, Cognitum, Nubium, and Insularum), modifications of the crater size-frequency distributions have been identified in the Lunar Orbiter IV images, and the basalt thicknesses therein were estimated to be 20 to 220 m with an uncertainty of 8 m (Hiesinger et al., 2002). For several farside large basins (Lacus Luxuriae, Buys-Ballot, Campbell, and Kohlschütter, Apollo N, and Moscoviense), this feature was also found in their crater size-frequency distribution plots derived from the SELENE/Terran Camera (TC) images, and the inferred basalt thicknesses range from 13 to 60 m (Haruyama et al., 2009; Morota et al., 2009, 2011b).

There are several other methods that were seldom used in the basalt thickness estimation, including those based on the exposed crater depth (e.g., Williams and

Zuber (1998) and Yingst and Head (1997)) and the morphology of intrusive volcanic domes (Michaut, 2011).

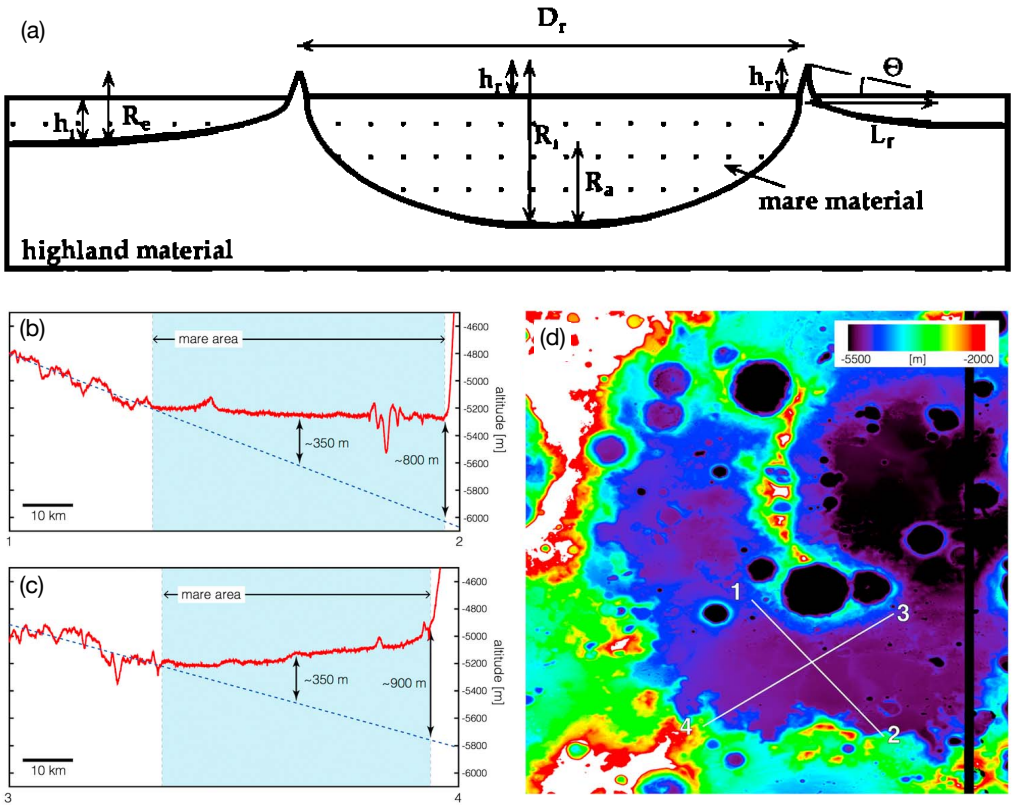

Figure 1.8: A diagram showing how to estimate the mare basalt thickness in the crater interior: the technique based on the exposed crater depth (a) (Yingst and Head, 1997) and the method based on the extrapolated crater floor elevation (b–d) (Taguchi et al., 2017). In (a), the basalt thickness is equal to the difference between the total crater depth (R_{i}) and the exposed crater depth (h_{r}). In (b) and (c), the red solid lines are the observed profiles and the black dashed lines are the extrapolated profiles. In (d), the lines 1–2 and 3–4 correspond to the elevation profiles in (b) and (c), respectively.

The partially buried craters studied above are usually small in size and located within the lunar nearside maria. Even if the crater floor is flooded by mare basalts, as is the exterior distal ejecta, the interior basalt thickness (and hence the volume) is thought to be trivial since the area of the crater interior is much smaller than that of the exterior, large-scale mare plains. In cases such as mare basalts in large nearside basins and lava ponds in small farside craters, however, we might be also interested in the basalt thickness interior to the crater rim, which can be estimated as the difference in the current total and exposed crater depths (Figure 1.8a) (Whitford-Stark, 1979). For instance, using the Clementine LIDAR data, Williams

and Zuber (1998) first derived the basin depth-diameter ratio for several unburied basins, which they thought have the same degradation states as the studied partially buried basins (Grimaldi, Serenitatis, Humorum, Smythii, Nectaris, Orientale, Crisium, and Imbrium). They then applied this technique to estimate the total basalt thicknesses therein, which were found to vary from 0.56 to 4.70 km. Based on the crater depth-diameter ratio for fresh lunar craters (Pike, 1977), Yingst and Head (1997) calculated the thicknesses of lava ponds inside the South Pole-Aitken basin to be 0.1–1.6 km using the Apollo and Clementine topography data. However, we note that Yingst and Head (1997) did not consider the degradation of the crater rim, and that although Williams and Zuber (1998) considered this effect, the determination on the degradation states may be subjective and not that quantitative.

However, the obtained crater depth-diameter ratio may not be applicable to basins that have a rolling, complex crater floor, or to basins that underwent significant viscous relaxation since their formation (Kamata et al., 2015). One way to retrieve the topography of the flooded crater floor is based on the extrapolation of that of nearby, unflooded regions (Figures 1.8b–d). For example, the southern part to the second inner ring of Apollo basin is buried by lava flows with no partially buried craters or penetrating craters being found. Assuming the buried terrain has the same surface slope as is the exposed region exterior to the basalts, the basalt thickness there was estimated to be 0–900 m using the SELENE/TC DTM (Taguchi et al., 2017). This method, however, is too simplified, and it may not be convincing to predict the topography of the buried crater floor in this way.

Intrusive magmatic materials on the Moon preferentially move along horizontal boundaries with large density and rigidity contrasts such as the interface between mare basalts and the underlying lunar crust. As a result, a lunar dome could form on the surface due to the intrusion of underlying magma (Figure 1.9a) (Michaut et al., 2016; Wöhler et al., 2009). The shape of the intrusive magma can be described by a dynamic model involving the physical parameters of the magma and the overlying elastic layer (e.g., density, Young's modulus and Poisson's ratio) and most importantly, the intrusion depth of the magma, i.e., the total basalt thickness (Figure 1 in Michaut (2011)). Since the materials overlying the intrusive magma deform elastically, it can be assumed that the overlying dome has the same shape as the underlying intrusive magma. The total basalt thickness can thus be inverted

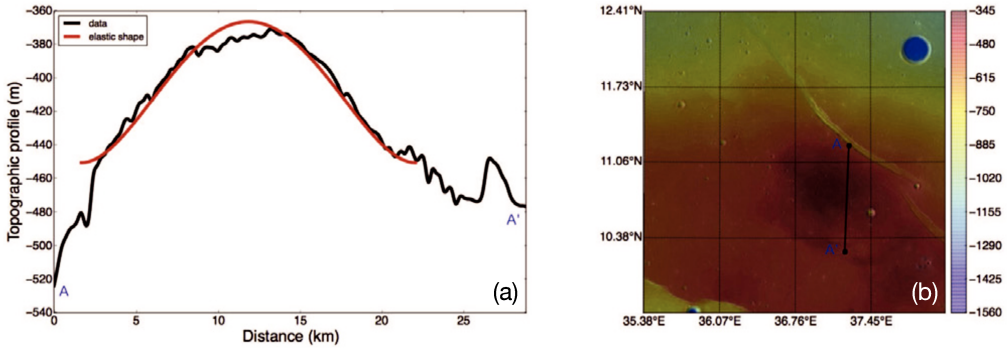

Figure 1.9: An example showing how to estimate the basalt thickness based on the morphology of domes (Michaut et al., 2016). The dome shown here is located at (36.75°N, 11.06°E) in Mare Tranquillitatis with a height of 84 m and a radius of 10.2 km. In (a), the black line is the observed profile, and the red line is the best-fitting modeled profile. In (b), the black line shows where the profile in (a) was extracted.

by matching the modeled morphology of the intrusive magma with the observed morphology of the dome (Michaut et al., 2016). Applying this inversion model to the topographic profiles of seven domes over the lunar surface (Mare Frigoris, Mare Serenitatis, Mare Tranquilitatis, Mare Insularum, Sinus Iridum and Grimaldi basin) extracted from the LOLA data, the basalt thicknesses were estimated to be at least 400–1900 m for these volcanic regions, with uncertainties of 50–220 m (Michaut et al., 2016). Unfortunately, lunar domes formed by intrusive magmas were found only in small maria or along mare-highland boundaries, since the mare basalts in the basin center are too thick to allow the intrusion of the magmatic materials (Michaut et al., 2016).

1.3.2 Smooth Plains Thickness

We note that there are only two missions that have visited the planet of Mercury: the Mariner 10 and the MESSENGER missions. Due to the limitations on the spatial resolution, data quality, data coverage, and sources of the remote sensing datasets, there are only a few studies that addressed the lava flow thicknesses on Mercury, and none of them has given precise, quantitative estimates.

Similar to the mare basalt thickness estimation on the Moon, the lava flow thickness on Mercury can also be estimated from the rim height of partially and completely buried craters. In Figure 1.10a, there is a rim-completely-exposed crater

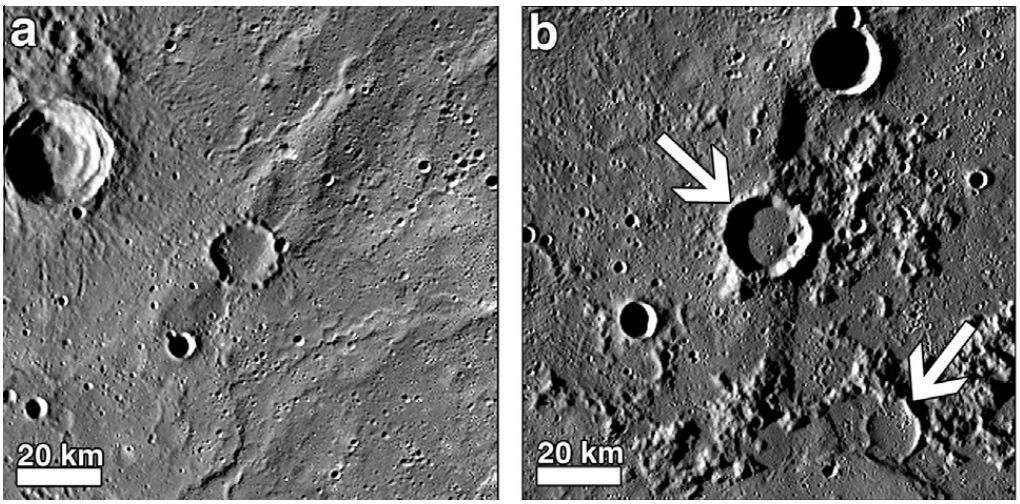

Figure 1.10: A partially buried crater (77.79°N, 110.41°W; D =18.0 km) inside the northern smooth plains (a). This a rim-completely-exposed crater. Two partially buried craters (82.59°N, 85.82°W; D =21.3 km; 83.15°N, 75.88°W; D =14.5 km) at the smooth plains-heavily cratered terrain boundary (b). The one in the center is a rim-completely-exposed crater, and the one on the lower right is a rim-partially-exposed crater. These two craters are taken from Ostrach et al. (2015).

inside the northern smooth plains, on which a wrinkle ridge formed later. Along the smooth plains-heavily cratered terrain boundaries in Figure 1.10b, there are one rim-completely-exposed crater and one rim-partially-exposed crater of which part of the rim was breached by lavas. For a partially buried crater, the lava flow thickness can be obtained from the difference between the total rim height and the exposed rim height. For a completely buried crater, the lower limit of the lava flow thickness is given by the total rim height. Head et al. (2011) identified completely buried craters within the northern smooth plain of Mercury using the MESSENGER/Mercury Dual Imaging System (MDIS) images, and the presence of completely buried craters with diameters greater than 100 km indicates that the lava flow thickness is at least 1–2 km. Later, as more images were acquired by MESSENGER/MDIS, Ostrach et al. (2015) did a more complete search on the partially and completely buried craters within the northern smooth plains, and then estimated surrounding lava flow thicknesses based on the crater rim height. For the completely buried craters with diameters of 25–157 km, the initial crater rim heights were estimated to be 0.7–1.8 km, which provides lower limits for lava flow thicknesses in these regions. For the partially buried craters with diameters of 8–157 km, the initial crater rim

heights were estimated to be 0.4–1.8 km, which can be either the lower (near the buried segment of crater rim) or upper (near the exposed segment of crater rim) limits for lava flow thicknesses. However, all these values only give either upper or lower limits of the lava flow thickness, and a precise estimate can not be obtained from this method.

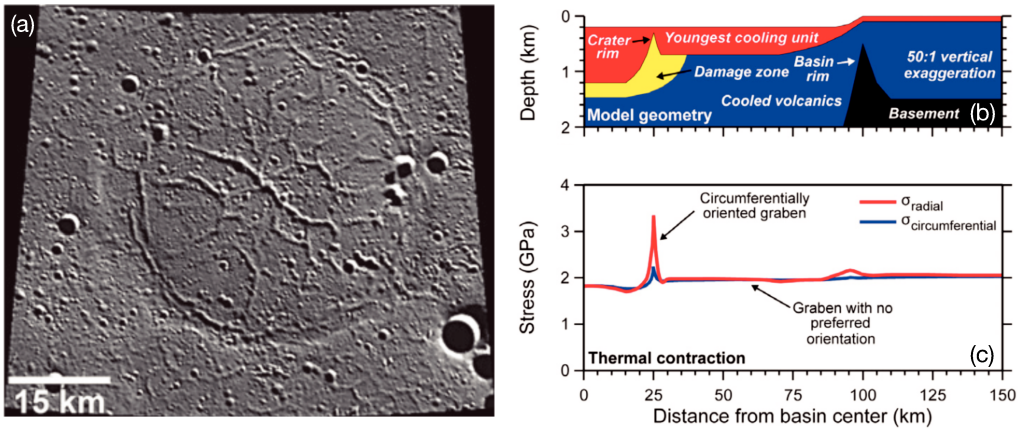

Figure 1.11: The graben system identified in a completely buried crater within the Goethe basin (a) (Watters et al., 2012). Geometry of a finite element model used to model the formation of graben and ridges (b). An example of forward modeling results due to the thermal contraction of the lava flow (c) (Freed et al., 2012; Watters et al., 2012).

Klimczak et al. (2012) undertook a systematic investigation of the wrinkle ridges and graben within the northern smooth plains, with the objective of putting some constraints on the thickness of the lava flows in these regions. An example is seen in Figure 1.11a, where a system of radial graben formed in the interior of a completely buried crater. The idea is that the graben width can be used to estimate the lower bound of lava flow thickness if one assumes a fault angle such as 60° (Watters et al., 2012). Their estimation shows that the lava flow thickness within the Goethe basin is at least 2 km. Again, this method can only predict a lower limit of the lava flow thickness. We note that Watters et al. (2012) and Freed et al. (2012) also implemented a forward modeling to correlate the formation of ridges and graben with the lava flow thickness. In Figures 1.11b and c, for example, Watters et al. (2012) first assumed a specific model geometry and then calculated the stress field on the surface. Then, they predicted that at 25 km from the crater center a circumferential graben would form due to a compressional stress. However, this finite element model they developed also involves another ∼15 free parameters (e.g., the temperature,

viscosity, Young's modulus, and Poisson's ratio of the lava flow), making it difficult to use this model for lava flow thickness inversion.

1.3.3 Crater Degradation on the Moon

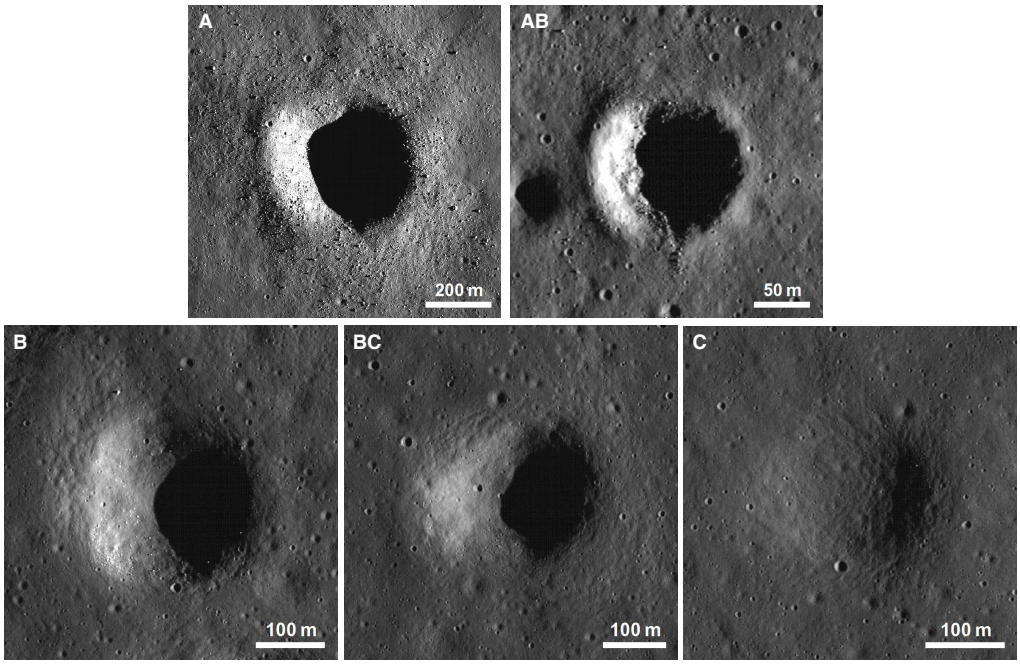

Figure 1.12: Examples of craters with different degradation states on the Moon. From Class A to D, craters are getting older and older (Basilevsky, 1976).

Using telescope observations, it has long been recognized that impact craters on the Moon degrade with time (e.g., Baldwin (1949), Pohn and Offield (1970), Basilevsky (1976)). Based on the morphorlogical characteristics of the inner wall, rim crest, and ejecta deposits, several criteria were proposed to categorize lunar craters into different degradation states in a qualitative way. As an example, Figure 1.12 shows how craters degrade with time. For the freshest crater A, the surface slope is large and the crater rim is sharp. The debris flow and fresh boulders are clearly visible on the inner wall and crater ejecta. For the fresh crater AB, the slope of the surface is still very large whereas the crater rim is a little bit subdued. A few boulders are still visible on the crater wall and ejecta. For the crater B with the intermediate state, the slope becomes smaller and the crater rim is subdued. We can hardly see any rocks on the surface. For the older crater BC, the surface slope is even much smaller, the edge is highly subdued, and the surface rocks are not visible

any more. For the oldest crater C, it has a gentle surface relief, the crater rim is almost invisible, and the surface rocks are not discernible (Basilevsky, 1976).

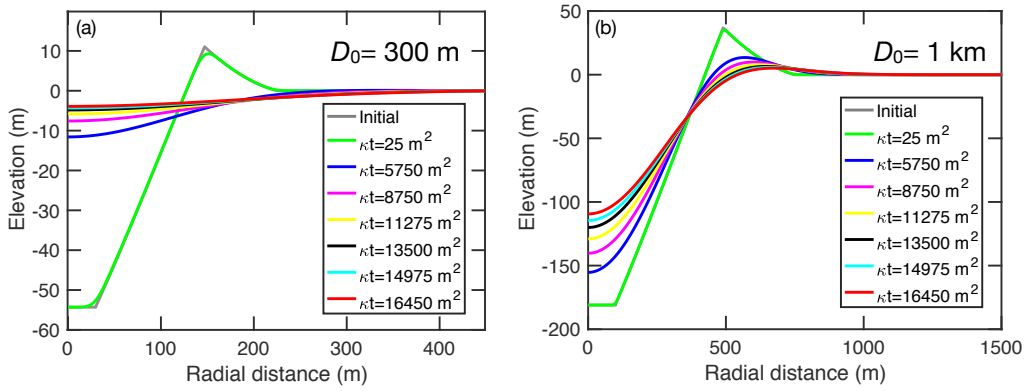

Figure 1.13: The temporal evolution of crater shape for craters with diameters of 300 m (a) and 1 km (b) at different degradation states (Fassett and Thomson, 2014). These are model calculations based on using a topographic diffusion model and assumed diffusivity-time products of 25, 5750, 8750, 11275, 13500, 14975, and 16450 m^2.

A major breakthrough in the theoretical modeling of the crater degradation process was achieved by using the classical diffusion equation (e.g., Culling (1960), Culling (1963), Soderblom (1970)), and recent efforts have been made to improve this model with improved knowledge of lunar crater morphology and high-quality topography datasets of the Moon (e.g., Richardson (2009), Fassett and Thomson (2014), Xie and Zhu (2016), and Minton et al. (2019)). It can now be concluded that the topographic degradation of lunar craters is mainly controlled by a combination of diffusive and non-diffusive processes. Micrometeoroid bombardments, thermal expansion and contraction, and seismic shaking are usually thought to be representative of a diffusive process, whereas mass-wasting events on steep slopes, and deposition of charged dust particles are considered as non-diffusive processes (Fassett and Thomson, 2014). Although the emplacement of ejecta from nearby craters was thought to be a non-diffusive process by Fassett and Thomson (2014), Minton et al. (2019) pointed out that this could be a diffusive process for small lunar mare craters. We note that during daytime part of the crater is illuminated by the sunlight and the other part is in the shadowed region. However, when we extracted the elevation profile of a crater, we actually took the azimuthal averages. Therefore, the illumination condition should not have any significant effect on our degradation model. We also note that although the thermal expansion and contrac-

tion due to the diurnal temperature variation can break up rocks and may result in small-scale debris flows, this is difficult to observe using the elevation data because the spatial resolution of the elevation data is usually as large as tens of meters per pixel. Nevertheless, it might be interesting to look into the crater degradation in the permanently shadowed region, as the craters therein may experience smaller temperature variation and thus the topographic degradation could be less significant.

As a recent study, Fassett and Thomson (2014) modeled the topographic degradation of small (0.8–5 km in diameter) craters in the lunar maria using the SELENE/TC DTM. The authors used a quantitative topographic diffusion model to quantify how the crater elevation profile varies with time, and they found that the average diffusivity over the past 3 Gyr is ∼5.5 m^2/Myr using age constraints from crater counting. As shown in Figure 1.13, after 3 Gyr a 1-km-diameter crater is still visible whereas a 300-m-diameter crater is not noticeable anymore.

1.3.4 Crater Degradation on Mercury

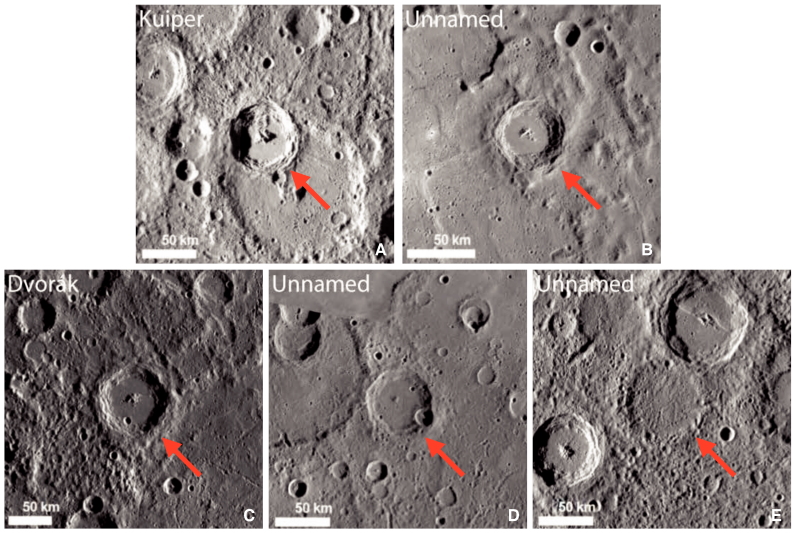

Figure 1.14: Examples of craters with different degradation states on Mercury. From Class A to E, craters are getting older and older (Kinczyk et al., 2016).

There are only a few studies that have addressed the crater degradation on Mercury, which is primarily a result of a lack of high-resolution optical images and elevation data. The qualitative classification on the degradation state of Mercury's crater is mainly based on characteristics of the crater rim and ejecta in the optical image (Kinczyk et al., 2016; Susorney et al., 2016; Trask, 1971). As shown in Figure

1.14, for example, Kinczyk et al. (2016) classified the craters on Mercury into five degradation states. The Class A crater is the freshest with a sharp crater rim, well preserved ejecta, and visible crater rays. The Class B crater may be superposed by a few subsequent craters and does not radial rays, but the crater rim and ejecta are still well preserved. The Class C crater has degraded rim and terraces and may be filled with smooth plains materials. The Class D crater lacks visible ejecta deposits, and the crater interior may be buried by volcanic materials and superposed by many subsequent craters. The Class E crater is the oldest and may only preserve a portion of the crater rim.

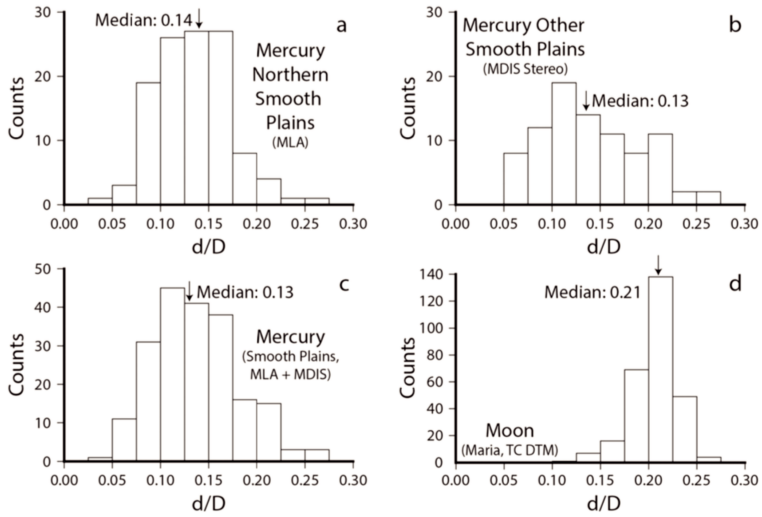

Figure 1.15: Measured depth-diameter ratios on Mercury (a–c) and the Moon (d) (Fassett et al., 2017). The depth-diameter ratios on Mercury were obtained by using two different datasets (MLA and MDIS) and a combination of them, which give a median value around 0.13. The depth-diameter ratios on the Moon were measured from lunar mare crates using SELENE/TC DTM and are 0.21 in median value.

In a different study, Fassett et al. (2017) measured the depth to diameter ratio of small craters (2.5 to 5 km in diameter) on the northern smooth plains of Mercury. The obtained median d/D ratio is 0.13, which is much lower than that of simple craters on lunar maria with a value of 0.21 (Figure 1.15). Furthermore, this study also estimated the topographic diffusivity for craters on Mercury by using a similar model used in Fassett and Thomson (2014) and age constraints from crater counting. The result shows that the median topographic diffusivity on Mercury (17 m^2/Myr) is about two times that on the Moon (9 m^2/Myr) for craters with diameters of 2.5–5 km. Both results indicate that the crater degradation on Mercury is more significant

than that on the Moon.

1.4 Objectives and Outlines

In this thesis, an improved method was developed for estimating the thickness of the lava flows on the Moon and Mercury based on the elevation profile of partially buried impact craters. By applying topographic diffusion theory, the evolution of a partially buried crater can be modeled through time, both before and after the emplacement of the lava flows. The modeled final elevation profile depends on the initial crater topographic profile, the lava flow thickness, the time durations between crater formation, flooding and the present, and the topographic diffusivity. By comparing the observed profile with a series of modeled profiles, the lava flow thickness can be estimated at the location of the partially buried crater. Our study improves upon previous works in several ways. First, the previous databases of partially buried craters were constructed several decades ago (De Hon and Waskom, 1976; De Hon, 1979b), and new remote sensing data with unprecedented spatial resolution and quality have since been acquired. Second, crater degradation modeling has been improved through the years (Fassett and Thomson, 2014), and high precision digital elevation models allow us to better characterize the morphology of both fresh and degraded impact craters. Third, based on the best-fitting parameters from the degradation model, we are able to investigate how the topographic diffusivity varies with both time and crater size.

The structure of this paper is organized as follows. First, in Chapter 2 all the remote sensing datasets and the derived data products that will be employed in this study are presented, the identification criteria of partially buried craters will be given, and the lava flow thickness estimation method will be described. Then, in Chapter 3 the procedures to derive the initial elevation profiles for fresh craters are presented. As a by-product, the crater morphometric parameters are also analyzed. Next, in Chapter 4 we describe our results for the thickness of mare basaltic lavas on the Moon, followed by analyses of their spatial and statistical characteristics. In this chapter, our results are also compared with those derived using other techniques, the cumulative volume and eruption rate of lava flows are then described, and the scale dependence of the crater degradation process is investigated. In Chapter 5, we present similar results for lava flow thicknesses on Mercury, and we also analyze

the difference in volcanism and impact cratering between the Moon and Mercury. Finally, we conclude in Chapter 6 by discussing several remaining issues, as well as the outlooks for other applications of the crater degradation model.

Chapter 2 Data and Methods

2.1 Overview

In this section, we will present the remote sensing data being used in this study and the method we developed to estimate lava flow thicknesses (Figure 2.1). First, we will use multiple remote sensing data to identify the partially buried craters. An initial profile of a fresh crater will be needed for the initial condition for the crater degradation model, and this is described in detail in Chapter 3. Based on the rim composition (highlands or maria) we will need to decide the type of the initial profile being used later for partially buried craters on the Moon. Finally, we will develop a degradation model that depends upon a total of six parameters. Output from this model is then compared with the observed topographic profile.

Meanwhile, we need to extract the elevation profile of a crater from a digital elevation model or raw altimetry data. In doing so, we need to first remove atypical features in the background region such as impact craters that formed after the lava flows erupted. A radial elevation profile is then produced by azimuthally averaging the elevations in the studied region. However, at distances far from the crater, the elevation profile may be contaminated by geology processes unrelated to the crater being investigated, and in these cases, we need to define a maximum range within which the elevations are considered to be valid.

The lava flow thickness can be obtained by finding those parameters that generate a model that best fits the observation. Using the acquired best-fitting model parameters, a better understanding of volcanism and impact cratering on the planet will be obtained.

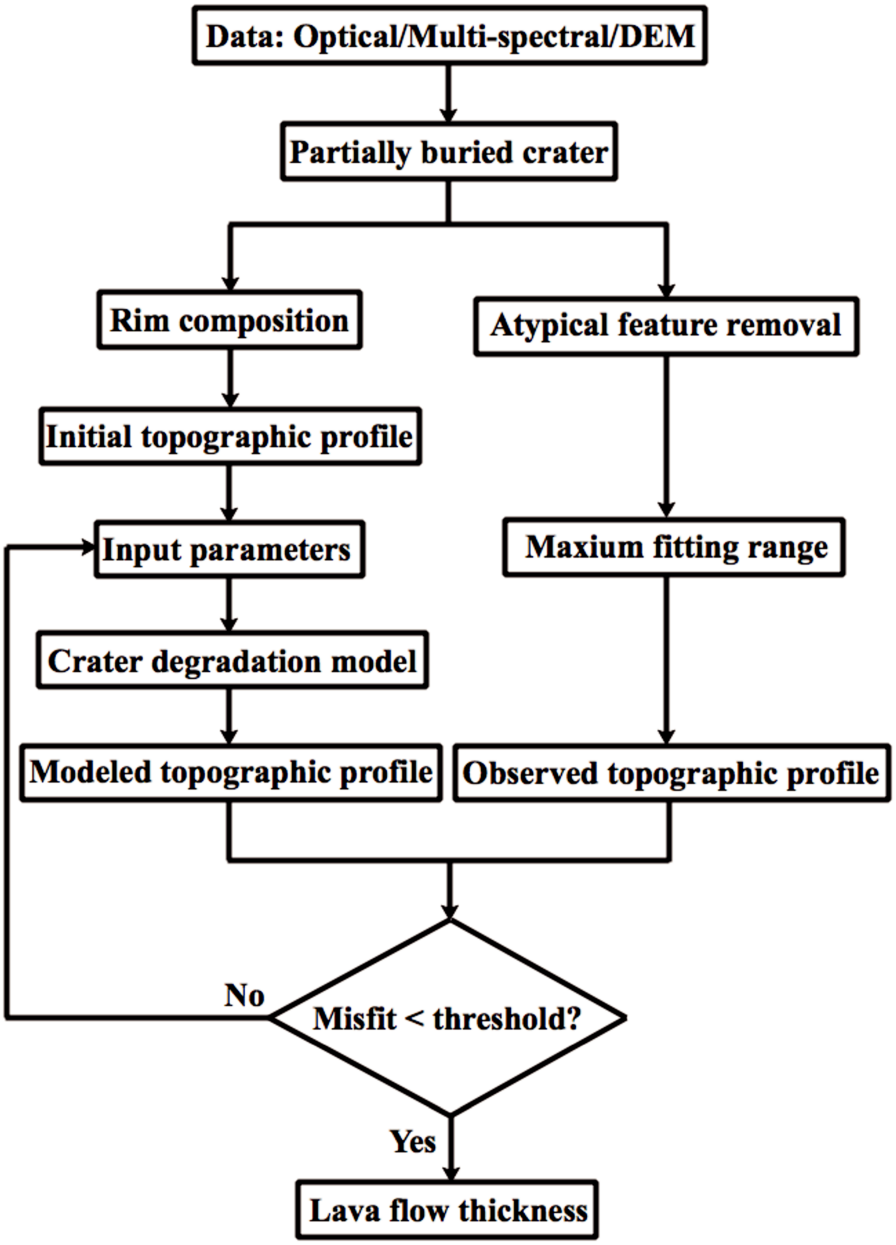

Figure 2.1: Flow chart for the lava flow thickness inversions.

2.2 Data

2.2.1 The Moon

Multiple remote sensing datasets are used in this study, which can be categorized into four main classes: optical images, topographic data, surface composition, and radar sounding observations. The first three types of data are used to identify partially buried craters over the lunar surface. The topographic data are used to extract the radial profiles of fresh craters and partially buried craters for initial crater profile modeling and basalt thickness estimation, respectively. The compositional data are used to determine the target materials (mare/highland) over which a partially buried crater formed, and to derive the dielectric permittivity for the estimation of the actual depth of subsurface reflectors in radar images. The radar sounding data are used to compare with the mare basalt thickness estimates from partially buried craters.

The final global LROC/WAC mosaics with a spatial resolution of 100 m/pixel are used in our study, which have been photometrically corrected with favorable solar incidence angles of 55°–75° for morphology recognition (Robinson et al., 2010; Speyerer et al., 2011) (Figure 2.2). Previous studies suggested that at least ten pixels are needed to identify a small lunar crater unambiguously (Fa et al., 2014; Fassett, 2016; Robbins et al., 2014), therefore we restrict our analysis to craters larger than 1 km in diameter.

Recent, widely-used lunar topographic datasets include the LRO/LOLA digital elevation model (Smith et al., 2010) and the SELENE/TC stereo-image derived digital terrain model (Haruyama et al., 2012). With a vertical accuracy of 1 m and covering the entire lunar surface, the LOLA DEM provides a geodetically accurate global control network, and the gridded data products were produced with a nominal spatial resolution of 29.6 m at the lunar equator (Smith et al., 2010). The SELENE/TC DTM has a vertical accuracy of 10 m, covers the non-polar region ($< 60°$N/S), and has a higher spatial resolution of 10 m (Haruyama et al., 2012). To combine the advantages of these two datasets, a SELENE-LRO merged digital elevation model (SLDEM) was generated by Barker et al. (2016) by co-registering the TC DTM to the LOLA geodetic framework. The resulting dataset covers latitudes between 60°N/S with a spatial resolution of 59 m and a vertical accuracy of 3–4

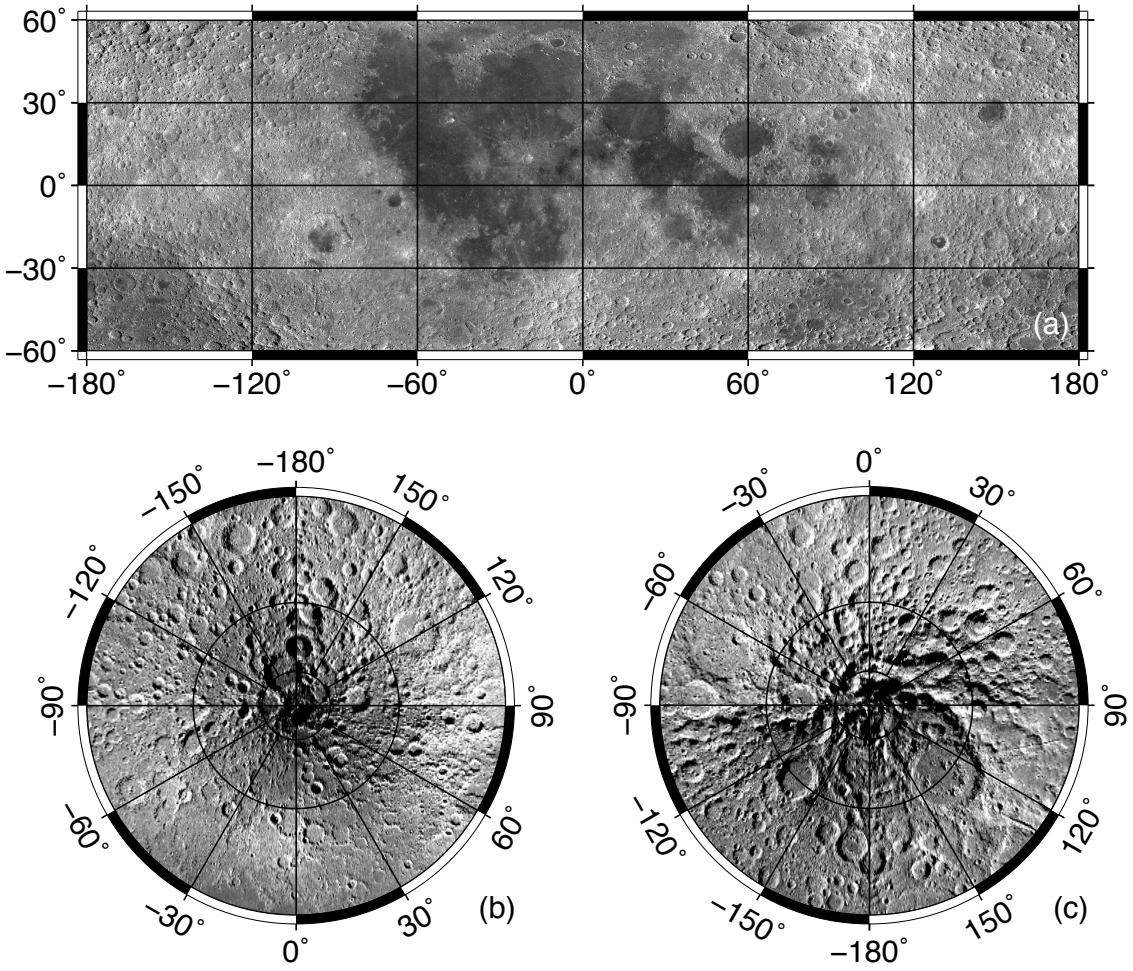

Figure 2.2: The LROC/WAC mosaic used for the Moon in this study: 60°S–60°N (a), 60°N–90°N (b), and 60°S–90°S (c).

m (Barker et al., 2016). In this study, the SLDEM was used as the elevation data for latitudes equatorward of 60 degrees (Figure 2.3a), and the LOLA DEM with a spatial resolution of 60 m was used for higher latitudes (Figures 2.3b and c).

The elevation data used by De Hon in his series of studies in the late 1970s come from three sources (De Hon, 1979b). As the first choice, he used the Lunar Topographic Orthophotomap to calculate rim heights where Apollo 15–17 mapping photographs were available. This data product consists of contours with an interval of 100 m and has an elevation uncertainty of 30–115 m (The Defense Mapping Agency, 1973). In regions beyond those imaged by the Apollo mapping cameras, the author used the Lunar Astronautical Chart derived from Earth-based telescopic photography or measured the shadow lengths in the Lunar Orbiter frames to extract rim heights. The Lunar Astronautical Chart has a sparser contour interval of 300 m

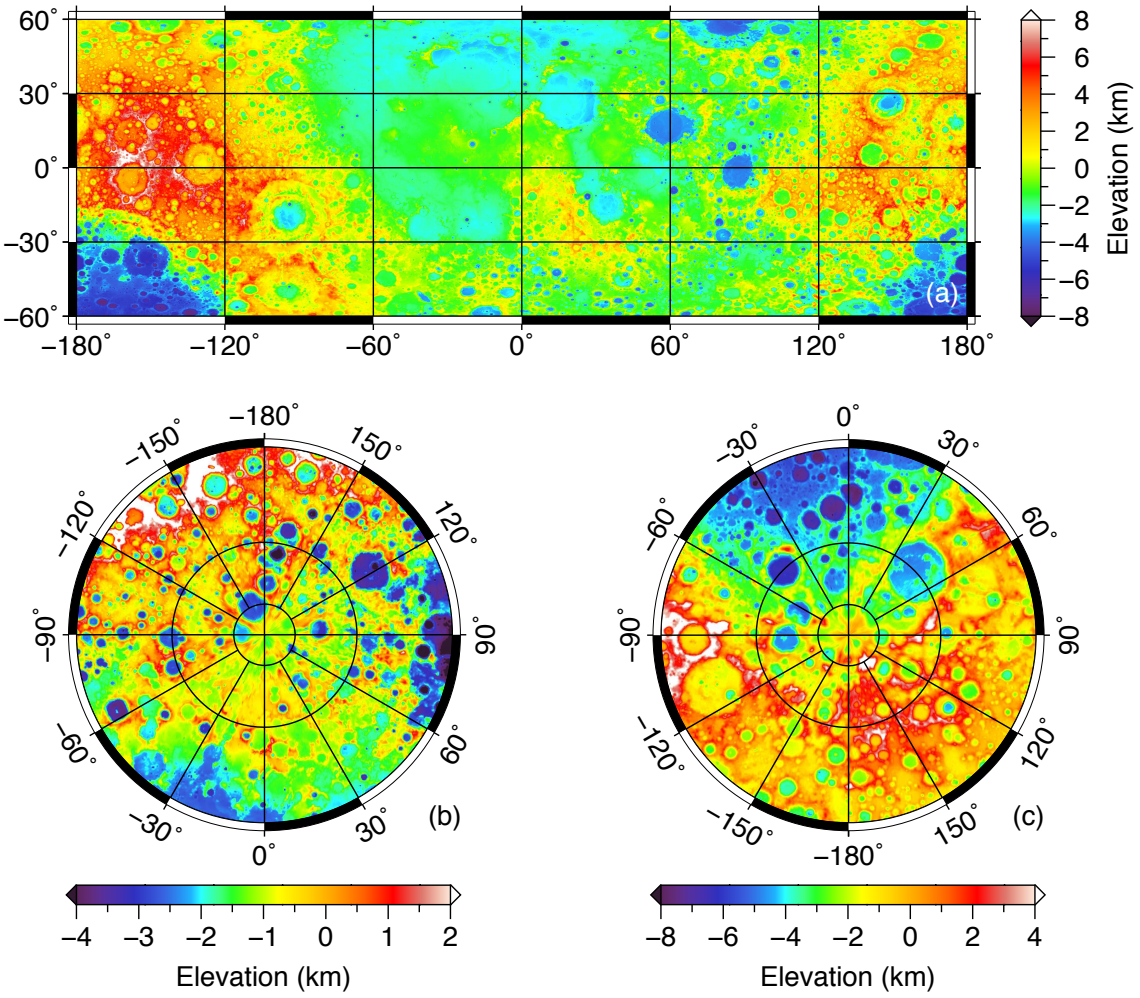

Figure 2.3: The elevation data used in this study: SLDEM for 60°S–60°N (a), LOLA for 60°N–90°N (b) and 60°S–90°S (c).

(Aeronautical Chart Information Center, 1973), and both derived elevations have an uncertainty of 100 m (De Hon, 1979b). It should be noted that the above elevation uncertainties of the LTO, LAC, and LO data are nominal values, and that the resulting, measured morphometric parameters could have an uncertainty as large as 700 m in regions with significant relief (see Table 1 in Pike (1974)). In comparison with these early topographic datasets used by De Hon, the newly acquired SLDEM and LOLA data have much better spatial resolution (2–5 times higher), coverage (globally covered) and accuracy (8–40 times higher). Therefore, the basalt thickness estimates given by our study should be considered to supercede those obtained by De Hon's pioneering studies over four decades ago (De Hon and Waskom, 1976; De Hon, 1979b).

Using multi-spectral data collected by the SELENE/Multiband Imager (Ohtake

et al., 2008) and the Clementine Ultraviolet/Visible camera (Eliason et al., 1999), FeO and TiO_2 abundance maps can be calculated (Lucey et al., 2000; Otake et al., 2012). The uncertainties of the FeO abundance are 0.8 wt.% for the MI and 1.0 wt.% for the UVVIS datasets, whereas the uncertainties for TiO_2 are respectively 0.4 wt.% and 0.9 wt.%. The recently released MI mineral abundance mosaics cover the lunar surface between 50°N/S with a spatial resolution as high as 60 m/pixel and include photometric corrections using surface topography (Lemelin et al., 2016). The UVVIS composition maps have a lower spatial resolution of 200 m/pixel and are not topographically corrected, but they have better coverage at latitudes higher than 50° in comparison to the MI maps (Eliason et al., 1999). Therefore, in this study we will use the MI abundance maps for regions equatorward of 50 degrees latitude (Figures 2.4a and 2.5a) and the UVVIS composition maps at higher latitudes (Figures 2.4b and c, and Figures 2.5b and c).

Table 2.1: A summary of the remote sensing data used in this study for the Moon.

Class	Datasets	Resolution	Coverage	Uncertainty	Reference
Optical	LROC/WAC	100 m/pixel	Global	–	Speyerer et al. (2011)
Elevation	SLDEM	60 m/pixel	⩽60°N/S	4 m	Barker et al. (2016)
	LOLA	60 m/pixel	>60°N/S	1 m	Smith et al. (2010)
TiO_2	MI	60 m/pixel	⩽50°N/S	0.8 wt.%	Lemelin et al. (2016)
	UVVIS	200 m/pixel	>50°N/S	1.0 wt.%	Lucey et al. (2000)
FeO	MI	60 m/pixel	⩽50°N/S	0.4 wt.%	Lemelin et al. (2016)
	UVVIS	200 m/pixel	>50°N/S	0.9 wt.%	Lucey et al. (2000)
Radar	LRS	Along-track: 600 m Range in vaccum: 75 m	–	–	Kobayashi et al. (2012)

The SELENE Lunar Radar Sounder operated at a center frequency of 5 MHz with a bandwidth of 2 MHz, resulting in a 75-m range resolution in vacuum. After surface clutter reduction with synthetic aperture radar (SAR) processing techniques, the final released data have an along-track resolution of 600 m (Kobayashi et al., 2012). The LRS data provide the received backscattered echo as a function of time delay. The data formats include the one-dimensional A-scope plot (where the radar echo strength at a given location is plotted against time delay), and the two-dimensional SAR-processed image (where the radar echo strength is plotted with the along-track distance and the time delay). To convert apparent depth, which is the product of half the time delay and the speed of light in vacuum, to actual depth, the vertical profile of dielectric permittivity (often assumed to be constant) for the

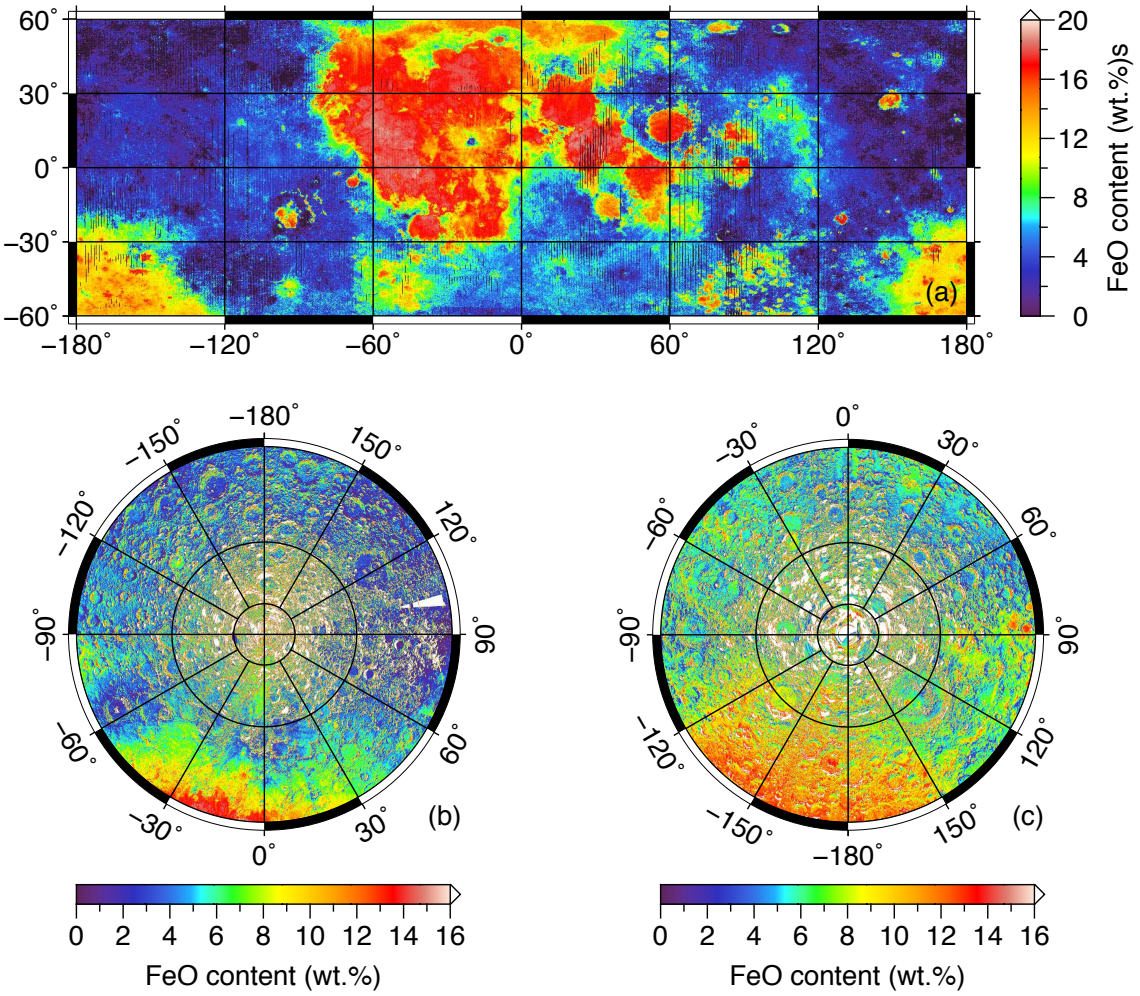

Figure 2.4: FeO abundance maps used in this study: MI for 60°S–60°N (a), Clementine for 60°N–90°N (b) and 60°S–90°S (c).

studied region is required.

Two derived data products are also used in this study to aid our understanding of the geological context of partially buried craters. A mare basemap derived from the monochromatic and color ratio images from the LROC/WAC and Clementine/UVVIS datasets provides the locations of regions flooded by mare basalts (Nelson et al., 2014). The boundaries of individual basaltic units defined by the LROC/WAC and Clementine/UVVIS data products are also used to determine the surface unit that embayed the partially buried crater (Hiesinger et al., 2006, 2011; Morota et al., 2009, 2011a; Pasckert et al., 2018). The absolute model age of each unit was previously derived from the crater-counting results (Hiesinger et al., 2006, 2011; Morota et al., 2009, 2011a; Pasckert et al., 2018).

A summary of the remote sensing data used for the Moon is shown in Table

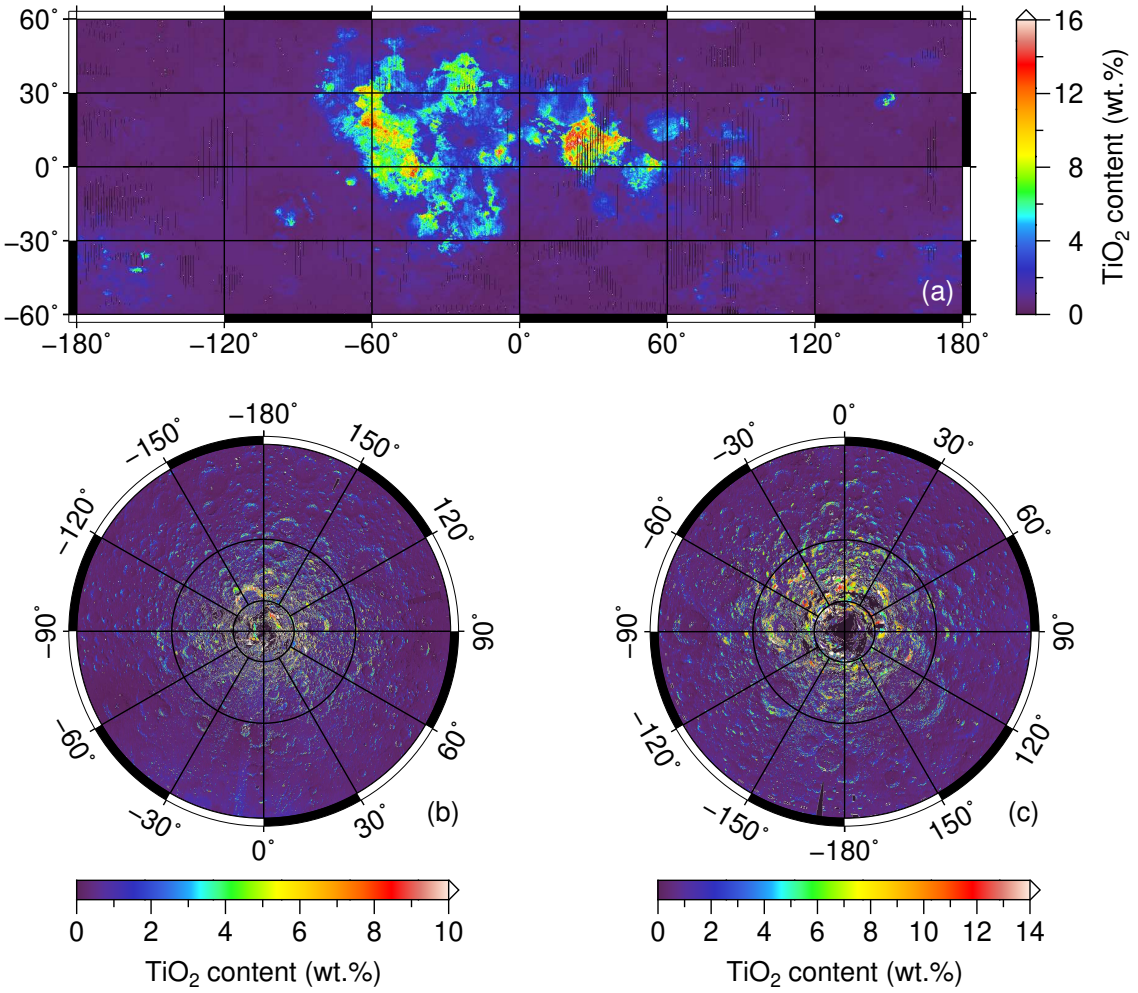

Figure 2.5: TiO_2 abundance maps used in this study: MI for 60°S–60°N (a), Clementine for 60°N–90°N (b) and 60°S–90°S (c).

2.1. The data resolution, coverage, uncertainty and the corresponding reference are given.

2.2.2 Mercury

The remote sensing datasets used for Mercury can be divided into three categories. For the surface reflectance, optical images acquired by the Mercury Dual Imaging System camera onboard the MESSENGER spacecraft were used. For the surface composition, a color ratio image produced by the MDIS images with multiple wavelengths was used to aid our understanding of the geological context of the region. For the surface topography, the elevations measured by the Mercury Laser Altimeter onboard the MESSENGER spacecraft were used to extract the elevation

profiles of both fresh and partially buried craters.

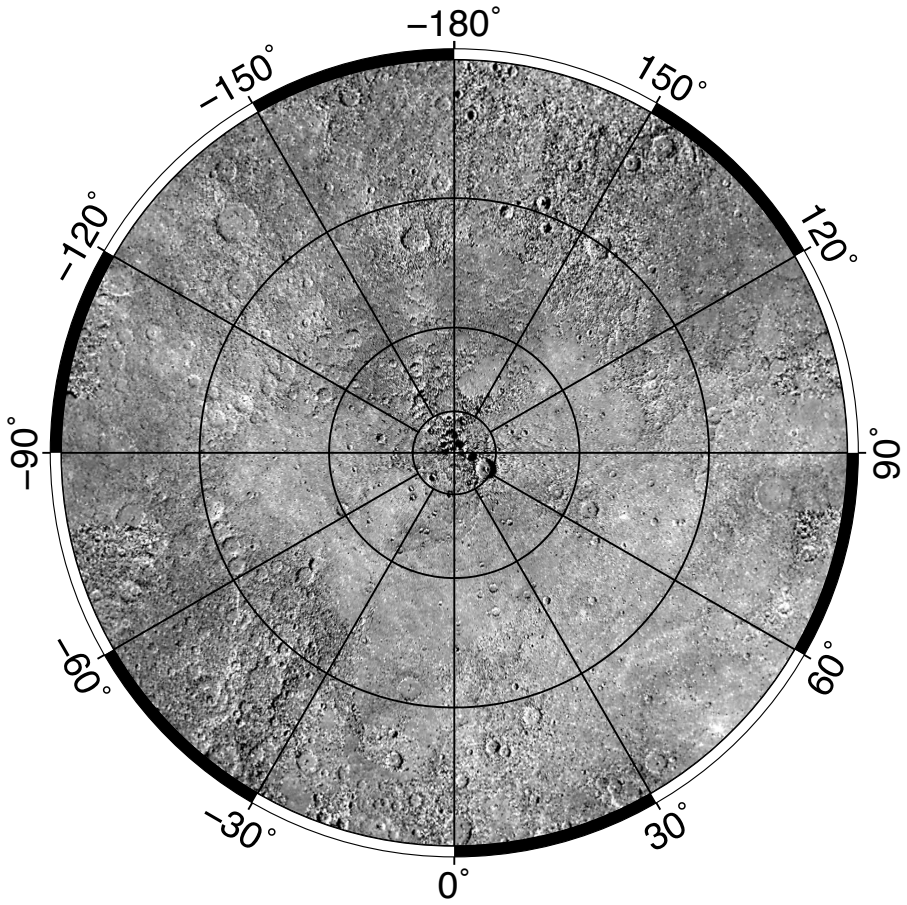

Figure 2.6: The MDIS mosaic used in this study (45°N–90°N).

The final released MESSENGER/MDIS global mosaics were produced with a spatial resolution of 166 m/pixel. The data products have four separate versions with different incidence angles: moderate incidence angle, low incidence angle, east illumination, and west illumination, and the one with moderate incidence angle is shown in Figure 2.6 (Denevi et al., 2016). Images with moderate incidence angle (about 74° with respect to the surface normal) highlight the surface morphological structures, those with low incidence angle feature the reflectance variations, and those with east and illumination conditions (usually with high incidence angles) are helpful when identifying structures with large relief such as craters and wrinkle ridges. Considering that images with different viewing geometries (thus different light and shadow contrasts) can provide complementary information on the recognition of surface features, all of these four versions of global mosaics are used in this study.

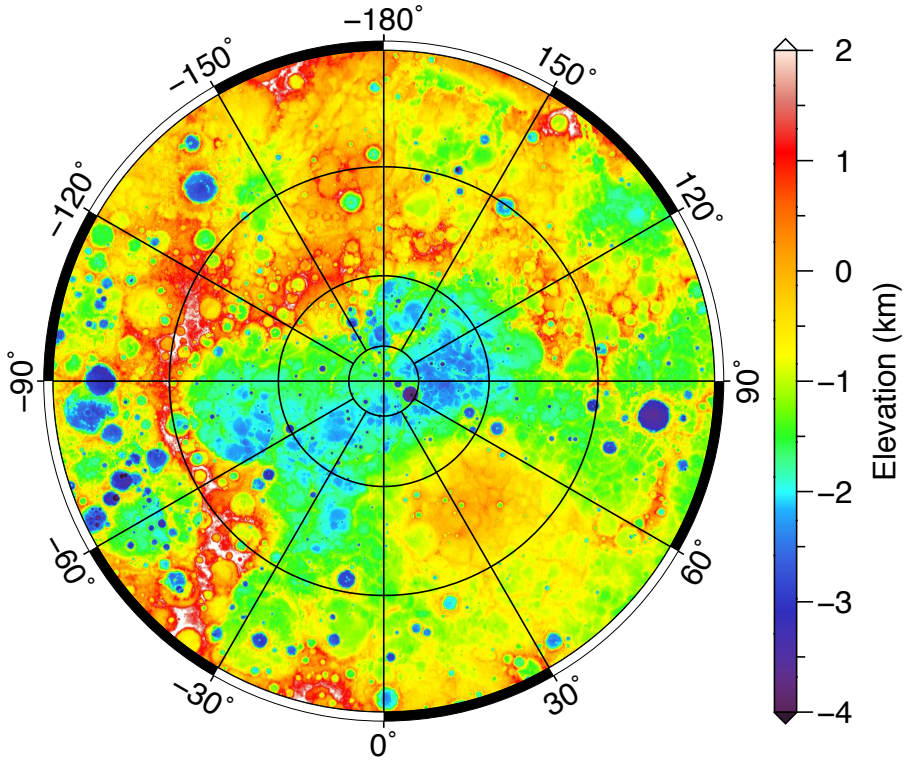

Figure 2.7: The MLA elevation data used in this study (45°N–90°N). This is an interpolated DEM.

The topography of the surface of Mercury has been acquired by the Mercury Laser Altimeter and the MESSENGER Dual Imaging System stereo images. The MESSENGER spacecraft observed the surface of Mercury along a highly elliptical orbit with a periapsis of 200 to 400 km and an apoapsis of 15,000 km, and only the northern hemisphere has densely distributed laser footprints of MLA (Sun and Neumann, 2015). The resulting, interpolated DEM is presented in Figure 2.7. The MLA transmits eight pulses per second at the wavelength of 1064 nm with a width of 6 ns. The size of the footprint is 15–100 m in diameter, and the gap between two adjacent nadir points is roughly 400 m (Zuber et al., 2012). The returned signal is sent to three matching filters. The first matching filter is designed for flat surfaces, so the impulse response is set to 8.5 ns, which is close to the transmitted pulse width. The convolved signal with this filter is sent to two threshold discriminators (high and low), which have range biases of 3.57 m and 4.64 m and are designated as channel IDs 0 and 1. The second matching filter is designed for surfaces with moderate roughness, and the impulse response is set to 63 ns, which is larger than the transmitted pulse width. The convolved signal with this filter is sent to one

low-threshold discriminator, which has a range bias of 16.04 m and is designated as channel ID 2. The third matching filter is designed for surfaces with large topographic relief, and the impulse response is set to 283 ns, which is much larger than the transmitted pulse width. The convolved signal with this filter is sent to another one low-threshold discriminator, which has a range bias of 52.91 m

and is designated as channel ID 4. As a result, once a signal is transmitted, multiple pulses with different time delays may be detected by the receiver, and hence multiple elevations may be deduced. The above mentioned parameters (e.g., surface elevations, mission elapsed time, longitude and latitude of the nadir point, and channel ID) were recorded in the MLA Reduced Data Records (RDR). The MLA gridded DEM records (MLA GDR) were produced by interpolating the RDR data with a spatial resolution of 250 m/pixel, covering the $> 55°$N region (Becker et al., 2016; Neumann et al., 2016).

The MDIS-derived DTM data were produced with a spatial resolution of 665 m/pixel and a global coverage. The offset between the MDIS-derived DTM and the MLA GDR can be as large as 1.0 km in the northern hemisphere, possibly due to the changes in camera focal length of MDIS arising from the complicated thermal environment experienced by the spacecraft that orbits Mercury (Neumann et al., 2016). We notice that, no matter the MDIS-derived DTM or the MLA GDR is used as the elevation data, this 1-km offset is unimportant as the crater degradation is controlled by the relative elevation difference (i.e., slope) instead of the absolute value of the elevation.

We next compared the elevation data and profiles derived from MLA RDR, MLA GDR and MDIS DTM for a given crater (51.88°N, 54.26°W; D=29.6 km) (Figure 2.8). The spatial distribution of the channel ID, the measured elevations as a function of radial distance, and the spatial distribution of the measured elevations are respectively shown in Figures 2.8a, b and c. The two-dimensional MLA GDR and MDIS DTM are presented in Figures 2.8d and e. The azimuthally averaged elevation profiles extracted from MLA RDR, MLA GDR and MDIS DTM are plotted in Figure 2.8f. When comparing the MLA RDR data with the MLA GDR data, we found that (1) there are lots of artificial stripes in the MLA GDR map that result from the interpolation processing, and that (2) the two data are offset by roughly 600 m due to the fact that the MLA RDR assumed a reference radius of 2439.4 km

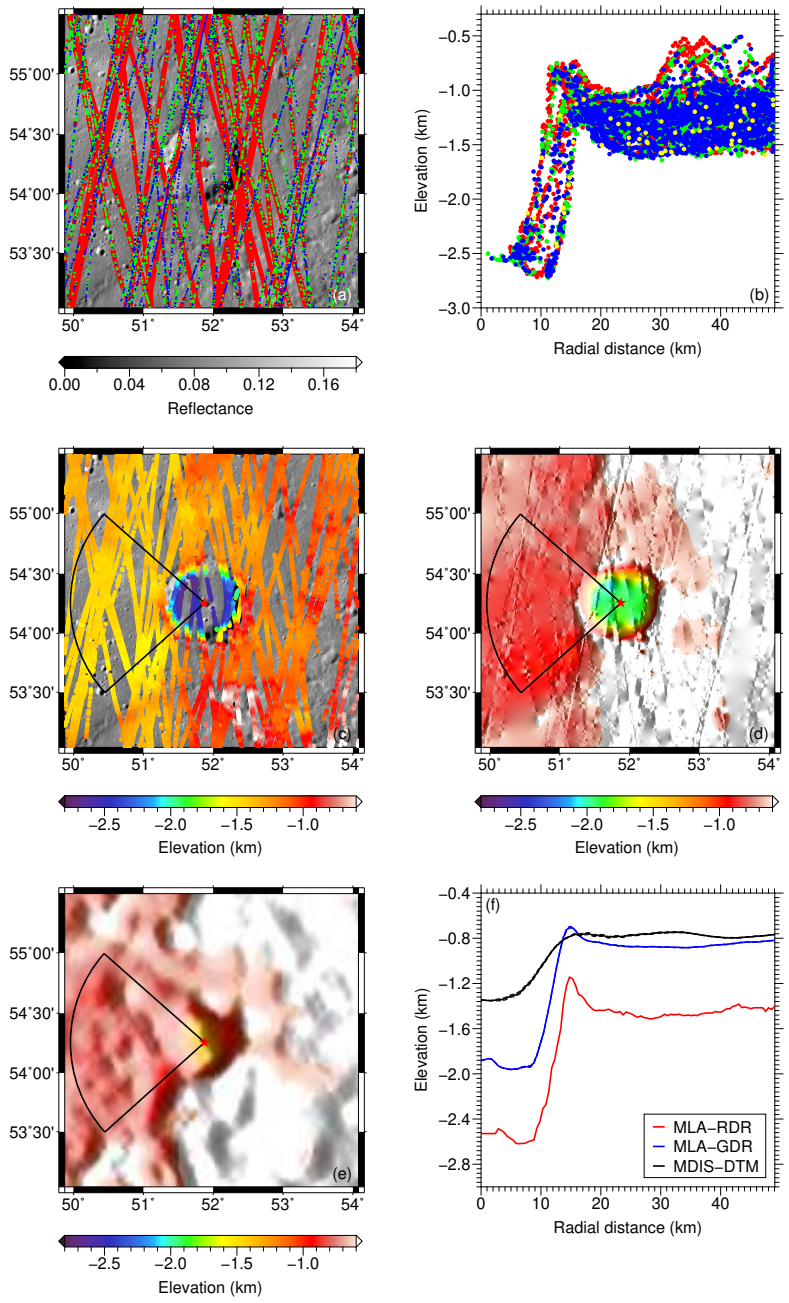

Figure 2.8: An example illustrating the differences between the RDR, GDR and MDIS elevation datasets. A typical partially buried crater (D=29.6 km) is shown here. In (a), the red, green and blue dots denote the nadir points of the MLA with channel IDs equal to 0, 1, and 2, respectively, overlain on a MDIS image. In (b), the elevation is shown as a function of the radial distance from the crater center. In (c–e), the two-dimensional elevations measured by MLA RDR, MLA GDR and MDIS DTM are plotted, respectively. The black fans show the region where the elevations were extracted for the elevation profile of the partially buried crater. In (f), the azimuthally averaged radial profiles extracted from the MLA RDR, MLA GDR and MDIS DTM are plotted.

for Mercury whereas the MLA GDR used a value of 2440.0 km. When comparing the MLA RDR data with the MDIS DTM data, a systematic offset of 600 m also exsits, but more importantly, the topographic relief in the MDIS DTM data has been significantly suppressed.

As seen from the comparison above, the MLA RDR have a much better performance in preserving the original surface topography, and therefore in this study we decided to use the MLA RDR data to calculate the radial elevation profile. We took the following steps to do so: (1) we imported the MLA RDR data in a table form, and ranked all the records by mission elapsed time (in seconds); (2) if multiple records have the same mission elapsed time, we sorted them by pulse number; (3) if multiple records have the same pulse number, we ranked them by channel ID; (4) finally, we only used the data record with the lowest channel ID as it has the smallest range bias (for example, if one transmitted pulse returns three channel IDs=0, 2 and 4, we will only use the record with channel ID=0). It should be noted that, however, most of the data records have channel IDs equal to 0 or 1, and that in practice, measurements with channel ID equal to 4 are usually unreliable. Using the studied region in Figure 2.8 as an example, channel IDs with 0 and 1 account for over 95% of the total measurements.

As we do not have any samples from Mercury, it is difficult to construct a quantitative relationship between mineral content and its surface reflectance. Currently, we use a RGB composite map produced by the MDIS multi-band images to qualitatively divide the surface of Mercury into different regions (Figure 2.9) (Denevi et al., 2016). This was done by implementing a principle component analysis (PCA) on the MDIS images at 430, 750 and 1000 nm, and assigning red, green, and blue to the second component, the first component, and the 430 nm to 1000 nm ratio. The resulting image product covers the entire the surface of Mercury with a spatial resolution of 665 m/pixel. Note that this mosaic was created to emphasize color differences on Mercury's surface by simply applying a mathematical analysis, and it is not linked to the abundance of any specific type of elements/minerals/rocks. Nevertheless, we did notice that the smooth plains appear in yellow and the heavily cratered terrain appears in blue. We also note that although element ratios on the surface of Mercury acquired by the MESSENGER/X-Ray Spectrometer (XRS) can also show spatial variation in composition, they are poor in resolution (42–3200 km)

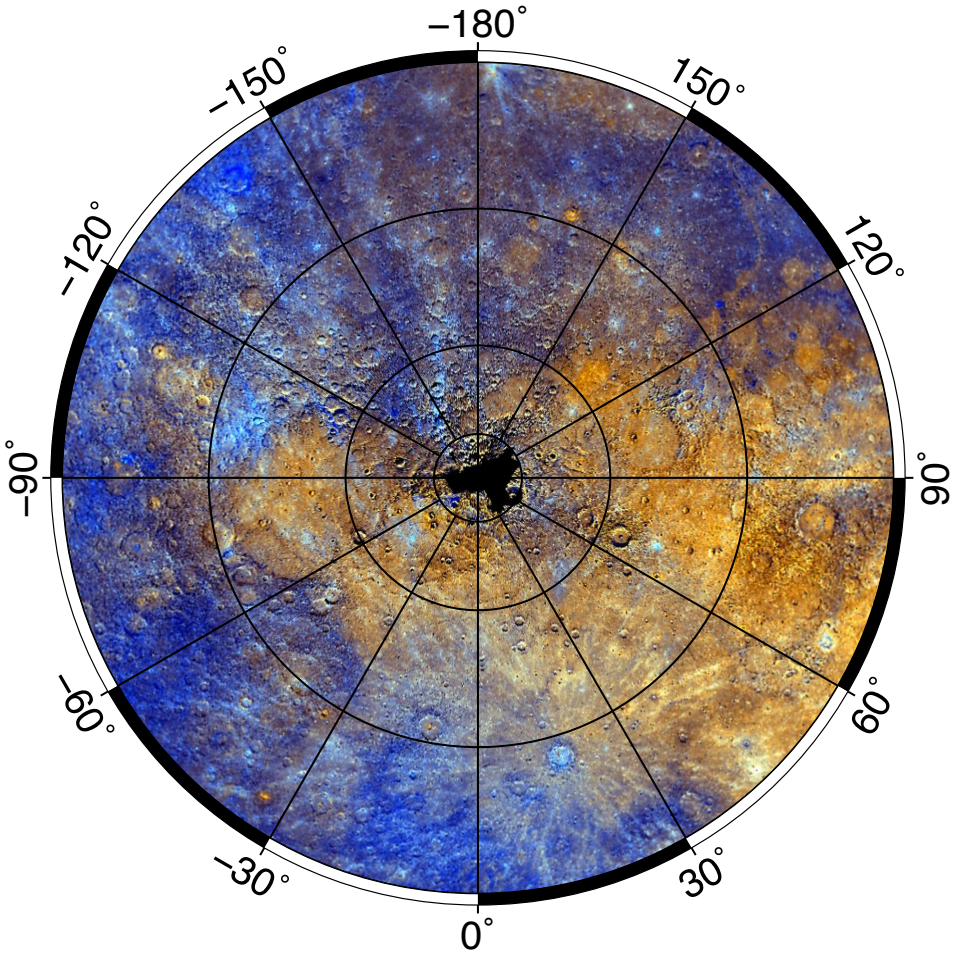

Figure 2.9: The false color composite map used in this study (45°N–90°N). Note that this mosaic was created to emphasize color differences on Mercury's surface by simply applying a mathematical analysis, and it is not linked to the abundance of any specific type of elements/minerals/rocks. Nevertheless, we did notice that the smooth plains appear in yellow and the heavily cratered terrain appears in blue.

and thus were not used in this study (Schlemm et al., 2007).

The smooth plains on Mercury are characterized by sparsely distributed craters, a flat surface topography, and a well-defined boundary with surrounding terrains (Trask and Guest, 1975). Using the MDIS images, MDIS DTM and MLA GDR, Denevi et al. (2013) mapped the boundary of the smooth plains on Mercury based on these characteristics mentioned above. In order to date the surface of the northern smooth plains, Ostrach et al. (2015) randomly divided the entire region into four subregions and obtained crater-size frequency distributions for each. They found that no matter how they divided the region, they always obtained the same surface

age of 3.7 Gyr for all the subregions. Therefore, the last episode of volcanism within the northern smooth plains must have taken place at 3.7 Ga and have flooded the entire region. Ostrach et al. (2015) also found that in some cases a larger completely buried crater is surrounded by many much smaller completely buried craters, indicating that multiple phases of volcanic eruption must have occurred in the region. However, the authors did not find a deflection point in the obtained crater-size frequency distributions, which suggests that the temporal gap between two successive phases must be short.

A summary of the remote sensing data used for Mercury is shown in Table 2.2. The data resolution, coverage, uncertainty and the corresponding reference are given.

Table 2.2: A summary of the remote sensing data used in this study for Mercury.

Class	Datasets	Resolution	Coverage	Uncertainty	Reference
Optical	MDIS	166 m/pixel	Global	–	Denevi et al. (2016)
Elevation	MLA RDR	Along track: 400 m	>45°	3–5 m	Sun and Neumann (2015)
Composition	MDIS	665 m/pixel	Global	–	Denevi et al. (2016)

2.3 Identification of Partially Buried Craters

On the Moon, partially buried craters are those whose crater ejecta are partially covered by lava flows whereas the crater rim is partially protruding above the surrounding lavas (De Hon, 1974). By this definition, two criteria are proposed for the identification of a partially buried crater: (1) the transition between crater ejecta and post-impact lava flows should be abrupt and well-defined, and (2) the extent of the exposed proximal ejecta should be smaller than one crater radius. The first criterion is a result of the fact that ejecta deposits grade smoothly from continuous to discontinuous deposits. Lava flows that embay the crater simply truncate the preexisting ejecta. The second criterion is a result of the fact that continuous ejecta of unburied lunar craters usually extend about one crater radius from the crater rim (Moore et al., 1974).

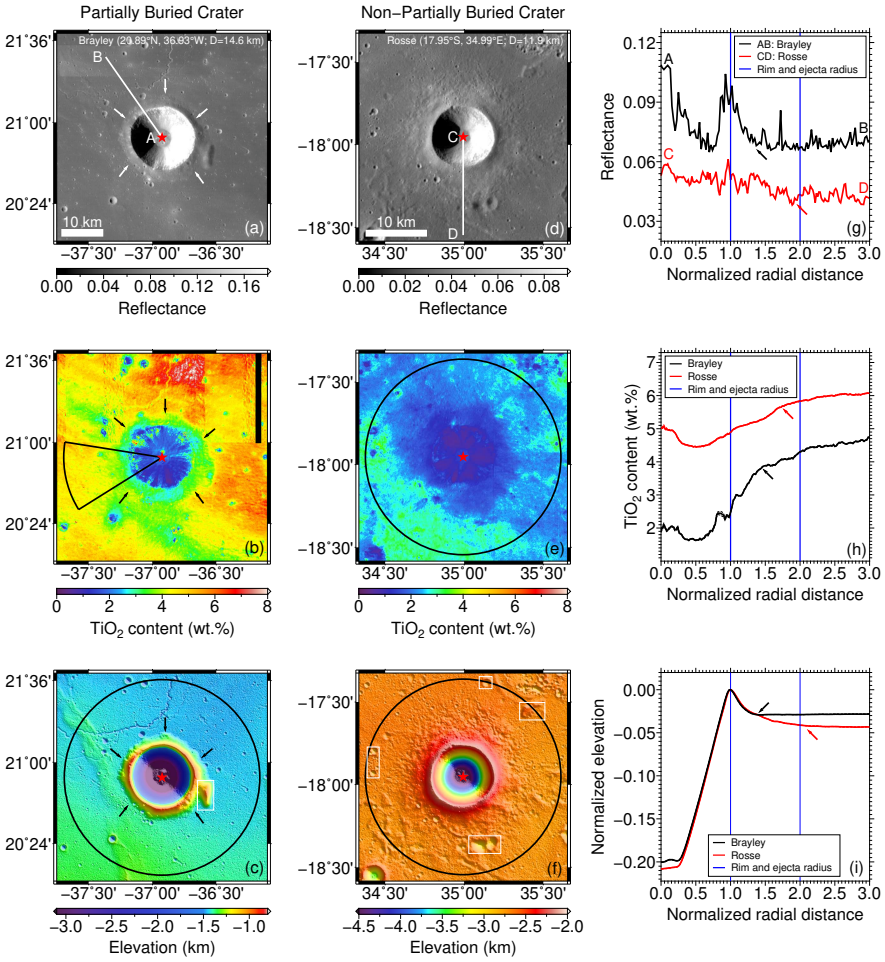

Figure 2.10: Examples of a typical partially buried crater Brayley (D=14.6 km) and a normal, unburied crater Rosse (D=11.9 km) on the Moon. LROC/WAC reflectance, SELENE/MI derived TiO_2 content, and SLDEM elevation maps for Brayley (a–c) and Rosse (d–f) are shown in the top, middle, and bottom rows, respectively. The right column plots selected individual radial profiles (AB and CD) of reflectance (g), and the azimuthally averaged radial profiles of TiO_2 content (h) and elevation (i), for Brayley (solid black lines) and Rosse (solid red lines). In (a–f), the red stars denote the locations of crater centers. In (b), (c), (e) and (f), the solid black lines give the boundaries where the azimuthally averaged radial profiles were extracted. In (a–c), the white and black arrows indicate the boundaries of the crater ejecta. In (c) and (f), the white boxes are areas excluded when calculating elevation profiles. In (g–i), the black and red arrows point to the manually identified ejecta boundaries for Brayley and Rosse, respectively, and the solid blue lines denote the crater radius and the predicted continuous ejecta radius for unburied crater ejecta. All the profiles are plotted with the radial distance normalized by crater radius, and the elevation profile is plotted with the vertical elevation normalized by crater diameter. The rim crest elevation of Brayley was set to be 0, and the crater profile of Rosse was shifted vertically to have the same rim crest elevation as Brayley.

Evidence for these two diagnostic characteristics can be found easily in the reflectance, composition, and elevation maps of impact craters. As an example, in Figure 2.10, the partially buried crater Brayley (20.89°N, 36.93°W; D=14.6 km) and the unburied crater Rosse (17.95°S, 34.99°E; D=11.9 km) are selected here for a detailed comparison. Both craters are simple craters with a bowl shape and a similar size. The ejecta boundary of Brayley is seen to have an abrupt boundary in the reflectance, TiO_2 content, and elevation data (arrows in Figures 2.10a–c). In contrast, the crater ejecta of Rosse gradually degrade to the background terrain, and the ejecta boundary is not well defined (Figures 2.10d–f). The ejecta radii of Brayley (black) and Rosse (red) were obtained by using the abrupt changes in the reflectance, TiO_2 content, and elevation radial profiles (Figures 2.10g–i). For the crater Brayley, the radial profiles reach the background level at about 1.4 times the crater radius (black arrows), whereas for the crater Rosse, the ejecta boundaries (red arrows) are difficult to determine but are with no doubt larger than those of Brayley.

Because the crater diameters of Brayley and Rosse are similar, a comparison of the exposed rim heights derived from the elevation profiles can provide additional evidence on the burial of Brayley's ejecta by lava flows (Figure 2.10i). In this study, the azimuthally averaged radial profile of the crater is used to calculate its rim height, which is defined as the elevation difference between the rim crest and the background terrain as averaged within 2.5–3 crater radii from the crater center. The exposed rim height of Brayley is estimated to be 415 m, in comparison with 512 m for Rosse. Since Brayley is about 2.7 km larger and also appears morphologically younger (shaper rim crest and more prominent streaks of fresh boulders in the crater inner wall) than Rosse, the most likely explanation for the smaller exposed rim height of Brayley is the emplacement of lava flows exterior to the crater rim.

For partially buried craters on Mercury, the identification criteria are almost the same, except that the continuous ejecta extent is usually 0.8 times the crater radius (Gault et al., 1975). In Figure 2.11, we present a typical partially buried crater (54.26°N, 51.98°E; D=29.6 km) and an unburied crater (82.64°N, 42.73°W; D=26.7 km). For the partially buried crater, we found a clear, well-defined boundary between the crater ejecta and surrounding lava flows (Figures 2.11a and b). For the unburied crater, the ejecta blanket has a diffusive, continuous transition to the

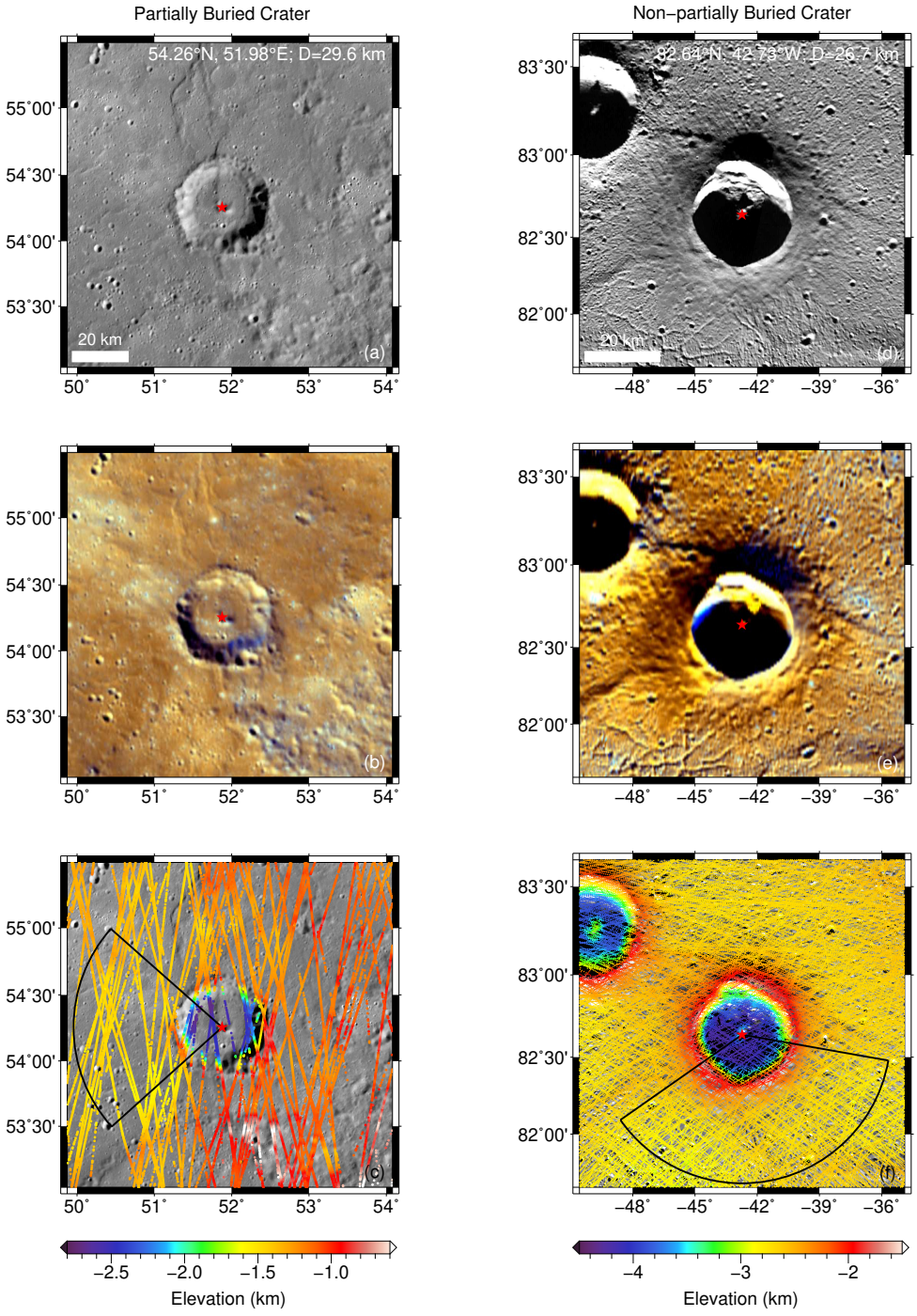

Figure 2.11: Examples of a typical partially buried crater (D=29.6 km) and a normal, unburied crater (D=26.7 km) on Mercury. MDIS reflectance, MDIS RGB color composite, and MLA elevation maps for the partially buried crater (a–c) and the unburied crater (d–f) are shown in the top, middle, and bottom rows, respectively. In (a–f), the red stars denote the locations of crater centers. In (a) and (b), the white arrows indicate the boundaries of the exposed crater ejecta. In (c) and (f), the solid black lines give the boundaries where the azimuthally averaged radial profiles were extracted.

background region and does not have a clear boundary (Figures 2.11d and e). Considering the facts that the optical and color ratio images are poor in spatial resolution and that a large shadow region exists inside the high-latitude unburied crater, we did not produce azimuthally averaged radial profiles for the surface reflectance and composition. Nevertheless, the azimuthally averaged elevation profiles can still be extracted from the MLA RDR data for these two craters. By looking for the abrupt change in slope along the radial profile, the ejecta boundary of the partially buried crater was found at about 1.25 times the crater radius (black arrow), which is with no doubt smaller than that of the unburied crater at about 2.05 times the crater radius (red arrow) (Figure 2.12).

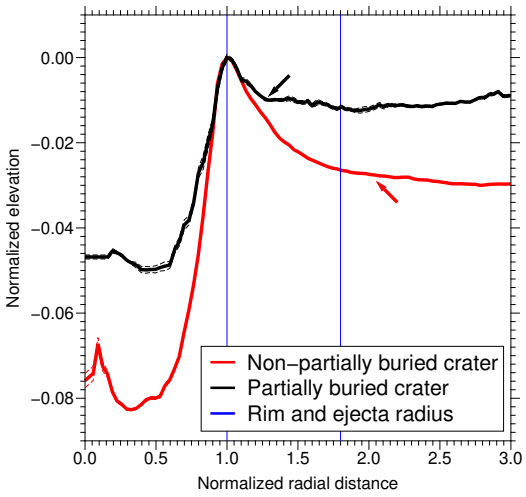

Figure 2.12: Azimuthally averaged elevation profiles for the partially buried crater (D=29.6 km) (black) and the unburied crater (D=26.7 km) (red) shown in Figure 2.11. The black and red arrows point to the manually identified ejecta boundaries for the two craters, and the solid blue lines denote the crater radius and the predicted continuous ejecta radius for an unburied crater. The elevation profiles are plotted with the radial distance normalized by crater radius and with the vertical elevation normalized by crater diameter. The rim crest elevation of the partially buried crater was set to be 0, and the crater profile of the unburied crater was shifted vertically to have the same rim crest elevation as the partially buried crater.

In addition, we can find that the exposed rim height of the partially buried crater is 286 m, which is much smaller than that of the unburied crater with a value of 801 m. Considering the fact that the partially buried crater is larger than the unburied crater in size by ∼3 km, we infer that the smaller exposed rim height of

the partially buried crater is due to the burial of lava flows.

2.4 Lava Flow Thickness Estimation Method

2.4.1 Model Descriptions

Given an initial crater profile, we can make use of a topographic degradation model to determine how the profile varies with time. Micrometeoroid bombardment is thought to be one of the major processes that degrade craters. It can be modeled as a diffusive process, where ejecta that are newly excavated by small craters trigger downslope movement under the influence of gravity. Other processes, such as seismic shaking and ejecta fragment emplacement, can also be modeled as diffusive processes and may be more important for craters on asteroids and small craters on the lunar maria (Minton et al., 2019; Richardson et al., 2005). The topographic diffusion model assumes that the volume flux on a sloped surface is proportional to the topographic gradient, as shown below (Culling, 1960):

$$\overrightarrow{q} = -\kappa \cdot \nabla H \tag{2.1}$$

where κ is topographic diffusivity, H is elevation, ∇ denotes gradient.

Based on the mass conservation law, we can then obtain that (details can be found in Culling (1960)):

$$\frac{\partial H}{\partial t} = -\nabla \cdot \overrightarrow{q} \tag{2.2}$$

Based on Equations 2.1 and 2.2, the topographic diffusion equation can be deduced as (Culling, 1960):

$$\frac{\partial H}{\partial t} = \kappa \nabla^2 H \tag{2.3}$$

Equation 2.3 is a diffusion equation widely used in thermal physics, and in the cylindrical coorodinate it can be written as:

$$\frac{\partial H}{\partial t} = \kappa\left(\frac{\partial^2 H}{\partial r^2} + \frac{1}{r}\frac{\partial H}{\partial r}\right) \tag{2.4}$$

We can then separate $H(r,t)$ as $H(r,t) = R(r)T(t)$ where r is radial distance and t is time, and rewrite the diffusion equation:

$$\frac{1}{R}\left(\frac{d^2 R}{dr^2} + \frac{1}{r}\frac{dR}{dr}\right) = \frac{1}{a^2 T}\frac{dT}{dt} \tag{2.5}$$

The solution of $R(r)$ is $R(r) = J_0(\mu r/L)$, where J_0 is the Bessel function of the first kind and zeroth order. The boundary condition requires that $R(L)$=0 where L is the maximum value of r, so it yields $J_0(\mu) = 0$ where there is an infinite number of constants μ_k. Then, for the temporal part of the solution $T(t)$, we have

$$\frac{dT_\mathrm{k}}{dt} + \frac{\mu_\mathrm{k}^2 \kappa}{L^2} T_\mathrm{k} = 0 \tag{2.6}$$

, and it has the solution:

$$T_\mathrm{k}(t) = A_\mathrm{k} \exp(-\mu_\mathrm{k}^2 \kappa / L^2 t) \tag{2.7}$$

Therefore, the product solution is

$$H_\mathrm{k}(r, t) = A_\mathrm{k} J_0(\mu_\mathrm{k} r/L) \exp(-\mu_\mathrm{k}^2 \kappa / L^2 t) \tag{2.8}$$

The total solution will be the sum of a series of H_k:

$$H(r_\mathrm{nd}, t) = \sum_{\mathrm{k}=1}^{\infty} A_\mathrm{k} J_0(\mu_\mathrm{k} r_\mathrm{nd}) \exp(-\kappa t R^{-2} \mu_\mathrm{k}^2) \tag{2.9}$$

where r_nd is the radial distance from the crater center normalized by crater radius R as the crater shape is diameter-depdendent. A_k is a coefficient that can be written as (Duffy, 2016):

$$A_\mathrm{k} = 2 \int_0^L r_\mathrm{nd} H(r_\mathrm{nd}, 0) J_0(\mu_\mathrm{k} r_\mathrm{nd}) \mathrm{d}r_\mathrm{nd} / (L^2 J_1^2(\mu_\mathrm{k} L)) \tag{2.10}$$

where J_1 is the first-order Bessel function and $H(r_\mathrm{nd}, 0)$ is the initial crater profile.

We can then develop a method for determining the thickness of lava flows that partially bury a crater. This method uses an initial crater topographic profile, and crater degradation is accounted for by use of a diffusive topographic degradation model. Topographic degradation occurs both before and after the emplacement of the lava flows. Model parameters include the initial diameter of the crater (D_init), the time at which the crater formed (t_c), the time when the lava flows were emplaced (t_l), the thicknesses of the lava flows exterior and interior to the crater rim (T_ext and T_int), and diffusion parameters that determine the rate of the topographic degradation between crater formation and lava emplacement (κ_c) and after lava emplacement (κ_l). Model parameters are then determined by minimizing the root-mean-square

difference (σ) between the modeled final topographic profile (H_{final}) and the observed profile (H_{obs}):

$$\sigma = \sqrt{\sum_{i=1}^{N} \left[H_{\mathrm{final}}\big(D_{\mathrm{init}}, T_{\mathrm{ext}}, T_{\mathrm{int}}, \kappa_{\mathrm{c}} t_{\mathrm{c}}, \kappa_{\mathrm{l}} t_{\mathrm{l}}, z_0; i\big) - H_{\mathrm{obs}}\big(i\big)\right]^2 / N} \tag{2.11}$$

where z_0 is a vertical offset between the modeled final and the observed profiles, and i is the ith of N points along the profile. Though we can also solve for the thickness of the lava flows that erupted interior to a crater's rim, this will not be discussed further.

To obtain the final modeled profile, we need two steps of crater degradation. Before the eruption of the lava flow, the initial condition is the topographic profile of the newly formed, fresh crater. After the lava flow emplacement, the initial condition is the topographic profile of the crater that was just flooded by the lava flows, and then the present-day profile can be solved. Once the observed profile and a series of modeled profiles are acquired, the lava flow thickness can be estimated by finding those parameters that minimize the difference between the modeled and observed profiles.

The first step in estimating the initial topographic profile of a partially buried crater on the Moon is to determine whether the crater formed on a mare or highland target. This is necessary because the initial crater profile for fresh lunar craters is slightly different in the highlands and maria. The composition of the rim and proximal ejecta of the identified crater is used to determine the composition of the target, and here we used the FeO content as an indicator. The FeO content of mare materials is typically greater than 18 wt.%, whereas that of the highland crust is typically less than about 10 wt.% (Heiken et al., 1991). We use the intermediate value of 14 wt.% to discriminate between the two target compositions. For Mercury, we do need to distinguish between fresh craters that formed on the northern smooth plains and the heavily cratered terrain, as the two have similar crater shapes (Susorney et al., 2016).

Next, we need to extract the azimuthally averaged radial elevation profiles of the partially buried craters. In this study, the studied region is defined as a circle that extends three crater radii from the crater center. We first excluded atypical topographic features (larger than half of the crater radius in dimension) in the studied region such as small young impact craters, rilles, and faults, and then

extracted the elevations in the remaining area. If there are too many of them, we otherwise defined a fan-shaper region with no atypical topographic features, and then only extracted the elevations therein. For lunar craters, the radial profiles of craters smaller than 18 km in diameter were binned with a width of 100 m, whereas for craters larger than 18 km in diameter, the radial profiles were binned within 300 equally spaced annuli. For craters on Mercury, the bin width was set to 500 m, given that the gap between two adjacent MLA nadir points is about 400 m. Finally, we defined a maximum radial range for each profile by looking for any abrupt changes in slope that might result from either a non-flat initial surface or post-impact modification processes. Only the elevations with radial distances smaller than this maximum range are compared with the modeled profiles when estimating the lava flow thickness. Among the 74 mare craters with rims completely exposed to be studied, 11 of them have maximum radial ranges smaller than two crater radii. Among the 21 rim completely exposed craters to be studied on Mercury, 7 of them have maximum radial ranges smaller than two crater radii.

When performing the numerical inversion for the best-fitting parameters and uncertainties, one would ideally like to perform a global exhaustive search of the parameter space. Given the number of free parameters and their extensive ranges, however, this task would have been computationally prohibitive. In order to reduce the computation time, a global optimization algorithm using the sequence quadratic polynomial (SQP) technique (Schittkowski, 1986) was used to search for the best-fitting model parameters in the six-dimensional parameter space. This method uses a series of quadratic polynomial functions to approximate the nonlinear objective function, and the global optimal solution is found by searching along the direction with the largest gradient in the model parameter space. In this study, the Global Optimization Toolbox in MATLAB (MATLAB Documentation, 2017) was used to solve this optimization problem. In our lunar study, the standard error of the crater profiles selected for inversion varies from 1 to 6 m with a median value of 3 m. As the maximum tolerable RMS misfit for the objective function should be close to this value, it is then set to 5 m in this study. Once the objective function is below this value, the search for the global minimum stops. If not, the search continuous until the maximum iteration number is reached, which is set to 50 in this study.

We tested the applicability of this optimization algorithm in two different ways.

First, we conducted a forward simulation of a 3-Gyr-old, 10-km-diameter lunar mare crater that was embayed by basalt flow with an assumed thickness of 43 m, and then ran the global optimization toolbox to search for the basalt thickness. The result shows that the obtained basalt thickness differs only by 1 m with respect to the true value. Second, we varied the number of starting points used to initialize the optimization in the toolbox where each starting point consists of initial guesses for the six parameters in Equation 2.11. We increased the number of starting points from 20 to 100, and set the initial values to be uniformly distributed in the parameter space. We found that, although different starting points gave slightly different results, the final results were all within the uncertainties obtained from our numerical inversion, as described below. Therefore, we can conclude that this global optimization toolbox converges adequately to the global minimum.

2.4.2 Model Setup

First, we need to clarify that we used the products of diffusivity and time between crater formation and lava flow emplacement $K_c = \kappa_c t_c$ and after lava flow emplacement $K_l = \kappa_l t_l$ as model parameters, instead of only using diffusivity or time alone. This is because the product of the two completely determines the topographic degradation, and we have few constraints on either the ages or diffusivities. For simplicity, and with no impact on our determination of the thickness of the lava flow exterior to the crater, we assume that any lava flows interior to the crater rim were emplaced at the same time as those exterior to the rim. There could be lava flows in the crater interior (with no breaches on the crater rim) because there are fractures created under the crater floor during the formation of the crater. As a result, these fractures result in favourable stress conditions for the ascent of the magmas, making them easier to reach the crater floor. Besides, there could be multiple basaltic flows that were emplaced on top of the crater ejecta, but can not be traced because all the subsurface basaltic units were buried by the surface basaltic layer. Therefore, we assumed that they were emplaced at the same time in order to reduce the number of parameters and thus simplify our inversion model. Nevertheless, this assumption does not affect our estimated basalt thickness in any significant manner.

Our estimation method quantifies the misfit between the observed and modeled

profiles as a function of six model parameters. We first introduce how we parameterize them for partially buried craters on the Moon. The initial crater diameter (D_{init}) must be smaller than the final diameter (D_{f}), and we investigated a range from $0.6D_{\mathrm{f}}$ to D_{f} with a step size of 0.1 km. The exterior lava flow thickness (T_{ext}) must be less than the initial rim height (h_{r}), so we investigated values from 0 to h_{r} with a step size of 1 m. The interior lava flow thickness needs to be less than the depth of the crater floor below the rim crest (d_{cf}), and we investigated values up until this value with an interval of 1 m. The topographic profile of a partially buried crater was initially shifted to a vertical position where the background (2.5 to 3 crater radii) elevation is 0, and later the vertical offset parameter z_0 was allowed to vary from the lowest elevation (h_{r}–d_{cf}) to the highest elevation (h_{r}) along the profile with a step size of 1 m. The upper limit of the product of diffusivity and time after crater formation ($K_{\mathrm{max}} = K_{\mathrm{c}} + K_{\mathrm{l}}$) is more difficult to constrain a priori. Nevertheless, it was suggested that the diffusivity could be expressed as the product of the diffusivity at a reference scale (e.g., 1 km) and the crater diameter to the power of about 1 (Xie et al., 2017). In our simulations, K_{max} for crater formation was assumed to be equal to $5.5{\times}3900{\times}D_{\mathrm{f}}$ m^2 where 5.5 m^2/Myr is a reference diffusivity for a 1 km crater (Fassett and Thomson, 2014) and 3900 Myr is an upper limit for the crater age in our study (Stöffler and Ryder, 2001). We used a step size of 500 m^2 for the diffusivity-time product. After performing our simulations, we checked to ensure that our chosen maximum value for the product did not correspond to the best-fitting value, and that the maximum value was sufficient to obtain an error bar for the diffusivity-time product.

For Mercury, the model setup is almost the same as the Moon, except for the parameter K_{max}. We multiplied the lunar K_{max} value by a factor of five for Mercury, as studies have shown that the topographic diffusivity on Mercury could be twice the strength of that on the Moon (Fassett et al., 2017) and that the heavily cratered terrain may have an age of 4.0–4.1 Gyr (Marchi et al., 2013). Nevertheless, we have checked the inversion results to make sure that this model setup has allowed us to fully explore the parameter space.

Two of the outputs from the lava flow thickness estimation model are the best-fitting products of diffusivity and time before ($K_{\mathrm{c}} = \kappa_{\mathrm{c}} t_{\mathrm{c}}$) and after ($K_{\mathrm{l}} = \kappa_{\mathrm{l}} t_{\mathrm{l}}$) the emplacement of lava flows. If an age for the lava flow can be obtained, such as from

crater counting, then it would be possible to determine the absolute value of the topographic diffusivity. In particular, the average diffusivity since the eruption of the lava flow is given by $\kappa_l = K_l/t_l$. Furthermore, if we assume that the diffusivity was constant at all time ($\kappa_c = \kappa_l$), then we can estimate when the crater formed ($t_c = (K_c + K_l)/\kappa_l$).

2.4.3 Uncertainty Analyses

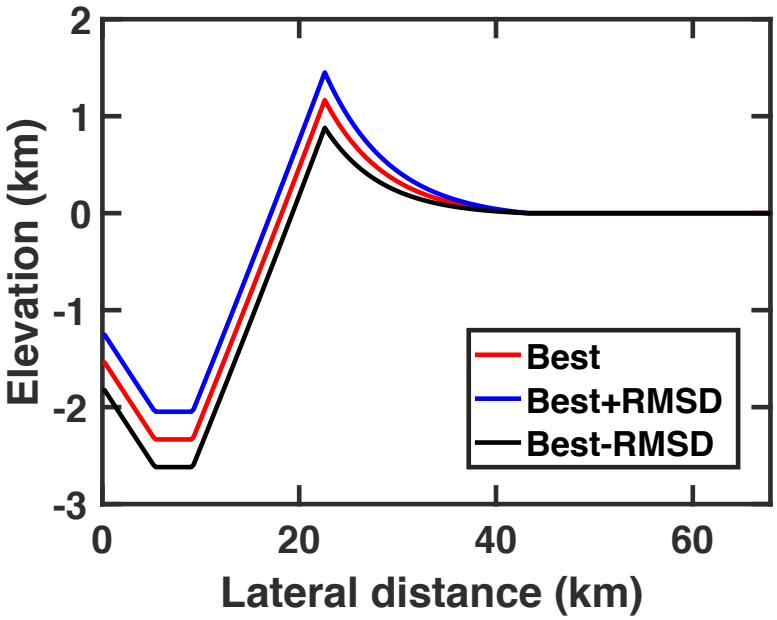

Figure 2.13: The initial profiles considering the uncertainty in initial rim height. The red profile corresponds to the best fitting initial rim height, and the blue and black profiles correspond to the best fitting initial rim height plus and minus one root-mean-square misfit.

The largest source of uncertainty in our numerical inversions is by far related to the natural variability of the rim height of the initial fresh crater. We first quantified this by performing three inversions: one using the nominal initial topographic profile for fresh craters, and two using initial topographic profiles where the rim height was modified by the $\pm\sigma$ natural variability as quantified in Table 3.7 for the Moon and Table 3.15 for Mercury. The best-fitting model parameters for these three cases were obtained using the procedure described above. Not surprisingly, the thickness of the lava flow exterior to the

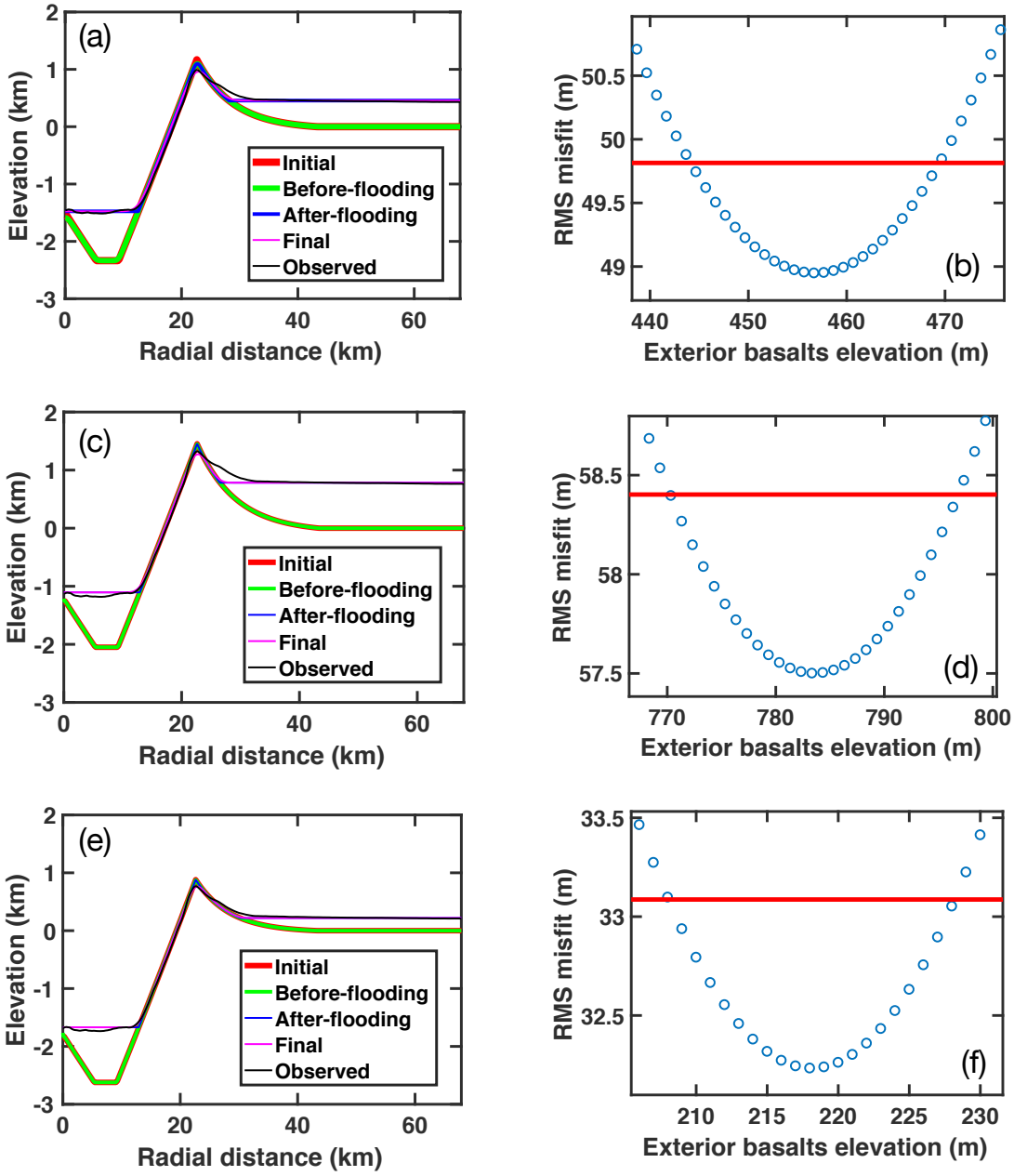

Figure 2.14: The three inversion results (a, c, and e) and the corresponding unvcertaty ranges of lava flow thicknesses (b, d, and f). The first row corresponds to the best fitting initial rim height, and the second and third rows correspond to the best fitting initial rim height plus and minus one root-mean-square misfit.

crater for the two modified initial crater profiles differs with respect to that for the nominal profile by the uncertainty in the initial rim height. An example is shown here with an initial diameter of 45.2 km. The best fitting initial rim height thus is 1168 m (red), and the root-mean-square misfit of the initial rim height-crater diameter relation is 286 m, so another two initial profiles with initial rim heights of 1454 (blue) and 882 (black) m are generated (Figure 2.13). Figures 2.14a, c and e then show the three inversion results, and the corresponding lava flow thicknesses obtained using three different initial profiles are 455, 783, and 218 m.

After obtaining the best-fitting parameters for the three initial topographic profiles, for each case we next used a simplified one-dimensional search to determine the uncertainties of the six model parameters. With the model parameters set to the best-fitting values, the misfit was calculated by varying a single parameter. The 1-σ limits of this parameter were then defined as those values that could fit the observations to within a maximum allowable misfit. This maximum allowable misfit was defined as the global minimum found by the optimization toolbox plus the average standard error of the observed elevation profile. The standard error here is an estimate of how uncertain the mean elevation of the observed profile is at each radial distance. On the Moon, the average standard error of the entire elevation profile of the selected 41 partially buried craters ranges from 1 to 6 m with a mean value of 3 m. On Mercury, the average standard error of 21 partially buried craters ranges from 1 to 37 m with a mean value of 11 m. The standard error of the elevation profile on Mercury is much larger than that on the Moon, simply as a result of the fact that we used more preliminary MLA RDR data for Mercury and interpolated, smoothed SLDEM data for the Moon. We note that this technique for determining the limits of the parameters does not consider correlations with the other five parameters: quantifying such correlations by computing the full six-dimensional misfit function would be computationally demanding.

We apply this technique to the three inversion results mentioned above. As a result, we obtain three different uncertainty ranges: 444–470 m, 770–797 m, and 208–228 m (Figures 2.14b, d, and f). Finally, we define the 1-σ limits for each parameter as the maximum and minimum 1-σ limits of the three inversions using the three separate initial crater profiles, which is 208–797 m.

Chapter 3 Initial Shape Modeling of Fresh Craters

3.1 Method Overview

Before solving the topographic diffusion equation (Equation 2.3), we require an initial condition, which is, for the topographic degradation model, the elevation profile of a fresh impact crater. For modeling of initial crater shape on the Moon, previous studies have investigated simple mare craters ($0.8 \leqslant D \leqslant 5$ km) (Fassett and Thomson, 2014) and complex highland craters ($20 \leqslant D \leqslant 166$ km) (Xie and Zhu, 2016), whereas our partially buried craters cover a diameter range of 1.5 to 130 km and formed on both mare and highland crust. For modeling of initial crater shapes on Mercury, there are no previous studies we can refer to. Therefore, we need to develop a more complete series of initial crater topographic profiles for craters on the Moon, and a brand new initial crater shape model for craters on Mercury (Figure 3.1).

For lunar craters, we first choose optical rayed craters as crater candidates (Werner and Medvedev, 2010). Conceptually, the craters are divided into six classes: simple ($1 \leqslant D \leqslant 15$ km), transitional ($15 < D \leqslant 20$ km), and complex ($D > 20$ km) craters over maria and highlands, as the crater shape changes with both crater diameter and target type (Melosh, 1989). Then, we need to remove the atypical features (e.g, crater/basin rims, wrinkle ridges, and large nearby craters) in the background before extracting the elevations from there, as they would otherwise result in a non-flat elevation profile. But even so, the resulting azimuthally averaged radial profile may not be flat in the background, and in this case, we need to define a maximum range within which the elevations are considered to be representative and valid. Next, for craters within the three diameter regimes, different strategies are taken to produce the radial elevation profile: for simple craters, the elevation profile is directly fitted in a normalized coordinate; for transitional and complex craters, we first derive the morphometric parameter-crater diameter relation, then retrieve

the coordinate of the tie point from this relation, and finally connect the tie points to generate the entire profile.

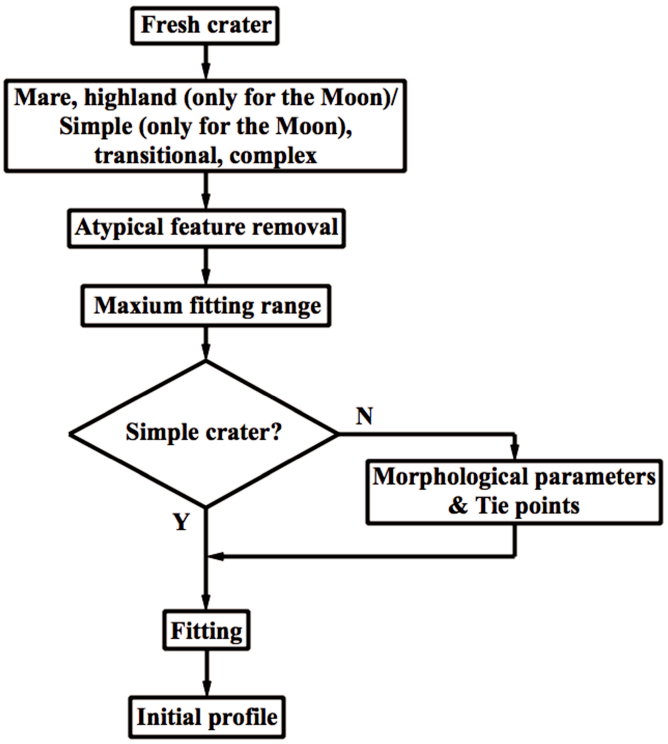

Figure 3.1: Flow chart to construct the initial profiles for fresh craters both on the Moon and Mercury.

For craters on Mercury, we first choose craters with sharp rims and well-preserved ejecta deposits as candidates (Susorney et al., 2016). As we did to lunar craters, craters on Mercury should have been divided into six classes as well. However, considering the facts that (1) the fidelity of the elevation data for small craters can not be warranted (Fassett et al., 2017) and that (2) previous studies have shown that there is no signifiant difference in crater morphology between craters on the northern smooth plains and heavily cratered terrain (Barnouin et al., 2012; Susorney et al., 2016), we simply work on two classes of craters on Mercury: transitional and complex craters. In order to produce the initial elevation profile, then we need to remove the atypical features in the background, define a maximum fitting range for each extracted profile, and derive the morphometric parameter-crater diameter relation, which are similar to the procedures as we applied to fresh craters on the Moon.

3.2 Database, Preprocessing, and Classification

3.2.1 Database

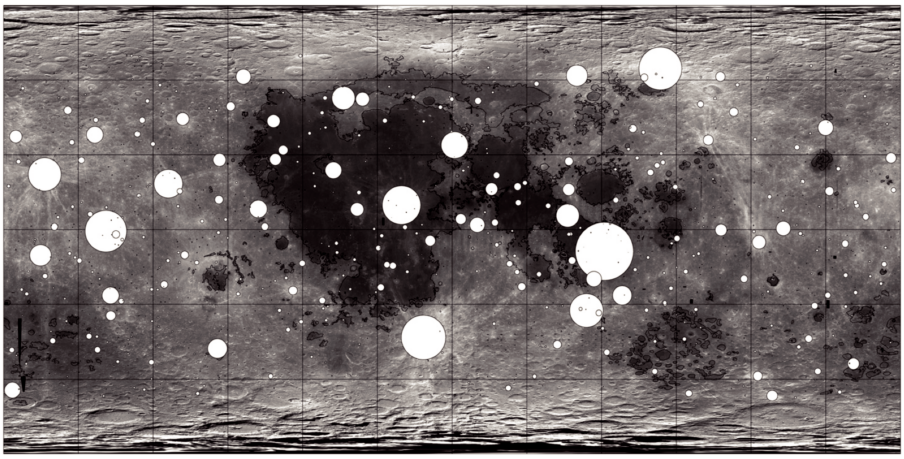

Figure 3.2: Spatial distribution of optical rayed craters on the Moon (Werner and Medvedev, 2010). The basemap is the Clementine 750 nm image. The size of the circle is five times the radius of the crater.

After a crater forms, the excavated ejecta materials and the resulting secondary craters produce radial structures that are seen as high-reflectance rays emanating from the crater rim in optical images (Hawke et al., 2004; Oberbeck, 1971). These radial features fade with time due to subsequent weathering processes, and therefore the presence of optical rays implies that the parent crater is young. In this study, the optical rayed craters are used to derive the initial crater profiles on the Moon.

The most recent global database of optical rayed craters on the Moon was constructed using the Clementine 750 nm images by Werner and Medvedev (2010). In total, 1211 optical rayed craters were identified with diameters of 1–139 km, which cover the full size range of our identified partially buried craters. The crater size-frequency distribution of the 1211 optical rayed craters indicates a crater retention age of ∼750 Myr (Werner and Medvedev, 2010), suggesting that these craters are very young.

Due to limitations on the resolution, quality, coverage of the acquired remote sensing data, there are only a few studies working on the fresh craters on Mercury. Based on the criteria proposed by Trask (1971), Susorney et al. (2016) divided Mercury's craters into five classes. Among them, Class 5 craters have ejecta rays

and well-preserved ejecta blanket and Class 4 craters have well-preserved ejecta blanket without emanating rays, and therefore they were thought to be young and fresh (Figure 3.3). In this study, we will focus on Class 4 and Class 5 craters, which has a total number of 126 and a diameter range of 8–130 km.

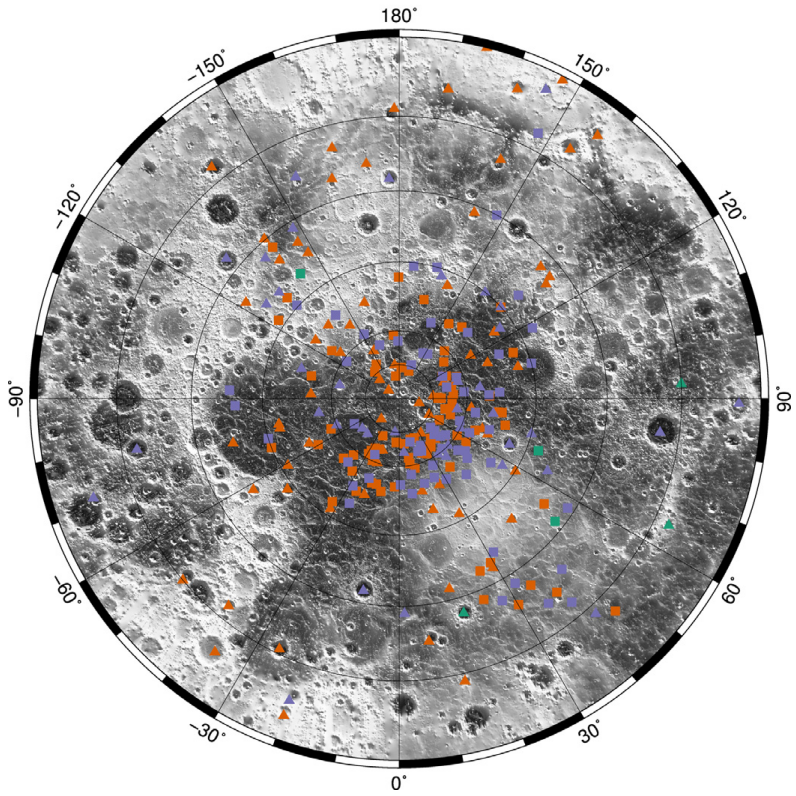

Figure 3.3: Spatial distribution of fresh craters on Mercury (Susorney et al., 2016). The basemap is the MLA GDR. The red, purple and green squares denote Class 3, Class 4 and Class 5 craters. The triangles are complex craters, and the squares are simple craters.

3.2.2 Preprocessing

Since multiple remote sensing datasets of the Moon are used, co-registration between different datasets should be considered first. For example, the SLDEM shares the same ground control network with the LOLA data (Barker et al., 2016), the WAC images use a WAC-derived digital terrain model in non-polar regions and the LOLA DEM in polar regions for geo-registration (Speyerer et al., 2011), and the Clementine 750 nm images are mapped using the Unified Lunar Control Network 2005 (ULCN2005) (Hare et al., 2008). In Werner and Medvedev (2010), the center coordinate and diameter of optical rayed craters were originally identified

and recorded based on the Clementine basemap. For small craters with diameters less than 2 km ($N = 540$), the mis-registration between the Clementine data and the SLDEM and LOLA data can be as large as 5 km.

The same issue also exists on Mercury, and becomes more serious as Mercury's data are much worse in data quality and spatial resolution. The center coordinate and diameter of the fresh craters identified by Susorney et al. (2016) were determined based on the MDIS mosaics, whereas we will use the MLA RDR data when extracting the elevation profile. For all the selected crater candidates, we then compared their crater center coordinates given by the MDIS and MLA RDR data, and we found a significant mis-registration between them, which can be as large as 10 km and exists for the entire crater diameter range.

Considering that the fresh craters were identified using optical images and that the elevation profiles will be produced using elevation data for both the Moon and Mercury, we apply the same strategy to co-register the optical images with the elevation data (in the form of interpolated DEM) on the two bodies. First, we will find the fresh crater in the optical image based on the provided coordinate. Next, based on the provided center coordinate of the crater as well as the projection and resolution information of the elevation data, we can obtain a rough estimate on the crater center coordinate in the elevation data. By comparing the interpolated DEM with the corresponding optical image, finally we can pinpoint the crater, and the crater center coordinate will only be determined and recorded based on the DEM.

When extracting the radial profile of an impact crater, another issue that has not been considered in previous studies is the contamination from other unrelated geologic features such as nearby craters, rilles, and wrinkle ridges. This is of great importance in our study, since the rim height used later depends on the elevation of background terrain (defined as the average elevation from 2.5 to 3 times the crater radius) where the topographic relief should be small. This background atypical feature removal can be easily done by either masking out the atypical geologic features if they are small, or only extracting the elevation in several fan-shaped regions that exclude atypical geologic features. However, if the crater formed on top of these atypical geologic features, then they will be discarded.

The radial elevation profiles will be produced by azimuthally averaging the elevations in a circular region with radial distance less than three crater radii from

the crater center. On the Moon, considering the data resolution of SLDEM and LOLA (both ∼60 m/pixel), the radial profiles of craters smaller than 18 km in diameter were binned with a width of 100 m. For craters larger than 18 km in diameter, the radial profiles were binned with 300 equidistant intervals (which for our craters correspond from 90 to 700 meters). For craters on Mercury, the bin width was set to 500 m, given that the gap between two adjacent MLA nadir points is about 400 m.

Sometimes even if these atypical features have been excluded, the background region might still have large variations in relief. In this case, we had no choice but to manually define a maximum fitting range in the background region where the topographic relief is considered to be small. Later, only the elevations with radial distances smaller than this maximum range were used for study. In the end, the spatial distributions and azimuthally averaged elevation profiles of the selected fresh craters on the Moon and Mercury are presented in Figures 3.4–3.7. Note that for the elevations profiles, the vertical elevation is normalized by crater diameter, and the lateral distance is normalized by crater radius.

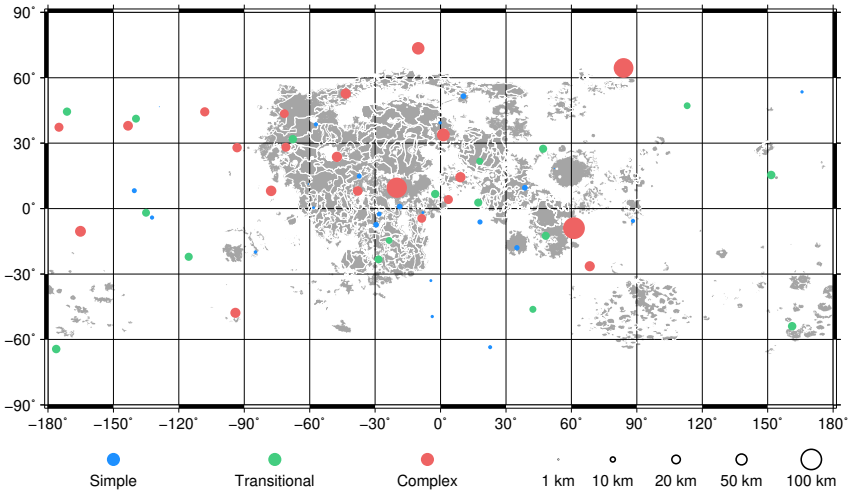

Figure 3.4: Spatial distribution of simple (red), transitional (green), and complex (blue) fresh craters used to construct the initial shape model for lunar craters. The lunar maria basemap (black) is from Nelson et al. (2014), and the basaltic unit boundaries (white) are from a compilation of previous studies (Hiesinger et al., 2006, 2011; Morota et al., 2009, 2011a; Pasckert et al., 2018). The circle size is proportional to the crater diameter.

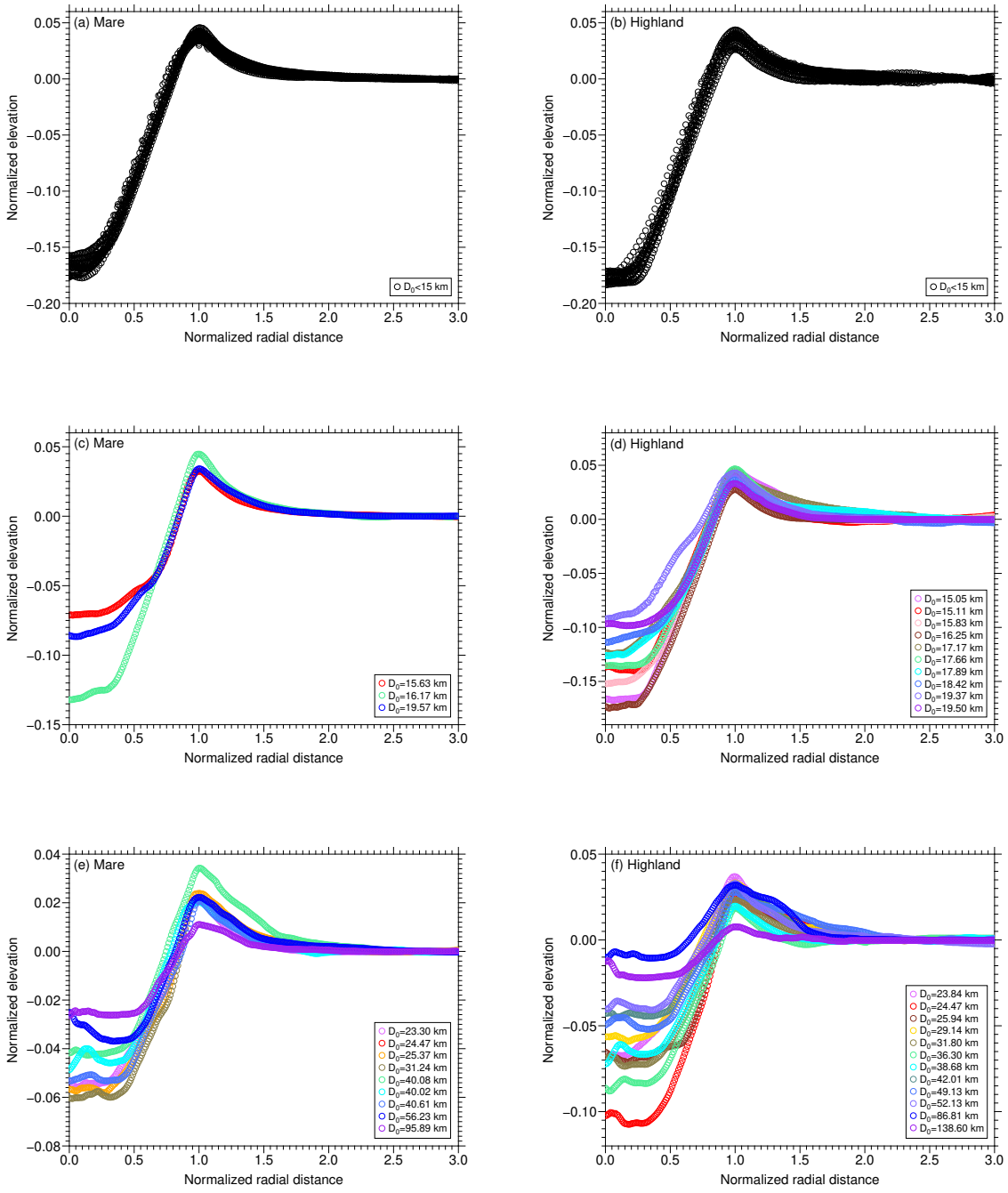

Figure 3.5: Radial elevation profiles of optical rayed craters that were selected to model the initial profiles for simple mare (a) and highland (b) craters, transitional mare (c) and highland (d) craters, and complex mare (e) and highland (f) craters. For all the transitional and complex craters, their crater diameters are labeled.

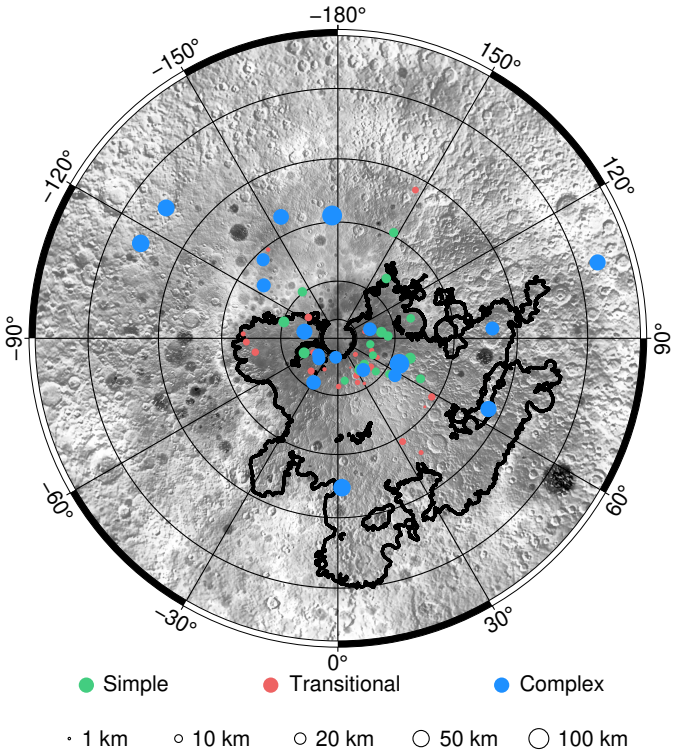

Figure 3.6: Spatial distribution of simple (red), transitional (green), and complex (blue) fresh craters used to construct the initial shape model for Mercury's craters. The basemap is MLA GDR, and the northern smooth plains boundary is taken from Denevi et al. (2013). The circle size is proportional to the crater diameter.

3.2.3 Classification

Impact crater morphology mainly depends on crater size and target properties (Melosh, 1989). Considering our current knowledge of the crater morphometry and the data quality on the Moon and Mercury, we used two different schemes to classify fresh craters on the two bodies.

On the Moon, we divided craters into three diameter regimes: simple ($1 \leqslant D_{\text{init}} \leqslant 15$ km), transitional ($15 < D_{\text{init}} \leqslant 20$ km), and complex ($D_{\text{init}} > 20$ km). This classification scheme of crater size regimes has been widely accepted and used in lunar sciences. All the simple craters have exactly the same radial profile if the vertical elevation is normalized by crater diameter and the radial distance is normalized by crater radius. For transitional and complex craters, morphometric parameters, such as central peak height, central peak radius, crater floor radius, crater depth, rim height, and continuous ejecta radius, were treated together. The

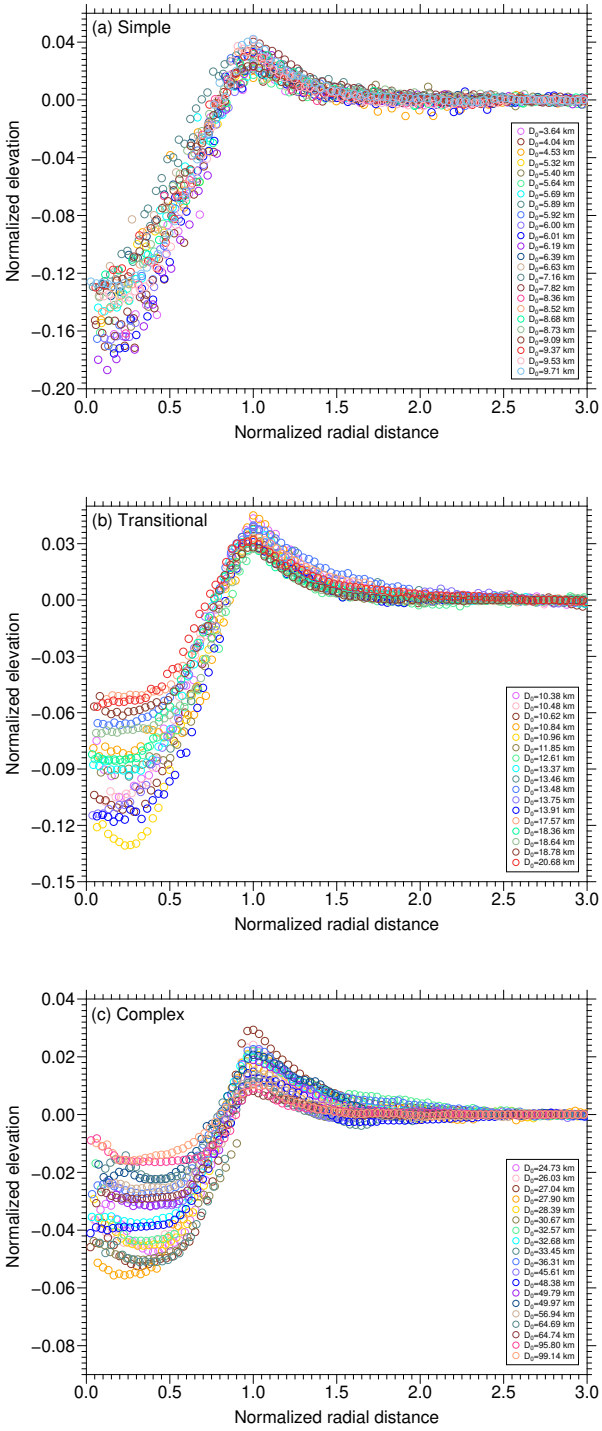

Figure 3.7: Radial elevation profiles of optical rayed craters that were selected to model the initial profiles for simple (a), transitional (b), and complex (c) craters on Mercury. For all the transitional and complex craters, their crater diameters are labeled.

only difference between transitional and complex regimes in our model is that transitional craters do not have a central peak whereas the complex craters do. Note that the existence of the central peak structure will not affect our estimation of the exterior lava flow thickness, as the central peak materials will never "move" to the crater exterior. Note that the partially buried craters used for inversion in this study are only those that located in the mare region, and that we only seek to invert the basalt thickness exterior to the crater rim. Some large basins like the Orientale (930 km) are not located within the mare region and are way much bigger than the largest partially buried craters (130 km) identified. Besides, the ejecta of these basins are not buried by lava flows. Therefore, in this study we will not work on these large basins.

For target type, we considered either mare or highland crust. This is because, for example, a larger porosity of lunar highland crust could result in a smaller yield strength and hence a larger crater depth (Kalynn et al., 2013). The target type for the optical rayed craters was determined by their locations in the lunar maria basemap of Nelson et al. (2014). As a result, six types of initial profiles were produced for lunar craters, including simple, transitional and complex craters over both lunar maria and highlands.

For Mercury, we proposed a simpler classification scheme. For the crater size dependence, we will only work on the transitional and complex craters. The reason we discarded simple craters is that the crater elevation profiles derived from the MLA RDR may not be convincing for simple craters: (1) there might be only a few MLA tracks that pass through the crater center or even the crater interior; (2) even if there are several MLA tracks found in the crater interior, there might be only a few eligible elevation measurements with channel ID=0 and 1 as the crater interior always has a high surface roughness; (3) it is difficult to determine the crater center in the GDR data with a poor spatial resolution of only 250 m/pixel.

Since there is an inflection point in the crater morphometry relations (see Figures 3.17a and b) at 10 km, we set the smallest diameter in the crater shape modeling for Mercury to be 10 km. Next, we need to decide the boundary between transitional and complex craters, which has been poorly constrained so far. Conceptually, complex craters should have a central peak whereas transitional craters should not. However, this strict dichotomy could be somehow blurred by the datasets, crater

location and tectonic activities for craters on Mercury. First, optical images on Mercury are poor in resolution, making it difficult to identify features in the crater interior. Second, our studied craters are located in the high-latitude region where the illumination conditions may not be favorable to recognize structures at the crater center. Third, tectonic activities are expected to be once quite active on Mercury, triggering mass-wasting events on the crater inner walls, and as a result, there could be a central mound that formed at the crater center where the crater wall materials collapsed and then converged together. To solve the image resolution and crater location issues, optical images with different viewing angles are extremely helpful. To distinguish the central peak, which results from the rebound of the target materials during the impact cratering event, from the central mound, which arises from the landslides of the crater materials, we have to check the optical images of the candidate crater and make sure that the central topographic high is an isolated feature at the crater center and can not be traced back to the crater wall materials. Our investigation shows that the smallest crater with a discernible central peak has a crater diameter of 24.7 km, and thus we set the transitional-complex boundary at 25 km. Note that on Mercury, we will not work on craters or basins larger than 100 km in diameter, as usually these craters are not fresh craters and have complex crater morphologies and geologic contexts.

For the target type, we will not distinguish between craters on the northern smooth plains and heavily cratered terrain. This is because previous studies have shown that there is no significant difference in crater morphology between the two (Barnouin et al., 2012; Susorney et al., 2016). In the end, only two types of initial profiles were produced for fresh transitional and complex craters on Mercury.

3.3 Methods

3.3.1 Definitions of Morphometric Parameters

The six morphometric parameters (rim height, crater depth, crater floor radius, continuous ejecta radius, central peak height, and central peak radius) are defined using the azimuthally averaged radial topographic profiles as follows:

(1) Rim height: the elevation difference between rim crest and background surface (averaged from 2.5 to 3 crater radii);

(2) Crater depth: the elevation difference between rim crest and the lowest point in the crater interior;

(3) Crater floor radius: the radial position where the surface slope abruptly increases in the crater interior;

(4) Continuous ejecta radius: the radial position where the surface slope abruptly decreases in the crater exterior;

(5) Central peak height: the elevation difference between central peak crest and central peak base boundary;

(6) Central peak radius: the radial position of the central peak base boundary where the surface slope abruptly decreases in the crater interior.

3.3.2 Simple Craters

To decide which simple craters should be used for fitting, we first constructed a crater profile database of all the candidate craters. We first plotted the extracted crater profiles of all the candidate craters using the same normalized coordinate, where the vertical axis is the elevation normalized by crater diameter and the horizontal axis is the radial distance normalized by crater radius. These data points were then binned by one-tenth of the normalized crater radius, and for each bin, the average (h_{avg}) and one standard deviation (σ) were calculated. Finally, each individual candidate profile was examined again, and only the profiles lying between one standard deviation around the average ($h_{\mathrm{avg}} \pm \sigma$) at all the bin centers were selected for fitting. In the end, 12 mare simple craters and 11 highland simple craters were selected for fitting (Figures 3.5a and b) on the Moon. For Mercury, although we also extracted the elevation profiles for simple fresh craters (Figure 3.7a), we will not construct a generic shape model as we can not guarantee the fidelity of the topographic data from which we produced the elevation profiles.

As shown in Figure 3.8, in order to fit the initial crater profile we first need to determine the crater floor radius and continuous ejecta radius, which can be done by varying these two quantities in the ranges of 0–0.5R and 1.5–2.5R with an interval of 0.1R (orange arrows). Meanwhile, we also need to find the crater floor elevation, which we vary from -0.2R to -0.15R also with an interval of 0.1R (orange arrows),

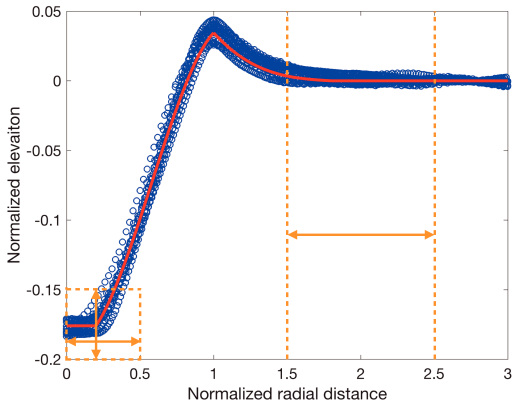

Figure 3.8: Example of how to fit simple craters. The craters shown here are simple highland crater (blue). The orange arrows and dashed lines show how to determine the crater floor boundary, crater floor elevation, and crater ejecta boundary. The red solid line is the best-fitting result.

and we note that the background elevation has already been set to 0. In the end, the crater inner wall and crater ejecta can be directly fitted using cubic polynomial functions.

3.3.3 Transitional and Complex Craters

To decide which transitional and complex craters should be used for fitting, we applied two criteria: (1) craters that have large background topographic variations were excluded (e.g., those that formed on basin rims or wrinkle ridges), and (2) selected transitional craters do not have a central peak whereas selected complex craters do (we note that fresh craters smaller than our proposed critical diameter sometimes could have a central peak, and those larger than the critical diameter do not necessarily have a central peak). In the end, 3 mare transitional craters, 10 highland transitional craters, 9 mare complex craters, and 12 highland complex craters on the Moon were selected (Figures 3.5c–f); 17 transitional craters and 19 complex craters on Mercury were chosen (Figures 3.7c–f).

The procedures applied to transitional and complex craters are more complicated than for simple craters because the normalized crater shapes in these two regimes are diameter dependent. The detailed steps are exactly the same for craters on the Moon and Mercury, including first handling every selected fresh crater and then working on a virtual, generalized fresh crater.

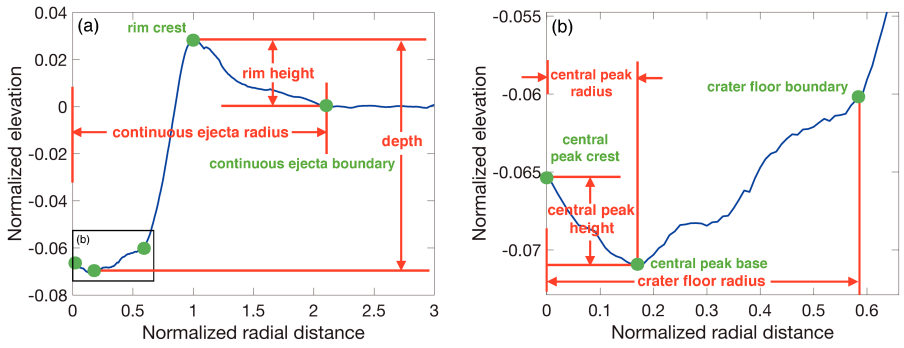

Figure 3.9: An example of how to identify tie points and calculate morphometric parameters for lunar craters. The crater shown here is the highland crater Stefan L (D=25.9 km). The green points are tie points, and the red arrows denote morphometric parameters. (b) is a zoom-in of (a) showing the detailed features on the crater floor.

First, we need to treat every selected fresh crater. To illustrate this, here we make use of representative fresh craters on the Moon and on Mercury: crater Stefan L (44.35°N, 108.13°W; D=25.9 km) that formed on the lunar highland (Figure 3.9), and a young crater (79.31°N, 38.62°E; D=32.8 km) that formed on the heavily cratered terrain of Mercury (Figure 3.11). Then, five horizontal "tie points" were identified manually on each extracted profile that correspond to the top of the central peak, the foot of the central peak, the crater floor boundary, the rim crest and the continuous crater ejecta boundary (green dots). Next, six morphometric parameters were determined using the coordinates of the above five tie points, including the central peak height, the central peak radius, the crater floor radius, the crater depth, the rim height, and the continuous ejecta radius (red arrows). These morphometric parameters were then fitted as a function of crater diameter.

Using these relations, we can predict both the morphometric parameters and then the tie point coordinates for any given, generalized crater diameter. To illustrate this, here we make use of lunar highland complex craters (Figure 3.10) and Mercury's complex craters (Figure 3.12) as examples. Note that in the coordinate presented here, the vertical elevation is normalized by crater diameter and the radial distance is normalized by crater radius. To fix the rim crest, for example, its vertical position can be retrieved as the rim height-diameter ratio and its radial position should be exactly 1. Similarly, we can predict the positions of the other five tie points (stars) in this normalized coordinate. Finally, we tested several different functions (e.g., polynomials, exponential, power-law, logarithmic) to connect

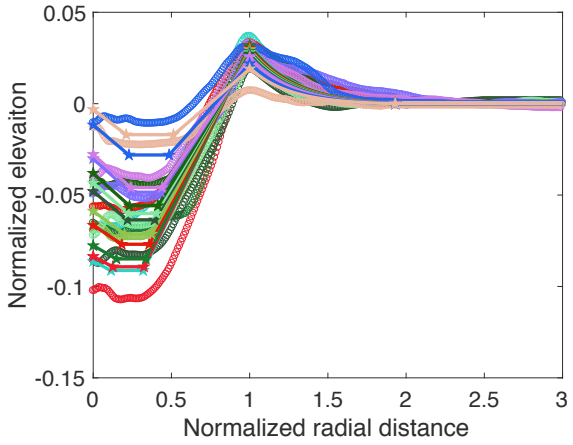

Figure 3.10: An example of how to connect the tie points. Craters shown here are highland complex craters on the Moon. The circles are the extracted elevations. The stars are the predicted tie points. The solid lines are plotted using the connecting functions, which are exponential functions in this figure. It should be noted that for a given crater, the circles, stars, and solid lines have the same color. Note that the background elevation has been already been set to 0.

the tie points in each section. Since the coordinates of two tie points are obtained from the crater diameter, the proposed known function should have at most two unknown coefficients that need to be solved. Substituting the two solved coefficients into different forms of known functions, we can then calculate the resulting misfit and finally determine the best-fitting functions.

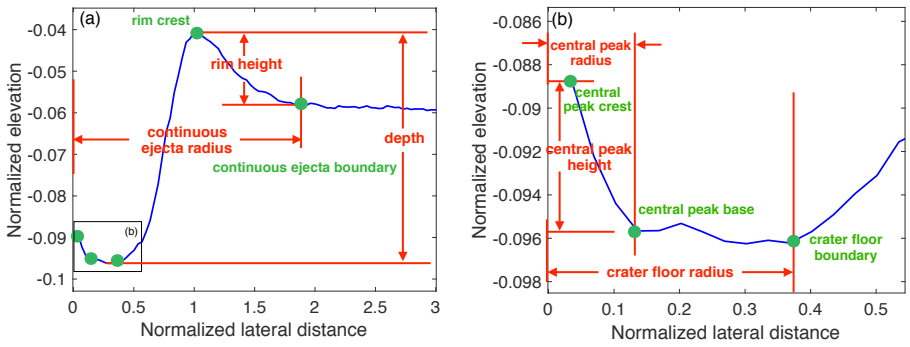

Figure 3.11: An example of how to identify tie points and calculate morphometric parameters for Mercury's craters. The crater shown here is located on the heavily cratered terrain (D=32.8 km). The green points are tie points, and the red arrows denote morphometric parameters. (b) is a zoom-in of (a) showing the detailed features on the crater floor.

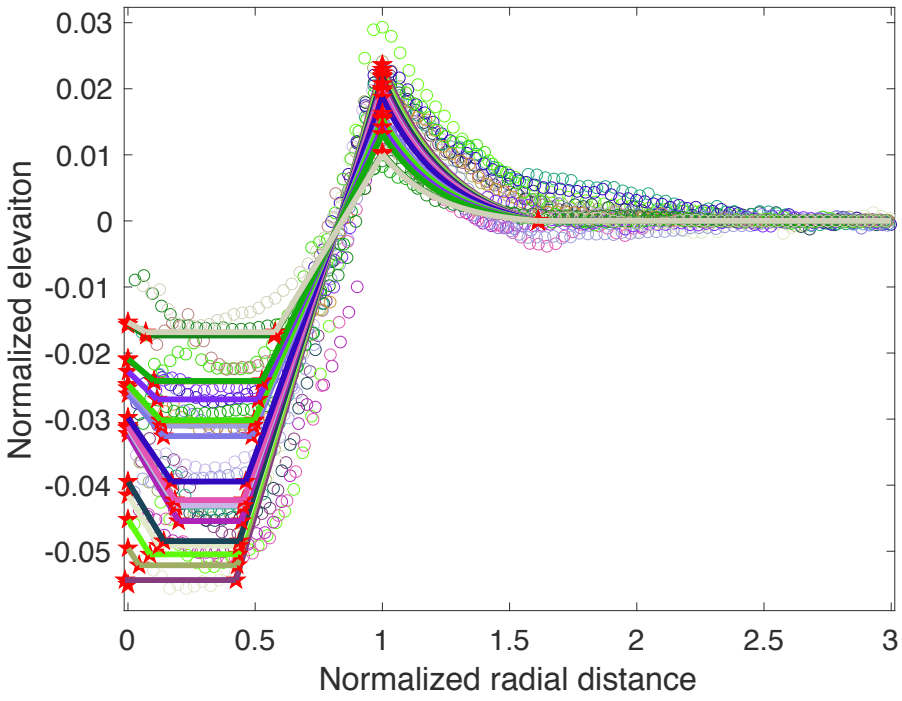

Figure 3.12: An example of how to connect the tie points. Craters shown here are complex craters on Mercury. The circles are the extracted elevations. The stars are the predicted tie points. The solid lines are plotted using the connecting functions, which are exponential functions in this figure. It should be noted that for a given crater, the circles, stars, and solid lines have the same color. Note that the background elevation has been already been set to 0.

3.4 Results and Comparisons

3.4.1 The Moon

A. Morphometric Parameters

The resulting morphometric parameter-crater diameter relations are plotted in Figures 3.13 and 3.14, along with those determined from other studies. The corresponding formulas are given in Tables 3.1–3.6. In these tables, h_{r}, d_{cf}, R_{cf}, R_{e}, h_{cp}, and R_{cp} denote morphometric parameters rim height, crater depth, crater floor radius, continuous ejecta radius, central peak height, and central peak radius.

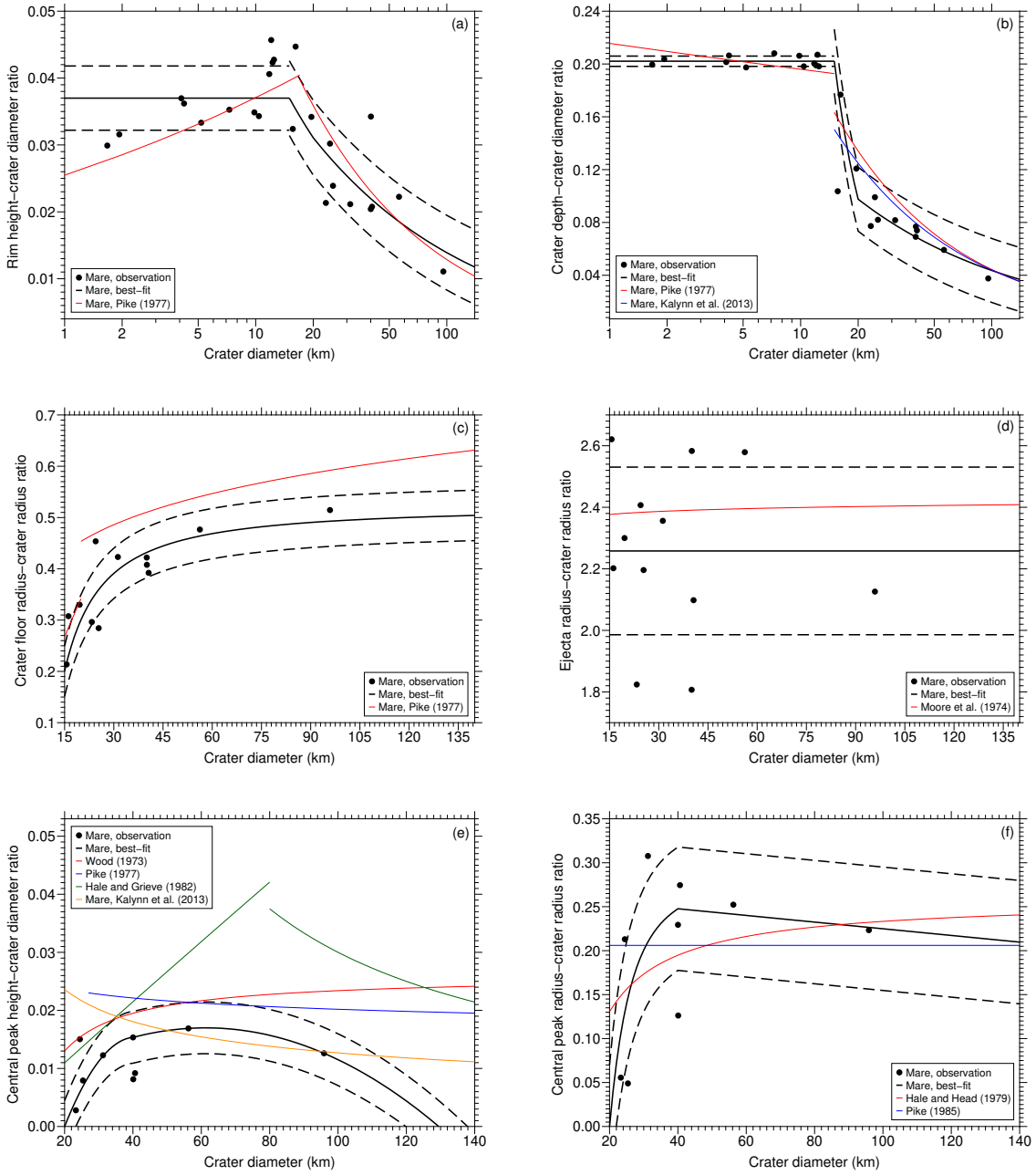

Figure 3.13: Morphometric parameters used to model the initial profiles of transitional and complex mare craters: rim height (a), crater depth (b), crater floor radius (c), continuous ejecta radius (d), central peak height (e), and central peak radius (f), including measured results and best-fits. Morphometric parameters derived in other studies are also plotted as a comparison: Hale and Grieve (1982), Hale and Head (1979), Kalynn et al. (2013), Moore et al. (1974), Pike (1977), Pike (1985), and Wood (1973).

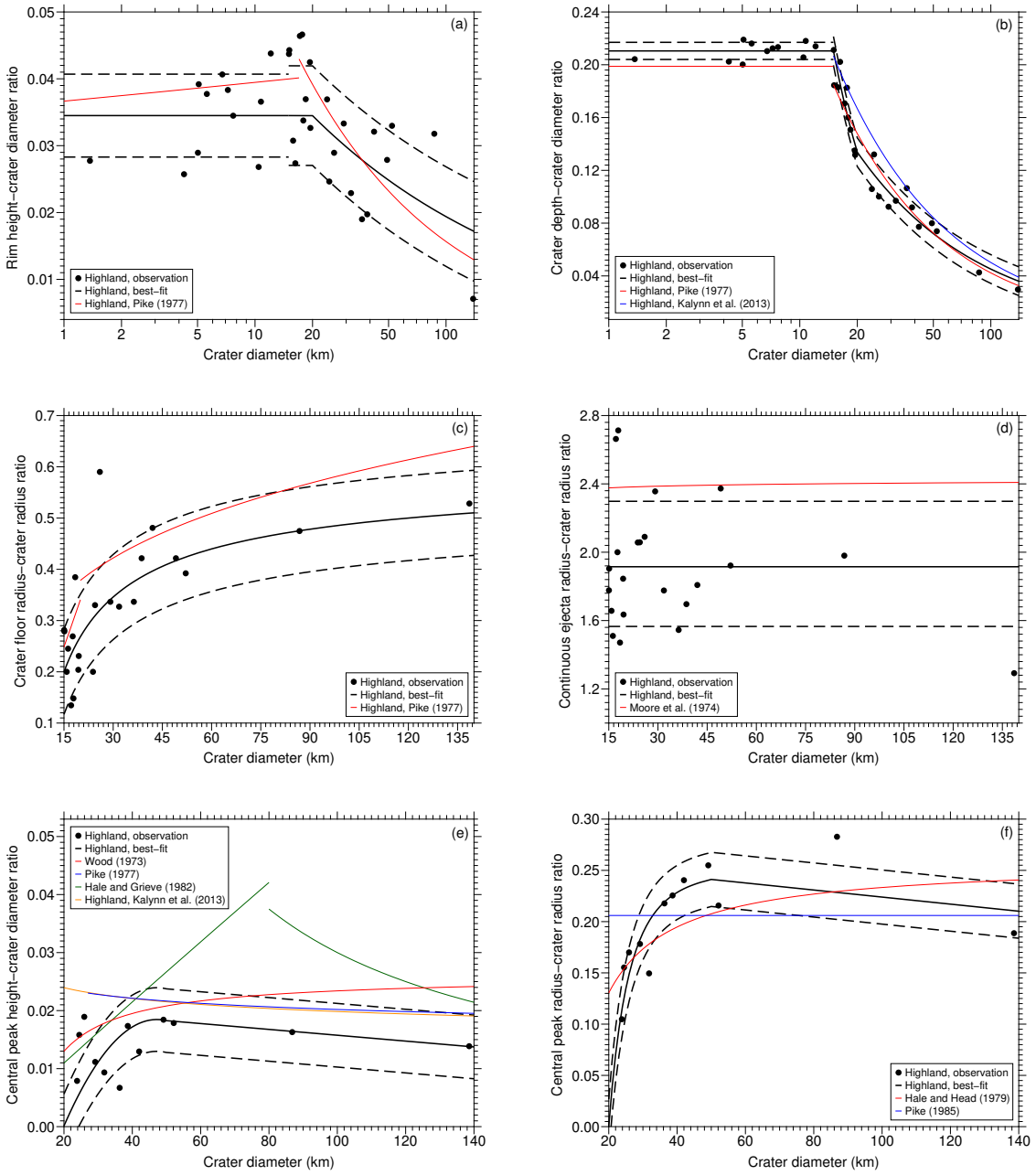

Figure 3.14: Morphometric parameters used to model the initial profiles of transitional and complex highland craters: rim height (a), crater depth (b), crater floor radius (c), continuous ejecta radius (d), central peak height (e), and central peak radius (f), including measured results and best-fits. Morphometric parameters derived in other studies are also plotted as a comparison: Hale and Grieve (1982), Hale and Head (1979), Kalynn et al. (2013), Moore et al. (1974), Pike (1977), Pike (1985), and Wood (1973).

Table 3.1: A brief summary of morphometric parameters for fresh lunar craters: rim height.

Formula	Diameter range (km)	Crater number	Target type	Elevation data	Reference
$h_r = 0.0370$	$1 < D \leqslant 15$	12	Mare	SLDEM and LOLA	This study
$h_r = 0.191D^{-0.606}$	$15 < D \leqslant 20$	3			
$h_r = 0.139D^{-0.500}$	$20 < D < 100$	9			
$h_r = 0.0345$	$1 < D \leqslant 15$	11	Highland		
$h_r = 0.0386D^{-0.0416}$	$15 < D \leqslant 20$	14			
$h_r = 0.0837D^{-0.300}$	$20 < D < 140$	12			
$h_r = 0.0255D^{1.16}$	$D \leqslant 17$	73	Mare	LTO	Pike (1977)
$h_r = 0.242D^{0.363}$	$17 < D$	7			
$h_r = 0.0367D^{1.03}$	$D \leqslant 17$	32	Highland		
$h_r = 0.216D^{0.430}$	$17 < D$	31			

Table 3.2: A brief summary of morphometric parameters for fresh lunar craters: crater depth.

Formula	Diameter range (km)	Crater number	Target type	Elevation data	Reference
$d_{\mathrm{cf}} = 0.202$	$1 < D \leqslant 15$	12	Mare	SLDEM and LOLA	This study
$d_{\mathrm{cf}} = 191D^{-2.53}$	$15 < D \leqslant 20$	3			
$d_{\mathrm{cf}} = 0.437D^{-0.500}$	$20 < D < 100$	9			
$d_{\mathrm{cf}} = 0.211$	$1 < D \leqslant 15$	11	Highland		
$d_{\mathrm{cf}} = 9.97D^{-1.42}$	$15 < D \leqslant 20$	14			
$d_{\mathrm{cf}} = 1.14D^{-0.700}$	$20 < D < 140$	12			
$d_{\mathrm{cf}} = 0.216D^{0.959}$	$D \leqslant 15$	126	Mare	LTO	Pike (1977)
$d_{\mathrm{cf}} = 1.05D^{0.313}$	$15 < D$	9			
$d_{\mathrm{cf}} = 0.199D^{1.00}$	$D \leqslant 15$	39	Highland		
$d_{\mathrm{cf}} = 1.52D^{0.223}$	$15 < D$	29			

Table 3.3: A brief summary of morphometric parameters for fresh lunar craters: crater floor radius.

Formula	Diameter range (km)	Crater number	Target type	Elevation data	Reference
$R_{\mathrm{cf}} = 0.2$	$1 < D \leqslant 15$	12	Mare	SLDEM and LOLA	This study
$R_{\mathrm{cf}} = -10.7D^{-1.30} + 0.522$	$15 < D < 100$	12			
$R_{\mathrm{cf}} = 0.2$	$1 < D \leqslant 15$	11	Highland		
$R_{\mathrm{cf}} = -3.48D^{-0.827} + 0.572$	$15 < D < 140$	26			
$R_{\mathrm{cf}} = 0.0269D^{1.85}$	$D \leqslant 20$	128	Mare	LTO	Pike (1977)
$R_{\mathrm{cf}} = 0.273D^{1.17}$	$20 < D$	7			
$R_{\mathrm{cf}} = 0.0128D^{2.10}$	$D \leqslant 20$	44	Highland		
$R_{\mathrm{cf}} = 0.169D^{1.27}$	$20 < D$	24			

Table 3.4: A brief summary of morphometric parameters for fresh lunar craters: ejecta radius.

Formula	Diameter range (km)	Crater number	Target type	Elevation data	Reference
$R_e = 1.7$	$1 < D \leqslant 15$	12	Mare	SLDEM and LOLA	This study
$R_e = 2.26$	$15 < D < 100$	12			
$R_e = 1.8$	$1 < D \leqslant 15$	11	Highland		
$R_e = 1.93$	$15 < D < 140$	26			
$R_e = 2.35D^{1.01}$	$0.65 \leqslant D \leqslant 218$	84	Mare and highland	LAC, LO, and Apollo photographs	Moore et al. (1974)

Table 3.5: A brief summary of morphometric parameters for fresh lunar craters: central peak height.

Formula	Diameter range (km)	Crater number	Target type	Elevation data	Reference
$h_{\mathrm{cp}} = -3.56 \times 10^{-5} D^2 + 2.90 \times 10^{-3} D - 0.0438$	$20 < D \leqslant 40$	4	Mare	SLDEM, LOLA	This study
$h_{\mathrm{cp}} = -3.65 \times 10^{-6} D^2 + 4.47 \times 10^{-4} D + 3.23 \times 10^{-3}$	$40 < D < 100$	5			
$h_{\mathrm{cp}} = -2.48 \times 10^{-5} D^2 + 2.34 \times 10^{-3} D - 0.0368$	$20 < D \leqslant 50$	9	Highland		
$h_{\mathrm{cp}} = -5.04 \times 10^{-5} D + 0.0208$	$50 < D < 140$	3			
$h_{\mathrm{cp}} = (0.026D - 0.26)/D$	$15 \leqslant D \leqslant 132$	93	Mare and highland	Earth-based photographs, LO IV, and Apollo 15 metric camera photography	Wood (1973)
$h_{\mathrm{cp}} = 0.032 D^{0.900}$	$27 \leq D$	22	Mare and highland	LTO	Pike (1977)
$h_{\mathrm{cp}} = 6 \times 10^{-4} D^{0.97}$	$D \leqslant 51$	15	Mare and highland	LTO	Hale and Grieve (1982)
$h_{\mathrm{cp}} = 3/D$	$51 \leq D$	8			
$h_{\mathrm{cp}} = 0.075 D^{-0.386}$	$15 \leqslant D \leqslant 93$	14	Mare	LOLA	Kalynn et al. (2013)
$h_{\mathrm{cp}} = 0.034 D^{-0.117}$	$21 \leqslant D \leqslant 167$	49	Highland		

Table 3.6: A brief summary of morphometric parameters for fresh lunar craters: central peak radius.

Formula	Diameter range (km)	Crater number	Target type	Elevation data	Reference
$R_{\mathrm{cp}} = -3.18 \times 10^{3} D^{-3.12} + 0.280$	$20 < D \leqslant 40$	4	Mare	SLDEM and LOLA	This study
$R_{\mathrm{cp}} = -3.80 \times 10^{-4} D + 0.263$	$40 < D < 100$	5			
$R_{\mathrm{cp}} = -7.07 \times 10^{3} D^{-3.42} + 0.252$	$20 < D \leqslant 50$	9	Highland		
$R_{\mathrm{cp}} = -3.44 \times 10^{-4} D + 0.258$	$50 < D < 140$	3			
$R_{\mathrm{cp}} = (0.13D - 1.29)/D$	$17 \leqslant D \leqslant 175$	175	Mare and highland	LO, LTO and Apollo images	Hale and Head (1979)
$R_{\mathrm{cp}} = 0.103$	$17 \leqslant D \leqslant 175$	175	Mare and highland	LO, LTO and Apollo images	Pike (1985)

For the rim height-crater diameter ratio on lunar maria (Figure 3.13a), although there is much scatter, we can see that the ratio remains constant from 1 to 15 km and decreases after 15 km. We used a horizontal line to fit the measurements of simple craters and a power-law function for transitional and complex craters. Our result is in general consistent with Pike (1977), and we note that the result obtained by Pike (1977) is within our one-sigma uncertainty after 4 km.

For the rim height-crater diameter ratio on lunar highlands (Figure 3.14a), the scatter is much more obvious, as the background topographic variation on highlands is more significant. Similar to mare craters, the ratio of highland craters remains constant from 1 to 15 km and decreases after 15 km. We used a horizontal line to fit the measurements of simple craters and a power-law function for transitional and complex craters. Our result is in general consistent with Pike (1977), and we note that the result obtained by Pike (1977) is within our one-sigma uncertainty.

For the depth-diameter ratio on lunar maria (Figure 3.13b), we can see that the ratio remains constant from 1 to 15 km and decreases after 15 km. We made use of a horizontal line to fit the measurements of simple craters and a power-law function for transitional and complex craters. Our result is in general consistent with Pike (1977) and Kalynn et al. (2013), and we note that the results obtained by Pike (1977) and Kalynn et al. (2013) are within our one-sigma uncertainty.

For the depth-diameter ratio on lunar highlands (Figure 3.14b), we can see that the ratio remains constant from 1 to 15 km and decreases after 15 km. We made use of a horizontal line to fit the measurements of simple craters and a power-law function for transitional and complex craters. Our result is in general consistent with Pike (1977) and Kalynn et al. (2013), and we note that the results obtained by Pike (1977) is within our one-sigma uncertainty.

For the floor radius-crater radius ratio on lunar maria (Figure 3.13c), we can see that it increases after 15 km and then reaches to about half the crater radius, and we used a power-law function to fit the measurements. Our result is in general consistent with Pike (1977) for diameter smaller than 20 km and then becomes smaller afterwards.

For the floor radius-crater radius ratio on lunar highlands (Figure 3.14c), we can see that it increases after 15 km and then reaches to about half the crater radius, and we used a power-law function to fit the measurements. Our result is

in general consistent with Pike (1977) for diameter smaller than 81 km and then becomes smaller afterwards.

For the continuous ejecta radius-crater radius ratio on lunar maria (Figure 3.13d), because it is difficult to identify the ejecta boundary along the elevation profile, our result has a large uncertainty. Therefore, we simply used the average value of the measurements to represent the normalized continuous ejecta radius, which is about 5% smaller than that given by Moore et al. (1974).

For the continuous ejecta radius-crater radius ratio on lunar highlands (Figure 3.14d), as our result has a large uncertainty, we simply used the average value of the measurements to represent the normalized continuous ejecta radius. We found that Moore et al. (1974) is only slightly larger than our one-sigma upper bound.

The above four parameters decide the initial crater shape on the Moon on the first order. Although the morphology of the central peak does not have any significant effect on the erosion of the crater rim, we still take it into consideration when modeling the initial crater profile.

For the central peak height-crater diameter ratio on lunar maria (Figure 3.13e), we can find that it first increases and then decreases with crater diameter. This can be explained as follows: as the impact energy increases, the rebound of target materials would be more significant; however, when the height of the central uplift reaches to a critical value, it would collapse due to gravity instability, which transforms the central peak to a peak ring (Baker and Head, 2013). We then used two polynomial functions to fit the measurements for craters smaller and larger than 40 km. The result in Hale and Grieve (1982) is similar to ours in trend but much larger than ours in value. Although those in Wood (1973), Pike (1977) and Kalynn et al. (2013) are closer to our result, they have a monotonous trend.

For the central peak height-crater diameter ratio on lunar highlands (Figure 3.14e), we can find that it also first increases and then decreases with crater diameter. We then used two polynomial functions to fit the measurements for craters smaller and larger than 50 km. The result in Hale and Grieve (1982) is similar to ours in trend but much larger than ours in value. Although those in Wood (1973), Pike (1977) and Kalynn et al. (2013) are closer to our result, they have a monotonous trend.

For the central peak radius-crater radius ratio on lunar maria (Figure 3.13f), we

found that it first increases and then decreases with crater diameter. This indicates the transition from a circular central base to a peak ring from a planar view. To fit the measurements, we then used a power-law function for craters smaller than 40 km and a polynomial function for those larger than 40 km. Comparing our result with Hale and Head (1979) and Pike (1985), although they are consistent with our result, they have a monotonous trend instead.

For the central peak radius-crater radius ratio on lunar highlands (Figure 3.14f), we also found that it first increases and then decreases with crater diameter. To fit the measurements, we then used a power-law function for craters smaller than 50 km and a polynomial function for those larger than 50 km. Comparing our result with Hale and Head (1979) and Pike (1985), although they are consistent with our result, they have a monotonous trend instead.

Differences between this and other studies may arise from different parameter definitions, the employed craters, the elevation dataset, and whether one was using azimuthally averaged profiles (as in this study), individual profiles or an interpolated digital elevation model. For example, Kalynn et al. (2013) and this study calculated the crater depth of crater Copernicus to be 4.0 and 3.6 km, respectively, by using the SLDEM and LOLA datasets. In Kalynn et al. (2013), the crater depth was defined as the elevation difference between the rim crest and the interior impact melt pond. The rim crest elevation was defined as the average of the mode and maximum values within the annulus from $0.98R$ to $1.05R$, and the interior impact melt pond elevation was defined as the average of the mode and minimum values within the identified melt pond region. We found that the mode and the maximum elevations within the annulus from $0.98R$ to $1.05R$ were 0.032 and 0.819 km using the LOLA dataset (Kalynn et al., 2013), whereas the average elevation from $0.995R$ to $1.005R$ (bin width=$0.01R$) was 0.040 km in the SLDEM dataset (this study). We also found that the elevation histograms derived from these two slightly different radial ranges both follow a similar, Gaussian distribution, so the mode and the average do not differ significantly (0.032 km vs. 0.040 km). Therefore, which data (LOLA vs. SLDEM) to use, which statistic (mode or average) to use and where ($0.98R$–$1.05R$ vs. $0.995R$–$1.005R$) to sample the elevation should not have a significant effect in the derived crater depth in this case. As a conclusion, this comparison shows that the difference in the derived crater depth is a result of the different definitions: by

considering the maximum value around the rim crest, the crater depth given in Kalynn et al. (2013) might be larger than the one given in this study by 0.385 km for the case of the crater Copernicus.

When estimating the basalt thickness exterior to the crater rim, the variation of the crater rim height with crater diameter and degradation state is our primary concern. Our result shows that the rim height increases from 37 m to 1.4 km and from 35 m to 1.9 km for mare and highland craters with diameters of 1–100 km, respectively. For simple fresh craters, the rim height of mare craters is always slightly larger than that of highland craters (37 m vs. 35 m at 1 km, and 555 m vs. 518 m at 15 km). For transitional and complex fresh craters, the rim height of mare craters decreases with respect to highland craters with increasing diameter, becoming smaller than highland craters at 17 km (Figures 3.13a and 3.14a).

Table 3.7: Natural variability in the initial rim height as a function of crater diameter for lunar craters.

Crater diameter bin (km)	N	Initial rim height variability (m)
$1 \leqslant D \leqslant 5$	6	17
$5 < D \leqslant 10$	9	24
$10 < D \leqslant 15$	8	73
$15 < D \leqslant 20$	13	125
$20 < D \leqslant 35$	9	130
$35 < D \leqslant 50$	7	271

It should be noted that even though we selected fresh craters with simple geologic contexts to investigate the initial crater rim-height/diameter relation, natural variability of this quantity should be expected for any given crater diameter. Such variability could be the result of different impact conditions (including impact velocity and impact angle), as well as different target properties (such as porosity). This variability is quantified in Table 3.7, where we provide the root-mean-square deviation of the measured initial rim height with respect to the predicted initial rim height as a function of crater diameter. We note that the natural variability is similar for both mare and highland craters, so we combine them into one larger dataset for analysis. In particular, for simple, transitional, and complex (smaller

than 50 km in diameter) craters, the natural variabilities of the initial rim height are less than 73, 125 and 271 m, respectively.

B. Shape Model

Our derived shape profiles for fresh lunar craters are plotted in Figure 3.15. In the normalized coordinate, we can find that with increasing crater diameter the rim height and crater depth decrease, the crater floor radius increases, and the central peak height and central peak radius first increase and then decrease. This is to be expected as these initial profiles are constructed upon the morphometric parameters. In addition, we can also find that the elevations profiles with different diameters always have a smooth and continuous transition among them.

The corresponding formulas are presented in Table 3.8. The coefficients a–f that are required in this table can be numerically determined by setting the connecting function equal to the known values at the relevant tie points. All the vertical parameters ($h_{\rm cp}$, $d_{\rm cf}$, and $h_{\rm r}$) are normalized by crater diameter, and all the radial parameters (r, $R_{\rm cp}$, $R_{\rm cf}$, and $R_{\rm e}$) are normalized by crater radius. To fit the central peak, crater wall and crater ejecta, we use the exponential functions.

Table 3.8: Mathematic forms for fresh lunar impact craters.

Morphology	Target type	Elevation profile	Range
Simple	Mare	-0.165	$r \leqslant 0.2$
($1 < D \leqslant 15$ km)		$-0.292r^3 + 0.489r^2 + 0.028r - 0.188$	$0.2 < r \leqslant 1$
		$-0.081r^3 + 0.419r^2 - 0.731r + 0.430$	$1 < r \leqslant 1.7$
		0	$r > 1.7$
	Highland	-0.176	$r \leqslant 0.2$
		$-0.400r^3 + 0.693r^2 - 0.0727r - 0.186$	$0.2 < r \leqslant 1$
		$-0.0577r^3 + 0.312r^2 - 0.567r + 0.348$	$1 < r \leqslant 1.8$
		0	$r > 1.8$
Transitional	Mare and highland	$h_{\rm r} - d_{\rm cf}$	$r \leqslant R_{\rm cf}$
($15 < D \leqslant 20$ km)		$\exp(cr) + d$	$R_{\rm cf} < r \leqslant 1$
		$\exp(er) + f$	$1 < r \leqslant R_{\rm e}$
		0	$r > R_{\rm e}$
Complex	Mare and highland	$\exp(ar) + b$	$r \leqslant R_{\rm cp}$
($D > 20$ km)		$h_{\rm r} - d_{\rm cf}$	$R_{\rm cp} < r \leqslant R_{\rm cf}$
		$\exp(cr) + d$	$R_{\rm cf} < r \leqslant 1$
		$\exp(er) + f$	$1 < r \leqslant R_{\rm e}$
		0	$r > R_{\rm e}$

Shape models of fresh lunar craters have been developed by several workers. Exponential and Bessel functions were first proposed by Culling (1960), Culling

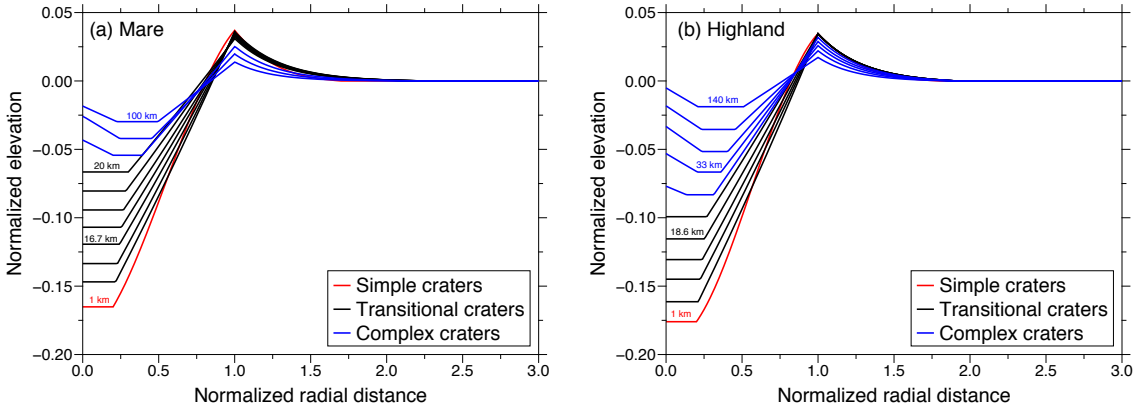

Figure 3.15: Radial elevation profiles for fresh lunar craters that formed on the mare (a) and highland (b). The radial distance is normalized by crater radius ($r_{\mathrm{norm}} = r/R_{\mathrm{init}}$), and the elevation is normalized by crater diameter ($H_{\mathrm{norm}} = H/D_{\mathrm{init}}$). The red curves denote simple craters, the black curves are transitional craters, and the blue curves represent complex craters. The plotted initial crater diameters were carefully selected to present the results for clarity and are labeled for several curves.

(1963), and Soderblom (1970). However, these profiles were carefully designed in order to help solve the diffusion equation in a convenient way, and did not accurately reflect the observed morphology of fresh lunar craters. These earlier models were then improved by considering the morphology of an actual lunar fresh crater using piece-wise functions for the crater interior and exterior (Craddock and Howard, 2000; Richardson, 2009; Richardson et al., 2005). More recently, with newly acquired, high-resolution topography datasets and improved knowledge of the impact cratering mechanisms, the crater shape models have been updated by taking into account the effect of target properties and the size-dependence of crater morphology (Fassett and Thomson, 2014; Xie and Zhu, 2016). We compared our results with the recent models of Fassett and Thomson (2014) and Xie and Zhu (2016), given that these two studies also considered the contribution from target properties and that the fresh craters they used to derive the initial profile were also taken from the same fresh crater database employed in our study (Werner and Medvedev, 2010). Here we compare the difference in rim heights among these three studies, since the rim height is the major factor that affects our estimation of the basalt thickness.

Using the SELENE/Terrain Camera-derived digital terrain model data of six mare craters that are 1.5 to 3.9 km in diameter, Fassett and Thomson (2014) derived an initial elevation profile for simple, mare craters (Figure 3.16a). The resulting

elevation profile was obtained by directly fitting the elevations extracted from the topography data, and they did not use azimuthal averages as did in our study. The rim heights from their study and ours have almost no difference (0.2–3 m), but there is a difference of 16–240 m in the crater depth for these two studies. This difference may be a result of a smaller number of craters (N=12 vs. N=6) and also the smaller range of crater diameters (1.7–12.5 km vs. 1.5–3.9 km) used in their study.

Xie and Zhu (2016) used the LOLA topography data of 53 highland craters that are 20 to 166 km in size to extract the initial elevation profiles for complex, highland craters (Figure 3.16b). Within the crater diameter range of 20 to 139 km, the rim heights used by their study and ours differ by 0 to 960 m. Xie and Zhu (2016) did not develop a new rim height-crater diameter relation in their study. Instead, they directly quoted the formula given by Pike (1977), where the crater rim height is defined as the mean elevation at the crater rim minus the mean elevation at the exterior rim flank foot in the Lunar Topographic Orthophotomap by using 38 mare and highland craters. As stated above, we think the difference between the rim height-crater diameter relations used in their study and ours is a result of the fact that different elevation datasets, fresh craters, and definitions of the parameters were used.

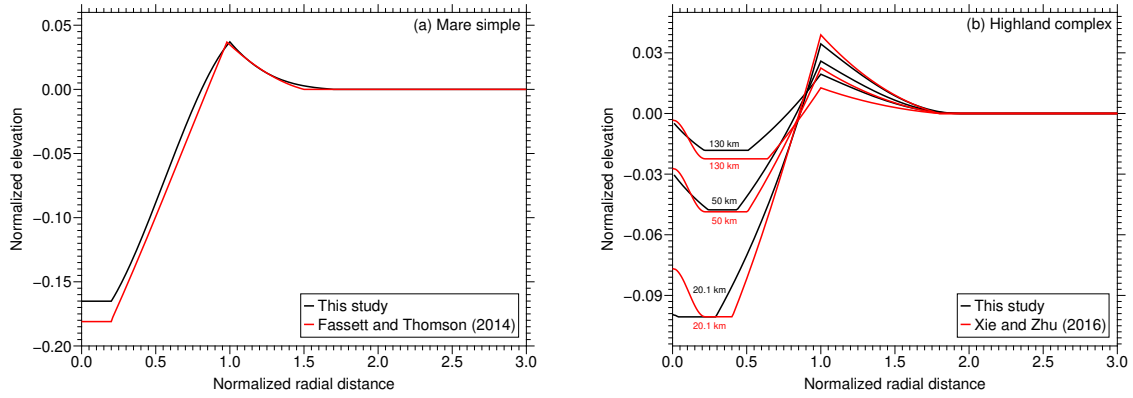

Figure 3.16: Comparison of the simple mare crater profiles of this study (black) and Fassett and Thomson (2014) (red) (a). Comparison of the complex highland crater profiles between this study (black) and Xie and Zhu (2016) (red) for selected crater diameters of 20.1, 50, 130 km (b).

Regardless of any differences with previous studies, our derived morphometric parameters of fresh impact craters and the resulting initial crater profiles represent a distinct improvement. Our results are the first to consider not only the size

dependence of crater morphology (simple, transitional, and complex) but also the target type (mare and highland). Our results are based on the freshest impact craters and should be more accurate than many previous investigations as we used newly acquired, high-quality elevation datasets and excluded surrounding atypical features. In addition, all the morphometric parameters are derived based on the same crater database and using the azimuthally averaged profiles, making our results more self-consistent. Lastly, we imposed the fitting functions at the simple-transitional, and transitional-complex boundaries to be continuous so that there are no abrupt changes in morphometric parameters at 15 km and 20 km diameters.

3.4.2 Mercury

A. Morphometric Parameters

The resulting morphometric parameter-crater diameter relations are plotted in Figure 3.17, along with those determined from other studies. The corresponding formulas are given in Tables 3.9–3.14. In these tables, h_{r}, d_{cf}, R_{cf}, R_{e}, h_{cp}, and R_{cp} denote morphometric parameters rim height, crater depth, crater floor radius, continuous ejecta radius, central peak height, and central peak radius. Note again that we will not study the morphometry of craters smaller than 10 km in diameter, as we can not guarantee the fidelity of the extracted elevation profiles of them.

For the rim height-crater diameter ratio on Mercury (Figure 3.17a), although there is much scatter, we can see that the ratio first increases from 1 to 10 km and then decreases after 10 km. We used two power-law functions to fit the measurements smaller and larger than 10 km. Our result is always smaller than that in Pike (1988), and is smaller than that in Susorney et al. (2016) when crater diameter is smaller than 30 km and then becomes larger afterwards.

For the depth-diameter ratio on Mercury (Figure 3.17b), we can see that the ratio first increases from 1 to 10 km and then decreases after 10 km. We used two power-law functions to fit the measurements smaller and larger than 10 km. When crater diameter is smaller than 10 km, our result is more consistent with Susorney et al. (2016) whereas Pike (1988) and Barnouin et al. (2012) show two constant best-fits. When crater diameter is larger than 10 km, our result is perfectly consistent with Susorney et al. (2016), and is larger than that in Pike (1988) before 22 km and then becomes smaller afterwards.

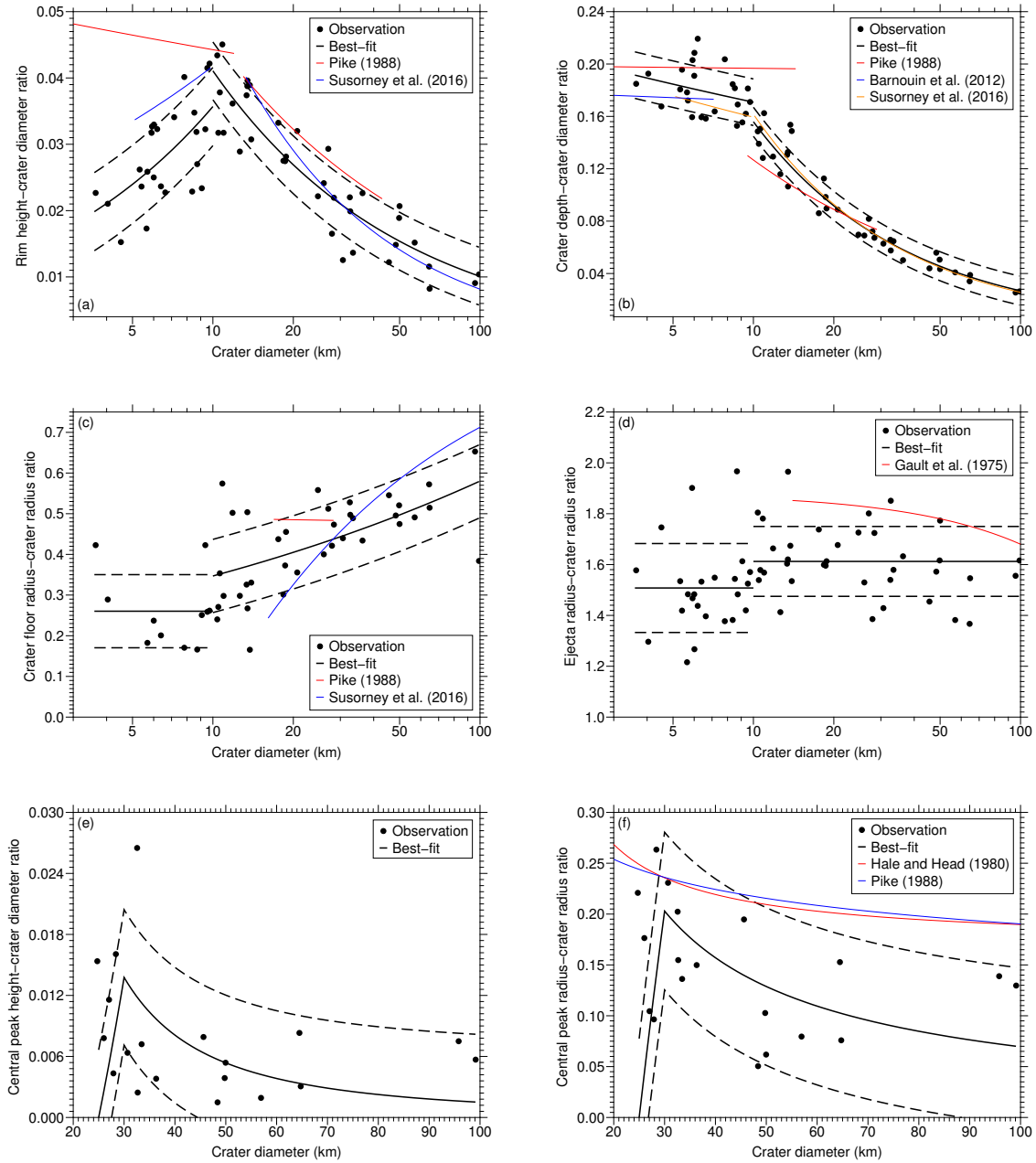

Figure 3.17: Morphometric parameters used to model the initial profiles of transitional and complex craters on Mercury: rim height (a), crater depth (b), crater floor radius (c), continuous ejecta radius (d), central peak height (e), and central peak radius (f), including measured results and best-fits. Morphometric parameters derived in other studies are also plotted as a comparison: Gault et al. (1975), Hale and Head (1980), Pike (1988), Barnouin et al. (2012), and Susorney et al. (2016).

Table 3.9: A brief summary of morphometric parameters for fresh Mercury's craters: rim height.

Formula	Diameter range (km)	Crater number	Elevation data	Reference
$h_r = 0.00950D^{0.575}$	$3.6 < D \leqslant 10$	24	MLA	This study
$h_r = 0.167D^{-0.610}$	$10 < D \leqslant 97$	36		
$h_r = 0.052D^{-0.070}$	$2.4 \leqslant D \leqslant 12$	32	Mariner 10	Pike (1988)
$h_r = 0.150D^{-0.513}$	$13 \leqslant D \leqslant 43$	25		
$h_r = 0.020D^{0.320}$	$5.1 \leqslant D \leqslant 9.8$	45	MLA and MDIS	Susorney et al. (2016)
$h_r = 0.310D^{-0.790}$	$13 \leqslant D \leqslant 311$	49		

Table 3.10: A brief summary of morphometric parameters for fresh Mercury's craters: crater depth.

Formula	Diameter range (km)	Crater number	Elevation data	Reference
$d_{\mathrm{cf}} = 0.221D^{-0.112}$	$3.6 < D \leqslant 10$	24	MLA	This study
$d_{\mathrm{cf}} = 0.907D^{-0.765}$	$10 < D \leqslant 97$	36		
$d_{\mathrm{cf}} = 0.199D^{-0.005}$	$0.2 \leqslant D \leqslant 14$	104	Mariner 10 images	Pike (1988)
$d_{\mathrm{cf}} = 0.410D^{-0.510}$	$9.5 \leqslant D \leqslant 29$	69		
$d_{\mathrm{cf}} = 0.180D^{-0.020}$	$1.0 \leqslant D \leqslant 7.1$	23	MLA and MDIS	Barnouin et al. (2012)
$d_{\mathrm{cf}} = 0.220D^{-0.140}$	$5.1 \leqslant D \leqslant 9.8$	50	MLA and MDIS	Susorney et al. (2016)
$d_{\mathrm{cf}} = 1.020D^{-0.800}$	$10 \leqslant D \leqslant 311$	68		

Table 3.11: A brief summary of morphometric parameters for fresh Mercury's craters: crater floor radius.

Formula	Diameter range (km)	Crater number	Elevation data	Reference
$R_{\mathrm{cf}} = 0.260$	$3.6 < D \leqslant 10$	24	MLA	This study
$R_{\mathrm{cf}} = 0.207D^{0.223}$	$10 < D \leqslant 97$	36		
$R_{\mathrm{cf}} = 0.50D^{-0.01}$	$17 < D \leqslant 28$	16	Mariner 10	Pike (1988)
$R_{\mathrm{cf}} = (D/2 - 1.65D^{0.47})/(D/2)$	$16 \leqslant D \leqslant 311$	37	MDIS	Susorney et al. (2016)

Table 3.12: A brief summary of morphometric parameters for fresh Mercury's craters: ejecta radius.

Formula	Diameter range (km)	Crater number	Elevation data	Reference
$R_e = 1.51$	$3.6 < D \leqslant 10$	24	MLA	This study
$R_e = 1.61$	$10 < D \leqslant 97$	36		
$R_e = 0.88 - 0.002D$	$14 \leqslant D \leqslant 250$	27	Mariner 10	Gault et al. (1975)

Table 3.13: A brief summary of morphometric parameters for fresh Mercury's craters: central peak height.

Formula	Diameter range (km)	Crater number	Elevation data	Reference
$h_{\mathrm{cp}} = 4.14 \times 10^{-5} D^{2.05} - 0.0304$	$25 < D \leqslant 30$	5	MLA	This study
$h_{\mathrm{cp}} = 7.32 D^{-1.85}$	$30 < D \leqslant 97$	14		

Table 3.14: A brief summary of morphometric parameters for fresh Mercury's craters: central peak radius.

Formula	Diameter range (km)	Crater number	Elevation data	Reference
$R_{\mathrm{cp}} = 2.67D^{0.209} - 5.22$	$25 < D \leqslant 30$	5	MLA	This study
$R_{\mathrm{cp}} = 4.19D^{-0.890}$	$30 < D \leqslant 97$	14		
$R_{\mathrm{cp}} = 0.17 + 1.97/D$	$15 \leqslant D \leqslant 175$	140	Mariner 10	Hale and Head (1980)
$R_{\mathrm{cp}} = 0.434D^{-0.179}$	$13 \leqslant D \leqslant 189$	138	Mariner 10	Pike (1988)

For the floor radius-crater radius ratio on Mercury (Figure 3.17c), we can see that it remains constant from 1 to 10 km and then increases to about half the crater radius. We used a horizontal line to fit the measurements for craters smaller than 10 km and a power-law function for craters larger than 10 km. Our result is smaller than Pike (1988) from 17 to 28 km, and is larger than Susorney et al. (2016) when crater diameter is smaller than 28 km and then becomes smaller afterwards.

For the continuous ejecta radius-crater radius ratio on Mercury (Figure 3.17d), because it is difficult to identify the ejecta boundary along the elevation profile, our result has a large uncertainty. Therefore, we simply used the average value of the measurements to represent the normalized continuous ejecta radius, which is smaller than that given by Gault et al. (1975).

The above four parameters decide the initial crater shape on Mercury on the first order. Although the morphology of the central peak does not have any significant effect on the erosion of the crater rim, we still take it into consideration when modeling the initial crater profile.

For the central peak height-crater diameter ratio on Mercury (Figure 3.17e), we can hardly see any clear tendency. Nevertheless, we still expect that the ratio may first increase and then decrease with crater diameter. This can be explained as the case of lunar complex craters: as the impact energy increases, the rebound of target materials would be more significant; however, when the height of the central uplift reaches to a critical value, it would collapse due to gravity instability, which transforms the central peak to a peak ring (Baker and Head, 2013). To fit the measurements, we then used two power-law functions for craters smaller and larger than 30 km, and there is no previous study we can compare with.

For the central peak radius-crater radius ratio on Mercury (Figure 3.17f), again, we can hardly see any clear tendency. Nevertheless, we still expect that the ratio may first increase and then decrease with crater diameter, which indicates the transition from a circular central base to a peak ring from a planar view. To fit the measurements, we then used two power-law functions for craters smaller and larger than 30 km. Comparing our result with Hale and Head (1980) and Pike (1988), we found that their results are larger than ours and have a monotonous trend.

The crater morphometric relations obtained in this study differ from those acquired by previous studies, mainly due to the parameter definitions, selected fresh

craters, and the elevation data being used. We found Susorney et al. (2016) could be comparable to our study in the crater depth-diameter ratio, as (1) this parameter is easy, clear to define, (2) the fresh craters used in this study (N=56) come from the database determined by Susorney et al. (2016) (N=126), and (3) both studies used the MLA RDR as the elevation data. As is shown in Figure 3.17b, the best-fitting curves derived from the two studies almost overlap with each other in the transitional and complex crater regimes, which shows the validity of the two results. For simple craters, the depth-diameter ratios derived from these two studies are somewhat different. This may arise from the mis-registration between the MDIS image and the MLA GDR data, the MLA tracks being utilized, and the fresh craters being used. First, the crater center coordinate used in this study is determined from the interpolated elevation data (i.e., MLA GDR), whereas that in Susorney et al. (2016) was determined based on the MDIS image. Since we are working on the elevation profiles, it is more reasonable to determine the coordinate of the crater center based on the elevation data. Second, we used all the MLA tracks within the crater, which varies from 3 to 43 with an average of 14 for the selected fresh craters, whereas Susorney et al. (2016) only used three tracks for each crater. Third, we selected 23 fresh simple craters from the 57 craters used by Susorney et al. (2016), and those chose by us have both a simple geological background and sufficient MLA observations.

Nevertheless, our derived morphometric parameters supercede previous ones in the following aspects. (1) More self-consistent: in this study, all the morphometric parameters are calculated from the same group of fresh craters, using the same elevation data, and based on the azimuthally averaged elevation profiles, whereas previous studies did not. For example, Susorney et al. (2016) used 118 fresh craters and the MLA RDR data to study the depth-diameter ratio, whereas Pike (1988) utilized 173 fresh crates and the Mariner 10 stereo-images. (2) More accurate: we used newly acquired, high-quality elevation datasets and performed atypical background feature removal, whereas other studies used old datasets and did not perform the background correction. (3) More reasonable: we imposed a boundary condition at the transitional-complex boundary. For example, in our result the central peak radius is 0 at 25 km (transitional-complex boundary), whereas other studies (e.g., Pike (1988)) show that the central peak radius would increase with decreasing diameter,

which is contradictory to the definition of a transitional crater.

Table 3.15: Natural variability in the initial rim height as a function of crater diameter for Mercury's craters.

Crater diameter bin (km)	N	Initial rim height variability (m)
$10 \leqslant D \leqslant 20$	16	55
$20 < D \leqslant 40$	11	136
$40 < D \leqslant 60$	5	167
$60 < D \leqslant 100$	4	179

When estimating the lava flow thickness exterior to the crater rim, the variation of the crater rim height with crater diameter and degradation state is our primary concern. Our result shows that the rim height increases from 411 to 1008 m with diameters of 10–100 km (Figure 3.17a). This result could constrain the upper limit of the lava flow thickness around the exposed rim of a partially buried crater or the lower limit around the buried rim of a partially or completely buried crater.

Similar to the Moon, the natural variability in rim height also exists for fresh craters on Mercury. This variability is quantified in Table 3.15, where we provide the root-mean-square deviation of the measured initial rim height with respect to the predicted initial rim height as a function of crater diameter. Within the diameter range of the studied partially buried craters (10–100 km), the natural variabilities of the initial rim height are less than 180 m.

B. Shape Model

Our derived shape models for fresh craters on Mercury are plotted in Figure 3.18. In this normalized coordinate, we can find that with increasing crater diameter the rim height and crater depth decrease, the crater floor radius increases, and the central peak height and central peak radius first increase and then decrease. This is to be expected as these initial profiles are constructed upon the morphometric parameters. In addition, we can also find that the elevations profiles with different diameters always have a smooth and continuous transition among them.

The corresponding formulas are presented in Table 3.16. In this table, h_{r}, d_{cf}, R_{cf}, R_{e}, h_{cp}, and R_{cp} denote morphometric parameters rim height, crater depth, crater floor radius, continuous ejecta radius, central peak height, and central peak

radius. The coefficients a–f that are required in this table can be numerically determined by setting the function equal to the known values at the relevant tie points. All the vertical parameters ($h_{\rm cp}$, $d_{\rm cf}$, and $h_{\rm r}$) are normalized by crater diameter, and all the radial parameters (r, $R_{\rm cp}$, $R_{\rm cf}$, and $R_{\rm e}$) are normalized by crater radius. To fit the central peak, crater wall and crater ejecta, we use different forms of exponential functions.

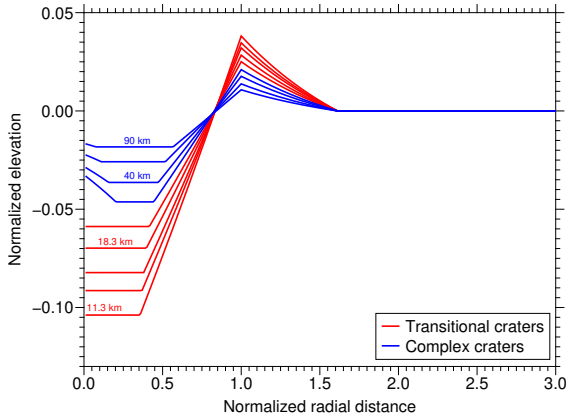

Figure 3.18: Radial elevation profiles for fresh Mercury's craters. The radial distance is normalized by crater radius ($r_{\rm norm} = r/R_{\rm init}$), and the elevation is normalized by crater diameter ($H_{\rm norm} = H/D_{\rm init}$). The red curves are transitional craters, and the blue curves represent complex craters. The plotted initial crater diameters were carefully selected to present the results for clarity and are labeled for several curves.

Table 3.16: Mathematic forms for fresh Mercury's impact craters.

Morphology	Elevation profile	Range
Transitional	$h_{\rm r} - d_{\rm cf}$	$r \leqslant R_{\rm cf}$
$(20 < D \leqslant 25$ km)	$\exp(cr) + d$	$R_{\rm cf} < r \leqslant 1$
	$e\exp(fr)$	$1 < r \leqslant R_{\rm e}$
	0	$r > R_{\rm e}$
Complex	$a\exp(r) + b$	$r \leqslant R_{\rm cp}$
$(D > 25$ km)	$h_{\rm r} - d_{\rm cf}$	$R_{\rm cp} < r \leqslant R_{\rm cf}$
	$\exp(cr) + d$	$R_{\rm cf} < r \leqslant 1$
	$e\exp(fr)$	$1 < r \leqslant R_{\rm e}$
	0	$r > R_{\rm e}$

Since this study is the first one to derive the initial elevation profiles for fresh

craters ever on Mercury, there is no previous study we can compare with. Nevertheless, our derived shape model is based on the analyses of the crater morphometric parameters, and we have shown that the new morphometric relations given by this study are better than others.

3.5 Effect of Crater Degradation on Rim Height

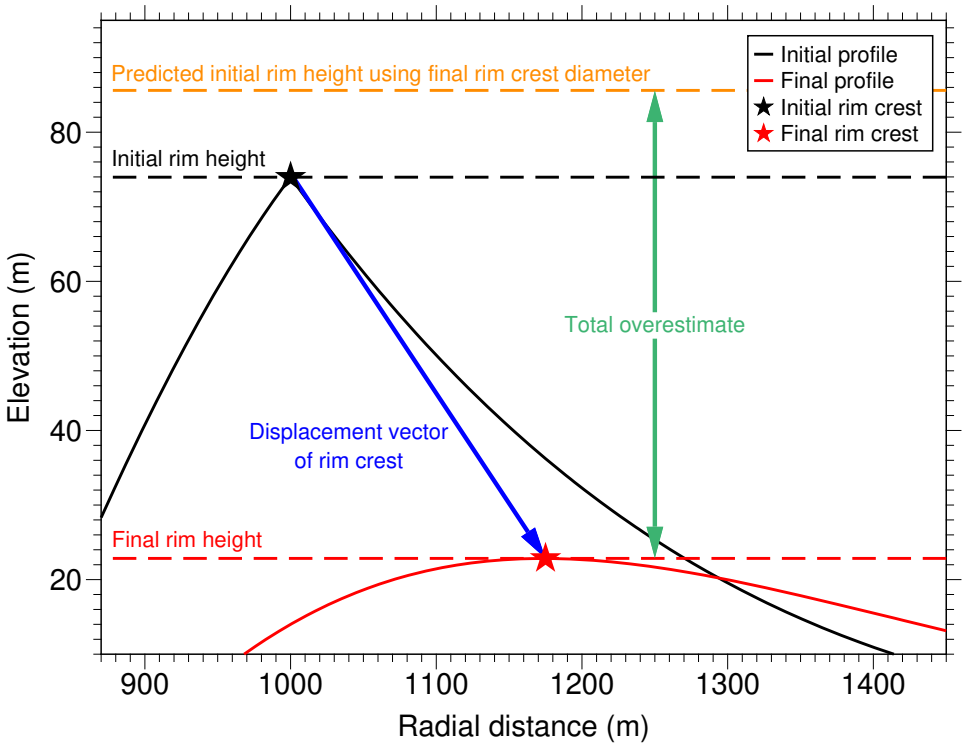

Figure 3.19: Diagram of rim height overestimation for a lunar crater with an initial diameter of 2 km that formed at 3.6 Ga. The solid black and red lines are the initial and final profiles, the dashed black and red lines are the initial and final rim heights, and the black and red stars are the corresponding initial and final rim crests. The dashed orange line is the predicted, initial rim height based on the final crater diameter using the rim height-crater diameter relation in Pike (1977). The vertical offset between the dashed horizontal orange and red lines is the resulting rim height overestimate. The blue arrow indicates the displacement of rim crest during crater degradation.

Given an initial crater profile, we model the crater degradation process and estimate the reduction in the rim height. As a consequence of crater degradation, the rim crest moves both downward and outward (Figure 3.19). For an elevation profile, this process can be seen as the rim crest at an initial position (D_0, h_0) moving

to $(D_0 + \Delta D,\, h_0 - \Delta h)$, where D_0 and h_0 are initial crater diameter and rim height, and ΔD and Δh are the increase in crater diameter and the decrease in rim height due to the erosion process. Previous studies (De Hon and Waskom, 1976; De Hon, 1979b), however, used the current crater diameter $(D_0 + \Delta D)$ to estimate the initial rim height. Since the current rim diameter will always be larger than the initial rim diameter, this approach will overestimate the initial height of the crater rim.

A quantitative case study is shown in Figure 3.19. This a lunar mare crater with an initial diameter of 2 km and an initial rim height of 74 m (black) that formed at 3.6 Ga. The present-day crater diameter and rim height are 2.3 km and 23 m (red), respectively. If the total rim height is estimated based on the present-day crater diameter, one would obtain a value of 86 m (orange). Therefore, the total overestimate on the total rim height would be 86-23=63 m (green).

3.5.1 The Moon

For lunar craters, we note that the manner by which the rim height degrades with time will be discontinuous at the simple-transitional boundary at 15 km. In particular, the rim-height to crater diameter ratio is constant for all simple craters, but this ratio decreases for craters with larger diameters. In addition to this, the formulas of the crater topographic profiles interior and exterior to the crater rim also change across this morphologic transition, as we used two different connecting functions for the crater inner wall and ejecta in the simple and transitional crater regimes. The resulting discontinuous change in slopes to each side of the rim has a strong effect on how simple and transitional/complex craters degrade. It is for this reason that we will demonstrate the degradation of simple and larger craters separately.

The effect of topographic degradation on the crater rim height (Δh) is shown in Figure 3.20. In the upper two panels, we plot the reduction in rim height as a function of time over the past 3.9 billion years using a diffusivity of 5.5 m^2/Myr (Fassett and Thomson, 2014). Results for representative crater diameters of 5, 10, 15, 20, 50, 100 km are plotted, and we emphasize that these diameters correspond to the initial diameter (and not the final eroded diameter). For simple craters, the reduction in rim height is nearly independent of diameter. After 3.9 billion years of erosion, the rim height reduction is about 45 m for a mare crater, and 41 m for a

highland crater. For transitional and complex craters, the

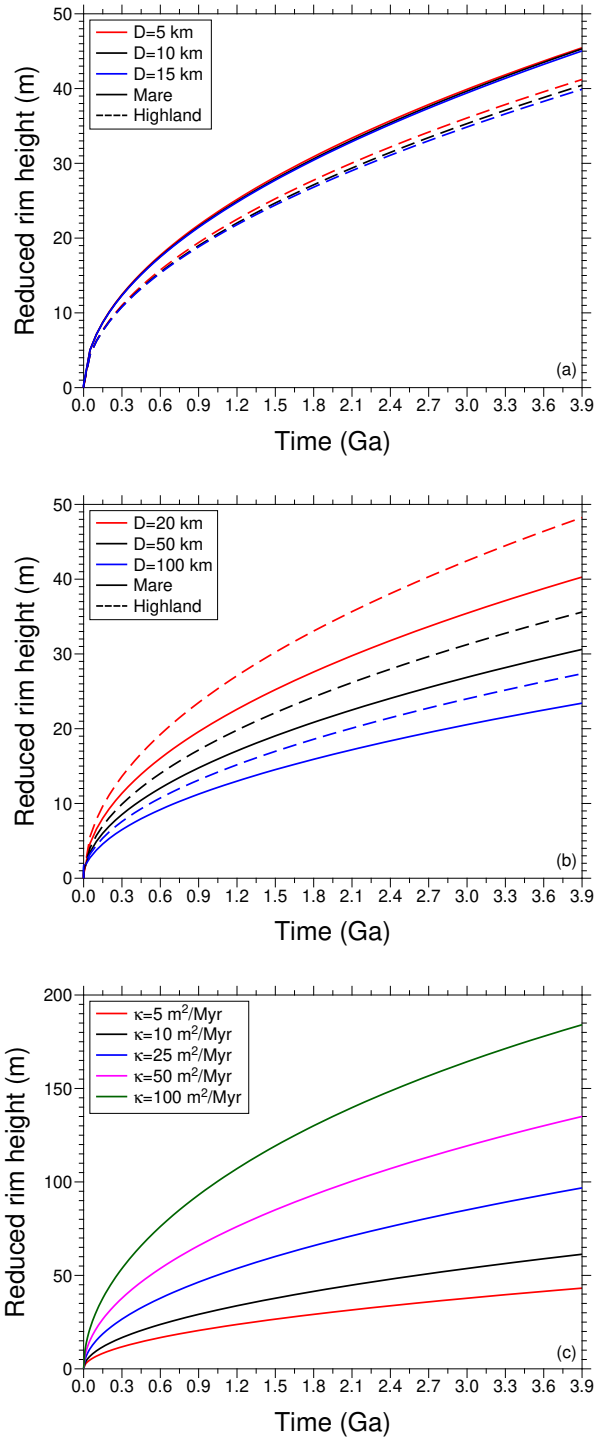

Figure 3.20: Predicted absolute rim height reduction during the degradation process for lunar craters. In (a) and (b), the diffusivity was set to 5.5 m^2/Myr and the results are plotted for several mare and highland craters with selected diameters in simple (a) and transitional/complex regimes (b). In (c), results are plotted for a 10-km-diameter mare crater for several different diffusivities.

amount of rim erosion is largest for the smallest craters, and smallest for the largest craters. Small craters simply erode faster than large craters, in part because the surface slopes decrease with increasing diameter. For mare craters, the rim erosion is about 40 m for a 20-km-diameter crater and 31 m for a 50-km-diameter crater. For highland craters, these values are larger by about 20 % and 16%.

In the lowermost panel of Figure 3.20, we demonstrate how the rim erosion depends upon the assumed diffusivity. For this plot, we considered values of 5, 10, 25, 50, and 100 m^2/Myr, and then plotted the rim erosion associated with a simple 10-km-diameter mare crater. These topographic diffusivity values are selected because it is expected that the topographic diffusivity is proportional to the crater diameter, and that a 1-km-diameter crater has a reference diffusivity of 5.5 m^2/Myr. The result shows that if this crater formed at 3.9 Ga, then the reduction in rim height could range from 43 to 184 m with an increasing diffusivity. We note that the erosion of a crater depends only upon the product of the diffusivity and time, and that these two parameters are hence not independent.

Previous basalt thickness estimates that did not consider crater degradation lie between 200 and 400 m (De Hon and Waskom, 1976; De Hon, 1979b). For a diffusivity of 5.5 m^2/Myr, our results show that the rim height could be reduced by up to 45 meters for a 3.9-Gyr-old, 10-km-diameter mare crater (Figure 3.20a). However, the amount of rim erosion increases substantially with increasing diffusivity. For a diffusivity of 100 m^2/Myr, Figure 3.20c shows that the rim height reduction could be 184 m, which is comparable to the basalt thicknesses that were previously estimated by De Hon and Waskom (1976) and De Hon (1979b).

3.5.2 Mercury

After obtaining the initial profiles for Mercury's craters, we can then quantitatively estimate the reduction of crater rim height as a function of time by inputting the initial profile to the crater degradation model. Currently, we do not have a good constraint on the topographic diffusivity for craters on Mercury. Nevertheless, considering the facts that (1) the kilometer-scale lunar craters have a reference diffusivity of 5.5 m^2/Myr (Fassett and Thomson, 2014), (2) the topographic diffusivity on Mercury may be twice the strength of that on the Moon, and (3) the topographic diffusivity scales linearly with crater diameter, we set the reference diffusivity for a

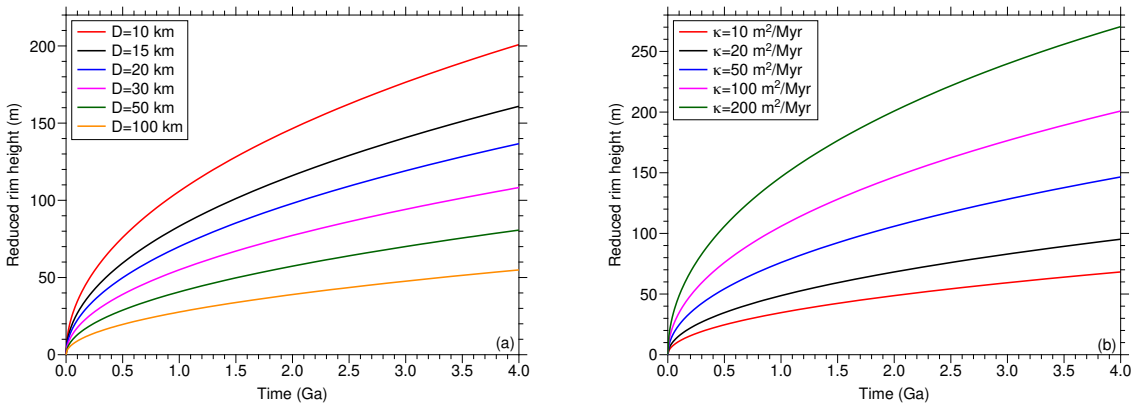

Figure 3.21: Predicted absolute rim height reduction during the degradation process for Mercury's craters. In (a), the diffusivity is set to 100 m^2/Myr, and results are plotted for several different diameters. In (b), results are plotted for a 10-km-diameter crater for several different diffusivities.

10-km-diameter Mercury's crater to be 100 m^2/Myr. We first assume the same diffusivity value for craters with diameters of 10, 15, 20, 30, 50, and 100 km, and look into how the rim height reduction varies with time. Meanwhile, we also take into account the diameter-dependence of crater topographic degradation by assuming different diffusivity values of 10, 20, 50, 100, and 200 m^2/Myr for a 10-km-diameter crater.

As is shown in Figure 3.21, if the same diffusivity value is assigned to craters with difference sizes, the reduced rim height could be 55–201 m. If the diameter-dependence of topographic diffusivity is considered, the rim height reduction could be 68–270 m, which is comparable to the upper limit of the previous lava flow thickness estimates around partially buried craters of 0.4–1.8 km (Ostrach et al., 2015).

Chapter 4 Mare Basalt Thickness on the Moon

4.1 Database and Classification of Buried Craters

We constructed a database of buried impact craters on the Moon (Table 4.1), making use of the LROC/WAC basemap and the ArcGIS platform with the Crater Helper Tools toolkit (Nava, 2011). In order to obtain the center and diameter of the crater, the crater rim needs to be determined first. The crater rim can be seen as an exposed crater rim, a wrinkle ridge or a topographic depression boundary. If the crater rim is intact and continuous, then three control points that are $\sim$120° apart along the rim were selected manually to define a circle that was used to determine the center and diameter of the crater. When less than 10% of the crater rim can be seen, then the determination of the crater center and diameter is problematic: we did not include this type of crater in our study, which may result in an underestimate of the total number of partially buried craters. In total, we identified 661 partially and completely buried craters on the lunar surface, all located within mare deposits or along mare margins. The diameter, longitude, latitude, classification, percentage of the rim that is buried, and composition of the rim/ejecta are given in Table A.1 in the Appendix.

We divided the identified buried craters into three classes based on the observed morphology of the crater rim: completely exposed, partially exposed, and completely buried. Craters with rims completely or partially exposed can be classified into two subclasses based on their locations. If the entire exposed ejecta are surrounded by mare basalts, then the crater is classified as being located in the mare, whereas if part of the exposed ejecta are contiguous with the surrounding highland terrain, then the crater is classified as being located on the mare-highland boundary. We note that craters located in the maria could have formed on the highland crust and later were flooded by basalts, such that the exposed crater rim and ejecta have a highland composition.

Table 4.1: Classification of buried impact craters on the Moon (N=661).

Class	Location	Description	Number
Rim completely exposed	Mare	Rim and proximal ejecta completely exposed, distal ejecta buried	74
	Mare-highland boundary	Mare side: rim and proximal ejecta completely exposed, distal ejecta buried; Highland side: rim and ejecta completely exposed	188
Rim partially exposed	Mare	Rim and proximal ejecta partially exposed, distal ejecta buried	112
	Mare-highland boundary	Mare side: rim and proximal ejecta partially exposed (N=239) or completely buried (N=9), distal ejecta buried; Highland side: rim and ejecta completely exposed	248
Rim completely buried	Mare	Rim and ejecta completely buried, characterized by a wrinkle ridge or an interior topographic depression	39

In an idealized case, a crater would form on a perfectly flat surface, the rim crest height would be the same everywhere, and any mare basalts that flooded the region would be uniform in thickness. There are several factors that complicate such an idealized scenario. First, the impact crater could form on a sloping surface and the lavas would only embay that portion of the crater at the lowest elevations. This is likely what occurred for partially buried craters that form along the mare-highland boundaries. In these cases (Figure 4.1a), the crater rim and ejecta can be divided into highland and mare parts: the crater ejecta of the highland part are not buried by lava flows, whereas the crater ejecta of the mare part are. Though these craters are included in our database, they will not be analyzed later as a result of this complication.

In a more complex scenario, a part of the crater rim could be breached by the exterior lavas in several places, leaving a crater rim that is discontinuous (Figures 4.1b–d). The formation of such a partially buried crater could arise as a result of several asymmetric processes. The crater rim height is not everywhere constant, either as a result of the initial formation processes, or by later erosional processes (such as small craters that formed on the rim). Alternatively, the basalt thickness might not be uniform everywhere, with the thicknesses being higher on the side of the crater rim that was breached.

To extend our database, we also searched for craters that are completely buried by mare basalts. This type of crater is usually characterized by a concentric wrinkle ridge over the crater rim (Figure 4.1e) or a subtle topographic low in the crater interior as a result of thermal contraction of the cooling lava flow (Figure 4.1f). The mare basalt thickness around a completely buried crater is difficult to estimate. On the one hand, the mare basalt thickness needs to be greater than the crater rim height. On the other hand, the crater rim height could have been degraded between the times of crater formation and lava infill. Therefore, although we include these entirely buried craters in our database, we will not use them later when estimating mare basalt thicknesses. We note that completely buried craters can also sometimes be identified in the Bouguer gravity anomaly maps (Evans et al., 2016, 2018; Sood et al., 2017; Zhang et al., 2018).

De Hon and Waskom (1976) and De Hon (1979b) constructed a global partially buried crater database that included 342 partially buried craters in the nearside east-

ern (30°S–30°N; 0–100°E) and western (45°S–45°N; 90°W–10°E) maria, of which the crater rim is either completely or partially exposed as defined by our classification. It is challenging to directly compare their database with ours, because there is a misregistration between the two databases in the coordinate systems used. By comparing the provided crater center coordinates for several of the largest and thus least ambiguous partially buried craters (e.g., Flamsteed P: D=108.9 km), this misregistration can be up to 10 km. Nevertheless, our database is expected to be more accurate and more complete than previous ones, because of our use of more recent remote sensing datasets with considerably higher accuracy and resolution.

4.1.1 Case Studies of Buried Craters

In addition to craters with rims completely exposed on the maria (as presented in Figure 2.10), the characteristics of the other four types of buried craters are presented here, including craters with rims completely exposed on the mare-highland boundaries, craters with rims partially exposed on the maria, craters with rims partially exposed on the mare-highland boundaries, and craters with rims completely buried on the maria. These four types of craters need to be discussed separately, since their geological contexts are more complicated. For each class, a representative crater was selected as a case study.

For the class of craters with rims completely exposed on the mare-highland boundaries, the crater rim can be divided into mare and highland parts. As a detailed study, crater Borman V (37.63°S, 151.40°W; D=27.4 km) that is located within the inner ring of Apollo basin was selected, of which the northern crater ejecta are buried by mare basalts whereas the southern crater ejecta are unburied and connected with the highland terrain (Figure 4.1a). In the optical image, the exposed crater rim can be seen as high-reflectance materials compared with the dark lava flow to the north. The ejecta boundary is identified as an abrupt contrast in reflectance between brighter crater ejecta and darker mare basalts (white arrows), and the exposed ejecta width is estimated to be half of the crater radius. On the other hand, the reflectance of the exposed crater ejecta on the south is similar to that of the surrounding highland region, and no clear boundary between crater ejecta and background terrain is found.

For the class of craters with rims partially exposed on the maria, the crater rim

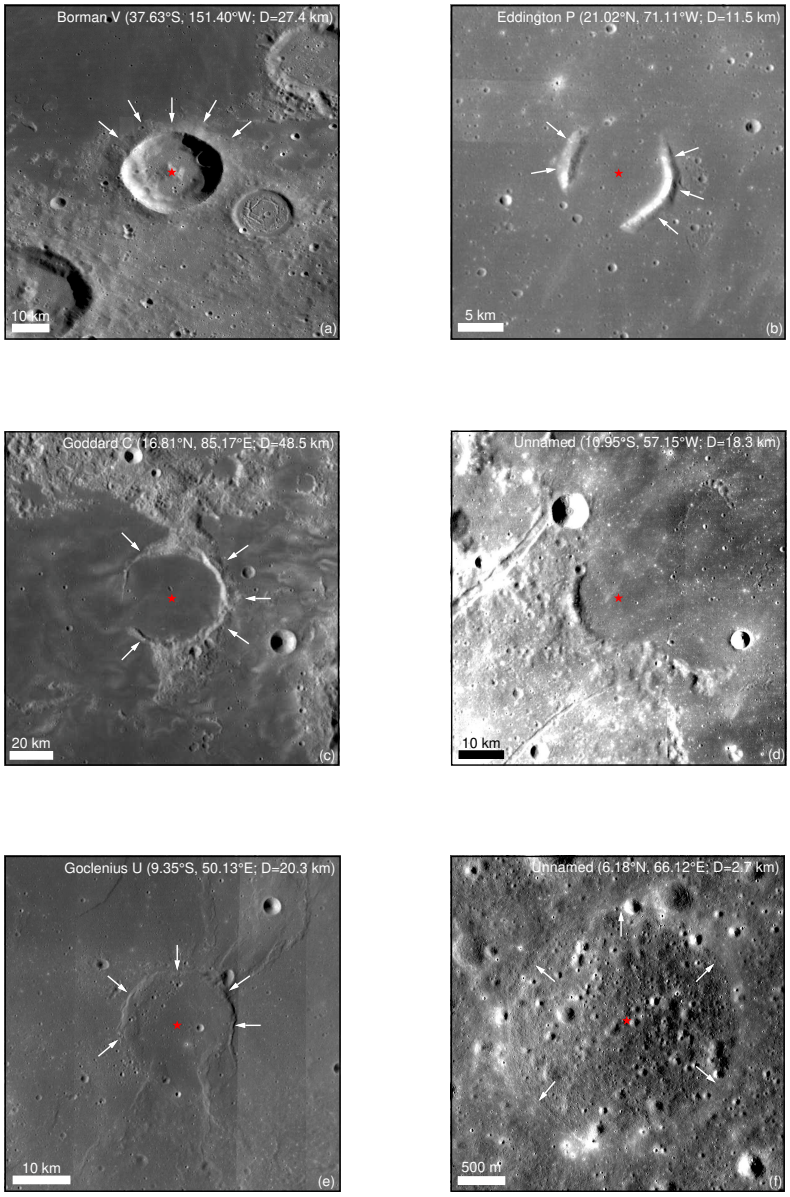

Figure 4.1: LROC/WAC images of four types of buried craters: crater Borman V (D=27.4 km) with rim completely exposed on the mare-highland boundary (a), crater Eddington P (D=11.5 km) with rim partially exposed on the mare (b), crater Goddard C (D=48.5 km) on the mare-highland boundary with rim partially exposed on the mare side (c), an unnamed crater (D=18.3 km) on the mare-highland boundary with rim completely buried on the mare side (d), and crater Goclenius U (D=20.3 km) with rim completely buried on the mare characterized by a wrinkle ridge (e). A high-resolution LROC/NAC (M1123163931RC) image of an unnamed crater (D=2.7 km) with rim completely buried on the mare featured by an interior depression (f) is also shown. The red stars give the locations for crater centers. The white arrows point to the boundaries of the exposed crater ejecta in (a–c) and the buried crater rim in (e) and (f).

can be divided into exposed and buried parts. As a detailed study, crater Eddington P (21.02°N, 71.11°W; D=11.5 km) that is located in the southeastern region of the flooded crater Eddington was selected, of which the eastern and western crater rims are exposed whereas the northern and southern crater rims are buried by lava flows (Figure 4.1b). In the optical image, the exposed crater rims are discernible as high-reflectance materials compared with the surrounding, dark lava flows. The ejecta boundary is seen as a distinct contrast in reflectance between brighter crater ejecta and darker mare plains (white arrows), and the exposed ejecta width is estimated to be only one-third of the crater radius. There are no reflectance variations between the buried crater rim regions and the surrounding lava flows.

For the class of craters with rims partially exposed on the mare-highland boundaries, there are actually two subclasses depending on whether or not the crater rim is completely buried on the mare side. In the case where the crater rim is partially buried on the mare side, the crater rim can be divided into three parts: an exposed part on the mare, a buried part on the mare, and an exposed part on the highland. In the case where the crater rim is completely buried on the mare side, the crater rim can be divided into two parts: a buried part on the mare, and an exposed part on the highland.

As for the first case, crater Goddard C (16.81°N, 85.17°E; D=48.5 km) that is located in the north of Mare Marginis was selected for a case study, of which the northern crater rim is contiguous with the highland terrain, the southwestern crater rim is buried by mare basalts, and the rest of the crater rim is exposed (Figure 4.1c). In the optical image, the exposed crater rim on the mare side can be seen as high-reflectance materials compared with the surrounding, dark lava flows. The exposed ejecta boundary is identified as an abrupt contrast in reflectance between the brighter crater ejecta and the darker mare basalts (white arrows), and the exposed ejecta width is estimated to be only ∼15% to 30% of the crater radius. For the buried crater rim on the southwest, there are no reflectance variations between this region and the surrounding lava flows. For the exposed crater rim and ejecta on the north, they have a similar reflectance with the surrounding highland region, and no clear boundary between crater ejecta and background terrain is found due to the rugged topographic relief there.

As for the second case, an unnamed crater (10.95°S, 57.15°W; D=18.3 km)

that is located on the southwestern corner of Oceanus Procellarum was selected for a detailed study, of which the western and southern crater rims are connected with the highland terrain whereas the northern and eastern crater rims are buried by mare basalts (Figure 4.1d). In the optical image, the buried crater rim region has the same surface reflectance as the surrounding lava flows and thus is undetectable, and the exposed crater ejecta on the highland side appear to be highly degraded and it is difficult to determine the ejecta boundary.

For the class of craters with rims completely buried on the maria, the entire crater rim should be mantled by the lava flow but a wrinkle ridge over the crater rim or a topographic depression in the crater interior can be still discernible. As a representative study for the wrinkle ridge case, crater Goclenius U (9.35°S, 50.13°E; D=20.3 km) in the southern Mare Fecunditatis was selected (Figure 4.1e). A circular wrinkle ridge can be seen clearly that is connected to the surrounding wrinkle ridges (white arrows). As a representative study for the topographic depression case, an unnamed crater (6.18°N, 66.12°E; D=2.7 km) that is located in the northwestern region of Mare Undarum was chosen (Figure 4.1f). In the high-resolution LROC/NAC image, this crater appears to be recognizable due to a gentle topographic depression seen in the crater interior and a favorable local incidence angle (buried rim indicated by the white arrows).

4.1.2 Spatial Distribution and Statistics of Buried Craters

The most prominent feature seen in the spatial distribution of buried craters is their preferential occurrence along the mare-highland boundaries (Figure 4.2). This distribution pattern is to be expected, since the mare basalts at the edge of the mare are expected to be thinner than elsewhere. Though the thicker flows in the mare centers can entirely flood craters of a given size, the thinner flows at the margins can only partially flood the crater. This interpretation is supported by the identification of ghost craters in Bouguer gravity anomaly maps in the central portions of the maria (Evans et al., 2016, 2018; Sood et al., 2017; Zhang et al., 2018). We also note that the smallest buried craters are distributed uniformly across the mare, whereas larger ones are concentrated along the mare-highland boundaries. Our interpretation of this observation is that the larger craters were completely buried in the central mare where the basalt thicknesses are the greatest. Many of

the smaller craters, in contrast, are younger and formed during the main phase of mare volcanism. Many of these craters thus formed on top of pre-existing lava flows. The thickness of the flows that buried these craters was thus only a fraction of the total thickness of lavas in the region. With thinner flows embaying the crater, the probability that the rim crest would remain unburied would be higher.

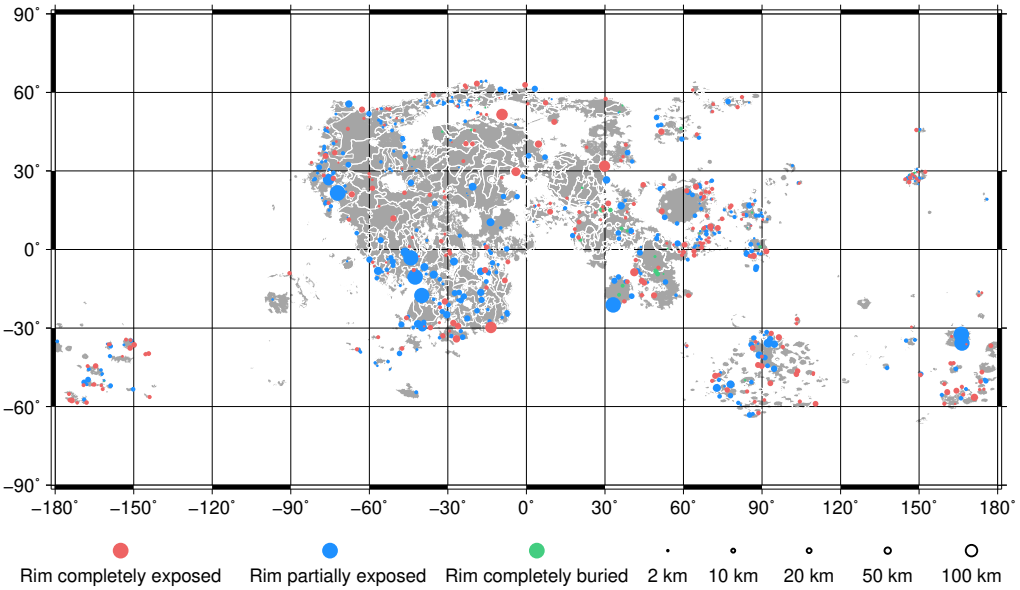

Figure 4.2: Distribution of buried craters with completely exposed rims (light red, N=262), partially exposed rims (blue, N=360), and completely buried rims (green, N=39). The lunar maria basemap (gray) is from Nelson et al. (2014), and the basaltic unit boundaries (white) are from a compilation of previous studies (Hiesinger et al., 2006, 2011; Morota et al., 2009, 2011a; Pasckert et al., 2018). The size of the circles increases with increasing crater diameter.

Histograms of the different classes of buried craters as a function of diameter are shown in Figure 4.3a. The diameters of all the partially and completely buried craters range from 1.5 to 130 km, of which craters with rims completely exposed in the maria range from 1.8 to 45.3 km. In general, the peak in the histogram is skewed towards smaller craters. This is in part because there are in general more smaller than larger craters, but also because the older and larger craters that formed before the main phase of mare volcanism have been completely buried. Analyzing the craters by class, the median crater diameter is found to increase from craters with rims completely buried (3.7 km), to those with rims partially exposed (9.3 km), and to those with rims completely exposed (11.6 km). This observation is easy

to explain: for a given basalt thickness, smaller craters with lower rim heights are easier to completely bury than larger craters with greater rim heights. In terms of location, the median diameter of partially and completely buried craters on maria (6.6 km) is smaller than that along mare-highland boundaries (12.9 km). As noted previously, we interpret this observation as being a result of the mare basalts being thicker in the center of the mare than those along their edges, therefore older, larger craters inside the maria are completely buried.

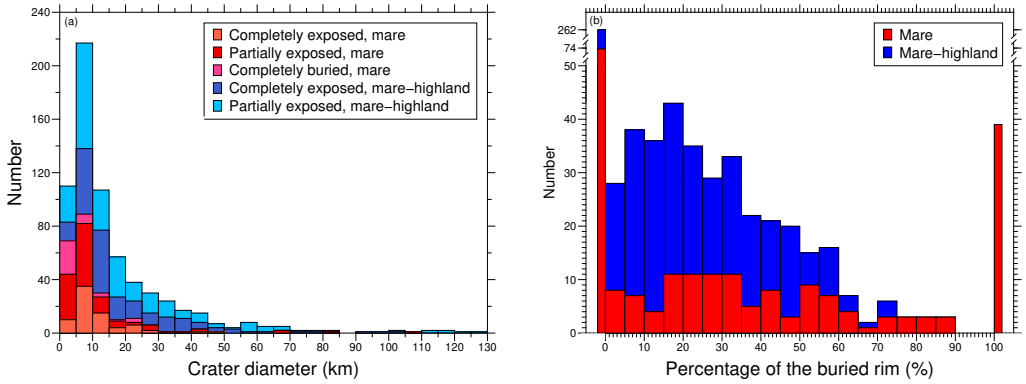

Figure 4.3: (a) Size-frequency distributions of the different classes of buried craters. (b) Percentage of the rim buried by mare basalts for craters that formed in the mare (red) and along the mare-highland boundary (blue). In (b), the scale of the vertical axis is discontinuous, and the total numbers of craters with rims completely exposed or completely buried are plotted in the leftmost and rightmost bins, respectively.

For all of the partially buried craters in our database, we have estimated the percentage of the crater rim crest circumference that was buried by lava flows (Figure 4.3b). The median percentage of rim burial of mare craters (24%) is larger than that of mare-highland boundary craters (7%). This is simply because the crater rim is never buried on the highland side of the mare-highland boundary. This figure also shows that we did not include any craters where more than 90% and less than 100% of the rim has been buried. Although we did find some short exposed crater rims that might indicate the presence of partially buried craters with rim exposure smaller than 10%, we are not confident to determine the crater center and diameter because no other indicators of the crater rim (e.g., wrinkle ridges or a topographic depression) were found that can help to outline the crater.

4.2 Mare Basalt Thickness Estimation Results

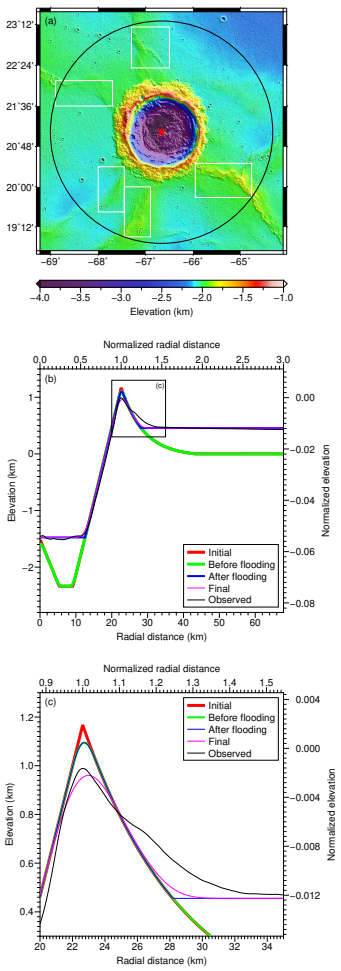

Figure 4.4: Elevation map (a) and radial elevation profiles at different points in time (b and c) for the crater Seleucus (D=45.3 km). In (a), the red star denotes the crater center, the black solid circle shows the boundary within which the azimuthally averaged radial profile was extracted, and the white boxes show the regions excluded from the elevation data. In (b) and (c), the red, green, blue, magenta, and black curves represent the initial crater profile, the profile just before mare flooding, the profile just after mare flooding, the final present day profile, and the observed profile. Panel (c) shows a zoom-in around the crater rim, which corresponds to the black box in (b).

Before presenting the best-fitting results, we first describe the details of a single representative inversion for the crater Seleucus (21.08°N, 66.67°W; D=45.3 km) (Figure 4.4a). This crater has a rim that is completely exposed and is located on the western margin of Oceanus Procellarum, and it was selected because it is one of the most degraded and best-fitting craters in our crater database. Based on the

best-fit model parameters determined by the crater degradation model, the history of Seleucus can be described as follows (Figures 4.4b and c). First, the crater formed on a highland target given that the FeO content of the exposed crater rim and proximal ejecta is about 12 wt.%. The initial crater diameter was 45.2 km with a rim height of 1168 m (red), and given the crater size, it should have formed with a central peak. Between the times of crater formation and mare flooding, the crater rim height degraded by 73 m to 1095 m (green). Then, mare basalts with a thickness of 455 ± 264 m erupted outside the crater rim partially flooding the crater ejecta, and mare basalts erupted inside the crater interior nearly completely burying the central peak. The crater profile then continued to erode to the present state, obtaining a rim height of 960 m with respect to the pre-flooding background. Thus, from crater formation to the present time, the rim was reduced in height by about 208 meters. If rim erosion was not considered, the mare basalt thickness would be estimated to be 663 m, which is considerably larger than when considering crater degradation.

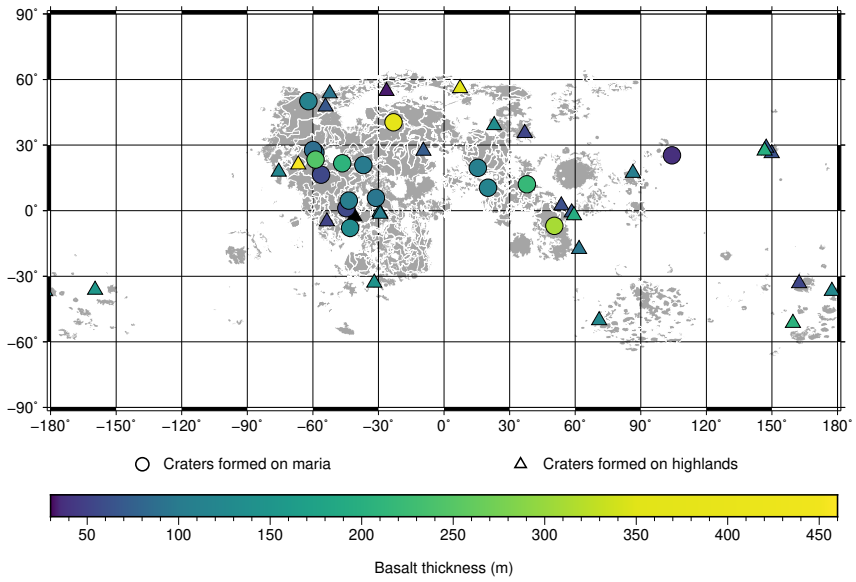

Figure 4.5: Basalt thickness estimates from craters with rims completely exposed on the maria. Craters that formed on maria and highlands are denoted by filled circles and triangles, respectively. The lunar maria basemap (gray) is from Nelson et al. (2014), and the basaltic unit boundaries (white) are from a compilation of previous studies (Hiesinger et al., 2006, 2011; Morota et al., 2009, 2011a; Pasckert et al., 2018).

In this study, basalt thicknesses were estimated around 74 mare craters with

rims completely exposed. Some of these craters either fit the observations poorly, or had large uncertainties. Thus, we first discarded craters that had atypically high misfits (larger than 50 m). We then removed from further consideration craters where the 1-σ lower limit in the basalt thickness was equal to 0.

In the end, we were left with 41 craters that were considered for further analyses, among which 16 formed on mare basement (circles) and 25 formed on highland basement (triangles) (Figure 4.5). The crater diameters vary from 3.7 to 45.3 km, and the obtained basalt thicknesses range from a minimum of 33 m to a maximum of 455 m (Figures 4.6a–c). There is no clear pattern of the derived basalt thicknesses when plotted in map form. This is to be expected because two adjacent partially buried craters could have formed at different times and could have been embayed by different thicknesses of basaltic flows. The crater diameter, longitude, latitude, the best-fitting lava flow thickness and other five model parameters are shown in Table A.2. The uncertainties of the lava flow thickness and the diffusivity-time product after lava flooding are presented in Table A.3. The unit number, age, and area of the basaltic unit that embayed the studied partially buried craters are given in Table A.4.

Figure 4.6c shows that there is a positive correlation between the estimated basalt thickness and crater diameter. This is simply because the crater rim height, which is the maximum thickness that can be retrieved from our method, increases with crater diameter (Pike, 1977). For the studied partially buried craters, the RMS misfits (Figure 4.6d) between the best-fitting and observed profiles are smaller than 50 m, with an average of 17 m. The initial crater diameter is found to be on average 95% of the present-day value. The uncertainty in the basalt thickness is on average 68 m. The thicknesses of basalts in the interiors of 36 craters were also estimated, and these are 1073 m on average (note that the crater floor is much deeper than the pre-flooding background).

If crater degradation was not included, these thicknesses would be considerably larger, ranging from 122 to 613 m. To be comparable with our obtained results, these results are based on the initial rim height-crater diameter ratio derived in this study instead of Pike (1977), and the initial rim height was estimated from the observed, present-day crater diameter. In this case, the median and average basalt thicknesses are 200 and 238 m, in comparison to the values of 105 and 130

m obtained when considering crater degradation. The ∼100 m overestimate in the average basalt thickness when neglecting degradation is therefore about 25–50% of the average value (200–400 m) that was previously estimated by De Hon and Waskom (1976) and De Hon (1979b).

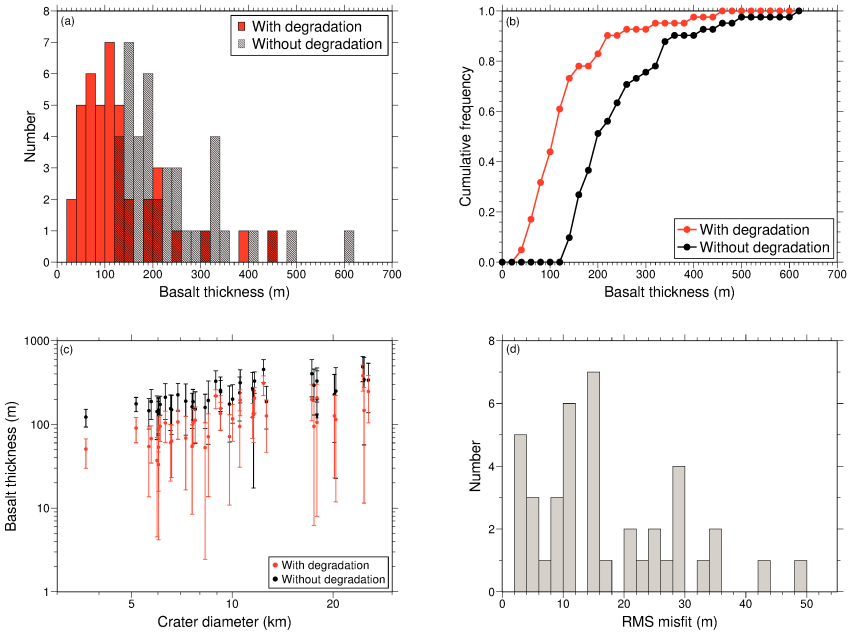

Figure 4.6: Histograms (a) and cumulative distributions (b) of basalt thicknesses with (red) and without (black) considering crater degradation. Basalt thicknesses as a function of crater diameter with (red) and without (black) considering the crater degradation process (c). Histogram of the RMS misfits between the modeled and observed profiles (d). The downward pointing arrow at 17.9 km in (c) indicates that the lower limit is 1 m.

4.3 Discussions

4.3.1 Comparison with Other Techniques

In this section, we compare our estimated mare basalt thicknesses with other techniques, including crater excavation depths, radar sounding observations, lava flow front measurements, and gravity constraints.

In southern Mare Serenitatis, a partially buried crater named Bobillier (19.61°N, 15.44°E; D=6.9 km) was identified (Figure 4.7a). For this crater, the TiO_2 content of the western and southern crater ejecta (> 5 wt.%) is distinctly higher than that of the surface lava flow flooding the distal ejecta (3–4 wt.%) (Figure 4.7b). Our simulation shows that the mare basalt emplaced on Bobillier's ejecta is 107±41 m

in thickness, which we interpret as corresponding to the thickness of the unit S13 (Hiesinger et al., 2011) in this image. Coincidently, in the same basaltic unit S13 five craters (black boxes) were identified by Ishiyama et al. (2013) with different TiO_2 contents (Figure 4.7b) in their ejecta. These craters penetrated through the surface unit and excavated the underlying unit with higher TiO_2 concentrations. The diameters for these craters vary from 2.0 to 3.1 km, so the maximum basalt thickness of the overlying surface unit should be 169 to 263 m based on their crater excavation depths. The existence of small craters (0.8–1.4 km in diameter) that did not excavate the underlying lava flow places a minimum thickness of 71–115 m on the surface unit. Our derived thickness is 107±41 m, which is consistent with the thickness range of 71–209 m given by the nearest crater pair to the partially buried crater (Figure 4.7b). We note that if crater degradation was not considered, the basalt thickness would be 225 m, which is larger than the upper bound of 209 m.

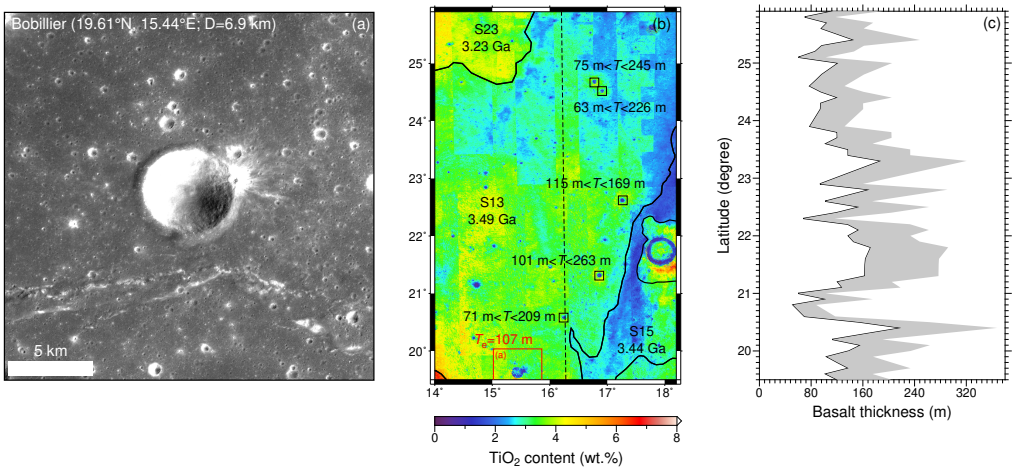

Figure 4.7: SELENE TC optical image (a) and SELENE MI-derived TiO_2 abundance map (b) near crater Bobillier (D=6.9 km). In (b), the basalt thickness estimate surrounding the crater Bobillier is labeled in red, and those based on crater excavation depths are given in black (Ishiyama et al., 2013). Basaltic units are outlined in black and are labeled by the unit names and ages from Hiesinger et al. (2011). The ground track where SELENE LRS data (Data ID: LRS_SAR05KM_C_25N_016214E, LRS_SAR05KM_C_20N_016273E, and LRS_SAR05KM_C_15N_016329E) were obtained is denoted by the north-south dashed line. In (c), the calculated basalt thicknesses from the radar data are presented using a range of porosities from 0 to 45% where 0 porosity is denoted by the leftmost black line.

In the same region of the crater Bobillier, the SELENE Lunar Radar Sounder

also detected subsurface reflectors (Ishiyama et al., 2013), and we reanalyzed the SAR-processed radargram to derive basalt thickness along its track with latitudes from 19.5°N to 26°N (Figure 4.7c). We first resampled the LRS radar data with an interval of 0.1° (3.0 km), and then identified the surface and subsurface echoes. Both the surface and subsurface echoes correspond to strong backscattered radar waves at the respective interface. Subsurface roughness and random scattering from imbedded inclusions may create additional subsurface echoes, but they are expected to be much weaker in amplitude than the echoes from planar interfaces. We identified subsurface echoes in the A-scope radargram of which the peak value is less than 10 dB smaller than the primary, surface peak value (see red and black arrows in Figure 4.8a). If this criterion was not satisfied, the radargram was discarded (see red and black arrows in Figure 4.8b). As a result, subsurface echoes were identified in 54 out of 66 radargrams, and the resulting, continuous subsurface layer is presented in the two-dimensional SAR image (red dashed line in Figure 4.9b, raw data plotted in Figure 4.9a as a comparison).

The apparent depths were converted to true depths by using an estimate of the dielectric permittivity of the unit, which can be derived from the FeO and TiO_2 contents. The FeO and TiO_2 contents were calculated at the locations where the subsurface echoes were identified using the MI data and the algorithm provided in Otake et al. (2012) (Figures 4.10a and b). Next, the grain densities along the sampled locations were estimated based on the calculated FeO and TiO_2 contents (Figure 4.10c) using the relations in Huang and Wieczorek (2012), and the corresponding real parts of the dielectric permittivities were calculated for assumed porosities of 0, 22.5%, and 45% (Figure 4.10d) using the technique described in Fa and Wieczorek (2012). The apparent depths of the subsurface echoes were converted to the actual depths using the above computed dielectric permittivities, and we found that the depth of this reflector to be on average 120 to 161 m below the surface for porosities of 0–45%. Close to the crater Bobillier at (19.61N°, 16.33E°), the thickness given by radar observations is 104 m (porosity=0), which is consistent with our estimate of 107±41 m.

The most direct estimation of the thickness of a lava flow is the measurement of lava flow front heights. On the northeastern floor of the crater Lee M, an unnamed partially buried crater (29.37°S, 39.09°W; D=3.6 km) was identified (Figure 4.11a).

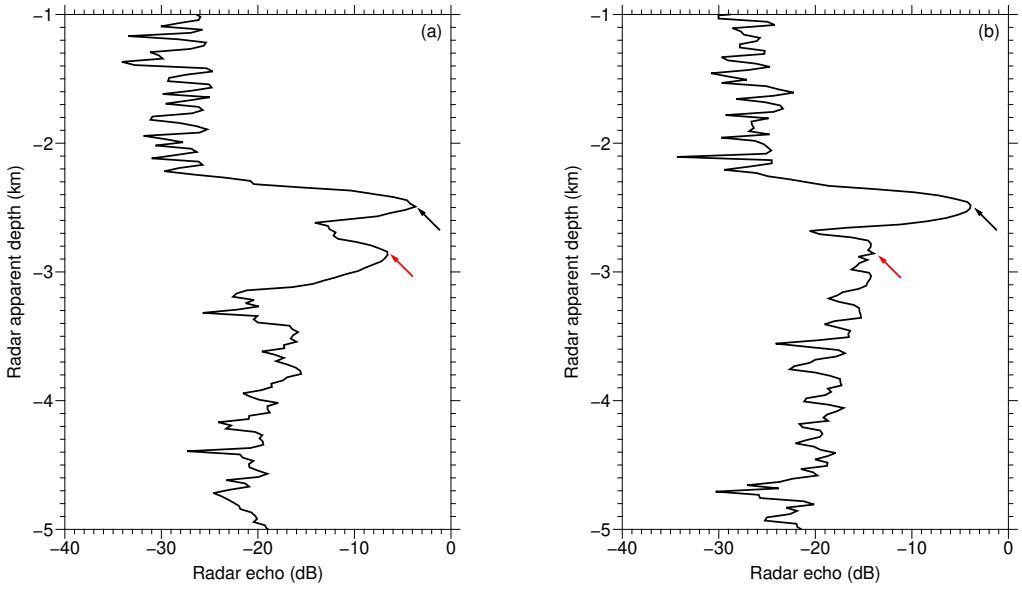

Figure 4.8: Examples of a selected radargram at (21.1°N, 16.3°E) (a) and a discarded radargram at (24.1°N, 16.3°E) (b). The primary (surface echo) and the potential (subsurface echo) secondary peaks are highlighted by black and red arrows, respectively.

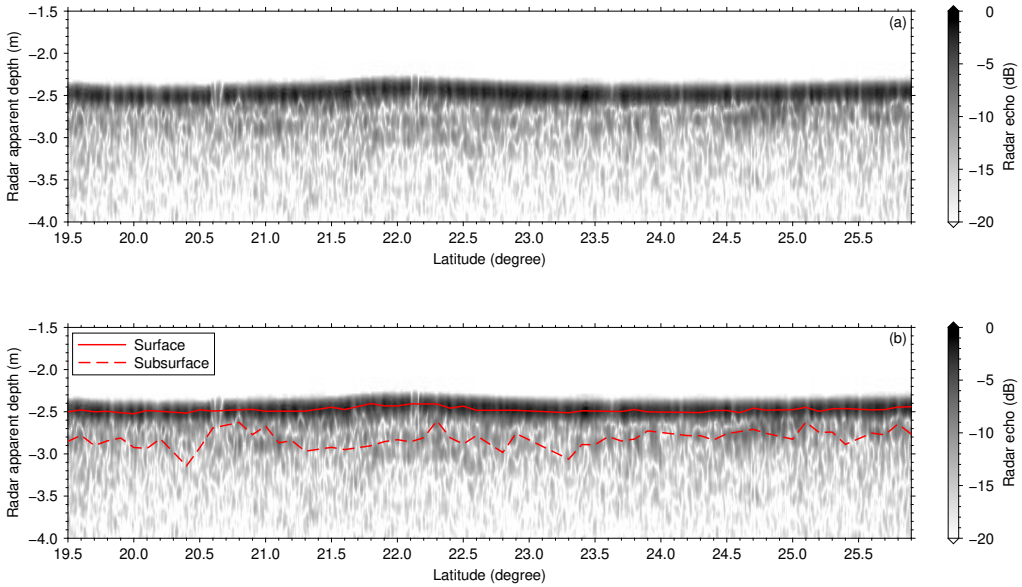

Figure 4.9: LRS raw data (a), and LRS raw data with interpretations of surface (solid red line) and subsurface echoes (dashed red line) (b) in the studied region (19.5°N–25.9°N, 16.3°E).

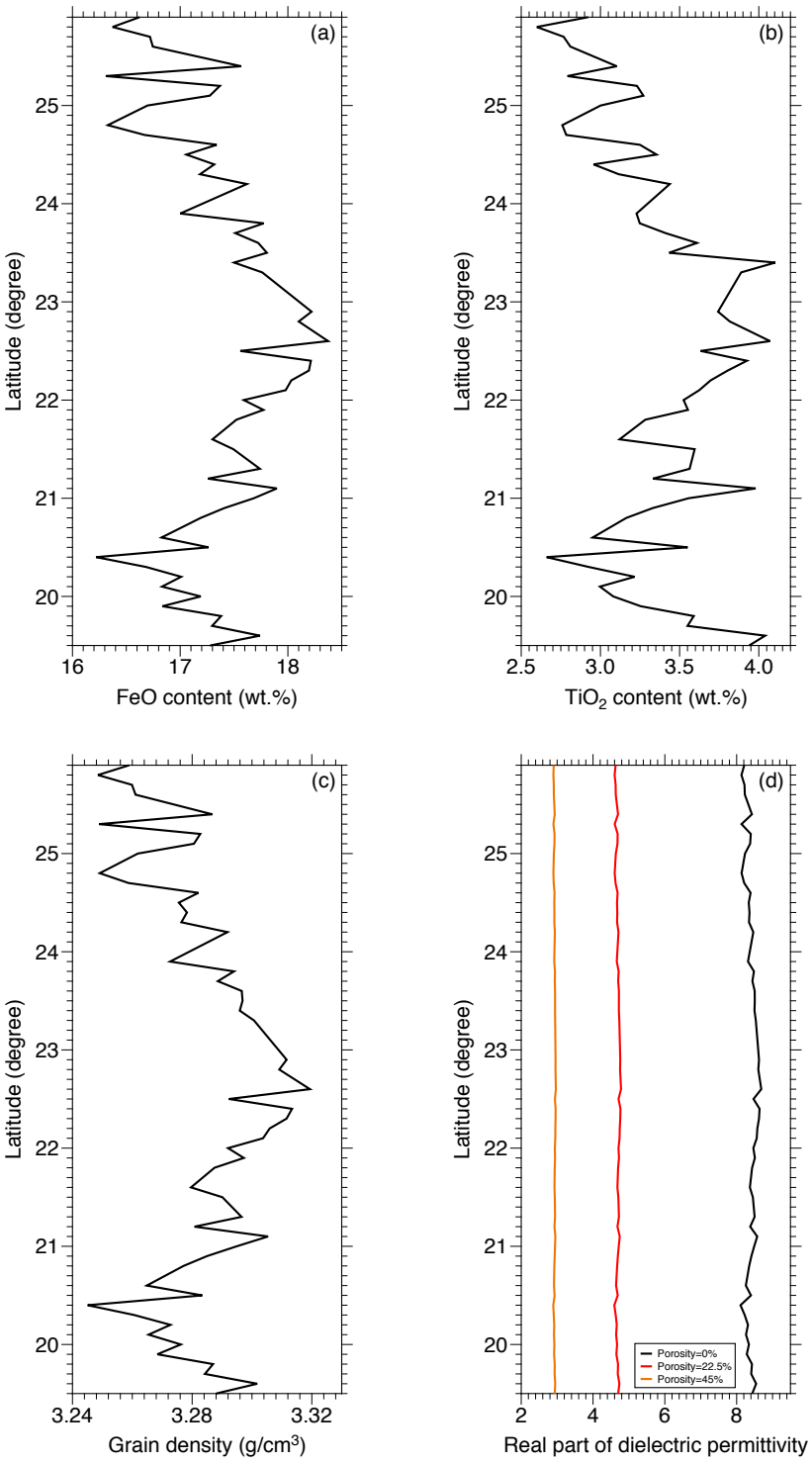

Figure 4.10: Calculated FeO (a) and TiO_2 (b) contents, grain density (c), and real part of the dielectric permittivity (d) along the radar nadir track.

This crater is embayed by a basaltic unit whose origin is to the north-east of the crater. Four radial topographic profiles were extracted, avoiding the topographic high to the southwest of the studied crater (white box in Figure 4.11a). The front heights were measured from the elevation difference between the upper and lower lava flows, providing estimates of the flow front height of 42, 43, 51 and 32 m (Figure 4.11b). Given the standard deviation in elevations of the surrounding plains and the lava flow, these estimates may have an uncertainty of about 8 m. Our estimated basalt thickness from the crater degradation model is 9 m with an upper limit of 29 m. This estimate is somewhat smaller than the lower limit of measured lava flow front heights. However, it should be noted that the about 40% variation of measured flow front heights may imply a natural variability of the basalt thickness in the region of this crater. We also note that if topographic degradation was not taken into account for this highly degraded crater, the basalt thickness would be 77 m, which is more inconsistent with the observations (average=42 m) than ours that takes into account crater degradation.

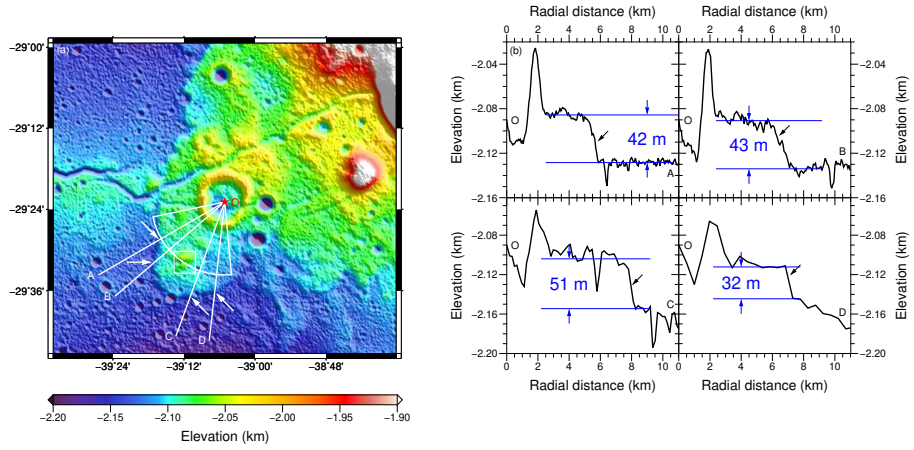

Figure 4.11: Elevation map of an unnamed partially buried crater (D=3.6 km) (a). The red star indicates the crater center, the white fan is the region where the elevation profile was extracted, the white arrows point to the lava flow fronts, and the white lines represent individual profiles OA, OB, OC, and OD. The elevation profiles are plotted in (b), where the black arrows point to the lava flow fronts, and the solid blue lines indicate the elevations above and below the lava flow fronts.

Basalt thicknesses derived from gravity observations are of great interest, because they represent the total thickness of lavas that erupted in the region. These estimates can be compared directly with our study only for craters that formed

initially on a highland target: for these craters, the estimated basalt thicknesses correspond to the total thickness of lava flows in the region. A recent study of the lunar gravity field shows that the total basalt thickness on the western nearside maria (19°S–45°N, 68°W–8°W) is 740 m on average (Gong et al., 2016), with these estimates representing averages within a circle with a diameter of 425 km. As a comparison, our estimated total basalt thickness using only those craters that formed on highland crust (N=25) is only 119 m on average. This discrepancy is largely a result of the fact that the craters that formed on highland basement in our study are mostly found near the mare-highland boundary, where we expect the basalt flows to be thinner than in the interior of the mare.

4.3.2 Cumulative Volume and Eruption Rates of Mare Basalts

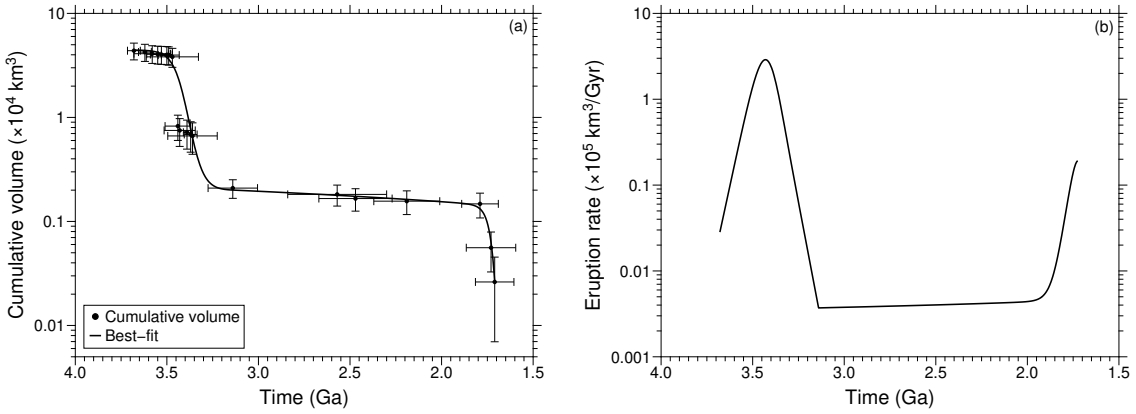

Figure 4.12: Cumulative volume of mare basalts for surfaces with ages less than a given value (a) and eruption rate (b) of the mare basalts as a function of time. In (a), the cumulative volume V_c is fitted using a sigmoid-like function before 3.14 Ga: $\log(V_{c1}) = 1.35/(1+\exp(-190.22\times\log(t_1)+100.63))+3.30$, and a sum of two exponential functions after 3.14 Ga: $\log(V_{c2}) = 3.03\times\exp(0.18\times\log(t_2)) - 2.49\times10^{14}\times\exp(-143.60\times\log(t_2))$, where V_{c1} and V_{c2} are cumulative volume and t_1 and t_2 are time. The uncertainty for the cumulative volume is calculated using the uncertainty of the thickness of basaltic unit, and the uncertainty of the basalt age is taken from a compilation of previous studies (Hiesinger et al., 2006, 2011; Morota et al., 2009, 2011a; Pasckert et al., 2018).

With our estimates for the thickness of basaltic lava flows, it is possible to estimate the volume of the erupted basalts and their long-term eruption rate. Our craters sampled 23 of the basalt units mapped by a compilation of previous studies

(Hiesinger et al., 2006, 2011; Morota et al., 2009, 2011a; Pasckert et al., 2018), for which their surface ages vary from 1.7 to 3.7 Gyr with surface areas ranging from 1,429 to 95,727 km^2. We note that if multiple estimates are obtained in the same unit, we then take their average value. We also assume that the mare basalt thickness is uniform across the entire unit.

The cumulative volume of the sampled lava flows is plotted for all ages less than a given value in Figure 4.12a, showing that there is a total of 4.4×10^4 km^3 of lavas that erupted from 3.7 to 1.7 Ga. The total cumulate volume that erupted on the Moon is of course greater than this, as our study did not sample all lava flow units, and there may be additional flows beneath the surficial flows we investigated. We can correct this effect approximately by using the average total thickness of mare basalts from the subset of mare craters that formed on highland basement (25 triangles in Figure 4.5) and using the known surface area of all basaltic flows. With an average total thickness of 119 m and the total surface area of mare basalts (6.2×10^6 km^2) (Head, 1975), the resulting total volume is 7.4×10^5 km^3. As a comparison, the total basalt volume reported by previous studies varies from 1×10^6 to 1×10^7 km^3 (Budney and Lucey, 1998; Head and Wilson, 1992; Hörz, 1978). The discrepancy in estimates of total basalt volume is again due to the fact that the partially buried craters that formed on the highlands are preferentially located along mare margins where thinner lava flows are expected, whereas other studies used estimates of the basalt thickness in the mare centers that are considerably larger.

The eruption rate of mare basalts on the Moon can be calculated by taking the derivative of the best-fitting cumulative volume (Figure 4.12b). The most prominent feature in this plot is a peak at 3.4 Ga with a value of 2.9×10^5 km^3/Gyr, followed by a rapid decline to 3.7×10^2 km^3/Gyr at 3.1 Ga. The major phase of basalt eruption (3.7–3.1 Ga) in our study is consistent with thermal evolution models that take into account the asymmetric distribution of heat producing elements in the crust (Laneuville et al., 2013), where the main eruptive phase is found to lie between about 3.8 and 3.3 Ga. Then, the volcanic activity became less active until a secondary peak was reached at 1.7 Ga with a value of 1.9×10^4 km^3/Gyr, which corresponds to the several larger, thick basaltic units in the Oceanus Procellarum that we sampled in this study. This may indicate a more recent, episodic eruption, which is also seen in Hiesinger et al. (2011) and Morota et al. (2011a). We interpreted this recent

peak as a result of the high-concentration of the heating producing elements in the subsurface of Oceanus Procellarum, which keeps the region still warm enough to generate melts until 1.7 Ga. Hiesinger et al. (2011) also estimated the eruption rate from the cumulative volume plot of mare basalts, by assuming a constant basalt thickness of 10–100 m and that all the basalts erupted at the age of the uppermost surface unit. Their pattern is similar to ours, which shows that the mare basalt flux was extremely low from 3.7 to 4.0 Ga, reached a peak at 3.5 Ga with a value of 5.0×10^4–4.3×10^5 km^3/Gyr, and then gradually decreased with time but slightly peaked at 2.1 Ga with a value of 2.5×10^4–1.0×10^5 km^3/Gyr.

Above, we calculated the average eruption rate of lavas on the Moon over geologic time, by averaging over many units of different ages and areas. The rate at which lava is extruded to the surface during an individual eruptive event is thus not important for our analysis, as it is expected to occur over a period of time that is extremely short in comparison to the duration of mare volcanism. Regardless, some studies have attempted to estimate the eruption rates for individual eruptive events by dividing the volume of the basalt layer by the age difference between overlying and underlying layers. Weider et al. (2010) shows that the mare basalts have the largest eruption rate at 3.5 Ga with a value of 2×10^5 km^3/Gyr. Then, the eruption rate dramatically dropped to 3.7×10^4 km^3/Gyr at 3.4 Ga and finally reached to 1×10^4 km^3/Gyr. Oshigami et al. (2014) shows that the eruption rate peaked at 3.4–3.5 Ga with a maximum value of 1×10^6 km^3/Gyr. Then, the eruption rate decreased to 1×10^5 km^3/Gyr after 3.3 Ga, and in general remained little variation from 1×10^5 km^3/Gyr to 2×10^5 km^4/Gyr until 2.7 Ga. Their derived eruption rates should not be compared to the results in this study, as the two eruption rates correspond to two distinctly different geologic processes (i.e., how long it takes lava for a single event to reach the surface, vs. how much lava is being eruptive over the entire lunar surface as a function of time). Even for the latter method, we noticed that the resulting eruption rates are still much smaller than the instantaneous eruption rate. This is because the time scale between two eruptions derived from crater counting is usually on the order of several hundred million years, which is much, much longer than the duration of a single eruption. Nevertheless, we noticed that if the eruption rate is constrained a priori (e.g., from studies of volcanology on Earth) and the volume of the lava flow can be obtained from this study, it would be possible to calculate the

instantaneous temporal duration of a single eruption on a planetary surface.

4.3.3 Scale and Temporal Dependence of Crater Degradation

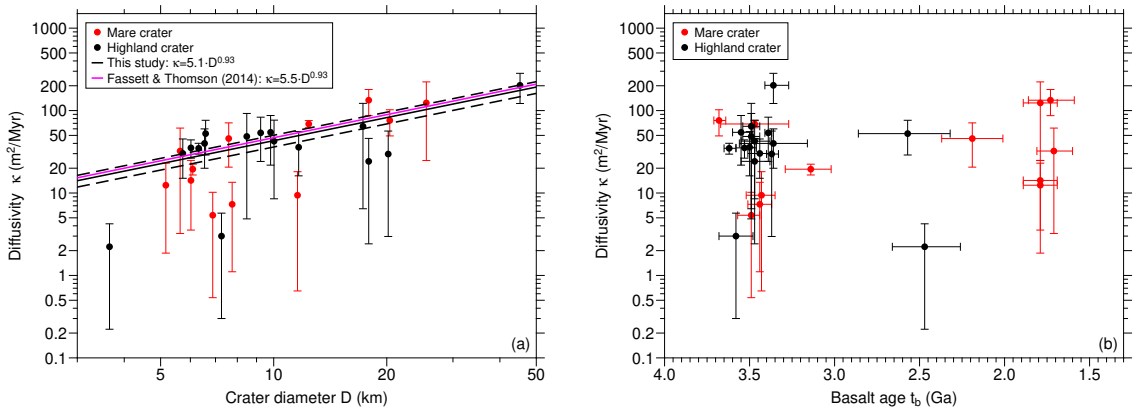

Figure 4.13: Diffusivity as a function of crater diameter (a) and basalt age (b). Craters that formed on mare and highland basements are shown in red and black, respectively. In (a), the solid and dashed black lines are the best-fit ($\kappa = 5.1 \times D^{0.93}$) and one standard deviation uncertainty respectively, and the magenta line is the best-fit inferred from Fassett and Thomson (2014). In (b), the basalt ages and their error bars were taken from a compilation of previous studies (Hiesinger et al., 2006, 2011; Morota et al., 2009, 2011a; Pasckert et al., 2018).

One of the outputs of our model is the product of diffusivity and time, both before the mare basalts erupted and embayed the crater and afterwards. The ages of the basaltic surface units can be estimated using the crater chronology technique (Hiesinger et al., 2011; Morota et al., 2011a), and using the ages of these flows, we can estimate the average diffusivity between the present day and when the lavas erupted. If we further assume that the diffusivity was the same before the crater was flooded, we can even estimate the age when the crater formed. In this section, we investigate the topographic diffusivity by examining its dependence on crater size, time, and target type (mare and highland).

The diameter-dependence of topographic diffusivity has a strong theoretical basis (Howard, 2007; Minton et al., 2019; Soderblom, 1970; Xie et al., 2017). Soderblom (1970) was the first to investigate the crater degradation process by modeling the downslope movement of crater ejecta due to micrometeoroid bombardment. This approach used the assumption of mass conservation, where the net mass of ejecta

materials moving into (out of) a volumetric unit must be equal to that accumulated (lost) in this unit per unit area and time. In this model, the topographic diffusivity is expressed as

$$\kappa = \frac{CAD_{\max}^{4-\lambda}}{4-\lambda} \tag{4.1}$$

where C is a constant related to the mass of the ejecta excavated by micrometeorite bombardment, A and λ are coefficients of the size-frequency distribution of the small craters that formed on the ejecta of parent crater ($N{=}AD^{-\lambda}$) where D is the diameter of the small craters (Shoemaker, 1965), and $D_{\max}$ is the maximum diameter of the small craters that diffusively erode the parent crater.

In this model, the maximum size of the crater diffusively eroding the host crater might be expected to scale with the host crater size. Previous studies proposed that a cutoff of 10% of the parent crater diameter would be an appropriate upper limit for the craters that erode the parent crater in a diffusive "sand-blasting" way (Minton and Fassett, 2016). The power-law coefficient λ is expected to be close to 3 (Shoemaker, 1965), implying that $\kappa{=}\kappa_0 D$, where D is the diameter of the parent crater with $D{=}10{\times}D_{\max}$ and κ_0 is a reference diffusivity at a diameter of 1 km (Xie et al., 2017). Though approximate, diffusivity might be expected to increase linearly with crater diameter.

Variations in the impact flux could also result in variations in the topographic diffusivity, primarily by changes in the parameter A. During the past 3 Gyr, the lunar impact flux is believed to have been relatively constant (Le Feuvre and Wieczorek, 2011; Neukum et al., 2001a; Shoemaker, 1965). However, the flux is known to increase at earlier times, with the flux at 3.9 Ga being about 500 times the flux at 3 Ga (Neukum et al., 2001a). Furthermore, the recent lunar impact flux could be modulated by the formation of asteroid families in the inner main belt such as the Flora and Baptistina asteroid families, which may have formed at 100s Ma and around 160 Ma respectively (Bottke et al., 2008; Nesvorný et al., 2002).

We examine the dependence of topographic diffusivity on crater diameter in Figure 4.13a. Though there is much scatter, the topographic diffusivity increases approximately linearly with crater diameter, as predicted by Equation 4.1 and Xie et al. (2017). Fitting these data to a power law of the form $\kappa = \kappa_0 D^{\beta}$ provides a reference diffusivity of 5.1±0.8 m^2/Myr with an exponent of 0.93 that is suggested by Xie et al. (2017). Fassett and Thomson (2014) investigated 13,657 small ($0.8 \leqslant$

$D \leqslant 5$ km), unburied craters on lunar maria and determined κ_0 to be 5.5 m^2/Myr, which is close to our value. The diameter dependence of topographic diffusivity has also been strongly supported by the study of mare crater degradation ($0.8 \leqslant D \leqslant 5$ km) where larger craters were found to have larger topographic diffusivities (Fassett et al., 2018), and the modeling of topographic degradation of craters ($D \leqslant 100$ m) at the Apollo 15 landing site where smaller craters were thought to have smaller topographic diffusivities (Minton et al., 2019). The partially buried craters used in this study cover a larger diameter range ($3.7 \leqslant D \leqslant 45.3$ km), which strongly supports the diameter dependence of the diffusivity that both we and they found.

The topographic diffusivity as a function of the basalt age is plotted in Figure 4.13b to investigate how diffusivity depends on the impact flux. As can be seen, there is no significant correlation between the topographic diffusivity and the basalt age before and after 3 Ga. From a statistical point of view, the mean topographic diffusivities before and after 3 Ga are 52.1±50.3 and 44.3±42.7 m^2/Myr, respectively, implying that the older and younger topographic diffusivities are almost indistinguishable. We further performed a Kolmogorov-Smirnov test on these two groups of topographic diffusivities, which can help to examine if they are sampled from the same population or not (Massey Jr, 1951). A null hypothesis indicates that the two distributions are drawn from the same population, and the P-value significance level is commonly set to be 0.05 (Robbins et al., 2014). The calculated P-value of 0.96 is much larger than this significance level, which means the null hypothesis can not be rejected. In other words, there is no evidence for temporal variations in the topographic diffusivity in our dataset. Fassett and Thomson (2014) suggested that the topographic diffusivity before 3 Ga was higher than that after 3 Ga. However, it should be noted that the diameter range of craters investigated in Fassett and Thomson (2014) varies by a factor of six, and the largest craters are found to be greater in age and have larger diffusivities. Therefore, the increasing topographic diffusivity before 3 Ga found in Fassett and Thomson (2014) could be biased by the inclusion of the largest and oldest craters in their study, which are expected to have the highest diffusivities.

It is difficult to constrain the effect of target properties on diffusivity as Equation 4.1 has no dependence on target properties. Nevertheless, we might expect highland terrain to be more fractured than the mare (Hartmann, 1973; Kreslavsky

and Head, 2016), and that this would increase the rate of impact crater degradation in the highlands. We investigated whether the diffusivity is different for craters that formed on mare and highland targets. The topographic diffusivities for mare and highland craters were fitted using a power-law function with the same exponent of 0.93, and we found that the reference diffusivities (5.5±1.6 m^2/Myr vs. 4.8±1.0 m^2/Myr) were almost the same. This suggests that highland and mare craters should degrade at a similar rate.

Chapter 5 Lava Flow Thickness on Mercury

5.1 Database and Classification of Buried Craters

We constructed a database of buried impact craters on Mercury (Table 5.1), making use of the MESSENGER/MDIS basemap and the ArcGIS platform with the Crater Helper Tools toolkit (Nava, 2011). In this study, we have identified 1022 partially and completely buried craters in total. Unlike their counterparts on the Moon with only 38 completely buried craters out of a total of 661, we found 765 completely buried craters on Mercury. The diameter, longitude, latitude, classification, and percentage of the rim that is buried are given in Table B.1 in the Appendix.

We divided the identified buried craters into three classes based on the observed morphology of the crater rim: completely exposed, partially exposed, and completely buried. Craters with rims completely or partially exposed can be classified into two subclasses based on their locations. If the entire exposed ejecta are surrounded by lava flows, then the crater is classified as being located in the smooth plains, whereas if part of the exposed ejecta are contiguous with the surrounding heavily cratered terrain, then the crater is classified as being located on the smooth plains-heavily cratered terrain boundary. We note that craters located in the smooth plains could have formed on the heavily cratered terrain and later were flooded by lavas, such that the exposed crater rim and ejecta have a composition of heavily cratered terrain.

In an idealized case, a crater would form on a perfectly flat surface, the rim crest height would be the same everywhere, and any lavas that flooded the region would be uniform in thickness. There are several factors that complicate such an idealized scenario. First, the impact crater could form on a sloping surface and the lavas would only embay that portion of the crater at the lowest elevations. This is likely what occurred for partially buried craters that form along the smooth plains-heavily cratered terrain boundaries. In these cases (Figure 5.1a), the crater rim and ejecta can be divided into heavily cratered terrain and smooth plains parts: the crater

Table 5.1: Classification of buried impact craters on Mercury (N=1022).

Class	Location	Description	Number
Rim completely exposed	Smooth plains	Rim and proximal ejecta completely exposed, distal ejecta buried	7
	Smooth plains-heavily cratered terrain boundary	Smooth plains side: rim and proximal ejecta completely exposed, distal ejecta buried; Heavily cratered terrain side: rim and ejecta completely exposed	52
Rim partially exposed	Smooth plains	Rim and proximal ejecta partially exposed, distal ejecta buried	90
	Smooth plains-heavily cratered terrain boundary	Smooth plains side: rim and proximal ejecta partially exposed, distal ejecta buried; Heavily cratered terrain side: rim and ejecta completely exposed	108
Rim completely buried	Smooth plains	Rim and ejecta completely buried, characterized by a wrinkle ridge	765

ejecta of the heavily cratered terrain part are not buried by lava flows, whereas the crater ejecta of the smooth plains part are. Though these craters are included in our database, they will not be analyzed later as a result of this complication.

In a more complex scenario, a part of the crater rim could be breached by the exterior lavas in several places, leaving a crater rim that is discontinuous (Figures 5.1b and c). The formation of such a partially buried crater could arise as a result of several asymmetric processes. The crater rim height is not everywhere constant, either as a result of the initial formation processes, or by later erosional processes (such as small craters that formed on the rim). Alternatively, the lava flow thickness might not be uniform everywhere, with the thicknesses being higher on the side of the crater rim that was breached.

To extend our database, we also searched for craters that are completely buried by lava flows. This type of crater is usually characterized by a concentric wrinkle ridge over the crater rim (Figure 5.1d). The lava flow thickness around a completely buried crater is difficult to estimate. On the one hand, the lava flow thickness needs to be greater than the crater rim height. On the other hand, this crater rim height could have been degraded between the times of crater formation and lava infill. Therefore, although we include these entirely buried craters in our database, we will not use them later when estimating lava flow thicknesses. We note that completely buried craters can also sometimes be identified in the Bouguer gravity anomaly maps (Deng et al., 2018).

We noted that for some craters the circular topographic high along the crater rim could be either the actual crater rim or a wrinkle ridge. For several cases it was difficult to discriminate between the two as the spatial resolution of optical images on Mercury is poor. Nevertheless, we found that both sides of the crater rim are more or less symmetric, whereas the wrinkle ridge usually formed due to a compressional force and hence one of the sides is usually tilted and hence both sides are asymmetric (Plescia and Golombek, 1986).

5.1.1 Case Studies of Buried Craters

In Chapter 2, we have shown an example of craters with rims completely exposed on the smooth plains. In addition to this type of crater, the characteristics of the other four types of buried craters are presented here, including craters with

rims completely exposed on the smooth plains-heavily cratered terrain boundaries, craters with rims partially exposed on the smooth plains, craters with rims partially exposed on the smooth plains-heavily cratered terrain boundaries, and craters with rims completely buried on the smooth plains. For each type, a representative crater is chosen and discussed as a case study. We note that although the smooth plains boundaries have been released (Denevi et al., 2013), it is still a bit challenging to distinguish between the smooth plains and the heavily cratered terrain. This is because the surface of Mercury lacks a significant albedo contrast between smooth plains (0.08-0.12) and heavily cratered terrain (0.11–0.19), comparing with lunar maria (0.1) and highlands (0.17) (Ernst et al., 2010; Murray et al., 1974).

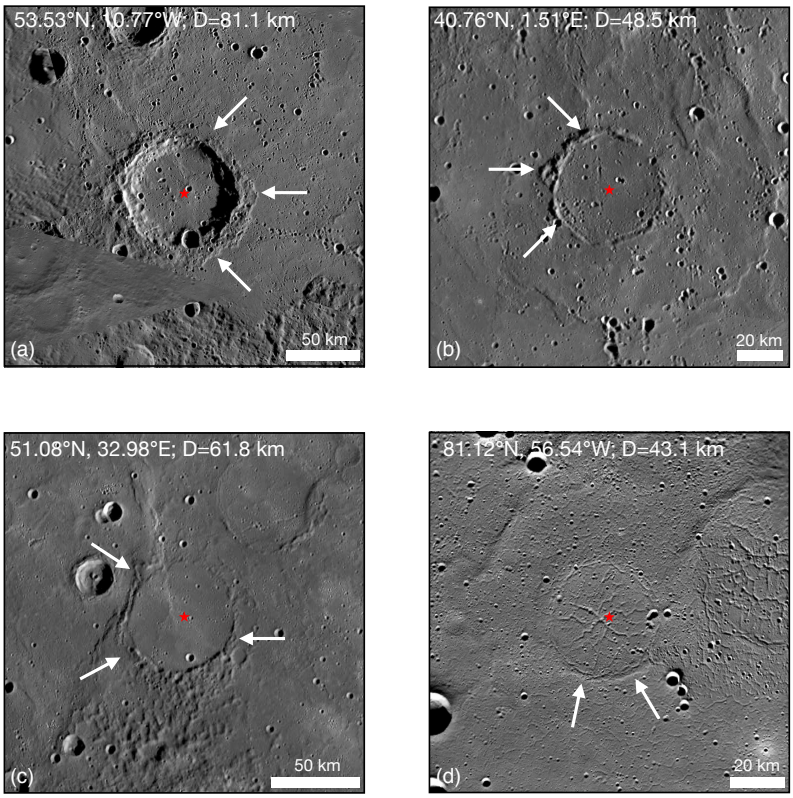

Figure 5.1: MDIS images of four types of buried craters: rim completely exposed on the smooth plains-heavily cratered terrain boundary (D=81.1 km) (a), rim partially exposed on the smooth plains (D=48.5 km) (b), rim partially exposed on the smooth plains-heavily cratered terrain boundary (D=61.8 km) (c), and rim completely buried on the smooth plains (D=43.1 km) (d). The red stars give the locations for the crater centers. The white arrows point to the boundaries of the exposed crater ejecta in (a–c) and the buried crater rim in (d).

For the class of craters with rims completely exposed on the smooth plains-heavily cratered terrain boundaries, the crater rim can be divided into smooth plains and heavily cratered terrain parts. In Figure 5.1a, we show an 81-km-diameter crater located at (53.53°N, 10.77°W). Most of the crater rim is buried by lava flows and only the southwestern crater ejecta are unburied and connected with the heavily cratered terrain. In the optical image, the exposed crater rim can be seen as high-reflectance materials compared with the surrounding dark lava flow. The ejecta boundary is identified as an abrupt contrast in reflectance between brighter crater ejecta and darker smooth plains basalts (white arrows), and the exposed ejecta width is estimated to be one-third of the crater radius. On the other hand, the reflectance of the exposed crater ejecta on the southwest is similar to that of the surrounding heavily cratered terrain region, and no clear boundary between crater ejecta and background terrain is found.

For the class of craters with rims partially exposed on the smooth plains, the crater rim can be divided into exposed and buried parts. For the selected crater (40.76°N, 1.51°E; D=48.5 km), the northern and western crater rims are exposed whereas the southern and eastern crater rims are buried by lava flows (Figure 5.1b). What is interesting is that discontinuous wrinkle ridges are found to form on the southern and eastern crater rims. In the optical image, the exposed crater rims are discernible as high-reflectance materials compared with the surrounding, dark lava flows. The ejecta boundary is seen as a distinct contrast in reflectance between brighter crater ejecta and darker smooth plains on the north and west (white arrows), and the exposed ejecta width is estimated to be only one-sixth of the crater radius. There are no reflectance variations between the buried crater rim regions and the surrounding lava flows on the south and east.

For the class of craters with rims partially exposed on the smooth plains-heavily cratered terrain boundaries, the crater rim can be divided into three parts: an exposed part on the smooth plains, a buried part on the smooth plains, and an exposed part on the heavily cratered terrain. For the selected crater (51.08°N, 32.98°E; D=61.8 km) the southern crater rim is contiguous with the heavily cratered terrain, the northern crater rim is buried by lava flows, and the rest of the crater rim is exposed (Figure 5.1c). Again, we notice that wrinkle ridges have formed over the western exposed crater rim. In the optical image, the exposed crater rim on

the smooth plains side can be seen as high-reflectance materials compared with the surrounding, dark lava flows to the east and west. The exposed ejecta boundary is identified as an abrupt contrast in reflectance between the brighter crater ejecta and the darker lava flows (white arrows), and the exposed ejecta width is estimated to be only ∼15% of the crater radius. For the buried crater rim on the north, there are no reflectance variations between this region and the surrounding lava flows. For the exposed crater rim and ejecta on the south, they have a similar reflectance with the surrounding heavily cratered terrain region, and no clear boundary between crater ejecta and background terrain is found due to the rugged topographic relief there.

For the class of craters with rims completely buried on the smooth plains, the entire crater rim should be mantled by the lava flow but a wrinkle ridge over the crater rim can be still discernible. For the selected crater (81.12°N, 56.54°W; D=43.1 km) that is located in the Goethe basin, a circular wrinkle ridge can be seen clearly that formed over the buried crater rim (Figure 5.1d). We also noted that radial grabens have formed within this completely buried crater, suggesting the tectonic activities were once active in this region.

5.1.2 Spatial Distribution and Statistics of Buried Craters

The most prominent feature seen in the spatial distribution of partially buried craters is their preferential occurrence along the smooth plains-heavily cratered terrain boundaries (Figure 5.2). This distribution pattern is to be expected, since the lava flows at the edge of the smooth plains are expected to be thinner than elsewhere. Though the thicker flows in the smooth plains centers can entirely flood craters of a given size, the thinner flows at the margins can only partially flood the crater. Unlike the Moon, the completely buried craters are abundant and are distributed all over the entire smooth plains of Mercury. We interpreted this as a result of a higher abundance of wrinkle ridges that formed on top of the buried rims, which makes it easier to identify the completely buried craters. In particular, the global contraction on Mercury is more significant than the Moon, which gives rise to higher stresses in the crust which favor the formation of wrinkle ridges. We also found some isolated regions with sparsely distributed buried craters, either as a result of burial by subsequent basin/crater ejecta or due to the poor illumination conditions that inhibit the identification of craters. For buried craters of different

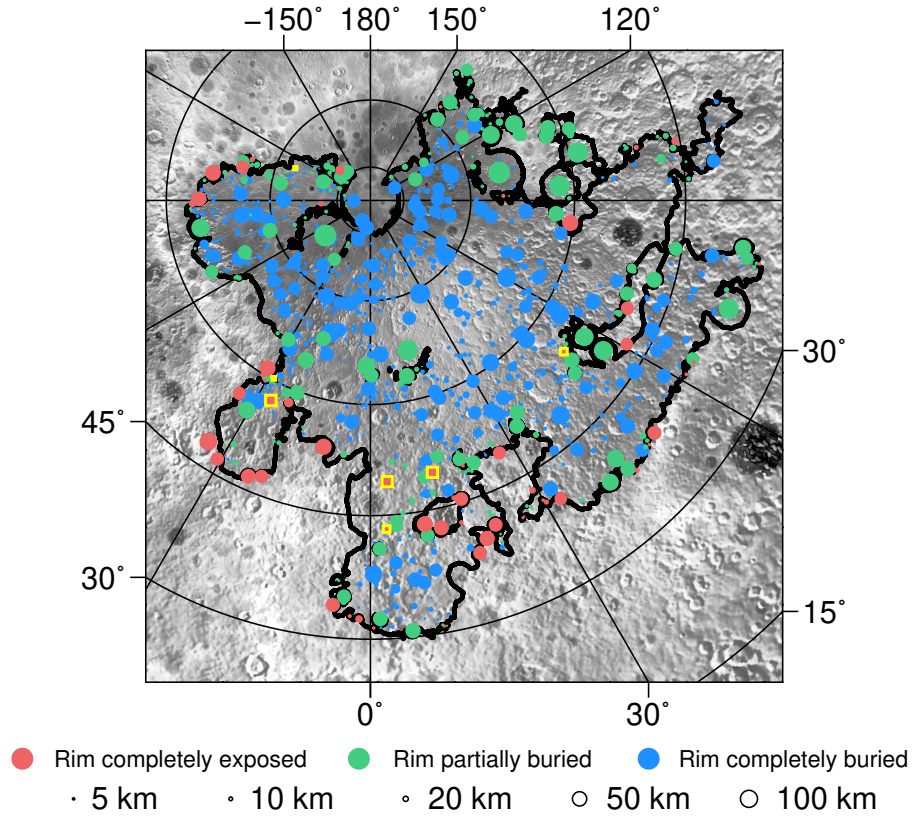

Figure 5.2: Distribution of buried craters with completely exposed rims (light red, N=59), partially exposed rims (green, N=198), and completely buried rims (blue, N=765). The smooth plains boundary (black) is from Denevi et al. (2013), and the base map is the MDIS-derived DEM. The size of the circles is proportional to the crater diameter. Seven craters with completely exposed rims in the smooth plains are bounded by the yellow squares.

sizes, we did not find any obvious pattern.

Histograms of the different classes of buried craters as a function of crater diameter are shown in Figure 5.3a. The diameters of all the partially and completely buried craters range from 2.6 to 323 km, of which craters with rims completely exposed in the smooth plains ($N = 7$) range from 15.2 to 56.1 km. In general, the peak in the histogram is skewed towards smaller craters. This is in part because there are in general more smaller than larger craters, but also because the older and larger craters that formed before the main phase of volcanism in the smooth plains have already been completely buried (Deng et al., 2018). Analyzing the craters by class, the median crater diameter is found to increase from craters with rims completely buried (11.4 km), to those with rims partially exposed (20.9 km),

and to those with rims completely exposed (30.6 km). This observation is easy to explain: for a given lava flow thickness, smaller craters with lower rim heights are easier to completely bury than larger craters with greater rim heights. In terms of location, the median diameter of partially and completely buried craters on smooth plains (11.8 km) is smaller than that along smooth plains-heavily cratered terrain boundaries (24.8 km). We interpret this observation as being a result of the lava flows being thicker in the center of the smooth plains than those along their edges, therefore older, larger craters inside the smooth plains are completely buried (Deng et al., 2018). Comparing with the buried craters on the Moon, we found that the statistics shown here are usually larger. This is because we were biased by not identifying smaller buried craters on Mercury due to a poor spatial resolution and illumination condition (high-latitude on Mercury) of the MDIS images.

For all of the partially buried craters in our database, we have estimated the percentage of the crater rim crest circumference that was buried by lava flows (Figure 5.3b). The median percentage of rim burial of smooth plains craters (40%) is larger than that of smooth plains-heavily cratered terrain boundary craters (9%). This is simply because the crater rim is never buried on the heavily cratered terrain side of the smooth plains-heavily cratered terrain boundary.

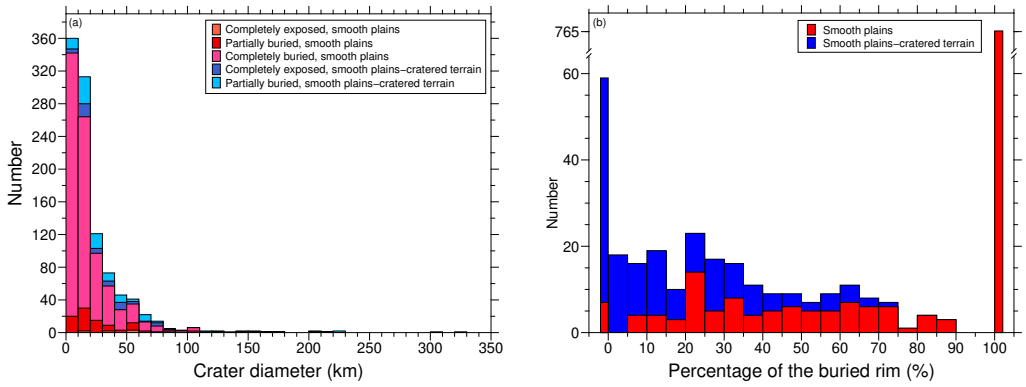

Figure 5.3: Size-frequency distributions of the different classes of buried craters (left) and percentage of the rim buried by lava flows for craters that formed in the smooth plains and along the smooth plains-heavily cratered terrain boundary (right). In (b), the scale of the vertical axis is discontinuous, and the total numbers of craters with rims completely exposed or completely buried are plotted in the leftmost and rightmost bins, respectively.

Because most of the completely buried craters within the northern smooth plains are discernible due to the wrinkle ridges over their crater rims, we expect to

see that the total population of partially buried craters, completely buried craters, and newly formed craters within the northern smooth plains should be similar to that of all the craters in the surrounding heavily cratered terrain. Due to the limitations of the image quality and spatial resolution, here we used $N(20)$ (the total number of craters larger than 20 km in diameter per km^2) to denote the spatial density of craters. For the crater databases, we made use of Herrick et al. (2018) for craters that formed on top of the northern smooth plains, Ostrach et al. (2015) for craters in the surrounding heavily cratered terrain, and our identified partially and completely buried craters within the northern smooth plains.

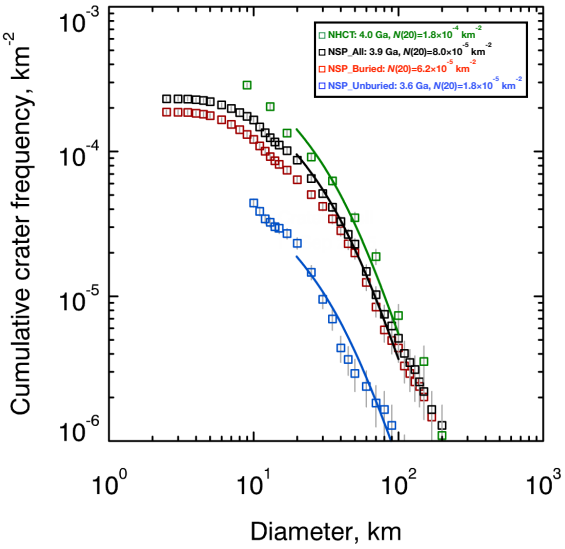

Figure 5.4: The cumulative crater-size frequency distributions in the northern smooth plains (NSP) and heavily cratered terrain (HCT). The red squares denote the buried craters in the northern smooth plains identified in this study, the blue squares correspond to the craters that formed on top of the northern smooth plains, and the black squares represent the sum of the two. The green squares refer to craters in the heavily cratered terrain. Solid lines are the best-fitting size-frequency distributions generated by Craterstats II (Michael, 2014) using the production and chronology functions from Neukum et al. (2001b). The database of newly formed craters on the northern smooth plains is taken from Herrick et al. (2018), and that of craters in the heavily cratered terrain is given by Ostrach et al. (2015). The $N(20)$ value is provided in the plot legend.

The cumulative size-frequency distributions for these types of craters are shown in Figure 5.4. The results show that, the $N(20)$ of buried craters in the northern smooth plains is 6.2×10^{-5} km^{-2}, the $N(20)$ of unburied, younger craters in the northern smooth plains is 1.8×10^{-5} km^{-2}, and the sum of the two is 8.0×10^{-5} km^{-2}.

This is smaller than the $N(20)$ of the surrounding heavily cratered terrain of 1.4×10^{-4} km^{-2}. Using chronology functions in Neukum et al. (2001b), the age of the northern smooth plains is estimated to be 3.6 Gyr, the age of the heavily cratered terrain underlying the northern smooth plains is calculated to be 3.9 Gyr, and the age of the heavily cratered terrain surrounding the northern smooth plains is derived to be 4.0 Gyr. These results suggest that we might have underestimated the crater density by neglecting some of the deeply seated, completely buried craters in the region, which can be complemented by using gravity anomaly maps (Deng et al., 2018).

Note that a similar research can be carried out for lunar mare and highland craters. However, unlike those on the northern smooth plains on Mercury, most of the small completely buried craters on the lunar maria do not have a wrinkle ridge and thus are not traceable any more. Therefore, population of the large completely buried craters identified in the Bouguer gravity anomaly maps on the lunar maria should be used to compare with that of the large highland craters (Neumann et al., 2015).

5.2 Lava Flow Thickness Estimation Results

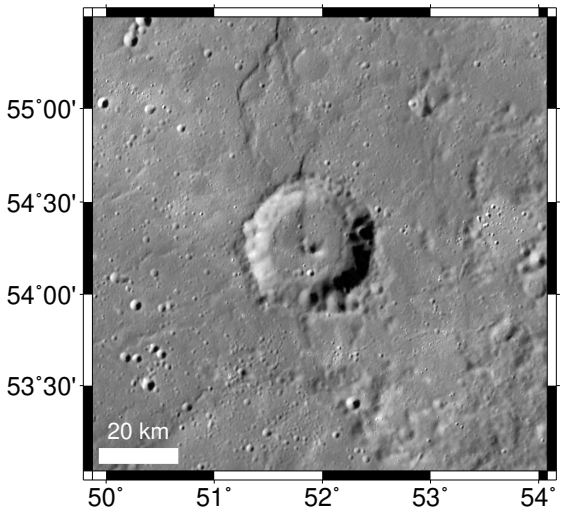

Figure 5.5: The MDIS image of the partially buried crater (D=29.6 km) that is used in the case study. This is a crater with its rim completely exposed.

Before presenting the best-fitting results, we first describe the details of a single representative inversion for a selected crater (54.26°N, 51.98°E; D=29.6 km) (Fig-

ure 5.5). This crater has a rim that is completely exposed and is located on the southwestern margin of the northern smooth plains. It was selected because it is one of the most degraded and best-fitting craters in our crater database. Based on the best-fit model parameters determined by the crater degradation model, the history of this crater can be described as follows (Figures 5.6a and b).

First, the crater formed on the heavily cratered terrain given its vicinity of the heavily cratered terrain. The initial crater diameter was 29.4 km with a rim height of 630 m (red), and given the crater size, it should have formed with a central peak. Between the times of crater formation and lava flow flooding, the crater rim height degraded by 33 m to a total height of 597 m (green). Then, lava flows with a thickness of 250 ± 93 m erupted outside the crater rim partially flooding the crater ejecta, and lava flows erupted inside the crater interior completely burying the central peak. Note that although a central peak is still visible in the optical image (see Figure 5.5), which means our central peak height-crater diameter relation may not be applied to this specific crater, the existence of such a structure should not have any significant effects on the exterior lava flow thickness estimation. The crater profile then continued to erode to the present state, obtaining a rim height of 580 m with respect to the pre-flooding background. Thus, from crater formation to the present time, the rim was reduced in height by about 50 meters. If rim erosion was not considered, the lava flow thickness would be estimated to be 300 m, which is 20% larger than when considering crater degradation.

For lava flow thickness estimation on the Moon, we only worked on craters with completely exposed rims in the maria. Within the northern smooth plains of Mercury, however, there are only seven craters of this type. In order to include more crater samples for inversion, in this study we started with craters with fully exposed rims both within the smooth plains and along their edges. We then discarded craters that formed on basin/crater rims and wrinkles ridges. Next, we further deleted craters without any elevation measurements within half of the crater radius. Next, we hope to use craters with an axis-symmetrical topography, which means the rim crest elevation should have a small variation. Therefore, those with rim crest elevation variability (i.e., the standard deviation of the rim crest elevation) larger than the rim height were removed. After inversion, some of these craters either fit the observations poorly, or had large uncertainties. Thus, we discarded craters

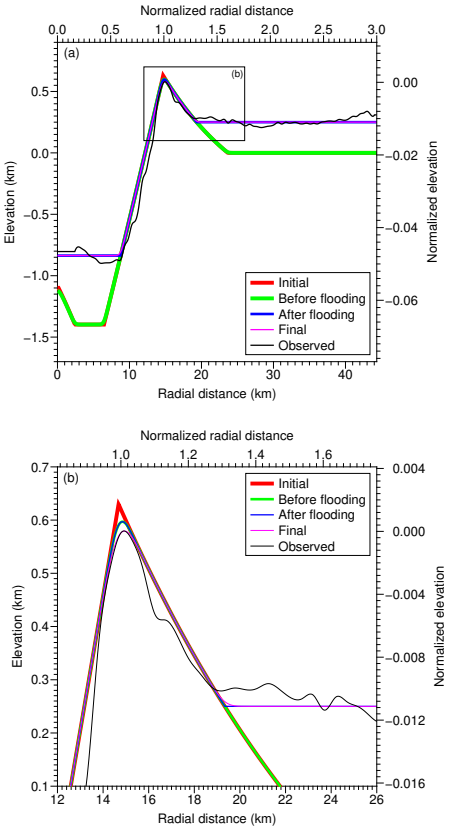

Figure 5.6: Radial elevation profiles at different points in time for the studied partially buried crater (D=29.6 km). The red, green, blue, magenta, and black curves represent the initial crater profile, the profile just before lava flooding, the profile just after lava flooding, the final present-day profile, and the observed profile. Panel (b) shows a zoom-in around the crater rim, which corresponds to the black box in (a).

that had atypically high misfits (larger than 100 m). We then removed from further consideration craters where the lower limit in the lava flow thickness was equal to 0.

In the end, we were left with 21 craters that were considered for further analyses (Figure 5.7). The crater diameters vary from 11.4 to 83.4 km, and the obtained lava flow thicknesses range from a minimum of 23 m to a maximum of 536 m (Figures 5.8a–c). All these craters are located along the margin of the northern smooth plains, and there is no clear pattern of the derived lava flow thicknesses in their spatial distribution. The crater diameter, longitude, latitude, the best-fitting lava flow thickness and other five model parameters are shown in Table B.2. The uncertainties of the lava flow thickness and the diffusivity-time product after lava flooding are presented in Table B.3.

Figure 5.8c shows that there is a weak positive correlation between the esti-

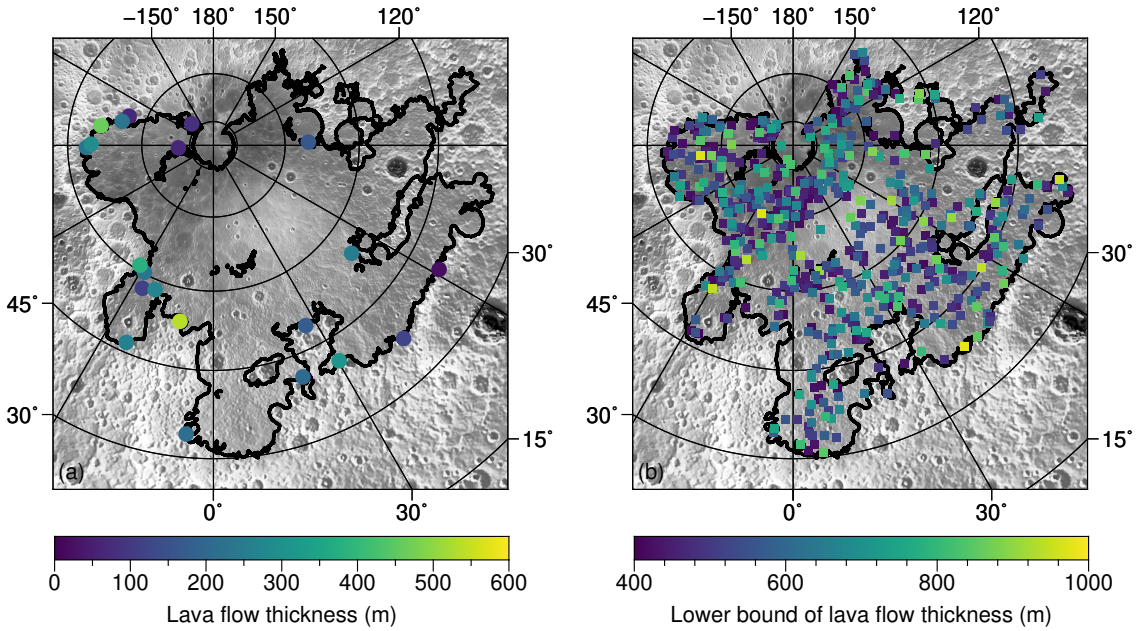

Figure 5.7: Lava flow thicknesses estimated from the craters with rim fully exposed (a). Lower bounds of lava flow thicknesses from the craters with rims partially and completely buried assuming no crater degradation (b). The black line is the boundary of the northern smooth plains (Denevi et al., 2013).

mated lava flow thickness and crater diameter. This is simply because the crater rim height, which is the maximum thickness that can be estimated from our method, increases with crater diameter (Pike, 1988). For the studied partially buried craters, the RMS misfits (Figure 5.8d) between the best-fitting and observed profiles are smaller than 100 m, with an average of 41 m. The initial crater diameter is found to be on average 95% of the present-day value. The uncertainty in the lava flow thickness is on average 91 m. All the 21 selected craters are infilled with lava flows, and the lava flow thicknesses are 1138 m on average (note that the crater floor is much deeper than the pre-flooding background).

If crater degradation was not included, these thicknesses would be considerably larger, ranging from 135 to 608 m. In this case, the median and average lava flow thicknesses are 346 and 372 m, in comparison to the values of 228 and 224 m obtained when considering crater degradation. This 118 m overestimate in the average lava flow thickness therefore suggests that previous studies that neglected crater degradation would overestimate the lava flow thickness by about 50%.

We also made use of rim partially and completely buried craters to provide

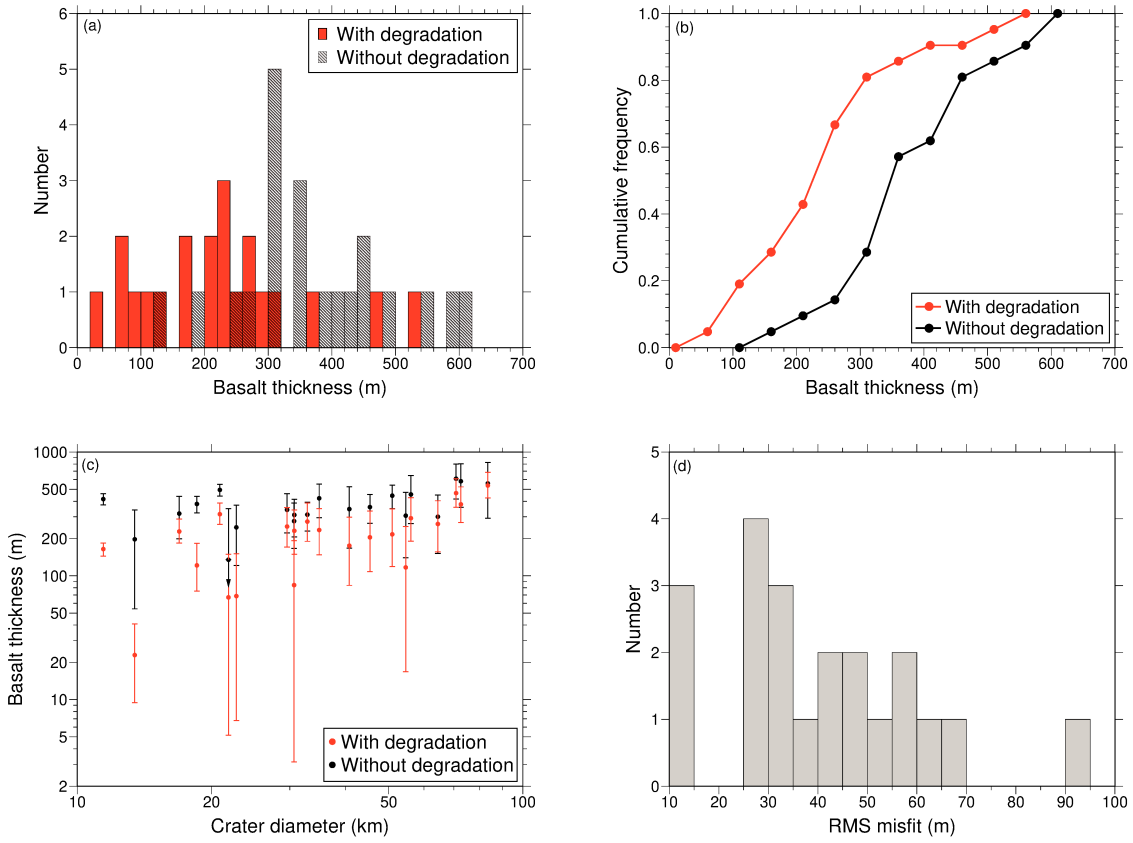

Figure 5.8: Histograms (a) and cumulative distributions (b) of lava flow thicknesses with (red) and without (black) considering crater degradation. Lava flow thicknesses as a function of crater diameter with (red) and without (black) considering the crater degradation process (c). Histogram of the RMS misfits between the modeled and observed profiles (d).

constraints on the lava thicknesses in the center of the northern smooth plains. For them, a part of the crater rim was buried by lava flows, and thus the initial crater rim height for these craters may provide a lower bound for the lava flow thickness in this region assuming no crater degradation. We used 585 craters with buried rims and diameters of 10–93 km (where the rim height-crater diameter relation is applicable) for estimation. Their initial crater rim height ranges from 411 to 978 m, which can serve as lower bounds for the lava flow thicknesses there in.

5.3 Discussion

5.3.1 Comparison with Other Techniques

Due to the limitations on the spatial resolution, data quality, and sources of the remote sensing datasets, there are only a few studies that have investigated the

lava flow thickness on Mercury, and none of them has given precise, quantitative estimates. In this section, we compare our estimated lava flow thicknesses with these previous studies, which include those based on crater morphology and graben width.

Ostrach et al. (2015) identified partially and completely buried craters within the northern smooth plains, and studied their crater size-frequency distribution and surrounding lava flow thicknesses. For the completely buried craters with diameters of 25–157 km, the initial crater rim heights are predicted to be 0.7–1.8 km, which provide lower limits for lava flow thicknesses. For the partially buried craters with diameters of 8–157 km, the initial crater rim heights are predicted to be 0.4–1.8 km, which can be either the lower (for the buried segment of the crater rim) or upper (for the exposed segment of the crater rim) limits for lava flow thicknesses. However, all these value are crude, and the authors did not provide a complete list for the craters studied, making it difficult to compare our results with these values.

Klimczak et al. (2012) provided a systematic investigation on the wrinkle ridges and graben within the northern smooth plains, with the goal of obtaining some constraints on lava flow thicknesses. The idea is that the graben width can be used to estimate the lower bound of lava flow thickness if one assumes a fault angle typcially 60°, as the graben fault continues into the subsurface (Watters et al., 2012). Their estimation shows that the lava flow thickness within the Goethe basin is at least 2 km. The crater depth-diameter ratio derived in this study predicts a depth of 3.8 km for the crater with a diameter (317 km) equal to Goethe's. Without considering crater degradation, this could serve as a lower limit for the lava flow thickness in the interior of Goethe basin that is completely buried by lavas.

5.3.2 Total Volume of the Lava Flows

The total surface area of the northern smooth plains is estimated to be 5.4×10^6 km^2, and hence the total volume of lava flows is estimated to be 1.2×10^6 km^3 using an average thickness of 224 m. In addition, if a lower limit of the lava flow thickness (0.4–1.0 km) can be obtained from the initial rim height of the partially and completely buried craters, the total volume should be at least 2.2–5.4×10^6 km^3.

It should be noted that the smooth plains are widely distributed all over the surface of Mercury. The northern smooth plains account for ∼7% of the global sur-

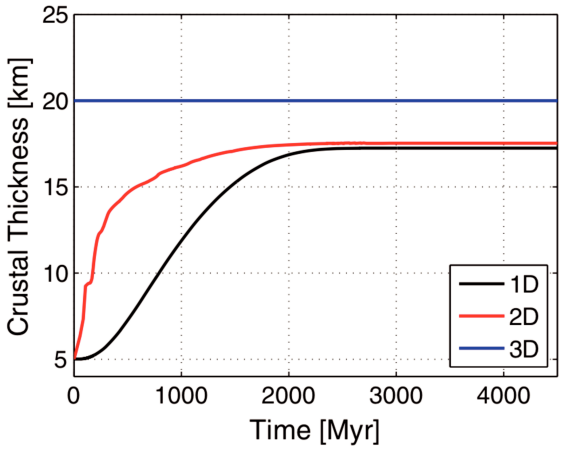

Figure 5.9: The thickness of produced volcanic materials for Mercury as a function of time from Tosi et al. (2013). The black, red, and blue lines are simulation results in the one-, two-, and three-dimensional scenarios, respectively. Note that for the three-dimensional scenario, the thickness is fixed at 20 km due to computational burden concerns.

face area, and other isolated smooth plains with a clear volcanic origin occupy ∼10% (Denevi et al., 2013). Therefore, if we assume the same lava flow thickness for the other smooth plains units as those for the northern smooth plains, the total volume of smooth plains materials at the global scale will be at least doubled comparing with those for the northern smooth plains alone.

As a comparison, the thickness and volume of the produced magmas of Mercury can also be predicted by a thermal-chemical evolution model (Figure 5.9) (Tosi et al., 2013). It is shown that during the first 900 Myr the produced volcanic materials are 12–16 km thick, indicating a total volume of 6.5–8.6×10^7 km^3. This suggests that smooth plains only account for a small portion of the volcanic crust.

It is expected that the total volume and eruption rate on Mercury are larger than those on the Moon. As the magma entered the lunar crust, it could stall as it is negatively buoyant (Figure 5.10). This is because the density of the basaltic magma (3270–3460 kg/m^3) is larger than that of the anorthosites that made up the lunar crust (2200–2600 kg/m^3) (Kiefer et al., 2012). For Mercury, however, the magmas are expected to always be buoyant, as the molten magma is likely intruding a crust of a similar composition (Sori, 2018; Vander Kaaden and McCubbin, 2015) (Figure 5.11). As a result, the magmatic materials of Mercury can reach the surface more easily.

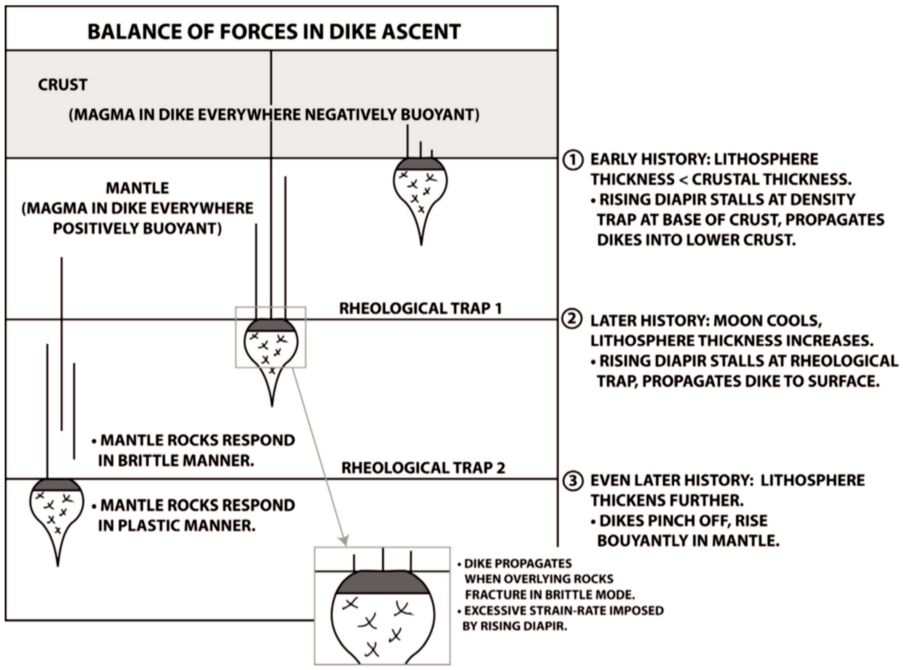

Figure 5.10: The volcanic history of the Moon, including diapir migration, dike propagation, and thickening of the lithosphere (Head and Wilson, 2017).

5.3.3 Scale Dependence of Crater Degradation

The topographic diffusivity of craters on Mercury can be obtained from the crater degradation model, and we found that in general it increases with increasing crater diameter, which is similar to what we found for lunar craters and to what Fassett et al. (2017) shows (Figure 5.12a). In addition, we found that the uncertainties of the derived topographic diffusivities can be extremely large. Given all these considerations, we did not fit the topographic diffusivity-crater diameter relation for craters on Mercury.

As crater topographic degradation is considered to be a result of micrometeoroid bombardment (Culling, 1960; Soderblom, 1970), the topographic diffusivity should be closely related to the impact cratering rate of the planet. Most of the partially buried craters investigated in this study are tens of kilometers in diameter. Studies have shown that the subsequent craters that diffusively erode the parent crater should be smaller than one-tenth of the parent crater diameter (Minton and Fassett, 2016), so here we focus on the impact cratering rate of craters at kilometer scales. Theoretical modeling based on orbital dynamics has shown that at kilometer scales the impact cratering rate on Mercury is 2.5–3 times that on the Moon (Figure

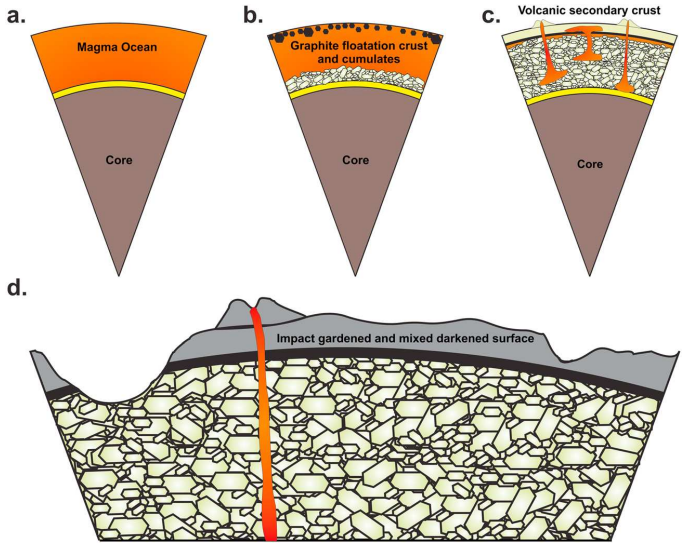

Figure 5.11: The volcanic history of Mercury: early stage featured by magma ocean (a), graphite ascending to form the primary crust (b), volcanic eruption to form the secondary crust (c), and the present-day structure considering the formation of large basins and craters (d) (Vander Kaaden and McCubbin, 2015).

5.13) (Le Feuvre and Wieczorek, 2011). Therefore, it can be expected that the topographic diffusivity of Mercury's craters should be twice or three times that of lunar craters (Fassett et al., 2017). After normalized by crater diameter, the median topographic diffusivities for Mercury's and Moon's craters given by our inversions are 11.1 and 4.5 m^2/Myr, respectively (Figure 5.12b). Therefore, the ratio of Mercury's topographic diffusivities to that of the Moon (nearly 2.5:1) is consistent with what the impact cratering rate predicts.

Using unburied, small, simple craters, Fassett and Thomson (2014) and Fassett et al. (2017) also estimated the crater topographic diffusivities on the Moon and Mercury in a diameter range of 2.5–5 km (Figure 5.14). Their results show that the median topographic diffusivities on the Moon and Mercury are respectively 9 and 17 m^2/Myr, which supports the idea that the impact cratering rate on the Moon is half of that on Mercury. After normalized by crater diameter, the median topographic diffusivities on Mercury is 5.0 m^2/Myr given by Fassett et al. (2017), which is half of that given by our study. We interpreted this as a result of the difference in the time length that two studies investigated. The topographic diffusivity given by our study corresponds to 3.7 Ga (the age of the smooth plains) to now, whereas Fassett et al. (2017)'s result corresponds to 3.5 Ga (the median age of the craters on the

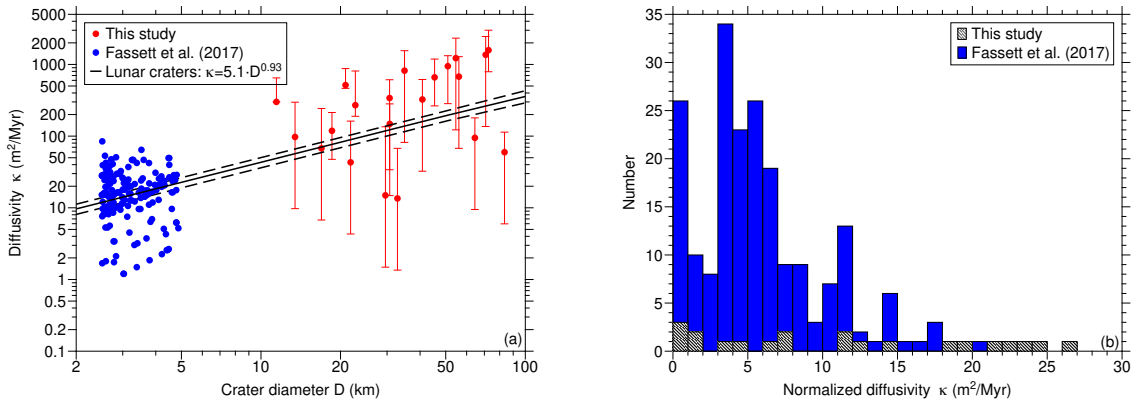

Figure 5.12: The inverted topographic diffusivity of craters on Mercury as a function of crater diameter (a). The best fitting topographic diffusivity on the Moon is shown as the black line. Fassett et al. (2017)'s result is plotted as the blue dots. The histograms of the inverted topographic diffusivities normalized by crater diameter given by this study (gray) and Fassett et al. (2017) (blue).

smooth plains) to present days. This implies that the impact flux on Mercury may decrease with time very significantly at the tail of the late heavy bombardments.

We should point out that the topographic diffusivities obtained in this study have large uncertainties, therefore any quantitative comparison should be dealt with caution. The uncertainty of topographic diffusivity could arise from the facts that: (1) the initial crater profile has large uncertainties; (2) the diffusion equation used in this study was constructed in an idealized, axisymmetric scenario, whereas actual topographic degradation on a planetary surface could be more azimuthally heterogenous; (3) the obtained topographic diffusivity relies on the age of the lava flows, which may also have a large uncertainty, especially for the northern smooth plains on Mercury where we do not have any returned sample as age constraints; (4) we implemented a simplified one-dimensional search looking for the uncertainty in this study, whereas the allowable parameter combinations may occupy a larger parameter space. In a word, it is still difficult to determine the topographic diffusivity for craters on planetary surfaces when using just a subset of them (e.g., partially buried craters in this study) and facing so many challenges mentioned above. However, once the topographic diffusivity can be well constrained, we will be able to date a single crater based on its crater morphology.

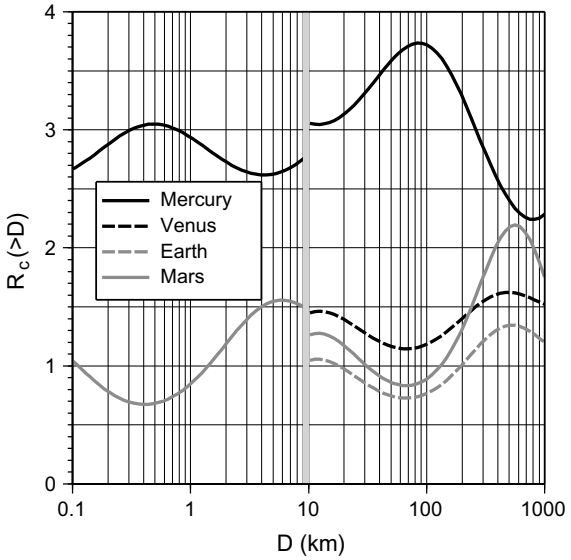

Figure 5.13: Impact cratering rates on terrestrial planets as a function of crater diameter (Le Feuvre and Wieczorek, 2011). The impact cratering rate on the Moon is fixed to 1. The black solid line, black dashed line, gray dashed line, and gray solid line represent impact cratering rates on Mercury, Venus, Earth, and Mars, which are normalized by that on the Moon.

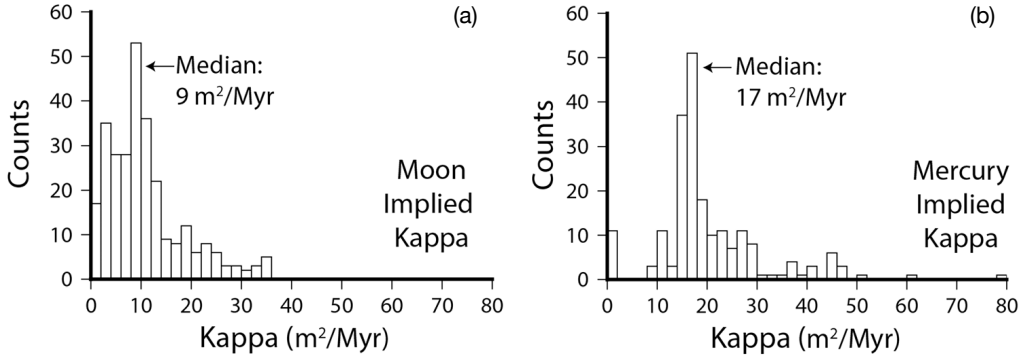

Figure 5.14: Histograms of topographic diffusivities for craters on Mercury (a) and the Moon (b) (Fassett and Thomson, 2014; Fassett et al., 2017). The median topographic diffusivities are respectively 9 and 17 m^2/Myr. The diameter range is 2.5–5 km.

Chapter 6 Conclusions

6.1 Summary of This Study

In this study, a global database of 622 partially buried and 39 completely buried craters was first constructed on the Moon using newly acquired remote sensing datasets. The identified buried craters were classified into three classes including craters with rims completely exposed, those with rims partially exposed, and those with rims completely buried. The spatial distribution and size-frequency distributions of these buried craters show that partially buried craters preferentially occur along mare-highland boundaries where the basalt thickness is expected to be thinner than in the central mare. A new elevation model for lunar fresh craters was constructed, and numerical modeling of the crater degradation process was then performed to estimate the thickness of mare basalts that embay the partially buried craters.

Our overall results show that the obtained basalt thicknesses on the Moon vary from 33 to 455 m and are significantly thinner than those obtained without considering the crater degradation process (a reduction of 95 m in median value). For selected craters, we demonstrated that the obtained basalt thicknesses were consistent with other estimates obtained from crater excavation depths and radar sounding observations, and comparable to those obtained from lava flow front height measurements. The estimated eruption rate of lunar mare basalts peaked at 3.4 Ga and then deceased with time, indicative of gradual cooling of the lunar interior. The best-fitting topographic diffusivity increases linearly with crater diameter and does not vary with time and terrain type, implying that the crater degradation process is scale-dependent.

For the northern smooth plains of Mercury, we also constructed a crater database with 257 partially buried craters and 765 completely buried craters. Like the Moon, their spatial distribution also shows that partially buried craters tend to form along

the smooth plains boundaries where lava flows are expected to be thinner. Lava flow thicknesses were inverted for 21 craters whose rim is fully exposed. The result shows that the lava flow thicknesses vary from 23 to 536 m, with a median value of 228 m. When not considering the crater degradation process, the median value would be 118 m larger. The lower limits of lava flow thicknesses in the interior of the smooth plains were predicted by the initial rim heights of 585 craters with partially or completely buried rims, and the results show that the lava flow thicknesses therein are at least 411 to 978 m thick. We then calculated the total volume of lava flows, and also found that the topographic diffusivity of craters on Mercury increases with diameter.

Although our work has improved upon previous studies, we have identified a number of complicating factors that should be addressed in future studies. As an example, we employed a simple axisymmetric geometry for the topographic degradation and lava emplacement model. This model, however, can not account for partially buried craters on the mare or smooth plains boundaries where a portion of the rim was breached. Second, our results show considerable scatter in how topographic diffusivity varies with crater size. A portion of this scatter may be related to our use of axisymmetric crater profiles, and the assumption of a uniform lava thickness surrounding the crater. We hope to better constrain the topographic diffusivity by looking into craters with simple geologic background, axisymmetric morphology and even with constraints on the formation age. Whereas in this study, the partially buried craters actually underwent the emplacement of the lava flow, thus the unburied, simple craters are better samples to work on. Third, although the initial crater profile for simple craters is well constrained, the initial crater shapes for transitional and complex craters have considerable variability. Finally, our work did not consider the contribution from non-diffusive processes.

6.2 Outlook for Lava Flow Thickness Estimation on Mars

Volcanism on Mars has been quite active throughout its entire history, being widespread in the Noachian and Hesperian and localized in the Amazonian (Tharsis and Elysium) (Head, 2007). Like the Moon, the volume of lava flows on Mars is an important parameter that can constrain the thermal evolution history, reveal the sources and styles of volcanism, and contribute to the subsequent tectonic activity

and lithospheric deformation (Broquet and Wieczorek, 2018; Head, 1982). Lava flow thicknesses on Mars have been investigated by only a few studies, which include direct measurements of lava flow front heights (Garry et al., 2007; Zimbelman, 1998) and those based on the crater rim heights of partially buried craters (De Hon, 1982; Plescia and Saunders, 1980).

On Mars, a partially buried crater forms when a lava flow covers the distal low-elevation ejecta, leaving the high-elevation rim crest visible (see Figure 2 in Fassett (2016)). The nearby lava flow thickness is thus simply the difference between the total rim height and the exposed rim height. In previous studies, the exposed rim height was directly measured, whereas the total rim height was estimated using scaling relations between crater rim height and diameter of fresh craters. For example, Plescia and Saunders (1980) and De Hon (1982) estimated the lava flow thicknesses in the Tharsis region to be 0–0.7 and 0–1.5 km respectively, based on the crater rim heights of the partially buried craters measured from the stereoscopic Viking images. However, craters on Mars suffer from different kinds of topographic degradation processes. Micrometeoroid bombardment, thermal expansion and contraction, seismic shaking, rain splash, and solifluction are thought to be diffusive erosion processes, whereas wind transport, surface runoff, and emplacement of ejecta from adjacent craters are considered as non-diffusive erosion processes (Craddock and Howard, 2002; Craddock et al., 1997, 2018). As a result, with increasing time, the crater diameter should increase and the rim height should decrease due to the downslope movement of rim and ejecta materials. In such a case, if the initial rim height were used to determine the lava flow thickness, the lava flow thickness would be overestimated.

With newly acquired orbital datasets on Mars (e.g., CTX, HiRISE, and MOLA), it is possible to reevaluate and update the previous databases of Martian partially buried craters that were constructed nearly four decades ago. By modeling the formation, degradation, and flooding processes of partially buried craters, the nearby lava flow thicknesses can be inverted and better constrained than in previous studies.

Aiming at a systematic study of partially buried craters at a global scale, we can use the global mosaic data products. For example, to work on the surface morphology, we can make use of the 100 m/pixel THEMIS global daytime infrared mosaic (Edwards et al., 2011), and to study the surface topography, we could use the

recently released 200 m/pixel Mars HRSC MOLA blended DEM (Fergason et al., 2018). We can also use the database of fresh Martian craters produced by Robbins and Hynek (2012a) and Robbins and Hynek (2012b) and the morphometric relations of fresh Martian craters described in several previous studies (Boyce and Garbeil, 2007; Craddock et al., 1997; Garvin and Frawley, 1998; Pike, 1980; Stewart and Valiant, 2006) to construct the initial crater elevation profiles.

Inversion for lava flow thicknesses on Mars would make use of the model parameters as those in our studies of the Moon and Mercury. If the partially buried crater formed quite early (e.g., Noachian period), we would need to consider the degradation from surface runoff, bedrock weathering, fluvial erosion, sediment transport and deposition, mass wasting, and impact cratering (see the parameters listed in Table 1 in Matsubara et al. (2018)). If the partially buried crater formed more recently (e.g., Amazonian period) when most of the eolian and fluvial activities had already ceased (Carr and Head, 2010; Head, 2007), we could perhaps only need to consider the erosion that results from micrometeoroid bombardment, although it could be very weak due to the presence of the atmosphere. In these cases, we could make use of the MARSSIM model, which is a powerful tool to simulate various geomorphic processes on Mars (Howard, 2007). Especially, it can allow us to quantify the non-diffusive erosion processes such as the eolian and fluvial activities, which we did not take into account in our simple topographic diffusive model. Furthermore, the model also allows for the erosion of a complicated, arbitrary, fully three-dimensional topography.

Bibliography

Aeronautical Chart Information Center, USAF. 1973. The Lunar Cartographic Dossier: Lunar Astronautical Chart (LAC) Series. Lunar and Planetary Institute: Houston.

Baker D M, Head J W. 2013. New morphometric measurements of craters and basins on Mercury and the Moon from MESSENGER and LRO altimetry and image data: An observational framework for evaluating models of peak-ring basin formation. Planetary and Space Science, 86: 91–116.

Baldwin R B. 1970. A new method of determining the depth of the lava in lunar maria. Publications of the Astronomical Society of the Pacific, 82(488): 857–864.

Baldwin R B. 1949. The face of the Moon. University of Chicago Press: Chicago.

Baldwin R B. 1963. The measure of the Moon. University of Chicago Press: Chicago.

Barker M K, Mazarico E, Neumann G A, Zuber M T, Haruyama J, Smith D E. 2016. A new lunar digital elevation model from the Lunar Orbiter Laser Altimeter and SELENE Terrain Camera. Icarus, 273: 346–355, doi: 10.1016/j.icarus.2015.07.039.

Barnouin O S, Zuber M T, Smith D E, Neumann G A, Herrick R R, Chappelow J E, Murchie S L, Prockter L M. 2012. The morphology of craters on Mercury: Results from MESSENGER flybys. Icarus, 219(1): 414–427.

Basilevsky A T. 1976. On the evolution rate of small lunar craters. Lunar and Planetary Science Conference Proceedings, 7: 1005–1020.

Becker K, Robinson M, Becker T, Weller L, Edmundson K, Neumann G, Perry M, Solomon S. 2016. First global digital elevation model of Mercury. Lunar and Planetary Science Conference, 47: #2959.

Bell J F, Hawke B R. 1984. Lunar dark-haloed impact craters: Origin and implications for Early Mare volcanism. Journal of Geophysical Research: Solid Earth, 89(B8): 6899–6910, doi: 10.1029/JB089iB08p06899.

Bottke W F, Levison H, Morbidelli A. 2008. Understanding the impact flux on the Moon over the last 4.6 Gy. Workshop on the Early Solar System Impact Bombardment: #1439.

Boyce J M, Garbeil H. 2007. Geometric relationships of pristine Martian complex impact craters, and their implications to Mars geologic history. Geophysical Research Letters, 34: 1–5.

Braden S E, Stopar J D, Robinson M S, Lawrence S J, van der Bogert C H, Hiesinger H. 2014. Evidence for basaltic volcanism on the Moon within the past 100 million years. Nature Geoscience, 7(11): 787–791, doi: 10.1038/NGEO2252.

Broquet A, Wieczorek M. A. 2018. The gravitational signature of Martian volcanoes. Journal of Geophysical Research: Planets, 124(8): 2054–2086.

Budney C J, Lucey P G. 1998. Basalt thickness in Mare Humorum: The crater excavation method. Journal of Geophysical Research: Planets, 103(E7): 16855–16870, doi: 10.1029/98JE01602.

Carr M H, Head J W. 2010. Geologic history of Mars. Earth and Planetary Science Letters, 294(3-4): 185–203.

Chen Y, Li C, Ren X, Liu J, Wu Y, Lu Y, Cai W, Zhang X. 2018. The thickness and volume of young basalts within Mare Imbrium. Journal of Geophysical Research: Planets, 123(2): 630–645.

Cooper B L, Carter J L, Sapp C A. 1994. New evidence for graben origin of Oceanus Procellarum from lunar sounder optical imagery. Journal of Geophysical Research: Planets, 99(E2): 3799–3812, doi: 10.1029/93JE03096.

Cooper M R, Kovach R L, Watkins J S. 1974. Lunar near-surface structure. Reviews of Geophysics, 12(3): 291–308, doi: 10.1029/RG012i003p00291.

Craddock R A, Howard A D. 2000. Simulated degradation of lunar impact craters and a new method for age dating farside mare deposits. Journal of Geophysical Research: Planets, 105(E8): 20387–20401, doi: 10.1029/1999JE001099.

Craddock R A, Howard A D. 2002. The case for rainfall on a warm, wet early Mars. Journal of Geophysical Research: Planets, 107(E11): 21-1–21-36.

Craddock R A, Maxwell T A, Howard A D. 1997. Crater morphometry and modification in the Sinus Sabaeus and Margaritifer Sinus regions of Mars. Journal of Geophysical Research: Planets, 102(E6): 13321–13340.

Craddock R A, Bandeira L, Howard A D. 2018. An assessment of regional variations in Martian modified impact crater morphology. Journal of Geophysical Research: Planets, 123(3): 763–779.

Croft S K. 1980. Cratering flow fields: Implications for the excavation and transient expansion stages of crater formation. Lunar and Planetary Science Conference Proceedings, 11: 2347–2378.

Culling W E H. 1960. Analytical theory of erosion. Journal of Geology, 68(3): 336–344, doi: 10.1086/626663.

Culling W E H. 1963. Soil creep and the development of hillside slopes. Journal of Geology, 71(2): 127–161, doi: 10.1086/626891.

De Hon R A. 1974. Thickness of mare material in the Tranquillitatis and Nectaris basins. Lunar and Planetary Science Conference Proceedings, 5: 53–59.

De Hon R A. 1975. Mare Spumans and Mare Undarum: Structural and depositional history. Lunar and Planetary Science Conference Proceedings, 6: 181–183.

De Hon R A. 1977. Mare Humorum and Mare Nubium: Basalt thickness and basin-forming history. Lunar and Planetary Science Conference Proceedings, 8: 633–641.

De Hon R A. 1979a. Structural model of the Imbrium basin. Lunar and Planetary Science Conference Proceedings, 10: 271–273.

De Hon R A, Waskom J D. 1976. Geologic structure of the eastern mare basins. Lunar and Planetary Science Conference Proceedings, 7: 2729–2746.

De Hon R. 1978. Maximum thickness of materials in the western mare basins. Lunar and Planetary Science Conference Proceedings, 9: 229–231.

De Hon R A. 1979b. Thickness of western mare basalts. Lunar and Planetary Science Conference Proceedings, 10: 274–276.

De Hon R A. 1982. Martian volcanic materials: Preliminary thickness estimates in the eastern Tharsis region. Journal of Geophysical Research: Solid Earth, 87 (B12): 9821–9828.

Defense Mapping Agency. 1973. The Lunar Cartographic Dossier: Lunar Topographic Orthophotomap (LTO) and Lunar Orthophotmap (LO) Series.

Denevi B W, Ernst C M, Meyer H M, Robinson M S, Murchie S L, Whitten J L, Head J W, Watters T R, Solomon S C, Ostrach L R, et al. 2013. The distribution and origin of smooth plains on Mercury. Journal of Geophysical Research: Planets, 118(5): 891–907.

Denevi B W, Seelos F P, Ernst C M, Keller M R, Chabot N L, Murchie S L, Domingue D L, Hash C D, Blewett D T. 2016. Final calibration and multispectral map products from the Mercury Dual Imaging System Wide-Angle Camera. Lunar and Planetary Science Conference, 47: #1264.

Deng Q, Li F, Yan J, Xiao Z, Rodriguez J A P. 2018. Buried impact features on Mercury as revealed by gravity data. Journal of Geophysical Research: Planets, 123(11): 3005–3019.

Duffy D G. 2016. Advanced engineering mathematics with MATLAB. CRC Press: Boca Raton.

Edwards C S, Nowicki K J, Christensen P R, Hill J, Gorelick N, Murray K. 2011. Mosaicking of global planetary image datasets: 1. Techniques and data processing for Thermal Emission Imaging System (THEMIS) multi-spectral data. Journal of Geophysical Research: Planets, 116(E10), doi: 10.1029/2010JE003755.

Eggleton R E. 1963. Thickness of the Apenninian Series in the Lansberg region of the Moon. Astrogeological Studies Annual Progress Report, pp: 19–31.

Eliason E M, McEwen A S, Robinson M S, Lee E M, Becker T, Gaddis L, Weller L A, Isbell C E, Shinaman J R, Duxbury T, et al. 1999. Digital processing for a global multispectral map of the Moon from the Clementine UVVIS imaging instrument. Lunar and Planetary Science Conference Proceedings, 30: #1933.

Ernst C M, Murchie S L, Barnouin O S, Robinson M S, Denevi B W, Blewett D T, Head J W, Izenberg N R, Solomon S C, Roberts J H. 2010. Exposure of spectrally distinct material by impact craters on Mercury: Implications for global stratigraphy. Icarus, 209(1): 210–223.

Evans A J, Soderblom J M, Andrews-Hanna J C, Solomon S C, Zuber M T. 2016. Identification of buried lunar impact craters from GRAIL data and implications for the nearside maria. Geophysical Research Letters, 43(6): 2445–2455, doi: 10.1002/2015GL067394.

Evans A J, Andrews-Hanna J C, Head III J W, Soderblom J M, Solomon S C, Zuber M T. 2018. Re-examination of early lunar chronology with GRAIL data: Terranes, basins, and impact fluxes. Journal of Geophysical Research: Planets, 123(7): 1596–1617.

Fa W, Wieczorek M A. 2012. Regolith thickness over the lunar nearside: Results from Earth-based 70-cm Arecibo radar observations. Icarus, 218(2): 771–787, doi: 10.1016/j.icarus.2012.01.010.

Fa W, Liu T, Zhu M H, Haruyama J. 2014. Regolith thickness over Sinus Iridum: Results from morphology and size-frequency distribution of small impact craters. Journal of Geophysical Research: Planets, 119(8): 1914–1935, doi: 10.1002/2013JE004604.

Fassett C I, Minton D A, Thomson B J, Hirabayashi M, Watters W A. 2018. Reanalysis of observations of crater degradation on the lunar maria accounting for anomalous diffusion. Lunar and Planetary Science Conference, 49: #1502.

Fassett C I. 2016. Analysis of impact crater populations and the geochronology of planetary surfaces in the inner solar system. Journal of Geophysical Research: Planets, 121(10): 1900–1926, doi: 10.1002/2016JE005094.

Fassett C I, Thomson B J. 2014. Crater degradation on the lunar maria: Topographic diffusion and the rate of erosion on the Moon. Journal of Geophysical Research: Planets, 119(10): 2255–2271, doi: 10.1002/2014JE004698.

Fassett C I, Crowley M C, Leight C, Dyar M D, Minton D A, Hirabayashi M, Thomson B J, Watters W A. 2017. Evidence for rapid topographic evolution and

crater degradation on Mercury from simple crater morphometry. Geophysical Research Letters, 44(11): 5326–5335, doi: 10.1002/2017GL073769.

Fergason R L, Hare T M, Laura J. 2018. HRSC and MOLA Blended Digital Elevation Model at 200m v2. Technical Report, Astrogeology PDS Annex, U. S. Geological Survey.

Freed A M, Blair D M, Watters T R, Klimczak C, Byrne P K, Solomon S C, Zuber M T, Melosh H J. 2012. On the origin of graben and ridges within and near volcanically buried craters and basins in Mercury's northern plains. Journal of Geophysical Research: Planets, 117(E12), doi: 10.1029/2012JE004119.

Garry W B, Zimbelman J R, Gregg T K P. 2007. Morphology and emplacement of a long channeled lava flow near Ascraeus Mons Volcano, Mars. Journal of Geophysical Research: Planets, 112(E8), doi: 10.1029/2006JE002803.

Garvin J B, Frawley J J. 1998. Geometric properties of Martian impact craters: Preliminary results from the Mars Orbiter Laser Altimeter. Geophysical Research Letters, 25(24): 4405–4408.

Gault D E, Guest J E, Murray J B, Dzurisin D, Malin M C. 1975. Some comparisons of impact craters on Mercury and the Moon. Journal of Geophysical Research, 80(17): 2444–2460.

Gifford A W, El-Baz F. 1981. Thicknesses of lunar mare flow fronts. Moon Planets, 24(4): 391–398, doi: 10.1007/BF00896904.

Gong S, Wieczorek M A, Nimmo F, Kiefer W S, Head J W, Huang C, Smith D E, Zuber M T. 2016. Thicknesses of mare basalts on the Moon from gravity and topography. Journal of Geophysical Research: Planets, 121(5): 854–870, doi: 10.1002/2016JE005008.

Hale W, Head J. 1979. Central peaks in lunar craters: Morphology and morphometry. Lunar and Planetary Science Conference Proceedings, 10: 2623–2633.

Hale W, Head J. 1980. Central peaks in Mercurian craters: Comparisons to the Moon. Lunar and Planetary Science Conference Proceedings, 11: 2191–2205.

Hale W, Grieve R A. 1982. Volumetric analysis of complex lunar craters: Implications for basin ring formation. Journal of Geophysical Research: Solid Earth, 87 (S01): A65–A76, doi: 10.1029/JB087iS01p00A65.

Hare T M, Archinal B A, Becker T L, Gaddis L R, Lee E M, Redding B L, Rosiek M R. 2008. Clementine mosaics warped to ULCN2005 network. Lunar and Planetary Science Conference Proceedings, 39: #2337.

Hartmann W K. 1973. Ancient lunar mega-regolith and subsurface structure. Icarus, 18(4): 634–636, doi: 10.1016/0019-1035(73)90066-3.

Haruyama J, Ohtake M, Matsunaga T, Morota T, Honda C, Yokota Y, Abe M, Ogawa Y, Miyamoto H, Iwasaki A, et al. 2009. Long-lived volcanism on the lunar farside revealed by SELENE Terrain Camera. Science, 323(5916): 905–908.

Haruyama J, Hara S, Hioki K, Iwasaki A, Morota T, Ohtake M, Matsunaga T, Araki H, Matsumoto K, Ishihara Y, Noda H, Sasaki S, Goossens S, Iwata T. 2012. Lunar global digital terrain model dataset produced from SELENE (Kaguya) Terrain Camera stereo observations. Lunar and Planetary Science Conference, 43: #1200.

Hawke B R, Blewett D T, Lucey P G, Smith G A, Bell III J F, Campbell B A, Robinson M S. 2004. The origin of lunar crater rays. Icarus, 170(1): 1–16, doi: 10.1016/j.icarus.2004.02.013.

Head J W. 1975. Lunar mare deposits: Areas, volumes, sequence, and implication for melting in source areas. Lunar and Planetary Institute Contribution, 234: 66–69.

Head J W. 1976. Lunar volcanism in space and time. Reviews of Geophysics, 14 (2): 265–300, doi: 10.1029/RG014i002p00265.

Head J W. 1982. Lava flooding of ancient planetary crusts: Geometry, thickness, and volumes of flooded lunar impact basins. Earth Moon Planets, 26(1): 61–88, doi: 10.1007/BF00941369.

Head J W. 2007. The geology of Mars: New insights and outstanding questions. Cambridge University Press: New York.

Head J W, Wilson L. 1992. Lunar mare volcanism: Stratigraphy, eruption conditions, and the evolution of secondary crusts. Geochimica et Cosmochimica Acta, 56(6): 2155–2175, doi: 10.1016/0016-7037(92)90183-J.

Head J W, Wilson L. 2017. Generation, ascent and eruption of magma on the Moon: New insights into source depths, magma supply, intrusions and effusive/explosive eruptions (Part 2: Predicted emplacement processes and observations). Icarus, 283: 176–223, doi: 10.1016/j.icarus.2016.05.031.

Head J W, Chapman C R, Strom R G, Fassett C I, Denevi B W, Blewett D T, Ernst C M, Watters T R, Solomon S C, Murchie S L, et al. 2011. Flood volcanism in the northern high latitudes of Mercury revealed by MESSENGER. Science, 333 (6051): 1853–1856.

Heiken G H, Vaniman D T, French B M. 1991. Lunar source book: A user's guide to the Moon. Cambridge University Press: New York.

Herrick R, Bateman E, Crumpacker W, Bates D. 2018. Observations from a global database of impact craters on Mercury with diameters greater than 5 km. Journal of Geophysical Research: Planets, 123(8): 2089–2109.

Hiesinger H, Head J W, Wolf U, Jaumann R, Neukum G. 2002. Lunar mare basalt flow units: Thicknesses determined from crater size-frequency distributions. Geophysical Research Letters, 29(8): 89-1–89-4, doi: 10.1029/2002GL014847.

Hiesinger H, Head III J, Wolf U, Jaumann R, Neukum G. 2006. New ages for basalts in Mare Fecunditatis based on crater size-frequency measurements. Lunar and Planetary Science Conference, 37: #1151.

Hiesinger H, Head J W, Wolf U, Jaumann R, Neukum G. 2011. Ages and stratigraphy of lunar mare basalts: A synthesis. Geological Society of America Special Papers, 477: 1–51, doi: 10.1130/2011.2477(01).

Hiesinger H, Head J W. 2006. New views of the Moon. Mineralogical Society of America: Chantilly.

Hörz F. 1978. How thick are lunar mare basalts. Lunar and Planetary Science Conference Proceedings, 9: 3311–3331.

Howard A D. 2007. Simulating the development of Martian highland landscapes through the interaction of impact cratering, fluvial erosion, and variable hydrologic forcing. Geomorphology, 91(3-4): 332–363.

Huang Q, Wieczorek M A. 2012. Density and porosity of the lunar crust from gravity and topography. Journal of Geophysical Research, 117: E05003, doi: 10.1029/2012JE004062.

Ishiyama K, Kumamoto A, Ono T, Yamaguchi Y, Haruyama J, Ohtake M, Katoh Y, Terada N, Oshigami S. 2013. Estimation of the permittivity and porosity of the lunar uppermost basalt layer based on observations of impact craters by SELENE. Journal of Geophysical Research: Planets, 118(7): 1453–1467, doi: 10.1002/jgre.20102.

Kalynn J, Johnson C L, Osinski G R, Barnouin O. 2013. Topographic characterization of lunar complex craters. Geophysical Research Letters, 40(1): 38–42, doi: 10.1029/2012GL053608.

Kamata S, Sugita S, Abe Y, Ishihara Y, Harada Y, Morota T, Namiki N, Iwata T, Hanada H, Araki H, et al. 2015. The relative timing of Lunar Magma Ocean solidification and the Late Heavy Bombardment inferred from highly degraded impact basin structures. Icarus, 250: 492–503.

Kiefer W S. 2013. Gravity constraints on the subsurface structure of the Marius Hills: The magmatic plumbing of the largest lunar volcanic dome complex. Journal of Geophysical Research: Planets, 118(4): 733–745.

Kiefer W S, Macke R J, Britt D T, Irving A J, Consolmagno G J. 2012. The density and porosity of lunar rocks. Geophysical Research Letters, 39(7), doi: 10.1029/2012GL051319.

Kinczyk M J, Prockter L M, Chapman C R, Susorney H C. 2016. A morphological evaluation of crater degradation on Mercury: Revisiting crater classification with MESSENGER data. Lunar and Planetary Science Conference, 47: #1573.

Klimczak C, Watters T R, Ernst C M, Freed A M, Byrne P K, Solomon S C, Blair D M, Head J W. 2012. Deformation associated with ghost craters and basins in volcanic smooth plains on Mercury: Strain analysis and implications

for plains evolution. Journal of Geophysical Research: Planets, 117(E12), doi: 10.1029/2012JE004100.

Kobayashi T, Kim J H, Lee S R, Kumamoto A, Nakagawa H, Oshigami S, Oya H, Yamaguchi Y, Yamaji A, Ono T. 2012. Synthetic aperture radar processing of Kaguya Lunar Radar Sounder data for lunar subsurface imaging. IEEE Transactions on Geoscience and Remote Sensing, 50(6): 2161–2174, doi: 10.1109/TGRS.2011.2171349.

Kreslavsky M A, Head J W. 2016. The steepest slopes on the Moon from Lunar Orbiter Laser Altimeter (LOLA) data: Spatial distribution and correlation with geologic features. Icarus, 273: 329–336, doi: 10.1016/j.icarus.2016.02.036.

Laneuville M, Wieczorek M A, Breuer D, Tosi N. 2013. Asymmetric thermal evolution of the Moon. Journal of Geophysical Research: Planets, 118(7): 1435–1452, doi: 10.1002/jgre.20103.

Le Feuvre M, Wieczorek M A. 2011. Nonuniform cratering of the Moon and a revised crater chronology of the inner Solar System. Icarus, 214(1): 1–20, doi: 10.1016/j.icarus.2011.03.010.

Lemelin M, Lucey P G, Gaddis L R, Hare T, Ohtake M. 2016. Global map products from the Kaguya Multiband Imager at 512 ppd: Minerals, FeO, and OMAT. Lunar and Planetary Science Conference, 47: #2994.

Li C, Xing S, Lauro S E, Su Y, Dai S, Feng J, Cosciotti B, Di Paolo F, Mattei E, Xiao Y, et al. 2018. Pitfalls in GPR data interpretation: False reflectors detected in lunar radar coss sections by Chang'E-3. IEEE Transactions on Geoscience and Remote Sensing, 56(3): 1325–1335.

Lucey P G, Blewett D T, Jolliff B L. 2000. Lunar iron and titanium abundance algorithms based on final processing of Clementine ultraviolet-visible images. Journal of Geophysical Research: Planets, 105(E8): 20297–20305, doi: 10.1029/1999JE001117.

Marchi S, Chapman C R, Fassett C I, Head J W, Bottke W, Strom R G. 2013. Global resurfacing of Mercury 4.0–4.1 billion years ago by heavy bombardment and volcanism. Nature, 499(7456): 59–61.

Marshall C H. 1963. Thickness and structure of the Procellarian system in the Lansberg region of the Moon. Astrogeological Studies Annual Progress Report, pp. 12–18.

Massey Jr F J. 1951. The Kolmogorov-Smirnov test for goodness of fit. Journal of the American Statistical Association, 46(253): 68–78, doi: 10.2307/2280095.

MATLAB Documentation. 2017. The MathWorks Inc.

Matsubara Y, Howard A D, Irwin R P. 2018. Constraints on the Noachian paleoclimate of the Martian highlands from landscape evolution modeling. Journal of Geophysical Research: Planets, 123(11): 2958–2979.

Melosh H J. 1989. Impact Cratering: A Geologic Process. Oxford University Press: New York.

Michael G G. 2014. Craterstats 2.0 Documents.

Michaut C. 2011. Dynamics of magmatic intrusions in the upper crust: Theory and applications to laccoliths on Earth and the Moon. Journal of Geophysical Research: Solid Earth, 116(B5), doi: 10.1029/2010JB008108.

Michaut C, Pinel V. 2018. Magma ascent and eruption triggered by cratering on the Moon. Geophysical Research Letters, 45(13): 6408–6416.

Michaut C, Thiriet M, Thorey C. 2016. Insights into mare basalt thicknesses on the Moon from intrusive magmatism. Physics of the Earth and Planetary Interiors, 257: 187–192.

Minton D A, Fassett C I. 2016. Crater equilibrium as an anomalous diffusion process. Lunar and Planetary Science Conference, 47: #2623.

Minton D A, Fassett C I, Hirabayashi M, Howl B A, Richardson J E. 2019. The equilibrium size-frequency distribution of small craters reveals the effects of distal ejecta on lunar landscape morphology. Icarus, 326: 63–87.

Moore H J, Hodges C A, Scott D H. 1974. Multiringed basins-illustrated by Orientale and associated features. Lunar and Planetary Science Conference Proceedings, 5: 71–100.

Morota T, Haruyama J, Honda C, Ohtake M, Yokota Y, Kimura J, Matsunaga T, Ogawa Y, Hirata N, Demura H, et al. 2009. Mare volcanism in the lunar farside Moscoviense region: Implication for lateral variation in magma production of the Moon. Geophysical Research Letters, 36(21), doi: 10.1029/2009GL040472.

Morota T, Haruyama J, Ohtake M, Matsunaga T, Honda C, Yokota Y, Kimura J, Ogawa Y, Hirata N, Demura H, et al. 2011a. Timing and characteristics of the latest mare eruption on the Moon. Earth and Planetary Science Letters, 302(3): 255–266, doi: 10.1016/j.epsl.2010.12.028.

Morota T, Haruyama J, Ohtake M, Matsunaga T, Kawamura T, Yokota Y, Honda C, Kimura J, Hirata N, Demura H, et al. 2011b. Timing and duration of mare volcanism in the central region of the northern farside of the Moon. Earth Planets Space, 63: 5–13.

Murray B C, Belton M J, Danielson G E, Davies M E, Gault D E, Hapke B, O'Leary B, Strom R G, Suomi V, Trask N. 1974. Mercury's surface: Preliminary description and interpretation from Mariner 10 pictures. Science, 185(4146): 169–179.

Nava R A. 2011. Crater Helper Tools for ArcGIS 10.0. US Geological Survey: Flagstaff.

Nelson D M, Koeber S D, Daud K, Robinson M S, Watters T R, Banks M E, Williams N R. 2014. Mapping lunar maria extents and lobate scarps using LROC image products. Lunar and Planetary Science Conference, 45: #2861.

Nesvorný D, Morbidelli A, Vokrouhlický D, Bottke W F, Brož M. 2002. The Flora family: A case of the dynamically dispersed collisional swarm? Icarus, 157(1): 155–172, doi: 10.1006/icar.2002.6830.

Neukum G, Ivanov B, Hartmann W. 2001a. Cratering records in the inner Solar System in relation to the lunar reference system. Space Science Review, 96(1-4): 55–86, doi: 10.1023/A:1011989004263.

Neukum G, Oberst J, Hoffmann H, Wagner R, Ivanov B. 2001b. Geologic evolution and cratering history of Mercury. Planetary and Space Science, 49(14-15): 1507–1521.

Neukum G, Horn P. 1976. Effects of lava flows on lunar crater populations. Moon, 15(3-4): 205–222, doi: 10.1007/BF00562238.

Neumann G A, Zuber M T, Wieczorek M A, Head J W, Baker D M, Solomon S C, Smith D E, Lemoine F G, Mazarico E, Sabaka T J, et al. 2015. Lunar impact basins revealed by Gravity Recovery and Interior Laboratory measurements. Science Advances, 1(9): e1500852, doi: 10.1126/sciadv.1500852.

Neumann G A, Perry M E, Mazarico E, Ernst C M, Zuber M T, Smith D E, Becker K J, Gaskell R E, Head J W, Robinson M S, Solomon S C. 2016. Mercury shape model from laser altimetry and planetary comparisons. Lunar and Planetary Science Conference, 47: #2087.

Oberbeck V R. 1971. A mechanism for the production of lunar crater rays. Moon, 2(3): 263–278, doi: 10.1007/BF00561880.

Ohtake M, Haruyama J, Matsunaga T, Yokota Y, Morota T, Honda C, et al. 2008. Performance and scientific objectives of the SELENE (Kaguya) Multiband Imager. Earth, Planets and Space, 60(4): 257–264, doi: 10.1186/BF03352789.

Ono T, Kumamoto A, Nakagawa H, Yamaguchi Y, Oshigami S, Yamaji A, Kobayashi T, Kasahara Y, Oya H. 2009. Lunar radar sounder observations of subsurface layers under the nearside maria of the Moon. Science, 323(5916): 909–912, doi: 10.1126/science.1165988.

Oshigami S, Yamaguchi Y, Yamaji A, Ono T, Kumamoto A, Kobayashi T, Nakagawa H. 2009. Distribution of the subsurface reflectors of the western nearside maria observed from Kaguya with Lunar Radar Sounder. Geophysical Research Letters, 36(18), doi: 10.1029/2009GL039835.

Oshigami S, Okuno S, Yamaguchi Y, Ohtake M, Haruyama J, Kobayashi T, Kumamoto A, Ono T. 2012. The layered structure of lunar maria: Identification of the HF-radar reflector in Mare Serenitatis using multiband optical images. Icarus, 218(1): 506–512.

Oshigami S, Watanabe S, Yamaguchi Y, Yamaji A, Kobayashi T, Kumamoto A, Ishiyama K, Ono T. 2014. Mare volcanism: Reinterpretation based on Kaguya

Lunar Radar Sounder data. Journal of Geophysical Research: Planets, 119(5): 1037–1045, doi: 10.1002/2013JE004568.

Ostrach L R, Robinson M S, Whitten J L, Fassett C I, Strom R G, Head J W, Solomon S C. 2015. Extent, age, and resurfacing history of the northern smooth plains on Mercury from MESSENGER observations. Icarus, 250: 602–622.

Otake H, Ohtake M, Hirata N. 2012. Lunar iron and titanium abundance algorithms based on SELENE (Kaguya) Multiband Imager data. Lunar and Planetary Science Conference, 43: #1905.

Padovan S, Tosi N, Plesa A C, Ruedas T. 2017. Impact-induced changes in source depth and volume of magmatism on Mercury and their observational signatures. Nature Communications, 8(1): 1945, doi: 10.1038/s41467-017-01692-0.

Pasckert J H, Hiesinger H, van der Bogert C H. 2018. Lunar farside volcanism in and around the South Pole-Aitken basin. Icarus, 299: 538–562.

Peeples W J, Sill W R, May T W, Ward S H, Phillips R J, Jordan R L, Abbott E A, Killpac T J. 1978. Orbital radar evidence for lunar subsurface layering in Maria Serenitatis and Crisium. Journal of Geophysical Research, 62: 3459–3468, doi: 10.1029/JB083iB07p0345.

Phillips R J, Adams G F, Brown Jr W E, Eggleton R E, Jackson P, Jordan R, Linlor W I, Peeples W J, Porcello L J, Ryu J, et al. 1973. Apollo Lunar Sounder Experiment. Apollo 17 Preliminary Science Report.

Pike R J. 1972. Geometric similitude of lunar and terrestrial craters. 24th International Geological Congress, pp: 41–47.

Pike R J. 1985. Some morphologic systematics of complex impact structures. Meteoritics & Planetary Science, 20(1): 49–68, doi: 10.1111/j.1945-5100.1985.tb00846.x.

Pike R J. 1967. Schroeter's rule and the modification of lunar crater impact morphology. Journal of Geophysical Research, 72(8): 2099–2106.

Pike R J. 1974. Depth/diameter relations of fresh lunar craters: Revision from spacecraft data. Geophysical Research Letters, 1(7): 291–294.

Pike R J. 1977. Size-dependence in the shape of fresh impact craters on the Moon. Impact and Explosion Cratering: Planetary and Terrestrial Implications, pp: 489–509.

Pike R J. 1980. Control of crater morphology by gravity and target type-Mars, Earth, Moon. Lunar and Planetary Science Conference Proceedings, 11: 2159–2189.

Pike R J. 1988. Geomorphology of impact craters on Mercury. Mercury. University of Arizona Press: Tucson.

Plescia J B, Saunders R S. 1980. Estimation of the thickness of the Tharsis lava flows and implications for the nature of the topography of the Tharsis plateau. Lunar and Planetary Science Conference Proceedings, 11: 2423–2436.

Plescia J B, Golombek M. 1986. Origin of planetary wrinkle ridges based on the study of terrestrial analogs. Geological Society of America Bulletin, 97(11): 1289–1299.

Pohn H A, Offield T W. 1970. Lunar crater morphology and relative-age determination of lunar geologic units–Part 1. Classification. US Geological Survey Professional Paper, pp: 153–162.

Richardson J E. 2009. Cratering saturation and equilibrium: A new model looks at an old problem. Icarus, 204(2): 697–715, doi: 10.1016/j.icarus.2009.07.029.

Richardson J E, Melosh H J, Greenberg R J, O'Brien D P. 2005. The global effects of impact-induced seismic activity on fractured asteroid surface morphology. Icarus, 179(2): 325–349, doi: 10.1016/j.icarus.2005.07.005.

Robbins S J, Hynek B M. 2012a. A new global database of Mars impact craters $\geq$ 1 km: 1. Database creation, properties, and parameters. Journal of Geophysical Research: Planets, 117(E5), doi: 10.1029/2011JE003966.

Robbins S J, Hynek B M. 2012b. A new global database of Mars impact craters ≥ 1 km: 2. Global crater properties and regional variations of the simple-to-complex transition diameter. Journal of Geophysical Research: Planets, 117(E6), doi: 10.1029/2011JE003966.

Robbins S J, Antonenko I, Kirchoff M R, Chapman C R, Fassett C I, Herrick R R, Singer K, Zanetti M, Lehan C, Huang D, et al. 2014. The variability of crater identification among expert and community crater analysts. Icarus, 234: 109–131, doi: 10.1016/j.icarus.2014.02.022.

Robinson M S, Brylow S M, Tschimmel M, Humm D, Lawrence S J, Thomas P C, Denevi B W, Bowman-Cisneros E, Zerr J, Ravine M A, Caplinger M A, Ghaemi F T, Schaffner J A, Malin M C, Mahanti P, Bartels A, Anderson J, Tran T N, Eliason E M, McEwen A S, Turtle E, Jolliff B L, Hiesinger H. 2010. Lunar Reconnaissance Orbiter Camera (LROC) instrument overview. Space Science Review, 150(1-4): 81–124, doi: 10.1007/s11214-010-9634-2.

Robinson M S, Ashley J W, Boyd A K, Wagner R V, Speyerer E J, Hawke B R, Hiesinger H, van der Bogert C H. 2012. Confirmation of sublunarean voids and thin layering in mare deposits. Planetary and Space Science, 69(1): 18–27, doi: 10.1016/j.pss.2012.05.008.

Schaber G G. 1973. Lava flows in Mare Imbrium: Geologic evaluation from Apollo orbital photography. Lunar and Planetary Science Conference Proceedings, 4: 73–92.

Schaber G G, Boyce J M, Moore H J. 1976. The scarcity of mappable flow lobes on the lunar maria: Unique morphology of the Imbrium flows. Lunar and Planetary Science Conference Proceedings, 7: 2783–2800.

Schaber G, Thompson T, Zisk S. 1975. Lava flows in Mare Imbrium: An evaluation of anomalously low earth-based radar reflectivity. The Moon, 13(4): 395–423, doi: 10.1007/BF02626384.

Schittkowski K. 1986. NLPQL: A FORTRAN subroutine solving constrained non-linear programming problems. Annals of Operations Research, 5(2): 485–500, doi: 10.1007/BF02022087.

Schlemm C E, Starr R D, Ho G C, Bechtold K E, Hamilton S A, Boldt J D, Boynton W V, Bradley W, Fraeman M E, Gold R E, et al. 2007. The X-Ray Spectrometer on the MESSENGER spacecraft. Space Science Reviews, 131(1-4): 393–415.

Sharpton V L, Head J W. 1982. Stratigraphy and structural evolution of southern Mare Serenitatis: A reinterpretation based on Apollo Lunar Sounder Experiment data. Journal of Geophysical Research: Solid Earth, 87(B13): 10983–10998, doi: 10.1029/JB087iB13p10983.

Shoemaker E M. 1965. Preliminary analysis of the fine structure of the lunar surface in Mare Cognitum. International Astronomical Union Colloquium, 5: 23–77, doi: 10.1017/S0252921100115714.

Smith D E, Zuber M T, Jackson G B, Cavanaugh J F, Neumann G A, Riris H, Sun X, Zellar R S, Coltharp C, Connelly J, Katz R B, Kleyner I, Liiva P, Matuszeski A, Mazarico E M, McGarry J F, Novo-Gradac A M, Ott M N, Peters C, Ramos-Izquierdo L A, Ramsey L, Rowlands D D, Schmidt S, V. Stanley Scott III, Shaw G B, Smith J C, Swinski J P, Torrence M H, Unger G, Yu A W, Zagwodzki T W. Jan. 2010. The Lunar Orbiter Laser Altimeter investigation on the Lunar Reconnaissance Orbiter mission. Space Science Review, 150: 209–241, doi: 10.1007/s11214-009-9512-y.

Snape J F, Curran N M, Whitehouse M J, Nemchin A A, Joy K H, Hopkinson T, Anand M, Bellucci J J, Kenny G G. 2018. Ancient volcanism on the Moon: Insights from Pb isotopes in the MIL 13317 and Kalahari 009 lunar meteorites. Earth and Planetary Science Letters, 502: 84–95.

Soderblom L A. 1970. A model for small-impact erosion applied to the lunar surface. Journal of Geophysical Research, 75(14): 2655–2661, doi: 10.1029/JB075i014p02655.

Solomon S C, Head J W. 1979. Vertical movement in mare basins: Relation to mare emplacement, basin tectonics, and lunar thermal history. Journal of Geophysical Research: Solid Earth, 84(B4): 1667–1682, doi: 10.1029/JB084iB04p01667.

Solomon S C, Head J W. 1980. Lunar mascon basins: Lava filling, tectonics, and evolution of the lithosphere. Reviews of Geophysics, 18(1): 107–141, doi: 10.1029/RG018i001p00107.

Sood R, Chappaz L, Melosh H J, Howell K C, Milbury C, Blair D M, Zuber M T. 2017. Detection and characterization of buried lunar craters with GRAIL data. Icarus, 289: 157–172, doi: 10.1016/j.icarus.2017.02.013.

Sori M M. 2018. A thin, dense crust for Mercury. Earth and Planetary Science Letters, 489: 92–99.

Speyerer E, Robinson M, Denevi B, et al. 2011. Lunar Reconnaissance Orbiter Camera global morphological map of the Moon. Lunar and Planetary Science Conference, 42: #2387.

Stewart S T, Valiant G J. 2006. Martian subsurface properties and crater formation processes inferred from fresh impact crater geometries. Meteoritics & Planetary Science, 41(10): 1509–1537.

Stickle A M, Patterson G W, Cahill J T S, Bussey D B J. 2016. Mini-RF and LROC observations of mare crater layering relationships. Icarus, 273: 224–236, doi: 10.1016/j.icarus.2016.03.014.

Stöffler D, Ryder G. 2011. Stratigraphy and isotope ages of lunar geologic units: Chronological standard for the inner solar system. Chronology and evolution of Mars, pp: 9–54.

Sun X, Neumann G A. 2015. Calibration of the Mercury Laser Altimeter on the MESSENGER spacecraft. IEEE Transactions on Geoscience and Remote Sensing, 53(5): 2860–2874.

Susorney H C, Barnouin O S, Ernst C M, Johnson C L. 2016. Morphometry of impact craters on Mercury from MESSENGER altimetry and imaging. Icarus, 271: 180–193.

Taguchi M, Morota T, Kato S. 2017. Lateral heterogeneity of lunar volcanic activity according to volumes of mare basalts in the farside basins. Journal of Geophysical Research: Planets, 122(7): 1505–1521.

Talwani M, Thompson G, Dent B, Kahle H G, Buck S. 1973. Traverse gravimeter experiment. Apollo 17 Preliminary Science Report.

Thomson B J, Grosfils E B, Bussey D B J, Spudis P D. 2009. A new technique for estimating the thickness of mare basalts in Imbrium Basin. Geophysical Research Letters, 36(12), doi: 10.1029/2009GL037600.

Tosi N, Grott M, Plesa A C, Breuer D. 2013. Thermochemical evolution of Mercury's interior. Journal of Geophysical Research: Planets, 118(12): 2474–2487.

Trask N J. 1971. Geologic comparison of mare materials in the lunar equatorial belt, including Apollo 11 and Apollo 12 landing sites. Geological Survey Research, US Geological Survey Professional Paper, pp: D138–D144.

Trask N J, Guest J E. 1975. Preliminary geologic terrain map of Mercury. Journal of Geophysical Research, 80(17): 2461–2477.

Vander Kaaden K E, McCubbin F M. 2015. Exotic crust formation on Mercury: Consequences of a shallow, FeO-poor mantle. Journal of Geophysical Research: Planets, 120(2): 195–209.

Watters T R, Solomon S C, Klimczak C, Freed A M, Head J W, Ernst C M, Blair D M, Goudge T A, Byrne P K. 2012. Extension and contraction within volcanically buried impact craters and basins on Mercury. Geology, 40(12): 1123–1126, doi: 10.1130/G33725.1.

Weider S Z, Crawford I A, Joy K H. 2010. Individual lava flow thicknesses in Oceanus Procellarum and Mare Serenitatis determined from Clementine multispectral data. Icarus, 209(2): 323–336, doi: 10.1029/2009GL037600.

Werner S C, Medvedev S. 2010. The Lunar rayed-crater population–Characteristics of the spatial distribution and ray retention. Earth and Planetary Science Letters, 295(1–2): 147–158, doi: 10.1016/j.epsl.2010.03.036.

Whitford-Stark J L. 1979. Charting the southern seas: The evolution of the lunar Mare Australe. Lunar and Planetary Science Conference Proceedings, 10: 2975–2994.

Williams K K, Zuber M T. 1998. Measurement and analysis of lunar basin depths from Clementine altimetry. Icarus, 131(1): 107–122.

Wilson L, Head J W. 1981. Ascent and eruption of basaltic magma on the Earth and Moon. Journal of Geophysical Research: Solid Earth, 86(B4): 2971–3001, doi: 10.1029/JB086iB04p02971.

Wilson L, Head J W. 2017. Generation, ascent and eruption of magma on the Moon: New insights into source depths, magma supply, intrusions and effusive/explosive eruptions (Part 1: Theory). Icarus, 283: 146–175, doi: 10.1016/j.icarus.2016.05.031.

Wöhler C, Lena R, Geologic Lunar Research (GLR) Group. 2009. Lunar intrusive domes: Morphometric analysis and laccolith modelling. Icarus, 204(2): 381–398.

Wood C A. 1973. Moon: Central peak heights and crater origins. Icarus, 20(4): 503–506, doi: 10.1016/0019-1035(73)90023-7.

Wu Y, Li L, Luo X, Lu Y, Chen Y, Pieters C M, Basilevsky A T, Head J W. 2018. Geology, tectonism and composition of the northwest Imbrium region. Icarus, 303: 67–90.

Xiao L, Zhu P, Fang G, Xiao Z, Zou Y, Zhao J, Zhao N, Yuan Y, Qiao L, Zhang X, et al. 2015. A young multilayered terrane of the northern Mare Imbrium revealed by Chang'E-3 mission. Science, 347(6227): 1226–1229, doi: 10.1126/science.1259866.

Xie M, Zhu M H. 2016. Estimates of primary ejecta and local material for the Orientale basin: Implications for the formation and ballistic sedimentation of multi-ring basins. Earth and Planetary Science Letters, 440: 71–80, doi: 10.1016/j.epsl.2016.02.012.

Xie M, Zhu M H, Xiao Z, Wu Y, Xu A. 2017. Effect of topography degradation on crater size-frequency distributions: Implications for populations of small craters and age dating. Geophysical Research Letters, 44(20): 10171–10179, doi: 10.1002/2017GL075298.

Yingst R A, Head J W. 1997. Volumes of lunar lava ponds in South Pole-Aitken and Orientale basins: Implications for eruption conditions, transport mechanisms, and magma source regions. Journal of Geophysical Research: Planets, 102: 10909–10931.

Zhang F, Zhu M H, Bugiolacchi R, Huang Q, Osinski G R, Xiao L, Zou Y L. 2018. Diversity of basaltic lunar volcanism associated with buried impact structures:

Implications for intrusive and extrusive events. Icarus, 307: 216–234, doi: 10.1016/j.icarus.2017.10.039.

Zhang J, Yang W, Hu S, Lin Y, Fang G, Li C, Peng W, Zhu S, He Z, Zhou B. 2015. Volcanic history of the Imbrium basin: A close-up view from the lunar rover Yutu. Proceedings of the National Academy of Sciences, 112(17): 5342–5347, doi: 10.1073/pnas.1503082112.

Zimbelman J R. 1998. Emplacement of long lava flows on planetary surfaces. Journal of Geophysical Research: Solid Earth, 103(B11): 27503–27516.

Zuber M T, Smith D E, Phillips R J, Solomon S C, Neumann G A, Hauck S A, Peale S J, Barnouin O S, Head J W, Johnson C L, et al. 2012. Topography of the northern hemisphere of Mercury from MESSENGER laser altimetry. Science, 336(13): 217–220.

Appendix A The Moon

A.1 Buried Crater Database

Table A.1: Database of all the partially and completely buried craters on the Moon. Crater class: A: rim-completely-exposed craters in maria; B: rim-completely-exposed craters on mare-highland boundaries; C: rim-partially-exposed craters in maria; D: rim-partially-exposed craters on mare-highland boundaries; E: rim-completely-buried craters in maria. Rim composition: M: mare; H: highland crust; Unknown: N/A.

Number	Diameter (km)	Lon. (°)	Lat. (°)	Class	Rim burial percentage (%)	Rim composition
1	1.8	41.02	6.05	A	0	M
2	2.2	38.34	14.64	A	0	M
3	2.5	-28.45	40.94	A	0	M
4	3.4	-47.50	30.90	A	0	M
5	3.4	-41.02	-2.66	A	0	H
6	3.6	-39.09	-29.37	A	0	H
7	3.7	-53.60	-4.96	A	0	H
8	3.8	-58.16	-6.35	A	0	H
9	3.8	-31.50	22.24	A	0	M
10	4.5	-49.56	50.11	A	0	M
11	5.1	-72.58	41.24	A	0	M
12	5.2	-58.86	26.63	A	0	M
13	5.3	38.47	14.35	A	0	M
14	5.6	-56.28	16.49	A	0	M
15	5.7	-54.24	47.56	A	0	H
16	6.0	104.25	25.33	A	0	M
17	6.0	-26.31	54.69	A	0	H
18	6.0	-59.96	27.78	A	0	M
19	6.0	162.44	-33.23	A	0	H
20	6.1	-31.17	5.87	A	0	M
21	6.2	-19.86	45.54	A	0	M
22	6.3	86.38	17.23	A	0	H
23	6.3	26.28	14.08	A	0	M
24	6.5	53.65	2.37	A	0	H
25	6.6	149.91	26.23	A	0	H
26	6.6	-29.34	-31.16	A	0	H
27	6.8	28.41	11.34	A	0	M
28	6.9	15.44	19.61	A	0	M

Number	Diameter (km)	Lon. (°)	Lat. (°)	Class	Rim burial percentage (%)	Rim composition
29	7.2	172.75	-17.63	A	0	H
30	7.3	58.37	-0.86	A	0	H
31	7.3	-60.10	28.96	A	0	M
32	7.5	29.31	14.81	A	0	M
33	7.5	69.65	4.41	A	0	M
34	7.6	-44.71	1.14	A	0	M
35	7.6	-43.57	4.63	A	0	M
36	7.8	-62.04	50.10	A	0	M
37	8.0	-53.34	53.80	A	0	H
38	8.3	36.92	35.46	A	0	H
39	8.5	147.35	28.74	A	0	H
40	8.9	29.19	16.22	A	0	M
41	8.9	37.88	12.06	A	0	M
42	9.0	144.66	26.84	A	0	H
43	9.2	22.94	39.05	A	0	H
44	9.2	-159.65	-36.24	A	0	H
45	9.8	-9.45	27.37	A	0	H
46	10.0	-29.48	-0.64	A	0	H
47	10.5	-52.28	53.61	A	0	H
48	10.6	59.44	-2.16	A	0	H
49	10.9	-24.10	33.74	A	0	M
50	11.0	62.25	-17.59	A	0	H
51	11.5	-75.61	17.77	A	0	H
52	11.6	-42.99	-7.88	A	0	M
53	11.7	159.62	-51.40	A	0	H
54	12.0	-68.19	46.12	A	0	M
55	12.3	20.25	14.32	A	0	H
56	12.4	50.44	-6.96	A	0	M
57	12.6	70.95	-50.16	A	0	H
58	13.5	-23.00	61.90	A	0	H
59	14.6	-36.93	20.89	A	0	M
60	14.9	20.00	4.57	A	0	M
61	17.3	146.66	27.45	A	0	H
62	17.5	61.78	-17.58	A	0	H
63	17.9	-46.57	21.66	A	0	M
64	17.9	-29.20	-1.48	A	0	H
65	20.1	-20.61	40.34	A	0	M
66	20.2	177.42	-36.73	A	0	H
67	20.4	20.11	10.49	A	0	M
68	21.9	7.34	56.01	A	0	H
69	24.5	-23.13	40.41	A	0	M
70	24.7	-31.91	-32.97	A	0	H
71	25.5	-58.79	23.38	A	0	M
72	28.1	-73.18	36.95	A	0	H
73	41.5	-50.83	11.90	A	0	M
74	45.3	-66.67	21.08	A	0	H
75	2.2	-19.89	49.88	B	0	H
76	2.3	-10.39	57.90	B	0	H
77	3.3	-71.80	33.17	B	0	H

Number	Diameter (km)	Lon. (°)	Lat. (°)	Class	Rim burial percentage (%)	Rim composition
78	3.4	2.90	16.71	B	0	H
79	3.6	-52.92	-9.15	B	0	H
80	3.7	149.71	29.50	B	0	H
81	3.7	168.06	-36.18	B	0	H
82	4.0	85.84	9.10	B	0	H
83	4.1	163.76	-58.98	B	0	H
84	4.1	18.57	6.25	B	0	H
85	4.2	68.13	8.65	B	0	H
86	4.3	71.00	19.17	B	0	H
87	4.4	-56.96	53.63	B	0	H
88	4.9	0.46	55.56	B	0	H
89	5.0	-154.32	-40.79	B	0	H
90	5.1	90.27	11.39	B	0	H
91	5.2	91.19	-0.27	B	0	H
92	5.2	147.07	-29.59	B	0	H
93	5.4	173.93	-16.50	B	0	H
94	5.4	-79.26	36.80	B	0	H
95	5.5	56.22	1.84	B	0	H
96	5.8	68.61	3.66	B	0	H
97	6.0	52.53	24.71	B	0	H
98	6.1	-33.21	-27.93	B	0	H
99	6.1	67.29	19.17	B	0	H
100	6.2	148.33	28.04	B	0	H
101	6.4	-42.73	35.38	B	0	H
102	6.4	82.18	11.50	B	0	H
103	6.6	67.83	2.44	B	0	H
104	6.7	-76.05	46.44	B	0	H
105	6.7	-21.32	55.01	B	0	H
106	6.8	70.66	7.52	B	0	H
107	6.8	-17.40	51.71	B	0	H
108	6.9	173.10	-53.52	B	0	H
109	6.9	0.54	55.73	B	0	H
110	7.1	-165.71	-51.68	B	0	H
111	7.3	174.76	-53.33	B	0	H
112	7.3	61.33	-36.80	B	0	H
113	7.4	36.02	34.10	B	0	H
114	7.4	36.21	33.90	B	0	H
115	7.5	-159.01	-36.25	B	0	H
116	7.6	-82.10	33.25	B	0	H
117	7.8	4.71	16.95	B	0	H
118	8.0	-15.22	51.53	B	0	H
119	8.1	103.20	-28.30	B	0	H
120	8.1	-30.77	-2.19	B	0	H
121	8.2	9.11	17.62	B	0	H
122	8.2	82.85	13.35	B	0	H
123	8.3	-58.72	-4.86	B	0	H
124	8.3	-171.56	-58.58	B	0	H
125	8.3	109.57	-47.67	B	0	H
126	8.4	-162.41	-51.95	B	0	H

Number	Diameter (km)	Lon. (°)	Lat. (°)	Class	Rim burial percentage (%)	Rim composition
127	8.4	109.66	-47.17	B	0	H
128	8.5	149.11	27.05	B	0	H
129	8.8	63.55	60.90	B	0	H
130	8.8	66.38	2.52	B	0	H
131	8.8	71.06	52.68	B	0	H
132	9.2	90.89	-57.50	B	0	H
133	9.2	-151.18	-34.63	B	0	H
134	9.7	63.62	8.05	B	0	H
135	9.8	71.39	55.48	B	0	H
136	9.9	-56.58	-33.47	B	0	H
137	10.0	68.77	25.44	B	0	H
138	10.1	-152.93	-34.41	B	0	H
139	10.2	-32.97	-22.06	B	0	H
140	10.3	-167.61	-44.53	B	0	H
141	10.3	89.94	-40.90	B	0	H
142	10.4	87.56	-35.32	B	0	H
143	10.5	-169.15	-51.83	B	0	H
144	10.6	-77.43	28.27	B	0	H
145	10.8	-31.17	19.96	B	0	H
146	10.9	87.22	-58.17	B	0	H
147	10.9	-174.72	-55.21	B	0	H
148	10.9	69.54	2.93	B	0	H
149	11.2	69.79	21.83	B	0	H
150	11.2	-161.84	-53.32	B	0	H
151	11.4	18.48	7.76	B	0	H
152	11.6	68.49	22.09	B	0	H
153	11.6	66.76	21.36	B	0	H
154	11.6	65.09	43.99	B	0	H
155	11.7	166.33	-52.44	B	0	H
156	11.7	41.02	17.41	B	0	H
157	11.9	37.98	40.01	B	0	H
158	12.0	85.31	-2.50	B	0	H
159	12.2	163.15	-43.39	B	0	H
160	12.2	152.35	29.62	B	0	H
161	12.3	104.43	-58.06	B	0	H
162	12.5	84.35	-54.23	B	0	H
163	12.6	73.48	-47.85	B	0	H
164	12.7	82.32	58.21	B	0	H
165	12.7	166.82	-55.43	B	0	H
166	12.9	159.64	-58.94	B	0	H
167	12.9	-143.94	-56.33	B	0	H
168	12.9	70.96	23.16	B	0	H
169	13.0	-145.51	-40.00	B	0	H
170	13.3	97.91	-37.23	B	0	H
171	13.5	-64.72	-38.12	B	0	H
172	13.6	162.01	-43.47	B	0	H
173	13.6	67.74	8.07	B	0	H
174	13.7	44.12	-17.46	B	0	H
175	13.8	66.99	2.14	B	0	H

Number	Diameter (km)	Lon. (°)	Lat. (°)	Class	Rim burial percentage (%)	Rim composition
176	13.9	30.28	57.52	B	0	H
177	14.0	-165.05	-51.58	B	0	H
178	14.1	67.90	20.09	B	0	H
179	14.3	37.37	-19.82	B	0	H
180	14.4	-174.45	-57.51	B	0	H
181	14.6	-15.28	-14.58	B	0	H
182	14.7	41.79	-4.03	B	0	H
183	14.7	103.34	-26.67	B	0	H
184	14.8	77.72	16.03	B	0	H
185	15.3	68.92	12.86	B	0	H
186	15.4	-67.76	11.41	B	0	H
187	15.4	-23.45	62.61	B	0	H
188	15.5	148.98	45.62	B	0	H
189	15.7	-90.45	-9.05	B	0	H
190	15.7	80.66	54.39	B	0	H
191	16.8	150.48	-47.90	B	0	H
192	16.9	78.23	16.71	B	0	H
193	17.0	-47.48	-37.79	B	0	H
194	17.1	173.49	-50.45	B	0	H
195	17.4	88.65	-62.44	B	0	H
196	17.7	146.17	25.75	B	0	H
197	18.1	-168.00	-58.46	B	0	H
198	18.2	-32.52	3.21	B	0	H
199	18.3	74.76	11.74	B	0	H
200	18.7	64.08	-2.20	B	0	H
201	18.8	-35.50	58.86	B	0	H
202	20.7	-45.85	-26.14	B	0	H
203	20.9	38.57	-12.33	B	0	H
204	20.9	66.91	0.72	B	0	H
205	21.4	-144.26	-39.75	B	0	H
206	21.4	173.99	-46.81	B	0	H
207	21.4	-7.05	-4.74	B	0	H
208	21.7	60.01	-0.96	B	0	H
209	21.8	93.53	-32.05	B	0	H
210	22.8	61.27	22.42	B	0	H
211	23.1	-36.66	-29.86	B	0	H
212	23.7	-73.74	27.12	B	0	H
213	24.2	64.02	-0.62	B	0	H
214	24.8	-15.23	0.92	B	0	H
215	25.0	44.63	24.73	B	0	H
216	26.2	76.72	-53.62	B	0	H
217	26.3	-149.80	-36.40	B	0	H
218	26.6	-164.55	-44.50	B	0	H
219	26.6	103.57	-46.44	B	0	H
220	27.4	-151.40	-37.63	B	0	H
221	27.7	103.14	-47.65	B	0	H
222	29.0	60.46	1.80	B	0	H
223	29.5	86.43	-37.65	B	0	H
224	30.1	45.00	-12.74	B	0	H

Number	Diameter (km)	Lon. (°)	Lat. (°)	Class	Rim burial percentage (%)	Rim composition
225	30.2	31.29	17.61	B	0	H
226	30.2	89.86	-44.54	B	0	H
227	30.2	-173.62	-57.66	B	0	H
228	31.3	-0.51	62.87	B	0	H
229	31.5	-8.20	-11.83	B	0	H
230	32.3	93.16	-51.08	B	0	H
231	33.1	110.44	-58.94	B	0	H
232	34.0	-76.77	35.74	B	0	H
233	34.7	164.27	-53.93	B	0	H
234	34.8	88.48	-44.10	B	0	H
235	35.2	160.75	-54.43	B	0	H
236	35.4	10.62	48.71	B	0	H
237	35.7	51.70	14.59	B	0	H
238	36.6	9.07	14.42	B	0	H
239	36.8	-18.93	63.38	B	0	H
240	37.1	44.05	-11.96	B	0	H
241	38.1	91.67	-0.74	B	0	H
242	39.0	73.10	8.20	B	0	H
243	39.5	86.81	-2.45	B	0	H
244	39.5	-62.80	53.42	B	0	H
245	42.4	72.13	-48.25	B	0	H
246	44.2	-15.81	-7.88	B	0	H
247	44.3	64.81	23.96	B	0	H
248	44.4	96.42	-33.52	B	0	H
249	44.9	48.78	-17.51	B	0	H
250	46.1	-26.12	-29.26	B	0	H
251	47.0	70.33	8.75	B	0	H
252	47.1	-27.90	-28.05	B	0	H
253	50.9	-31.10	-19.87	B	0	H
254	51.6	51.58	45.01	B	0	H
255	54.2	171.11	-56.48	B	0	H
256	56.5	4.63	40.27	B	0	H
257	61.3	-26.69	-34.10	B	0	H
258	70.0	41.19	-8.67	B	0	H
259	78.9	-4.04	29.73	B	0	H
260	92.0	29.84	31.83	B	0	H
261	97.7	-13.56	-29.77	B	0	H
262	101.6	-9.30	51.55	B	0	H
263	1.5	-28.99	41.75	C	17	M
264	1.7	-6.48	59.55	C	24	M
265	1.8	-45.88	35.42	C	18	M
266	1.9	-22.35	20.58	C	21	M
267	1.9	84.41	8.38	C	41	H
268	2.0	-43.72	31.65	C	41	M
269	2.1	-37.93	55.83	C	21	M
270	2.2	-22.76	21.49	C	18	M
271	2.5	-25.78	31.36	C	3	M
272	2.6	-51.87	50.47	C	28	M
273	2.6	-47.39	29.85	C	13	M

Number	Diameter (km)	Lon. (°)	Lat. (°)	Class	Rim burial percentage (%)	Rim composition
274	2.7	-53.87	29.78	C	28	H
275	2.7	-68.30	12.23	C	29	M
276	2.7	151.35	27.19	C	14	H
277	2.8	35.18	52.28	C	5	H
278	3.0	73.89	6.38	C	32	H
279	3.3	149.16	26.73	C	25	H
280	3.4	85.02	56.09	C	16	H
281	3.4	66.15	17.59	C	20	M
282	3.7	-52.05	-45.76	C	40	M
283	4.0	-68.45	-4.50	C	35	H
284	4.2	91.30	-35.70	C	14	M
285	4.2	-96.95	-19.10	C	43	M
286	4.3	-75.74	44.93	C	3	H
287	4.4	-29.09	56.55	C	25	H
288	4.5	145.34	27.43	C	21	M
289	4.5	-53.01	-3.73	C	15	H
290	4.5	-56.92	-44.40	C	34	M
291	4.5	75.64	-52.22	C	86	H
292	4.6	88.43	-35.93	C	42	H
293	4.7	-31.79	56.41	C	28	H
294	4.9	-28.36	58.17	C	83	M
295	4.9	65.89	1.53	C	7	H
296	4.9	-68.90	22.07	C	33	H
297	5.1	-41.80	-38.23	C	8	M
298	5.2	-54.76	46.71	C	32	H
299	5.3	103.79	25.59	C	2	H
300	5.3	-161.27	-50.09	C	6	H
301	5.3	-31.86	-13.14	C	50	M
302	5.3	-72.79	51.75	C	30	H
303	5.4	88.46	-1.53	C	46	H
304	5.6	68.47	8.62	C	21	H
305	5.6	92.02	11.53	C	1	M
306	5.9	-26.18	54.84	C	21	H
307	6.0	-75.39	30.54	C	51	H
308	6.0	-22.11	57.07	C	64	H
309	6.0	-50.62	37.54	C	66	M
310	6.1	-14.10	-0.43	C	31	H
311	6.1	-54.99	-8.54	C	57	H
312	6.2	-79.79	29.16	C	10	H
313	6.2	-4.21	47.74	C	61	H
314	6.2	-25.51	56.69	C	26	H
315	6.2	101.64	32.03	C	7	H
316	6.3	-53.91	47.54	C	16	H
317	6.3	-55.60	48.26	C	15	H
318	6.4	-38.02	3.46	C	35	H
319	6.4	-42.03	30.14	C	3	M
320	6.5	66.05	4.82	C	51	H
321	6.6	-22.74	56.17	C	35	H
322	6.6	64.66	1.44	C	52	M

Number	Diameter (km)	Lon. (°)	Lat. (°)	Class	Rim burial percentage (%)	Rim composition
323	6.6	90.12	12.71	C	13	H
324	7.0	-22.34	55.18	C	4	H
325	7.0	-56.43	49.40	C	18	H
326	7.0	-14.13	-0.41	C	57	H
327	7.4	-69.28	24.27	C	73	H
328	7.5	-76.67	33.74	C	56	H
329	7.5	-47.31	49.24	C	43	H
330	7.6	-57.79	-43.26	C	33	H
331	7.7	-55.58	49.00	C	53	H
332	7.8	-167.89	-51.58	C	40	H
333	7.8	88.52	2.09	C	23	M
334	8.0	68.99	8.70	C	80	H
335	8.1	-52.84	-42.82	C	0	H
336	8.2	-9.79	8.25	C	21	M
337	8.4	-31.28	55.86	C	39	H
338	8.5	23.53	17.83	C	26	M
339	8.7	-9.28	-25.94	C	54	M
340	8.8	-55.60	33.49	C	80	M
341	8.9	64.09	0.79	C	26	M
342	9.7	175.03	-49.67	C	57	H
343	9.8	37.70	18.69	C	57	M
344	10.4	61.65	-3.91	C	57	H
345	11.3	-11.49	-8.74	C	49	M
346	11.5	-71.11	21.02	C	43	H
347	12.0	-13.56	-1.37	C	32	H
348	12.6	-76.62	18.10	C	30	H
349	12.6	-70.06	36.77	C	40	M
350	12.6	-14.10	-27.37	C	35	M
351	12.8	-1.26	27.90	C	46	H
352	13.0	66.77	15.53	C	78	H
353	13.1	-45.17	-25.61	C	50	M
354	13.6	-53.30	-7.69	C	36	H
355	14.7	87.73	12.94	C	8	M
356	15.1	-25.42	5.24	C	1	M
357	15.8	146.36	26.83	C	20	H
358	17.3	35.37	4.14	C	29	H
359	17.4	85.94	-50.64	C	18	H
360	19.0	63.41	20.88	C	63	H
361	20.6	-50.92	-6.14	C	57	H
362	23.4	-46.36	35.61	C	85	H
363	25.6	-8.75	20.25	C	24	H
364	26.2	-18.86	-23.40	C	33	M
365	28.2	35.09	6.29	C	60	H
366	29.3	-68.02	32.40	C	24	M
367	31.9	0.84	35.83	C	37	M
368	35.9	43.35	-1.23	C	75	H
369	41.8	-55.67	3.57	C	88	H
370	42.4	-17.10	-19.25	C	76	H
371	65.5	-20.55	23.96	C	76	M

Number	Diameter (km)	Lon. (°)	Lat. (°)	Class	Rim burial percentage (%)	Rim composition
372	68.5	-35.41	-9.63	C	51	H
373	81.2	-46.38	-0.96	C	73	H
374	108.9	-44.15	-3.22	C	53	H
375	2.4	70.04	9.09	D	53	H
376	3.1	149.68	24.88	D	36	H
377	3.1	-13.17	-6.50	D	7	H
378	3.2	172.89	-16.08	D	8	H
379	3.3	-78.07	19.68	D	7	H
380	3.4	148.37	26.09	D	12	H
381	3.5	2.73	10.63	D	41	H
382	3.6	9.66	57.40	D	17	H
383	3.7	85.78	9.21	D	4	H
384	3.8	-37.87	56.91	D	15	H
385	3.9	66.39	7.00	D	15	H
386	4.0	149.86	45.24	D	24	H
387	4.0	81.87	-59.44	D	16	H
388	4.1	89.71	-1.55	D	50	H
389	4.1	86.99	4.26	D	8	H
390	4.1	-16.05	1.80	D	15	H
391	4.1	71.48	6.44	D	9	H
392	4.1	-15.87	2.12	D	45	H
393	4.3	-51.29	30.01	D	42	H
394	4.4	46.43	-12.58	D	15	H
395	4.5	90.73	-32.64	D	35	H
396	4.5	43.74	0.95	D	16	H
397	4.7	-160.16	-36.08	D	33	H
398	4.7	-162.21	-47.84	D	27	H
399	4.8	-81.46	26.45	D	13	H
400	4.9	70.82	52.90	D	9	H
401	5.0	89.48	-1.74	D	37	H
402	5.1	-33.31	56.83	D	20	H
403	5.2	-153.75	-36.42	D	26	H
404	5.4	150.19	45.82	D	18	H
405	5.4	-14.14	-27.93	D	32	H
406	5.5	150.42	45.88	D	26	H
407	5.5	-15.47	64.37	D	32	H
408	5.5	61.18	-37.16	D	22	H
409	5.5	-73.85	40.55	D	34	H
410	5.6	-26.02	55.13	D	25	H
411	5.7	66.75	4.00	D	40	H
412	5.7	149.20	30.62	D	39	H
413	5.8	-31.85	55.41	D	11	H
414	5.8	65.27	3.78	D	45	H
415	5.8	68.14	7.25	D	14	H
416	5.8	-50.06	47.96	D	39	H
417	5.9	-26.01	55.24	D	46	H
418	5.9	74.15	-46.98	D	8	H
419	5.9	-38.25	-9.35	D	39	H
420	6.0	-45.79	36.92	D	53	H

Number	Diameter (km)	Lon. (°)	Lat. (°)	Class	Rim burial percentage (%)	Rim composition
421	6.1	-28.61	-32.77	D	43	H
422	6.1	-77.18	38.40	D	22	H
423	6.2	-40.40	56.72	D	34	H
424	6.2	-77.15	38.63	D	5	H
425	6.2	52.16	23.97	D	14	H
426	6.2	-17.25	64.19	D	18	H
427	6.3	146.28	28.38	D	17	H
428	6.3	70.61	19.31	D	11	H
429	6.4	-37.96	54.44	D	38	H
430	6.4	75.57	15.12	D	26	H
431	6.5	175.95	19.19	D	6	H
432	6.5	-47.49	41.58	D	11	H
433	6.5	-48.18	-13.81	D	10	H
434	6.5	3.30	16.58	D	20	H
435	6.5	-25.84	54.42	D	31	H
436	6.7	92.52	-35.52	D	16	H
437	6.7	83.73	13.23	D	35	H
438	6.8	89.72	14.03	D	10	H
439	6.9	-73.94	28.88	D	21	H
440	7.0	73.56	6.51	D	26	H
441	7.2	-63.32	-39.18	D	11	H
442	7.2	71.95	5.98	D	23	H
443	7.3	-55.37	53.78	D	22	H
444	7.3	-162.01	-47.51	D	21	H
445	7.4	-10.82	-5.77	D	55	H
446	7.5	-47.08	42.72	D	56	H
447	7.6	78.22	14.37	D	1	H
448	7.7	-75.40	15.08	D	15	H
449	7.7	84.14	12.93	D	31	H
450	7.8	-26.26	-19.31	D	21	H
451	7.9	66.55	23.76	D	57	H
452	7.9	-34.02	56.05	D	20	H
453	8.0	68.94	7.04	D	37	H
454	8.1	-14.72	-23.00	D	34	H
455	8.1	57.17	-17.43	D	17	H
456	8.1	-78.16	33.45	D	24	H
457	8.1	-37.63	54.25	D	3	H
458	8.1	-77.40	38.40	D	10	H
459	8.2	-46.90	42.05	D	20	H
460	8.3	-73.63	40.49	D	70	H
461	8.3	83.98	-0.87	D	47	H
462	8.4	-162.46	-46.02	D	73	H
463	8.4	-52.14	30.74	D	55	H
464	8.5	-47.42	42.04	D	17	H
465	8.8	-47.55	42.70	D	32	H
466	8.8	-18.61	52.23	D	18	H
467	8.8	43.71	-9.21	D	18	H
468	8.9	87.30	18.64	D	18	H
469	8.9	-28.32	56.59	D	25	H

Number	Diameter (km)	Lon. (°)	Lat. (°)	Class	Rim burial percentage (%)	Rim composition
470	8.9	150.13	27.26	D	30	H
471	8.9	70.51	26.15	D	27	H
472	9.0	50.13	5.53	D	17	H
473	9.1	-33.13	-33.69	D	25	H
474	9.2	-63.91	-38.40	D	40	H
475	9.3	-35.43	-19.06	D	19	H
476	9.3	-77.21	39.36	D	25	H
477	9.5	-179.20	-35.09	D	15	H
478	9.6	-41.89	7.41	D	7	H
479	9.7	-51.33	45.48	D	30	H
480	9.7	-23.38	48.98	D	58	H
481	10.0	-46.66	39.15	D	11	H
482	10.2	-167.19	-45.76	D	1	H
483	10.4	164.38	-31.18	D	1	H
484	10.4	-43.17	-29.81	D	17	H
485	10.6	86.49	-62.80	D	29	H
486	10.8	83.96	13.24	D	25	H
487	10.8	148.15	27.84	D	19	H
488	11.0	-42.09	-54.52	D	24	H
489	11.2	66.16	24.72	D	57	H
490	11.2	167.90	-53.29	D	17	H
491	11.4	148.38	-34.53	D	6	H
492	11.4	51.30	23.46	D	31	H
493	11.9	-76.83	17.55	D	14	H
494	12.2	-73.64	29.38	D	36	H
495	12.2	-168.93	-57.32	D	20	H
496	12.3	-28.60	-33.09	D	12	H
497	12.5	158.65	-55.53	D	20	H
498	12.5	-159.10	-40.71	D	1	H
499	12.9	66.82	19.86	D	9	H
500	13.1	88.92	12.97	D	31	H
501	13.2	-25.07	-31.15	D	12	H
502	13.2	-33.16	-20.74	D	2	H
503	13.4	-74.66	16.53	D	15	H
504	13.5	79.51	12.41	D	28	H
505	13.9	70.87	26.30	D	8	H
506	14.1	145.05	-34.80	D	7	H
507	14.2	73.52	-49.77	D	21	H
508	14.4	70.82	8.43	D	11	H
509	14.7	-150.96	-34.80	D	37	H
510	14.9	40.39	33.62	D	43	H
511	15.1	65.92	42.73	D	5	H
512	15.5	50.28	47.36	D	18	H
513	15.7	14.77	15.74	D	33	H
514	15.8	80.95	-58.59	D	30	H
515	15.8	-80.82	26.94	D	48	H
516	15.9	-64.82	6.27	D	25	H
517	16.1	-158.81	-36.95	D	6	H
518	16.3	137.75	-45.22	D	18	H

Number	Diameter (km)	Lon. (°)	Lat. (°)	Class	Rim burial percentage (%)	Rim composition
519	16.6	49.82	4.00	D	32	H
520	16.7	165.97	-56.80	D	1	H
521	16.8	150.81	-47.55	D	30	H
522	16.9	64.40	12.90	D	57	H
523	17.0	86.02	-0.60	D	23	H
524	17.2	68.73	5.92	D	48	H
525	17.3	-44.47	-10.77	D	13	H
526	17.4	51.47	47.61	D	70	H
527	17.9	-7.21	-24.87	D	54	H
528	18.0	73.80	-56.07	D	17	H
529	18.0	57.55	9.95	D	5	H
530	18.1	-76.63	36.49	D	8	H
531	18.1	-33.09	-11.38	D	42	H
532	18.2	-150.25	-53.37	D	8	H
533	18.3	-57.15	-10.95	D	49	H
534	18.4	37.94	-12.23	D	9	H
535	18.5	50.87	23.21	D	49	H
536	18.5	-8.19	60.49	D	17	H
537	18.9	-158.83	-52.03	D	10	H
538	19.2	164.03	-45.59	D	38	H
539	19.6	92.10	-44.41	D	20	H
540	19.7	85.70	1.99	D	43	H
541	20.3	-15.32	-12.24	D	3	H
542	20.4	-29.74	-21.12	D	26	H
543	21.1	91.80	-31.56	D	26	H
544	21.4	-76.64	45.66	D	41	H
545	21.5	49.80	4.37	D	37	H
546	21.9	175.50	-50.19	D	4	H
547	22.0	-32.11	-23.69	D	44	H
548	22.3	17.64	5.32	D	13	H
549	22.4	-7.40	-24.14	D	50	H
550	23.0	86.90	-33.77	D	53	H
551	23.1	-51.73	-3.17	D	28	H
552	23.5	-12.94	-5.10	D	64	H
553	24.0	-39.18	-27.82	D	1	H
554	24.4	59.38	42.17	D	10	H
555	26.2	87.65	-7.58	D	4	H
556	26.6	35.19	-10.51	D	62	H
557	26.7	77.95	-55.85	D	42	H
558	26.9	49.70	50.40	D	7	H
559	26.9	53.13	-12.41	D	59	H
560	27.2	-7.54	0.20	D	22	H
561	27.6	-168.96	-50.70	D	9	H
562	28.1	-14.52	-8.88	D	30	H
563	28.1	-3.56	20.18	D	32	H
564	28.2	-60.16	51.86	D	22	H
565	28.7	-48.47	-39.69	D	14	H
566	29.0	42.43	-8.22	D	11	H
567	29.7	38.66	36.99	D	13	H

Number	Diameter (km)	Lon. (°)	Lat. (°)	Class	Rim burial percentage (%)	Rim composition
568	29.9	77.06	56.53	D	5	H
569	30.0	-25.68	-16.42	D	7	H
570	30.3	85.84	-36.33	D	2	H
571	30.9	40.21	-17.82	D	9	H
572	31.0	85.26	-63.21	D	45	H
573	31.0	-24.32	-33.47	D	51	H
574	31.2	-167.41	-49.68	D	1	H
575	32.2	52.84	12.34	D	6	H
576	32.4	7.12	35.27	D	63	H
577	32.6	-79.18	31.37	D	21	H
578	32.9	-34.96	17.56	D	41	H
579	33.1	91.07	-41.29	D	40	H
580	34.6	87.82	-6.73	D	20	H
581	34.9	39.98	7.09	D	48	H
582	36.4	-25.03	-19.47	D	71	H
583	37.2	61.80	21.95	D	40	H
584	38.0	-27.38	-16.64	D	22	H
585	38.2	-9.86	61.14	D	37	H
586	39.6	-47.75	-28.64	D	8	H
587	39.8	57.74	2.33	D	46	H
588	40.0	3.21	61.39	D	28	H
589	40.8	84.11	-1.66	D	13	H
590	43.3	-23.87	-17.90	D	4	H
591	43.6	-51.04	-4.71	D	33	H
592	44.0	93.08	-34.17	D	16	H
593	44.7	-22.59	-26.32	D	2	H
594	44.8	33.60	-11.93	D	10	H
595	46.1	-59.95	-3.87	D	48	H
596	46.3	-44.13	25.47	D	29	H
597	48.5	85.17	16.81	D	6	H
598	50.9	94.63	-45.53	D	46	H
599	55.3	88.91	-40.33	D	4	H
600	56.6	-17.42	-16.37	D	47	H
601	58.1	-67.83	55.58	D	43	H
602	59.1	30.61	26.58	D	19	H
603	59.3	-17.39	-8.34	D	39	H
604	59.6	-30.39	-24.89	D	24	H
605	59.6	36.18	16.67	D	32	H
606	63.2	94.68	-36.15	D	7	H
607	63.8	-27.70	-4.56	D	48	H
608	64.8	77.98	-51.53	D	11	H
609	64.9	-41.46	-28.43	D	17	H
610	65.3	-13.73	10.43	D	46	H
611	65.4	72.75	-52.87	D	12	H
612	65.4	-38.96	-6.68	D	56	H
613	71.8	-56.68	-8.15	D	35	H
614	77.2	92.30	-35.79	D	13	H
615	84.8	-39.75	-29.59	D	41	H
616	103.6	-75.56	26.66	D	27	H

Number	Diameter (km)	Lon. (°)	Lat. (°)	Class	Rim burial percentage (%)	Rim composition
617	110.3	-39.95	-17.57	D	0	H
618	110.9	166.36	-35.79	D	13	H
619	118.9	166.13	-32.42	D	13	H
620	119.8	33.14	-21.16	D	14	H
621	121.5	-42.50	-10.51	D	34	H
622	129.7	-72.09	21.58	D	14	H
623	1.7	147.59	28.31	E	100	N/A
624	1.8	84.47	8.23	E	100	N/A
625	1.8	-23.99	34.09	E	100	N/A
626	1.8	149.09	27.92	E	100	N/A
627	2.0	146.45	28.73	E	100	N/A
628	2.1	36.60	55.18	E	100	N/A
629	2.2	-161.24	-50.33	E	100	N/A
630	2.5	36.79	54.90	E	100	N/A
631	2.6	-15.72	54.20	E	100	N/A
632	2.7	66.13	6.18	E	100	N/A
633	2.9	-18.07	57.59	E	100	N/A
634	3.0	28.53	14.58	E	100	N/A
635	3.1	52.36	-9.37	E	100	N/A
636	3.2	148.39	29.43	E	100	N/A
637	3.2	149.94	45.07	E	100	N/A
638	3.2	148.14	29.13	E	100	N/A
639	3.4	53.91	0.34	E	100	N/A
640	3.5	67.09	7.73	E	100	N/A
641	3.6	147.80	28.88	E	100	N/A
642	3.7	147.91	29.17	E	100	N/A
643	3.7	35.59	52.60	E	100	N/A
644	3.7	83.54	-49.92	E	100	N/A
645	3.8	86.18	14.16	E	100	N/A
646	4.3	-32.11	45.00	E	100	N/A
647	4.4	21.29	23.57	E	100	N/A
648	5.4	-21.10	45.66	E	100	N/A
649	5.8	38.51	7.05	E	100	N/A
650	6.2	49.12	-2.71	E	100	N/A
651	6.3	-42.90	34.69	E	100	N/A
652	8.7	89.25	1.01	E	100	N/A
653	9.2	59.04	46.22	E	100	N/A
654	9.4	20.67	3.66	E	100	N/A
655	10.1	36.38	8.02	E	100	N/A
656	10.1	36.73	-13.85	E	100	N/A
657	11.5	35.39	-17.32	E	100	N/A
658	17.7	32.08	15.08	E	100	N/A
659	20.3	50.13	-9.35	E	100	N/A
660	24.2	49.43	-8.26	E	100	N/A
661	24.9	28.78	15.16	E	100	N/A

A.2 Mare Basalt Thickness Estimation Results

Table A.2: Lava flow thickness estimation results on the Moon from craters with rim completely exposed. D_{int}: initial crater diameter, kt_{c}: product of diffusivity and time between crater formation and lava emplacement, kt_{b}: product of diffusivity and time after lava emplacement, T_{ext}: lava flow thickness exterior to the crater rim, T_{int}: lava flow thickness interior to the crater rim, z_0: vertical offset.

Number	Diameter (km)	Lon. (°)	Lat. (°)	D_{int} (km)	kt_{c} (m^2)	kt_{b} (m^2)	T_{ext} (m)	T_{int} (m)	z_0 (m)
1	2.2	38.34	14.64	2.0	500	50072	16	271	14
2	2.5	-28.45	40.94	1.3	30100	26800	4	93	3
3	3.4	-47.50	30.90	3.0	500	57736	2	438	0
4	3.4	-41.02	-2.66	3.1	500	57046	22	467	23
5	3.6	-39.09	-29.37	3.2	19937	22587	9	540	8
6	3.7	-53.60	-4.96	3.0	52924	5500	51	0.06	52
7	3.8	-58.16	-6.35	3.5	500	62625	2	589	0
8	3.8	-31.50	22.24	3.4	500	74101	18	462	21
9	5.2	-58.86	26.63	4.7	42928	22259	90	5	90
10	5.3	38.47	14.35	4.8	65040	45174	20	54	23
11	5.6	-56.28	16.49	5.2	10000	55200	54	16	52
12	5.7	-54.24	47.56	5.2	15336	103728	67	946	69
13	6.0	104.25	25.33	5.7	500	115000	37	922	35
14	6.0	-26.31	54.69	5.5	500	124513	33	944	32
15	6.0	-59.96	27.78	5.8	500	25419	88	0	88

Number	Diameter (km)	Lon. (°)	Lat. (°)	D_{int} (km)	kt_{c} (m^2)	kt_{b} (m^2)	T_{ext} (m)	T_{int} (m)	z_0 (m)
16	6.0	162.44	-33.23	5.6	71290	5500	53	7	58
17	6.1	-31.17	5.87	6.1	500	61065	95	951	95
18	6.2	-19.86	45.54	6.1	500	23400	44	0	42
19	6.3	86.38	17.23	6.1	500	126149	104	518	104
20	6.3	26.28	14.08	5.8	30004	130036	33	897	31
21	6.5	53.65	2.37	6.2	500	134233	60	82	62
22	6.6	149.91	26.23	6.3	500	135035	63	968	54
23	6.8	28.41	11.34	6.5	500	139358	7	1069	0
24	6.9	15.44	19.61	6.4	109243	18743	107	0	108
25	7.2	172.75	-17.63	6.6	500	105430	33	994	35
26	7.3	58.37	-0.86	6.6	194000	10740	69	0	70
27	7.3	-60.10	28.96	6.9	500	53300	4	5	3
28	7.5	29.31	14.81	6.4	300000	151290	2	730	-3
29	7.6	-44.71	1.14	7.3	500	100256	54	89	62
30	7.6	-43.57	4.63	7.6	500	79847	105	83	100
31	7.8	-62.04	50.10	7.7	1000	25096	112	52	106
32	8.3	36.92	35.46	8.0	125783	40449	53	5	38
33	8.5	147.35	28.74	7.9	19999	169479	71	149	65
34	8.9	29.19	16.22	8.5	500	177166	29	639	8
35	8.9	37.88	12.06	8.1	500	177487	218	1123	214

Number	Diameter (km)	Lon. (°)	Lat. (°)	D_{int} (km)	kt_{c} (m^2)	kt_{b} (m^2)	T_{ext} (m)	T_{int} (m)	z_0 (m)
36	9.0	144.66	26.84	8.8	500	108810	56	1302	42
37	9.2	22.94	39.05	8.7	500	179734	135	1308	142
38	9.2	-159.65	-36.24	8.5	1021	181921	154	0	155
39	9.8	-9.45	27.37	9.4	500	193222	71	142	62
40	10.0	-29.48	-0.64	9.9	500	147566	116	1830	105
41	10.5	-52.28	53.61	9.8	500	205825	95	1430	92
42	10.6	59.44	-2.16	10.5	500	206450	195	93	202
43	11.5	-75.61	17.77	10.8	25894	196980	122	1929	120
44	11.6	-42.99	-7.88	11.5	500	32200	131	109	125
45	11.7	159.62	-51.40	11.2	40000	125600	205	1929	205
46	12.4	50.44	-6.96	11.9	500	238544	310	1136	307
47	12.6	70.95	-50.16	12.1	500	242820	126	1963	114
48	13.5	-23.00	61.90	13.4	500	51312	65	2052	64
49	17.3	146.66	27.45	16.4	500	224746	198	2907	208
50	17.5	61.78	-17.58	16.4	500	325710	95	2674	86
51	17.9	-46.57	21.66	17.7	500	230976	208	1987	197
52	17.9	-29.20	-1.48	17.4	500	83929	105	2950	104
53	20.2	177.42	-36.73	19.6	500	100073	126	3652	123
54	20.4	20.11	10.49	19.9	500	278911	114	1286	108
55	24.5	-23.13	40.41	24.5	500	140840	380	260	382

Number	Diameter (km)	Lon. (°)	Lat. (°)	D_{int} (km)	kt_{c} (m^2)	kt_{b} (m^2)	T_{ext} (m)	T_{int} (m)	z_0 (m)
56	24.7	-31.91	-32.97	23.8	500	444196	146	3321	140
57	25.5	-58.79	23.38	25.2	500	221488	247	0	232
58	45.3	-66.67	21.08	45.2	85031	680051	455	857	435

Table A.3: Uncertainties of the lava flow thickness and the diffusivity-time product. $T_{\text{ext\_min}}$ and $T_{\text{ext\_min}}$: minimum and maximum values of T_{ext}. $kt_{\text{b\_min}}$ and $kt_{\text{b_max}}$minimum and maximum values of kt_{b}.

Number	RMS misfit (m)	$T_{\text{ext\_min}}$ (m)	$T_{\text{ext\_max}}$ (m)	$kt_{\text{b\_min}}$ (m^2)	$kt_{\text{b\_max}}$ (m^2)
1	3	0	35	30043	85122
2	1	0	14	18760	40200
3	5	0	21	32564	75057
4	3	0	40	45637	74160
5	2	0	29	11294	38399
6	3	30	67	550	10450
7	5	0	23	61363	87044
8	4	0	39	59281	81511
9	4	60	121	2226	40066
10	6	0	52	4517	85831
11	16	14	93	5520	104880
12	3	35	96	62237	165964
13	3	5	69	92000	126500
14	5	4	67	99611	161867
15	10	47	122	2542	40670
16	14	16	91	550	10450

Number	RMS misfit (m)	$T_{\text{ext\_min}}$ (m)	$T_{\text{ext\_max}}$ (m)	$kt_{\text{b\_min}}$ (m^2)	$kt_{\text{b\_max}}$ (m^2)
17	2	62	127	48852	67171
18	14	0	78	2340	42120
19	8	60	143	100919	138764
20	14	0	64	117032	247068
21	12	21	100	13423	147656
22	10	23	99	108028	229559
23	9	0	45	83615	236908
24	6	66	148	1874	35611
25	15	0	73	73801	189774
26	23	16	125	1074	20406
27	9	0	47	5330	69290
28	19	0	47	121032	287451
29	9	8	99	20051	130333
30	12	57	151	31939	103801
31	35	60	161	1000	43571
32	16	2	105	4045	76852
33	29	14	133	16948	322009
34	18	0	86	106300	265749
35	16	154	259	141990	248482

Number	RMS misfit (m)	$T_{\text{ext\_min}}$ (m)	$T_{\text{ext\_max}}$ (m)	$kt_{\text{b\_min}}$ (m^2)	$kt_{\text{b\_max}}$ (m^2)
36	18	0	106	76167	256739
37	12	84	183	125814	233654
38	25	85	220	18192	218305
39	18	11	130	19322	251189
40	11	63	172	44270	280376
41	15	31	145	185243	391068
42	22	127	258	20645	289031
43	4	68	177	157584	256075
44	27	61	200	10000	69950
45	29	136	276	100480	238640
46	16	220	378	214689	262398
47	20	46	195	169974	437076
48	33	0	148	25656	97493
49	25	110	296	22475	427017
50	29	6	188	32571	618849
51	11	120	301	138586	300269
52	29	8	201	8393	159465
53	15	23	223	10007	190138
54	6	12	220	139456	334694

Number	RMS misfit (m)	$T_{\text{ext\_min}}$ (m)	$T_{\text{ext\_max}}$ (m)	$kt_{\text{b\_min}}$ (m^2)	$kt_{\text{b\_max}}$ (m^2)
55	34	249	512	56336	239428
56	36	11	276	355357	843973
57	44	104	384	22149	376529
58	49	208	797	493574	1035361

Table A.4: The basaltic units that embayed the studied partially buried craters. The unit number, age, and area are taken from Hiesinger et al. (2006, 2011); Morota et al. (2009, 2011a); Pasckert et al. (2018).

Crater number	Basaltic unit number	Age (Gyr)	Age lower bound (Gyr)	Age upper bound (Gyr)	Area (km^2)
1	T19	3.6	3.57	3.68	7232
2	I22	1.98	1.89	2.06	8117
3	P40	2.56	2.41	2.7	3266
4	P24	2.6	2.4	2.78	6330
5	H2	3.69	3.66	3.72	1116
6	P33	2.47	2.26	2.66	1855
7	P36	2.48	1.98	2.9	1082
8	I4	2.04	1.92	2.15	1719
9	P32	1.79	1.69	1.89	6475
10	T21	3.57	3.52	3.6	11074
11	P49	1.71	1.6	1.81	4822
12	P10	3.44	3.37	3.51	8419
13	N/A	N/A	N/A	N/A	N/A
14	F17	3.53	3.46	3.58	6558
15	P32	1.79	1.69	1.89	6475
16	N/A	N/A	N/A	N/A	N/A
17	In2	3.14	3.02	3.29	2861
18	I5	3.52	3.44	3.58	7531

Crater number	Basaltic unit number	Age (Gyr)	Age lower bound (Gyr)	Age upper bound (Gyr)	Area (km^2)
19	Ma2	3.62	3.58	3.65	14599
20	T5	3.74	3.69	3.77	3122
21	Fe8	3.36	3.16	3.56	15488
22	Ehtm	2.57	2.32	2.86	2544
23	T8	3.7	3.64	3.74	3132
24	S13	3.49	3.44	3.57	10173
25	Ai	3.3	3.24	3.35	1440
26	Fe9	3.58	3.48	3.68	7341
27	P53	2.1	1.99	2.21	5886
28	T2	3.76	3.69	3.78	2455
29	P47	2.19	2.01	2.37	1665
30	P47	2.19	2.01	2.37	1665
31	P10	3.44	3.37	3.51	8419
32	N/A	N/A	N/A	N/A	N/A
33	Iltm	3.49	3.44	3.54	3246
34	T10	3.69	3.61	3.71	4837
35	T21	3.57	3.52	3.6	11074
36	Iltm	3.49	3.44	3.54	3246
37	N/A	N/A	N/A	N/A	N/A
38	Ap6	3.39	3.37	3.41	2122

Crater number	Basaltic unit number	Age (Gyr)	Age lower bound (Gyr)	Age upper bound (Gyr)	Area (km^2)
39	I3	3.55	3.48	3.6	3106
40	P8	3.47	3.38	3.55	2525
41	P10	3.44	3.37	3.51	8419
42	N/A	N/A	N/A	N/A	N/A
43	N/A	N/A	N/A	N/A	N/A
44	P11	3.43	3.35	3.52	2383
45	Ho	3.5	3.47	3.53	1450
46	Fe1	3.47	3.27	3.67	95727
47	N/A	N/A	N/A	N/A	N/A
48	F28	3.45	3.34	3.52	6763
49	Iltm	3.49	3.44	3.54	3246
50	N/A	N/A	N/A	N/A	N/A
51	P60	1.73	1.59	1.86	1429
52	P8	3.47	3.38	3.55	2525
53	Le1	3.37	3.33	3.4	1740
54	T12	3.68	3.64	3.71	11252
55	I22	1.98	1.89	2.06	8117
56	N/A	N/A	N/A	N/A	N/A
57	P32	1.79	1.69	1.89	6475
58	P14	3.36	3.27	3.41	7939

Appendix B Mercury

B.1 Buried Crater Database

Table B.1: Database of all the partially and completely buried craters on Mercury. Crater class: A: rim-completely-exposed craters in the northern smooth plains; B: rim-completely-exposed craters on the northern smooth plains-heavily cratered terrain boundaries; C: rim-partially-exposed craters in the northern smooth plains; D: rim-partially-exposed craters on the northern smooth plains-heavily cratered terrain boundaries; E: rim-completely-buried craters in the northern smooth plains.

Number	Diameter (km)	Lon. (°)	Lat. (°)	Class	Rim burial percentage (%)
1	15.2	-113.20	77.77	A	0
2	18.9	-28.53	60.23	A	0
3	30.6	51.98	54.26	A	0
4	31.6	2.83	43.24	A	0
5	51.3	12.83	49.77	A	0
6	53.5	3.41	49.38	A	0
7	56.1	-26.46	57.29	A	0
8	5.2	25.99	40.40	B	0
9	7.6	25.67	40.33	B	0
10	8.4	9.85	30.76	B	0
11	9.1	0.45	31.27	B	0
12	9.4	143.08	72.54	B	0
13	10.1	80.74	35.17	B	0
14	10.1	48.82	38.01	B	0
15	10.6	29.96	41.10	B	0
16	10.6	19.25	49.48	B	0
17	10.7	61.18	39.27	B	0
18	11.0	-30.25	59.36	B	0

Number	Diameter (km)	Lon. (°)	Lat. (°)	Class	Rim burial percentage (%)
19	11.9	91.94	70.21	B	0
20	12.5	16.11	45.85	B	0
21	12.8	-2.83	32.61	B	0
22	14.2	15.77	42.53	B	0
23	15.4	63.39	39.18	B	0
24	17.6	15.64	45.82	B	0
25	18.4	-31.67	59.87	B	0
26	18.8	30.25	40.67	B	0
27	19.2	44.64	36.97	B	0
28	19.9	101.27	50.80	B	0
29	20.1	-85.79	82.62	B	0
30	20.9	-109.10	71.38	B	0
31	25.0	29.23	42.83	B	0
32	29.1	-1.56	32.30	B	0
33	29.4	100.99	45.62	B	0
34	29.8	-89.03	63.72	B	0
35	31.6	-134.65	83.57	B	0
36	32.9	-22.02	58.06	B	0
37	34.3	60.71	47.77	B	0
38	34.7	32.58	40.13	B	0
39	36.5	-104.70	70.32	B	0
40	38.8	27.09	49.15	B	0
41	40.0	-21.53	47.42	B	0
42	40.3	-34.21	55.94	B	0
43	42.0	-30.65	46.92	B	0
44	42.6	67.23	49.78	B	0
45	44.2	16.94	45.39	B	0
46	44.9	17.29	38.21	B	0
47	44.9	21.12	40.88	B	0
48	47.3	50.71	38.48	B	0
49	49.1	-5.31	33.76	B	0
50	56.5	12.23	42.46	B	0
51	58.7	-90.52	64.67	B	0
52	59.0	-23.85	46.75	B	0

Number	Diameter (km)	Lon. (°)	Lat. (°)	Class	Rim burial percentage (%)
53	65.5	19.05	39.63	B	0
54	72.0	-99.94	66.31	B	0
55	75.9	-31.50	61.04	B	0
56	78.4	9.56	43.33	B	0
57	79.7	83.54	60.41	B	0
58	81.1	-10.78	53.53	B	0
59	110.7	-33.89	48.21	B	0
60	4.9	10.20	30.76	C	17
61	5.1	27.67	40.69	C	22
62	5.4	-75.94	86.29	C	24
63	5.7	21.06	42.19	C	11
64	5.8	-106.75	70.85	C	66
65	6.6	27.63	40.93	C	7
66	7.0	-57.35	71.28	C	21
67	7.2	113.17	73.40	C	66
68	7.2	27.75	41.17	C	48
69	7.4	-87.37	63.41	C	25
70	7.4	21.38	42.16	C	8
71	7.8	-4.75	36.72	C	22
72	8.9	21.18	38.59	C	12
73	8.9	-83.10	72.00	C	29
74	9.3	-115.05	83.27	C	52
75	9.4	26.65	50.50	C	63
76	9.6	-109.58	83.24	C	24
77	9.7	20.84	42.21	C	24
78	9.8	-101.07	86.03	C	69
79	9.9	-127.68	85.55	C	56
80	10.0	128.31	78.69	C	23
81	10.0	-26.67	47.73	C	70
82	10.1	97.15	73.17	C	37
83	10.4	-27.49	82.82	C	64
84	10.4	-115.28	80.19	C	65
85	10.5	18.04	48.75	C	22
86	10.5	-119.95	80.35	C	75

Number	Diameter (km)	Lon. (°)	Lat. (°)	Class	Rim burial percentage (%)
87	10.5	-108.33	76.50	C	88
88	10.8	-16.52	55.50	C	8
89	11.0	-21.82	52.33	C	67
90	11.5	-26.93	82.53	C	69
91	12.2	-105.79	82.45	C	52
92	12.3	-106.83	71.59	C	45
93	12.6	-104.11	83.84	C	63
94	13.0	126.12	68.56	C	68
95	13.1	-72.03	78.12	C	33
96	14.8	35.17	38.50	C	81
97	14.8	-124.06	82.62	C	25
98	15.1	12.22	62.66	C	29
99	15.2	142.13	74.83	C	35
100	15.4	55.03	55.41	C	61
101	15.6	20.91	42.67	C	6
102	16.0	53.74	54.68	C	24
103	16.5	138.30	85.28	C	35
104	16.9	-111.34	85.06	C	34
105	17.8	-20.71	52.42	C	29
106	17.8	-100.90	67.98	C	19
107	20.0	122.72	73.96	C	72
108	20.5	7.49	51.27	C	47
109	20.6	-105.45	74.10	C	37
110	21.1	-27.60	47.56	C	23
111	21.3	26.21	50.81	C	41
112	22.2	5.97	45.12	C	22
113	22.9	108.17	73.85	C	22
114	23.2	-22.25	59.59	C	41
115	23.4	-29.30	49.67	C	62
116	24.6	4.64	52.02	C	83
117	24.6	12.06	47.13	C	12
118	26.1	7.90	46.54	C	71
119	26.4	49.15	39.30	C	40
120	27.2	-6.01	52.90	C	61

Number	Diameter (km)	Lon. (°)	Lat. (°)	Class	Rim burial percentage (%)
121	28.6	-103.42	74.39	C	17
122	29.4	-99.13	70.97	C	50
123	31.6	98.24	47.81	C	21
124	33.5	-23.60	59.19	C	50
125	34.1	11.02	49.34	C	31
126	37.7	4.52	43.57	C	50
127	38.2	4.68	44.11	C	56
128	38.3	14.56	51.67	C	55
129	39.6	-31.42	79.64	C	84
130	48.2	124.46	73.33	C	86
131	48.5	1.51	40.76	C	46
132	49.7	-67.56	69.80	C	60
133	50.4	115.23	82.56	C	27
134	50.7	49.82	51.25	C	30
135	51.6	0.32	64.13	C	46
136	55.0	34.78	52.59	C	56
137	56.7	140.30	74.31	C	12
138	57.1	1.37	32.32	C	35
139	59.0	-20.90	59.75	C	44
140	59.5	-73.34	74.35	C	84
141	59.8	-18.79	68.32	C	87
142	61.1	-111.53	82.37	C	43
143	62.1	-100.79	76.29	C	53
144	76.0	11.72	63.51	C	34
145	82.2	-22.08	64.53	C	45
146	100.4	-30.53	54.55	C	36
147	103.1	43.51	39.84	C	72
148	126.6	-1.38	65.46	C	75
149	217.4	14.00	67.11	C	70
150	6.6	21.32	39.58	D	21
151	7.3	-87.59	63.50	D	31
152	7.4	-28.78	59.51	D	1
153	7.6	96.98	44.66	D	45
154	7.6	9.68	30.94	D	14

Number	Diameter (km)	Lon. (°)	Lat. (°)	Class	Rim burial percentage (%)
155	7.8	126.12	68.08	D	1
156	7.8	143.82	74.02	D	3
157	8.1	-74.64	63.17	D	59
158	8.3	127.11	70.00	D	62
159	8.8	-129.10	82.88	D	15
160	9.1	-75.04	79.89	D	20
161	9.1	34.16	50.57	D	6
162	9.6	102.19	52.31	D	31
163	10.3	139.77	67.48	D	22
164	10.4	122.52	68.86	D	18
165	10.4	147.34	74.86	D	17
166	10.4	127.06	69.04	D	21
167	10.7	-120.24	84.70	D	5
168	11.1	-96.91	65.27	D	3
169	11.1	102.51	47.75	D	7
170	11.2	135.63	68.55	D	11
171	11.2	27.11	41.43	D	26
172	11.5	80.74	35.55	D	24
173	11.6	20.54	48.40	D	13
174	11.7	137.15	71.16	D	27
175	11.8	19.28	48.58	D	55
176	12.0	-60.21	66.92	D	3
177	12.2	-60.36	67.20	D	1
178	12.3	122.59	70.23	D	8
179	12.5	80.19	35.74	D	74
180	12.7	-75.84	83.15	D	21
181	13.1	-121.70	84.88	D	33
182	13.1	-34.93	65.99	D	41
183	13.1	19.10	51.37	D	37
184	13.3	-125.76	85.17	D	60
185	13.5	19.99	48.70	D	27
186	14.3	90.66	60.74	D	9
187	14.4	49.04	38.55	D	2
188	15.6	127.71	68.94	D	22

Number	Diameter (km)	Lon. (°)	Lat. (°)	Class	Rim burial percentage (%)
189	15.8	101.62	52.13	D	4
190	17.4	93.87	44.52	D	36
191	17.7	48.14	38.17	D	4
192	18.9	-28.26	59.81	D	33
193	19.2	74.99	50.57	D	18
194	19.9	15.32	64.12	D	58
195	19.9	140.04	66.96	D	11
196	20.4	-59.44	67.36	D	1
197	20.6	65.50	50.89	D	29
198	20.9	145.92	67.24	D	25
199	21.0	75.90	38.45	D	46
200	21.2	-102.89	70.04	D	31
201	23.1	102.32	46.67	D	15
202	23.5	-129.71	82.49	D	1
203	23.9	-3.85	34.22	D	7
204	23.9	35.26	48.68	D	40
205	24.0	-107.46	72.29	D	9
206	24.6	134.24	82.77	D	16
207	25.7	65.55	50.51	D	18
208	25.7	9.57	62.67	D	67
209	26.5	99.85	46.03	D	26
210	28.9	-136.70	84.96	D	54
211	28.9	121.23	67.60	D	37
212	29.3	74.86	46.21	D	40
213	29.4	108.17	59.12	D	26
214	30.3	-128.47	81.73	D	35
215	32.5	129.04	69.24	D	59
216	33.2	-30.38	59.87	D	19
217	33.3	125.51	80.17	D	2
218	33.8	75.44	50.97	D	13
219	34.8	143.52	65.95	D	12
220	36.6	-107.00	70.20	D	1
221	36.8	81.27	36.75	D	28
222	37.7	-141.74	84.47	D	1

Number	Diameter (km)	Lon. (°)	Lat. (°)	Class	Rim burial percentage (%)
223	37.9	63.84	39.45	D	10
224	42.2	-65.83	64.28	D	14
225	44.9	-128.78	84.30	D	36
226	45.3	129.61	70.00	D	6
227	45.5	80.97	45.77	D	22
228	46.7	18.98	50.43	D	38
229	47.0	-3.82	34.87	D	1
230	47.4	9.70	41.87	D	7
231	47.7	109.84	59.04	D	27
232	48.9	21.51	49.39	D	32
233	50.1	70.02	50.57	D	2
234	51.2	113.88	65.80	D	4
235	53.7	-30.49	66.06	D	61
236	60.9	140.98	71.18	D	6
237	61.8	32.98	51.08	D	14
238	63.8	110.07	62.40	D	38
239	64.3	5.66	30.73	D	39
240	64.7	43.82	37.88	D	62
241	66.2	85.88	62.55	D	29
242	67.7	56.74	40.35	D	57
243	68.5	51.57	52.70	D	29
244	71.7	112.24	61.76	D	43
245	75.6	74.38	47.67	D	12
246	87.0	82.72	37.42	D	27
247	92.7	40.41	38.10	D	49
248	113.7	118.07	65.91	D	12
249	120.3	118.54	69.60	D	26
250	136.4	-80.84	64.55	D	32
251	142.2	57.46	53.14	D	13
252	152.8	57.22	50.00	D	18
253	208.1	73.20	37.57	D	7
254	225.5	103.03	58.81	D	10
255	229.5	94.35	62.04	D	2
256	306.7	102.15	70.40	D	14

Number	Diameter (km)	Lon. (°)	Lat. (°)	Class	Rim burial percentage (%)
257	322.8	-52.07	81.43	D	69
258	2.6	-80.53	79.57	E	100
259	2.7	81.14	36.10	E	100
260	3.1	9.47	31.63	E	100
261	3.1	-80.92	79.69	E	100
262	3.2	132.02	74.24	E	100
263	3.6	-88.98	78.92	E	100
264	3.6	-28.61	56.08	E	100
265	3.7	-106.93	70.56	E	100
266	3.7	81.45	36.64	E	100
267	3.7	-64.82	66.28	E	100
268	3.7	133.61	74.32	E	100
269	3.7	97.03	42.95	E	100
270	3.8	-25.17	55.15	E	100
271	3.8	81.31	36.12	E	100
272	3.9	13.80	41.43	E	100
273	4.0	-86.72	63.67	E	100
274	4.0	101.11	46.79	E	100
275	4.0	-109.85	78.04	E	100
276	4.1	95.38	42.54	E	100
277	4.1	65.52	60.88	E	100
278	4.1	28.41	54.88	E	100
279	4.1	19.40	48.07	E	100
280	4.2	3.19	40.95	E	100
281	4.3	36.64	44.55	E	100
282	4.4	-86.91	65.03	E	100
283	4.4	24.06	52.20	E	100
284	4.4	79.87	35.46	E	100
285	4.5	28.25	51.95	E	100
286	4.5	14.59	46.39	E	100
287	4.5	19.20	48.23	E	100
288	4.5	35.51	50.89	E	100
289	4.5	-4.70	58.27	E	100
290	4.5	30.11	52.92	E	100

Number	Diameter (km)	Lon. (°)	Lat. (°)	Class	Rim burial percentage (%)
291	4.6	60.41	39.76	E	100
292	4.6	-89.87	80.03	E	100
293	4.7	-107.99	71.21	E	100
294	4.7	2.17	63.43	E	100
295	4.7	14.24	39.44	E	100
296	4.7	17.19	51.24	E	100
297	4.7	37.44	50.38	E	100
298	4.7	10.21	40.40	E	100
299	4.7	61.55	40.44	E	100
300	4.7	9.52	58.10	E	100
301	4.8	-105.39	78.62	E	100
302	4.8	61.69	40.43	E	100
303	4.8	-3.34	60.08	E	100
304	4.9	-25.98	67.25	E	100
305	4.9	-30.30	66.35	E	100
306	4.9	61.61	40.33	E	100
307	4.9	1.95	33.26	E	100
308	4.9	2.15	41.72	E	100
309	5.0	-17.65	65.10	E	100
310	5.0	-24.70	60.09	E	100
311	5.0	24.30	49.95	E	100
312	5.0	20.20	53.00	E	100
313	5.0	-24.09	55.42	E	100
314	5.0	101.14	48.35	E	100
315	5.0	61.15	54.25	E	100
316	5.1	50.42	52.17	E	100
317	5.1	131.31	74.07	E	100
318	5.1	-20.55	63.12	E	100
319	5.2	-122.03	80.99	E	100
320	5.2	73.16	43.56	E	100
321	5.2	-107.10	77.54	E	100
322	5.2	-104.85	77.24	E	100
323	5.2	65.27	52.41	E	100
324	5.2	-111.97	78.50	E	100

Number	Diameter (km)	Lon. (°)	Lat. (°)	Class	Rim burial percentage (%)
325	5.3	-24.75	59.11	E	100
326	5.3	-82.56	74.90	E	100
327	5.3	9.71	32.14	E	100
328	5.3	65.23	52.31	E	100
329	5.3	122.77	76.47	E	100
330	5.3	30.05	53.19	E	100
331	5.3	-72.00	64.26	E	100
332	5.4	62.92	51.14	E	100
333	5.4	-26.50	64.14	E	100
334	5.4	-50.15	75.17	E	100
335	5.4	-1.74	55.79	E	100
336	5.4	5.74	73.40	E	100
337	5.5	-17.93	65.04	E	100
338	5.5	126.97	76.89	E	100
339	5.5	6.85	62.69	E	100
340	5.5	-64.91	65.94	E	100
341	5.5	39.99	51.05	E	100
342	5.5	-45.63	76.40	E	100
343	5.5	-11.73	70.60	E	100
344	5.5	-46.63	76.43	E	100
345	5.5	65.11	52.13	E	100
346	5.6	-19.91	62.88	E	100
347	5.6	0.57	36.53	E	100
348	5.6	-74.33	70.52	E	100
349	5.6	2.87	74.87	E	100
350	5.6	-8.18	55.42	E	100
351	5.6	-92.58	66.04	E	100
352	5.7	-4.36	54.77	E	100
353	5.7	-24.86	61.88	E	100
354	5.7	-107.53	77.15	E	100
355	5.8	101.59	74.78	E	100
356	5.8	72.55	42.37	E	100
357	5.8	-5.16	56.13	E	100
358	5.8	17.09	52.36	E	100

Number	Diameter (km)	Lon. (°)	Lat. (°)	Class	Rim burial percentage (%)
359	5.8	4.73	74.86	E	100
360	5.8	-25.07	62.07	E	100
361	5.8	-75.39	71.49	E	100
362	5.8	19.57	52.71	E	100
363	5.8	-27.86	69.33	E	100
364	5.8	-26.82	64.91	E	100
365	5.9	95.39	42.76	E	100
366	5.9	-25.22	73.70	E	100
367	6.0	10.97	50.99	E	100
368	6.0	47.20	51.45	E	100
369	6.0	36.55	45.16	E	100
370	6.0	7.77	60.40	E	100
371	6.0	2.33	31.42	E	100
372	6.1	98.89	40.79	E	100
373	6.1	-91.13	86.14	E	100
374	6.2	72.63	42.80	E	100
375	6.2	-1.24	59.40	E	100
376	6.2	20.36	53.35	E	100
377	6.2	5.37	75.25	E	100
378	6.2	-4.97	73.15	E	100
379	6.2	-0.82	40.06	E	100
380	6.2	-75.29	77.59	E	100
381	6.2	-63.98	66.92	E	100
382	6.2	-16.91	65.77	E	100
383	6.2	-30.78	67.86	E	100
384	6.2	64.88	60.28	E	100
385	6.3	7.43	31.97	E	100
386	6.3	64.17	62.73	E	100
387	6.3	10.85	47.94	E	100
388	6.3	34.78	44.02	E	100
389	6.3	-86.33	72.43	E	100
390	6.3	-8.53	78.23	E	100
391	6.4	-94.81	86.13	E	100
392	6.4	-114.74	81.40	E	100

Number	Diameter (km)	Lon. (°)	Lat. (°)	Class	Rim burial percentage (%)
393	6.4	4.17	60.44	E	100
394	6.4	25.56	52.55	E	100
395	6.4	-81.33	79.71	E	100
396	6.4	2.20	36.30	E	100
397	6.5	82.94	37.58	E	100
398	6.5	-110.68	78.00	E	100
399	6.5	-85.89	64.11	E	100
400	6.6	25.56	60.60	E	100
401	6.6	-92.19	65.54	E	100
402	6.6	61.26	64.52	E	100
403	6.6	-24.99	62.24	E	100
404	6.7	-87.22	73.57	E	100
405	6.7	4.72	60.96	E	100
406	6.7	-106.03	77.52	E	100
407	6.8	-24.45	61.66	E	100
408	6.8	129.94	75.37	E	100
409	6.8	62.08	56.32	E	100
410	6.8	101.32	52.43	E	100
411	6.8	37.37	51.80	E	100
412	6.8	12.06	50.81	E	100
413	6.8	104.58	75.73	E	100
414	6.8	4.41	58.14	E	100
415	6.9	9.12	31.64	E	100
416	6.9	-1.66	33.64	E	100
417	6.9	-43.27	75.39	E	100
418	6.9	-98.18	67.78	E	100
419	6.9	-86.09	67.42	E	100
420	6.9	19.15	47.26	E	100
421	6.9	38.81	51.51	E	100
422	6.9	-72.58	64.82	E	100
423	7.0	-29.25	57.92	E	100
424	7.0	-102.43	70.38	E	100
425	7.0	-74.49	71.74	E	100
426	7.0	38.45	50.45	E	100

Number	Diameter (km)	Lon. (°)	Lat. (°)	Class	Rim burial percentage (%)
427	7.0	28.71	55.49	E	100
428	7.0	-6.77	77.28	E	100
429	7.0	49.24	50.37	E	100
430	7.0	7.71	77.36	E	100
431	7.0	24.80	56.53	E	100
432	7.0	1.40	31.30	E	100
433	7.0	118.80	65.39	E	100
434	7.1	61.37	64.74	E	100
435	7.1	64.74	51.62	E	100
436	7.1	-95.68	76.58	E	100
437	7.1	48.47	54.03	E	100
438	7.1	-83.72	66.92	E	100
439	7.1	8.72	34.24	E	100
440	7.1	62.90	60.40	E	100
441	7.1	-39.46	77.42	E	100
442	7.1	7.51	77.20	E	100
443	7.1	1.12	61.22	E	100
444	7.1	-10.23	65.70	E	100
445	7.1	-68.14	65.75	E	100
446	7.2	-38.52	68.51	E	100
447	7.2	22.65	83.13	E	100
448	7.2	2.54	33.36	E	100
449	7.3	51.99	55.22	E	100
450	7.3	45.85	52.64	E	100
451	7.3	2.22	33.09	E	100
452	7.3	-65.47	72.71	E	100
453	7.3	51.44	58.61	E	100
454	7.4	83.12	36.90	E	100
455	7.4	-27.80	69.15	E	100
456	7.4	-32.21	68.66	E	100
457	7.5	10.42	38.01	E	100
458	7.5	81.11	37.64	E	100
459	7.5	0.55	41.60	E	100
460	7.5	-112.79	84.19	E	100

Number	Diameter (km)	Lon. (°)	Lat. (°)	Class	Rim burial percentage (%)
461	7.5	43.54	54.57	E	100
462	7.5	51.61	48.74	E	100
463	7.5	-2.77	61.07	E	100
464	7.5	-63.88	70.44	E	100
465	7.6	64.03	51.57	E	100
466	7.6	20.73	61.78	E	100
467	7.6	99.59	41.48	E	100
468	7.6	45.86	52.78	E	100
469	7.6	17.77	78.19	E	100
470	7.6	133.32	71.00	E	100
471	7.6	129.72	77.55	E	100
472	7.7	24.33	49.66	E	100
473	7.7	107.69	70.07	E	100
474	7.7	-24.71	55.93	E	100
475	7.8	-98.48	84.60	E	100
476	7.8	-50.02	71.98	E	100
477	7.8	-57.26	78.56	E	100
478	7.8	-89.14	72.59	E	100
479	7.8	65.60	66.03	E	100
480	7.9	4.16	57.27	E	100
481	7.9	-112.39	79.25	E	100
482	7.9	19.06	62.58	E	100
483	7.9	14.98	50.81	E	100
484	8.0	11.27	78.47	E	100
485	8.0	-111.62	84.02	E	100
486	8.0	-106.49	72.23	E	100
487	8.0	-90.26	66.82	E	100
488	8.0	-7.24	54.43	E	100
489	8.0	-108.03	77.75	E	100
490	8.1	-97.42	68.99	E	100
491	8.1	-7.13	71.04	E	100
492	8.1	-89.65	66.64	E	100
493	8.1	79.99	37.29	E	100
494	8.1	103.32	68.35	E	100

Number	Diameter (km)	Lon. (°)	Lat. (°)	Class	Rim burial percentage (%)
495	8.2	-100.86	69.89	E	100
496	8.2	10.80	32.04	E	100
497	8.2	28.16	54.75	E	100
498	8.2	-5.80	76.44	E	100
499	8.2	-3.21	76.63	E	100
500	8.2	-15.16	75.16	E	100
501	8.3	-51.30	73.59	E	100
502	8.3	55.12	58.16	E	100
503	8.3	-48.94	71.45	E	100
504	8.3	18.06	43.48	E	100
505	8.3	-23.85	72.83	E	100
506	8.3	-29.52	58.71	E	100
507	8.3	61.97	40.69	E	100
508	8.3	63.05	55.98	E	100
509	8.3	-9.91	69.02	E	100
510	8.4	-1.23	60.63	E	100
511	8.4	24.96	56.33	E	100
512	8.4	-84.67	79.97	E	100
513	8.5	-38.54	68.31	E	100
514	8.5	-118.35	79.32	E	100
515	8.5	-52.25	71.64	E	100
516	8.5	131.94	76.19	E	100
517	8.5	-32.65	57.18	E	100
518	8.5	129.56	77.31	E	100
519	8.5	35.54	61.82	E	100
520	8.6	16.51	43.86	E	100
521	8.6	20.37	61.89	E	100
522	8.6	4.34	61.67	E	100
523	8.6	-85.84	79.84	E	100
524	8.6	28.78	54.16	E	100
525	8.7	23.15	55.70	E	100
526	8.7	-15.91	54.62	E	100
527	8.7	83.41	37.61	E	100
528	8.8	-0.81	38.77	E	100

Number	Diameter (km)	Lon. (°)	Lat. (°)	Class	Rim burial percentage (%)
529	8.8	8.95	76.26	E	100
530	8.8	-50.03	71.79	E	100
531	8.8	-100.74	78.37	E	100
532	8.9	95.64	55.93	E	100
533	8.9	-18.96	72.88	E	100
534	8.9	-4.64	58.07	E	100
535	8.9	18.89	60.93	E	100
536	9.0	-55.78	71.63	E	100
537	9.0	90.79	74.04	E	100
538	9.0	-82.95	80.08	E	100
539	9.0	66.00	65.98	E	100
540	9.1	123.92	79.03	E	100
541	9.1	36.20	43.49	E	100
542	9.1	-47.09	71.46	E	100
543	9.1	51.41	49.86	E	100
544	9.1	113.57	77.15	E	100
545	9.2	64.37	63.13	E	100
546	9.3	6.25	75.66	E	100
547	9.3	-29.66	74.36	E	100
548	9.3	29.50	60.34	E	100
549	9.3	56.50	40.07	E	100
550	9.3	6.29	61.50	E	100
551	9.3	-2.24	59.82	E	100
552	9.3	64.58	59.86	E	100
553	9.3	5.80	52.54	E	100
554	9.3	-89.47	74.99	E	100
555	9.4	1.79	83.52	E	100
556	9.4	-70.69	64.01	E	100
557	9.4	13.88	79.85	E	100
558	9.5	13.50	82.15	E	100
559	9.5	-79.18	73.34	E	100
560	9.5	-29.80	73.46	E	100
561	9.5	-73.70	64.74	E	100
562	9.6	32.12	56.18	E	100

Number	Diameter (km)	Lon. (°)	Lat. (°)	Class	Rim burial percentage (%)
563	9.6	-37.69	72.23	E	100
564	9.6	-6.85	70.84	E	100
565	9.6	-111.25	84.26	E	100
566	9.6	-111.45	82.98	E	100
567	9.7	-84.31	79.84	E	100
568	9.8	-75.63	67.01	E	100
569	9.8	-23.45	67.33	E	100
570	9.8	-25.77	69.36	E	100
571	9.8	-77.60	69.58	E	100
572	9.8	-14.23	76.43	E	100
573	9.8	-3.82	68.78	E	100
574	9.8	47.43	53.68	E	100
575	9.8	-28.14	64.40	E	100
576	9.8	17.22	50.90	E	100
577	9.9	-50.80	71.64	E	100
578	9.9	103.54	40.82	E	100
579	10.0	0.54	75.14	E	100
580	10.0	-83.14	71.75	E	100
581	10.0	10.36	41.02	E	100
582	10.1	5.70	39.66	E	100
583	10.1	-89.22	71.62	E	100
584	10.1	-16.87	70.17	E	100
585	10.1	47.53	54.01	E	100
586	10.1	0.12	74.88	E	100
587	10.1	15.93	78.46	E	100
588	10.1	8.64	76.99	E	100
589	10.2	-65.16	81.13	E	100
590	10.2	28.97	63.87	E	100
591	10.2	44.15	55.23	E	100
592	10.2	-3.25	55.44	E	100
593	10.2	-15.78	74.78	E	100
594	10.2	4.50	61.13	E	100
595	10.3	5.68	52.79	E	100
596	10.3	11.23	82.21	E	100

Number	Diameter (km)	Lon. (°)	Lat. (°)	Class	Rim burial percentage (%)
597	10.3	-47.77	71.41	E	100
598	10.3	-99.26	69.11	E	100
599	10.3	4.55	73.51	E	100
600	10.3	-30.60	57.71	E	100
601	10.3	80.61	39.24	E	100
602	10.4	30.91	52.23	E	100
603	10.4	18.39	79.18	E	100
604	10.4	-82.23	70.35	E	100
605	10.5	10.02	60.70	E	100
606	10.5	-52.84	71.52	E	100
607	10.5	9.83	47.19	E	100
608	10.5	131.94	76.36	E	100
609	10.5	-28.88	47.55	E	100
610	10.5	-91.16	66.94	E	100
611	10.6	-31.44	67.22	E	100
612	10.6	6.67	42.08	E	100
613	10.7	-63.76	66.37	E	100
614	10.7	55.76	57.29	E	100
615	10.7	-17.66	79.14	E	100
616	10.8	2.98	31.33	E	100
617	10.8	50.91	63.89	E	100
618	10.8	116.93	66.19	E	100
619	10.8	5.70	39.87	E	100
620	10.9	-56.80	71.72	E	100
621	10.9	4.98	41.78	E	100
622	10.9	-89.10	73.26	E	100
623	10.9	11.67	50.93	E	100
624	11.0	11.78	58.11	E	100
625	11.0	-74.71	72.75	E	100
626	11.0	122.49	74.92	E	100
627	11.0	-17.77	72.38	E	100
628	11.1	-26.74	69.98	E	100
629	11.1	51.49	61.00	E	100
630	11.1	-13.36	76.03	E	100

Number	Diameter (km)	Lon. (°)	Lat. (°)	Class	Rim burial percentage (%)
631	11.2	32.68	62.92	E	100
632	11.2	51.61	49.08	E	100
633	11.2	119.72	79.19	E	100
634	11.2	52.88	64.08	E	100
635	11.3	-7.81	71.06	E	100
636	11.3	-84.82	64.35	E	100
637	11.3	115.87	78.97	E	100
638	11.3	21.37	80.05	E	100
639	11.4	-42.82	74.73	E	100
640	11.4	17.05	62.56	E	100
641	11.4	4.10	32.17	E	100
642	11.4	28.75	79.12	E	100
643	11.5	12.82	82.46	E	100
644	11.5	-2.82	78.42	E	100
645	11.6	41.61	50.97	E	100
646	11.6	12.41	55.71	E	100
647	11.6	67.77	59.04	E	100
648	11.6	8.36	75.11	E	100
649	11.7	60.18	46.14	E	100
650	11.7	-6.11	80.29	E	100
651	11.7	-22.24	67.71	E	100
652	11.7	8.08	75.39	E	100
653	11.7	46.15	74.40	E	100
654	11.8	135.74	75.13	E	100
655	11.8	95.38	68.71	E	100
656	11.8	102.05	39.15	E	100
657	11.8	44.06	58.01	E	100
658	11.9	60.29	45.07	E	100
659	11.9	46.26	52.04	E	100
660	11.9	-41.74	68.29	E	100
661	12.0	-47.80	71.20	E	100
662	12.0	-40.25	76.74	E	100
663	12.0	-16.15	69.92	E	100
664	12.1	-7.66	76.55	E	100

Number	Diameter (km)	Lon. (°)	Lat. (°)	Class	Rim burial percentage (%)
665	12.1	63.83	63.79	E	100
666	12.2	-102.87	83.34	E	100
667	12.2	37.42	48.64	E	100
668	12.2	78.08	46.03	E	100
669	12.2	-58.45	72.12	E	100
670	12.3	-3.78	75.82	E	100
671	12.3	69.70	54.33	E	100
672	12.3	5.32	62.82	E	100
673	12.3	2.13	61.71	E	100
674	12.4	45.42	44.35	E	100
675	12.5	1.09	63.17	E	100
676	12.5	125.61	85.74	E	100
677	12.5	35.28	57.50	E	100
678	12.5	-87.17	64.04	E	100
679	12.5	28.03	65.31	E	100
680	12.6	52.15	66.16	E	100
681	12.6	16.69	80.89	E	100
682	12.7	25.39	77.72	E	100
683	12.7	72.40	39.26	E	100
684	12.7	-2.56	73.06	E	100
685	12.7	49.56	59.21	E	100
686	12.7	37.08	50.03	E	100
687	12.7	98.11	46.33	E	100
688	12.8	-0.32	77.22	E	100
689	12.9	-41.79	71.11	E	100
690	12.9	31.31	61.86	E	100
691	12.9	-84.00	75.34	E	100
692	12.9	-33.59	74.27	E	100
693	13.0	67.08	65.56	E	100
694	13.0	-25.56	62.60	E	100
695	13.0	-28.15	58.38	E	100
696	13.0	19.70	62.44	E	100
697	13.0	62.42	45.25	E	100
698	13.1	6.43	61.02	E	100

Number	Diameter (km)	Lon. (°)	Lat. (°)	Class	Rim burial percentage (%)
699	13.1	-29.91	69.88	E	100
700	13.2	67.15	46.69	E	100
701	13.2	-86.16	71.82	E	100
702	13.2	60.43	58.14	E	100
703	13.2	31.53	63.28	E	100
704	13.2	124.76	77.52	E	100
705	13.2	36.37	53.15	E	100
706	13.3	50.16	62.36	E	100
707	13.3	-82.17	74.16	E	100
708	13.3	47.99	51.94	E	100
709	13.3	-81.38	71.71	E	100
710	13.4	82.43	37.56	E	100
711	13.4	12.19	79.40	E	100
712	13.5	-6.50	76.50	E	100
713	13.5	70.71	47.95	E	100
714	13.5	-1.24	59.96	E	100
715	13.6	45.00	69.91	E	100
716	13.6	-39.75	72.88	E	100
717	13.7	-6.53	59.48	E	100
718	13.7	59.47	61.59	E	100
719	13.7	6.07	77.78	E	100
720	13.8	-2.11	75.44	E	100
721	13.9	7.77	65.18	E	100
722	13.9	-21.50	72.54	E	100
723	14.0	-79.11	76.81	E	100
724	14.0	50.64	43.11	E	100
725	14.0	31.42	54.63	E	100
726	14.1	-95.69	70.03	E	100
727	14.1	-4.60	80.61	E	100
728	14.1	5.08	60.47	E	100
729	14.1	18.39	52.07	E	100
730	14.2	29.12	81.58	E	100
731	14.2	3.14	35.23	E	100
732	14.3	-66.13	73.23	E	100

Number	Diameter (km)	Lon. (°)	Lat. (°)	Class	Rim burial percentage (%)
733	14.5	-25.10	63.30	E	100
734	14.5	81.69	68.77	E	100
735	14.5	-27.03	63.33	E	100
736	14.6	63.60	44.93	E	100
737	14.7	17.12	53.06	E	100
738	14.7	-4.87	55.12	E	100
739	14.7	-69.41	66.14	E	100
740	14.8	80.97	39.70	E	100
741	14.9	44.42	44.74	E	100
742	14.9	-27.32	84.40	E	100
743	15.1	16.95	63.55	E	100
744	15.3	-10.54	70.51	E	100
745	15.4	-6.86	70.41	E	100
746	15.4	24.51	58.11	E	100
747	15.6	-36.25	76.22	E	100
748	15.6	-26.20	59.93	E	100
749	15.6	10.45	50.55	E	100
750	15.7	-22.71	77.84	E	100
751	15.7	-93.57	65.00	E	100
752	15.8	0.91	36.37	E	100
753	15.8	-75.13	66.10	E	100
754	15.9	-102.60	82.39	E	100
755	15.9	-48.06	71.99	E	100
756	16.0	46.05	50.25	E	100
757	16.0	52.48	47.13	E	100
758	16.0	-12.20	77.76	E	100
759	16.1	-32.78	69.62	E	100
760	16.1	-3.56	61.06	E	100
761	16.3	30.91	55.52	E	100
762	16.3	51.00	76.36	E	100
763	16.4	-42.59	72.71	E	100
764	16.5	50.26	48.09	E	100
765	16.7	-3.85	58.14	E	100
766	16.7	22.76	59.72	E	100

Number	Diameter (km)	Lon. (°)	Lat. (°)	Class	Rim burial percentage (%)
767	16.7	50.77	50.67	E	100
768	16.7	70.36	47.75	E	100
769	16.8	40.06	56.44	E	100
770	16.8	58.40	62.38	E	100
771	17.0	76.17	79.38	E	100
772	17.0	-4.54	80.28	E	100
773	17.1	7.67	37.59	E	100
774	17.2	3.32	33.96	E	100
775	17.2	-85.81	66.56	E	100
776	17.2	47.92	57.60	E	100
777	17.6	13.21	75.04	E	100
778	17.6	105.91	39.38	E	100
779	17.6	3.74	33.61	E	100
780	17.7	49.60	59.55	E	100
781	17.9	44.59	42.59	E	100
782	17.9	39.74	67.42	E	100
783	17.9	46.60	61.20	E	100
784	18.0	53.66	42.63	E	100
785	18.0	51.03	79.59	E	100
786	18.0	40.38	67.64	E	100
787	18.2	47.13	44.90	E	100
788	18.2	58.67	62.55	E	100
789	18.2	75.60	45.55	E	100
790	18.4	51.33	46.63	E	100
791	18.5	47.25	52.32	E	100
792	18.5	66.50	45.49	E	100
793	18.6	50.26	66.21	E	100
794	18.6	89.49	74.27	E	100
795	18.6	71.81	39.15	E	100
796	18.7	41.16	47.15	E	100
797	18.7	8.41	32.94	E	100
798	18.8	97.77	51.40	E	100
799	18.8	-24.14	66.61	E	100
800	18.9	29.28	55.48	E	100

Number	Diameter (km)	Lon. (°)	Lat. (°)	Class	Rim burial percentage (%)
801	19.0	39.93	68.11	E	100
802	19.2	45.46	77.47	E	100
803	19.3	95.21	54.36	E	100
804	19.6	-85.48	65.17	E	100
805	19.7	29.18	52.40	E	100
806	19.8	120.68	74.91	E	100
807	19.8	-6.54	73.23	E	100
808	19.8	101.53	82.51	E	100
809	19.8	43.23	76.25	E	100
810	19.9	124.18	76.06	E	100
811	19.9	43.79	66.78	E	100
812	19.9	51.16	56.48	E	100
813	20.0	99.46	77.56	E	100
814	20.2	-83.60	68.90	E	100
815	20.2	65.57	60.03	E	100
816	20.3	23.12	81.68	E	100
817	20.3	-81.93	68.17	E	100
818	20.3	93.90	47.01	E	100
819	20.4	41.70	42.44	E	100
820	20.4	-44.28	71.25	E	100
821	20.6	-62.88	71.46	E	100
822	20.8	67.77	62.00	E	100
823	21.0	51.53	43.16	E	100
824	21.0	-28.51	78.02	E	100
825	21.1	20.80	37.98	E	100
826	21.2	46.38	76.86	E	100
827	21.2	33.12	65.15	E	100
828	21.2	-45.97	75.12	E	100
829	21.2	-41.89	75.44	E	100
830	21.3	37.27	67.01	E	100
831	21.3	41.52	58.07	E	100
832	21.4	-62.79	69.55	E	100
833	21.6	-28.28	59.26	E	100
834	21.6	22.85	61.25	E	100

Number	Diameter (km)	Lon. (°)	Lat. (°)	Class	Rim burial percentage (%)
835	21.7	-75.86	69.73	E	100
836	21.7	-0.20	68.29	E	100
837	21.8	22.83	59.12	E	100
838	21.9	40.26	62.15	E	100
839	21.9	38.64	80.84	E	100
840	22.0	52.32	56.19	E	100
841	22.0	39.45	45.36	E	100
842	22.0	120.30	69.61	E	100
843	22.2	-1.58	36.42	E	100
844	22.2	73.24	42.45	E	100
845	22.3	3.51	37.63	E	100
846	22.6	64.76	43.87	E	100
847	23.0	32.56	53.25	E	100
848	23.0	29.96	63.40	E	100
849	23.3	-24.21	74.04	E	100
850	23.3	74.93	66.87	E	100
851	23.4	23.09	57.52	E	100
852	23.4	6.63	39.03	E	100
853	23.5	10.32	39.71	E	100
854	23.6	99.59	81.47	E	100
855	23.7	0.67	60.78	E	100
856	23.7	66.68	65.11	E	100
857	23.7	6.18	33.56	E	100
858	23.9	12.39	51.96	E	100
859	24.0	59.05	63.60	E	100
860	24.5	-25.34	74.70	E	100
861	24.6	-31.84	75.32	E	100
862	24.9	77.41	41.95	E	100
863	24.9	130.55	72.42	E	100
864	25.1	64.75	80.73	E	100
865	25.2	35.71	54.78	E	100
866	25.2	43.97	50.20	E	100
867	25.4	52.49	69.72	E	100
868	25.5	38.09	57.09	E	100

Number	Diameter (km)	Lon. (°)	Lat. (°)	Class	Rim burial percentage (%)
869	26.6	69.85	63.29	E	100
870	26.9	-27.13	61.03	E	100
871	27.0	60.27	63.04	E	100
872	27.0	26.26	58.24	E	100
873	27.5	33.51	80.41	E	100
874	27.6	45.09	54.52	E	100
875	27.6	74.45	42.36	E	100
876	27.7	64.08	45.11	E	100
877	27.8	114.33	77.81	E	100
878	28.0	58.73	82.04	E	100
879	28.2	70.94	59.80	E	100
880	28.2	0.09	67.10	E	100
881	28.5	10.30	61.87	E	100
882	28.8	-52.63	76.40	E	100
883	29.1	-99.33	71.61	E	100
884	29.2	66.36	54.91	E	100
885	29.2	7.38	59.45	E	100
886	29.3	16.79	81.67	E	100
887	29.3	-17.36	67.17	E	100
888	29.3	57.83	62.38	E	100
889	29.6	33.23	78.69	E	100
890	29.6	67.13	62.48	E	100
891	29.7	19.73	53.11	E	100
892	29.7	-51.04	74.43	E	100
893	29.7	90.19	78.37	E	100
894	29.9	16.08	39.15	E	100
895	29.9	-28.58	67.22	E	100
896	30.2	19.84	64.16	E	100
897	30.6	66.21	41.20	E	100
898	30.6	10.84	47.16	E	100
899	30.8	91.95	83.26	E	100
900	31.0	-7.78	57.82	E	100
901	31.1	49.05	43.01	E	100
902	31.2	61.69	55.48	E	100

Number	Diameter (km)	Lon. (°)	Lat. (°)	Class	Rim burial percentage (%)
903	31.2	1.83	75.19	E	100
904	31.3	69.46	46.20	E	100
905	31.3	44.05	79.43	E	100
906	31.3	3.73	35.80	E	100
907	31.5	-36.72	69.01	E	100
908	31.8	40.45	57.94	E	100
909	31.9	-75.18	64.57	E	100
910	32.2	36.32	45.64	E	100
911	32.2	128.57	76.05	E	100
912	32.4	-73.71	73.26	E	100
913	32.6	38.18	68.84	E	100
914	33.1	24.81	52.81	E	100
915	33.3	40.48	54.57	E	100
916	33.6	53.83	45.74	E	100
917	33.8	-6.43	78.14	E	100
918	34.2	80.33	80.14	E	100
919	34.2	55.61	62.29	E	100
920	34.4	-31.47	76.59	E	100
921	34.6	12.07	51.39	E	100
922	35.0	69.69	66.73	E	100
923	35.1	-43.86	70.62	E	100
924	35.1	99.52	79.62	E	100
925	35.4	3.22	77.43	E	100
926	36.0	62.22	43.93	E	100
927	36.0	10.00	37.46	E	100
928	36.4	-6.68	75.38	E	100
929	36.9	15.03	46.97	E	100
930	37.1	-40.71	72.68	E	100
931	37.6	-32.08	56.13	E	100
932	37.8	69.28	68.36	E	100
933	38.3	71.17	45.70	E	100
934	38.6	13.49	57.74	E	100
935	39.1	49.00	48.90	E	100
936	39.1	71.91	52.42	E	100

Number	Diameter (km)	Lon. (°)	Lat. (°)	Class	Rim burial percentage (%)
937	39.2	59.44	77.73	E	100
938	39.3	26.16	55.47	E	100
939	39.4	15.99	54.47	E	100
940	39.4	-38.21	69.38	E	100
941	39.7	-36.81	78.00	E	100
942	39.8	-50.60	75.35	E	100
943	40.0	-6.80	75.34	E	100
944	40.2	55.54	75.69	E	100
945	40.3	-16.54	73.98	E	100
946	40.6	4.03	38.93	E	100
947	40.6	-50.27	71.23	E	100
948	40.9	18.23	71.52	E	100
949	41.6	53.58	76.80	E	100
950	42.5	29.55	59.48	E	100
951	42.7	80.22	61.56	E	100
952	42.9	91.21	79.92	E	100
953	43.1	-78.22	74.64	E	100
954	43.1	-56.54	81.12	E	100
955	43.6	65.36	62.72	E	100
956	43.6	8.05	36.16	E	100
957	43.7	47.44	38.22	E	100
958	44.1	-15.82	66.30	E	100
959	44.1	52.12	75.81	E	100
960	44.5	-88.19	87.52	E	100
961	44.5	39.66	43.89	E	100
962	44.7	117.53	85.89	E	100
963	44.8	96.59	41.17	E	100
964	45.5	-13.41	70.14	E	100
965	46.1	82.46	71.84	E	100
966	46.2	-70.56	65.29	E	100
967	47.2	18.58	60.32	E	100
968	47.7	64.43	81.58	E	100
969	50.5	33.89	55.31	E	100
970	51.0	19.30	59.31	E	100

Number	Diameter (km)	Lon. (°)	Lat. (°)	Class	Rim burial percentage (%)
971	51.7	77.24	82.47	E	100
972	52.1	119.03	80.43	E	100
973	52.8	-56.18	72.32	E	100
974	53.3	59.08	41.57	E	100
975	53.6	-4.77	57.46	E	100
976	54.0	30.80	53.75	E	100
977	54.7	29.87	54.72	E	100
978	55.2	-17.64	83.94	E	100
979	55.2	6.76	36.68	E	100
980	55.5	80.81	41.06	E	100
981	56.3	31.99	41.82	E	100
982	56.5	83.68	83.26	E	100
983	56.6	-0.77	70.89	E	100
984	56.6	-46.72	81.63	E	100
985	56.8	64.33	43.45	E	100
986	57.1	-0.57	62.19	E	100
987	58.3	3.05	80.22	E	100
988	59.6	-66.19	68.66	E	100
989	59.7	43.68	81.47	E	100
990	59.9	-7.76	85.84	E	100
991	60.0	86.04	66.89	E	100
992	61.0	-21.88	86.75	E	100
993	61.7	-10.94	74.33	E	100
994	62.5	79.55	78.00	E	100
995	62.6	-92.91	70.64	E	100
996	62.6	125.68	70.92	E	100
997	63.5	-28.54	65.05	E	100
998	64.0	65.28	45.65	E	100
999	64.8	48.72	41.61	E	100
1000	66.2	38.56	70.69	E	100
1001	67.8	48.48	60.44	E	100
1002	69.7	-82.93	72.86	E	100
1003	71.1	-90.33	77.00	E	100
1004	71.3	50.79	71.71	E	100

Number	Diameter (km)	Lon. (°)	Lat. (°)	Class	Rim burial percentage (%)
1005	72.5	85.54	73.38	E	100
1006	73.9	59.59	58.99	E	100
1007	76.2	65.52	54.42	E	100
1008	77.8	60.56	66.65	E	100
1009	79.1	3.72	67.10	E	100
1010	83.7	-29.29	56.43	E	100
1011	85.2	57.11	45.08	E	100
1012	90.6	-83.45	70.67	E	100
1013	90.7	-24.53	74.26	E	100
1014	101.6	48.26	59.31	E	100
1015	102.8	36.54	60.33	E	100
1016	109.1	107.47	77.35	E	100
1017	109.7	0.50	37.65	E	100
1018	144.6	41.53	48.70	E	100
1019	156.2	60.50	66.76	E	100
1020	163.0	58.94	57.65	E	100
1021	177.2	-16.77	69.47	E	100
1022	202.4	28.08	74.22	E	100

B.2 Lava Flow Thickness Estimation Results

Table B.2: Lava flow thickness estimation results on Mercury from craters with rims fully exposed. D_{int}: initial crater diameter, kt_{c}: product of diffusivity and time between crater formation and lava emplacement, kt_{l}: product of diffusivity and time after lava emplacement, T_{ext}: lava flow thickness exterior to the crater rim, T_{int}: lava flow thickness interior to the crater rim, z_0: vertical offset.

Number	Diameter (km)	Lon. (°)	Lat. (°)	D_{int} (km)	kt_{c} (m^2)	kt_{l} (m^2)	T_{ext} (m)	T_{int} (m)	z_0 (m)
1	11.4	91.94	70.21	10.0	500	1109615	164	852	165
2	13.5	61.18	39.27	11.3	582316	360354	23	936	10
3	16.9	-28.53	60.23	16.2	500	250000	228	1380	214
4	18.6	44.56	36.95	16.6	1700180	439403	121	1279	122
5	20.9	30.25	40.67	18.6	500	1907414	314	1471	313
6	21.8	-85.79	82.62	21.0	500	159565	67	949	45
7	22.8	-109.10	71.38	20.9	500	1000000	69	680	47
8	29.6	51.98	54.26	29.4	39900	55200	250	545	285
9	30.7	-134.65	83.57	30.2	500	1257722	84	910	99
10	30.7	-89.03	63.72	30.6	500	548298	231	693	231
11	32.8	-22.02	58.06	32.5	500	50000	274	1352	275
12	34.9	-104.70	70.32	34.4	500	3028371	234	1636	229
13	40.8	27.09	49.15	39.0	500	1200000	175	900	184
14	45.4	21.12	40.88	45.4	3019529	2444347	204	1592	200

Number	Diameter (km)	Lon. (°)	Lat. (°)	D_{int} (km)	kt_{c} (m^2)	kt_{l} (m^2)	T_{ext} (m)	T_{int} (m)	z_0 (m)
15	50.9	-5.40	33.78	47.0	500	3500000	216	1485	209
16	54.6	-26.46	57.29	51.0	500	4529110	117	1735	69
17	56.1	-90.52	64.67	54.0	500	2500000	292	1662	292
18	64.5	-23.85	46.75	64.2	400000	350000	262	823	238
19	70.8	-99.94	66.31	69.4	500	5043504	465	937	395
20	72.6	-31.50	61.04	71.1	500	5851998	378	1441	378
21	83.4	-10.78	53.53	82.0	500	221220	536	637	520

Table B.3: Uncertainties of the lava flow thickness and the diffusivity-time product after lava flooding. $T_{\text{ext\_min}}$ and $T_{\text{ext\_min}}$: minimum and maximum values of T_{ext}. $kt_{\text{l\_min}}$ and $kt_{\text{l_max}}$minimum and maximum values of kt_{l}.

Number	RMS misfit (m)	$T_{\text{ext\_min}}$ (m)	$T_{\text{ext\_max}}$ (m)	$kt_{\text{l\_min}}$ (m^2)	$kt_{\text{l\_max}}$ (m^2)
1	34	144	184	1109615	2400000
2	33	9	41	36035	1100000
3	29	184	287	25000	900000
4	13	75	183	175761	790925
5	13	260	387	1716672	3242603
6	46	5	149	15957	600000
7	45	7	151	700000	3000000
8	62	170	356	5500	500000
9	49	3	192	125772	2263899
10	28	149	340	54830	1041766
11	33	190	386	5000	250000
12	15	148	350	302837	5753904
13	51	84	297	120000	2280000
14	26	108	333	977739	4399825
15	29	119	346	1050000	4900000
16	38	17	250	452911	8605309
17	45	190	428	250000	4750000
18	58	156	404	35000	665000

Table B.3: Uncertainties of the lava flow thickness and the diffusivity-time product after lava flooding. $T_{\text{ext\_min}}$ and $T_{\text{ext\_min}}$: minimum and maximum values of T_{ext}. $kt_{\text{l\_min}}$ and $kt_{\text{l_max}}$minimum and maximum values of kt_{l}.

Number	RMS misfit (m)	$T_{\text{ext\_min}}$ (m)	$T_{\text{ext\_max}}$ (m)	$kt_{\text{l\_min}}$ (m^2)	$kt_{\text{l\_max}}$ (m^2)
19	57	357	609	504350	9078307
20	65	269	523	2925999	11118796
21	90	425	685	22122	420318